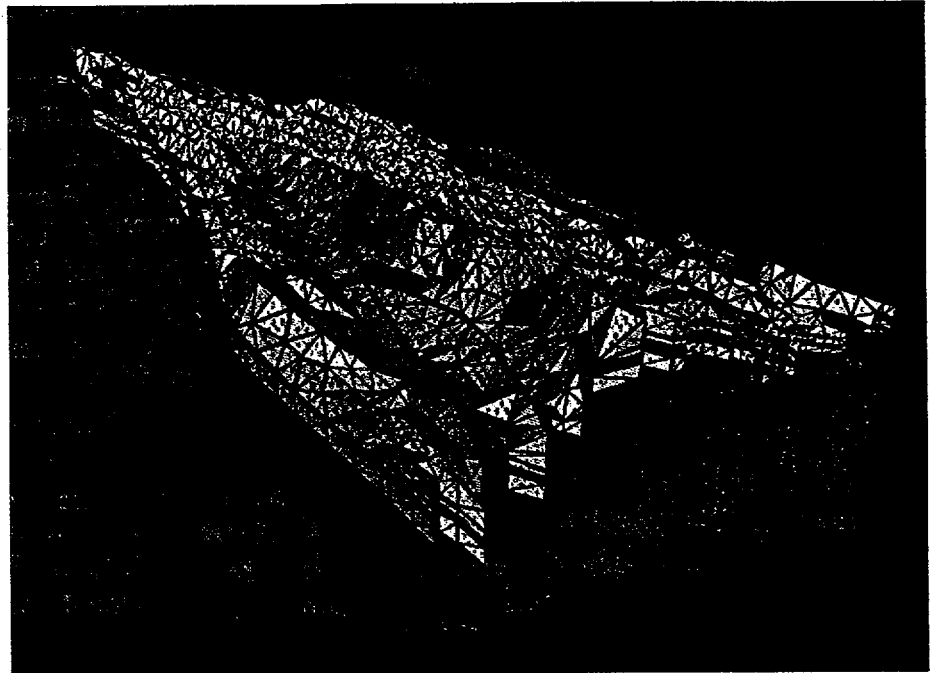


# Milestone SP25BM3

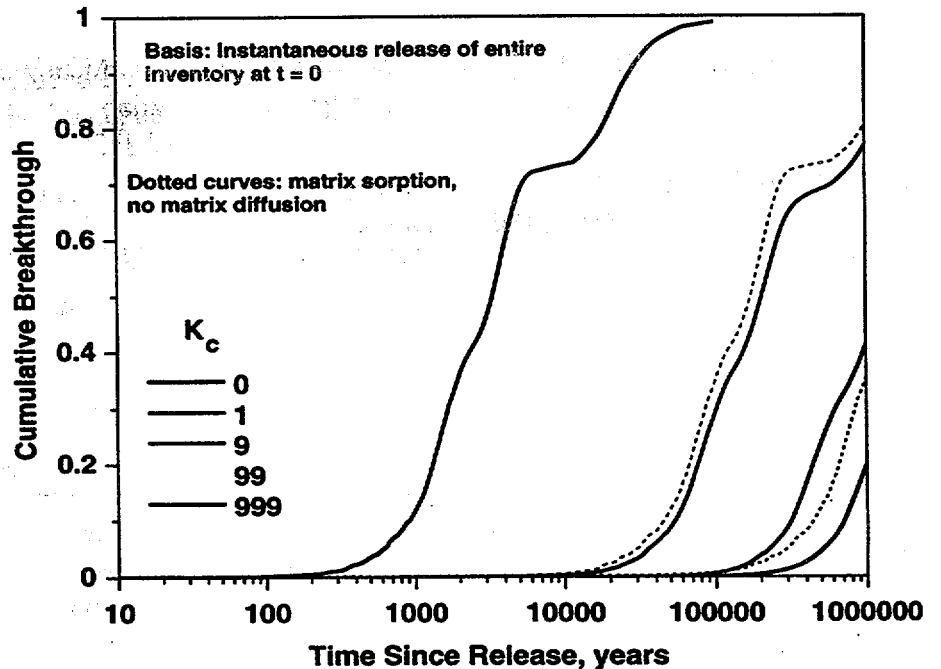
## The Site-Scale Unsaturated Zone Transport Model of Yucca Mountain



Bruce A. Robinson  
Andrew V. Wolfsberg  
Hari S. Viswanathan  
Gilles Y. Bussod  
Carl W. Gable  
Arend Meijer

September 29, 1997

Pu Cumulative Breakthrough, Case 6541, Base Infiltration Map



Los Alamos

9801210002 980112  
PDR WASTE  
WM-11 PDR

~ Part 1



TRW Environmental  
Safety Systems Inc.

1180 Town Center Drive  
Las Vegas, NV 89134  
702.295.5400

WBS: 1.2.3.4.1.5.1  
QA: N

Contract #: DE-AC01-91RW00134  
LV:SPO:PP.TAG.08/97-089

August 29, 1997

Stephan J. Brocoum, Assistant Manager  
for Licensing  
U.S. Department of Energy (DOE)  
Yucca Mountain Site Characterization Office  
P.O. Box 30307  
North Las Vegas, NV 89036-0307

Attention: Technical Publications Management

Dear Dr. Brocoum:

Subject: Completion of Level 3 Fiscal Year (FY) 1997 M&O Milestone  
SP25BM3, "The Site-Scale Unsaturated Zone Transport Model of  
Yucca Mountain," Work Breakdown Structure  
(WBS)1.2.3.4.1.5.1

Three copies of the above-referenced deliverable are being submitted for  
deliverable acceptance review in accordance with YAP-5.1Q. This action  
completes delivery of Milestone SP25BM3. A second YAR form is also  
included for the related deliverable SP342PM3. This YAR may be approved  
when acceptance of SP25BM3 is completed.

If you have any questions regarding this deliverable, please contact Roger  
Henning at (702) 295-5743, or me at (702) 295-5604.

Sincerely,

Larry R. Hayes, Manager  
Site Evaluation Program Operations  
Management and Operating Contractor

LRH/clt

Revision Date: 08/26/97

FY 1997 LEVEL 3 BASELINE DELIVERABLE SP25BM3

TO: DWIGHT HOXIE (Office Manager)

DATE: 8/28/97

Reviewer/Tech. Lead (assigned by Office Manager): ROGER HENNING

Due Date for Completion of Review: 8/29/97

SEE INSTRUCTIONS/GUIDANCE ON ATTACHED SHEET.

- Review complete on 8/29/97 (Date). Initial on  
Appropriate Line
- Comments forwarded to Office Manager? Yes RH  
No Comments
- "Roadmap" showing where deliverable acceptance criteria are addressed in deliverable is included with deliverable. Yes RH  
Hold for Revision
- For "synthesis reports," requirements of Jones to Foust letter are met? N/A RH  
Yes       
Hold for Revision
- Deliverable meets all technical and administrative requirements on the PPS sheet and is of the editorial and technical quality to allow release to DOE, regulators, the public, & the general scientific community? Yes RH  
Hold for Revision

Reviewer Signature Roger Henning Date 8/29/97

Office Manager approval for submittal Dwight Hoxie Date 08-29-97

Baseline Deliverable Due Date 8/29/97 (Date Deliverable should be at TPM)

Deliverable Received by SPO on                      Date Sent to TPM

**INSTRUCTIONS:** Reviewers are responsible for reviewing the attached deliverable against criteria/ description on the PPS sheet (also attached) and determining whether the deliverable should be forwarded to DOE for the YAP-5.1Q acceptance review. When the review is complete, reviewers complete the questions on the form by initialing on the appropriate line and sign at the bottom. Any comments, concerns, or recommendations arising from the review are forwarded to the Office Manager/Tech. Lead by the reviewer for possible action with the organization responsible for the deliverable. When any comments are resolved and the Office Manager determines the deliverable is ready for submission to DOE, the Office Manager signs the form and returns the form to Terry Grant (MS 423/822C).

- Completed Level 3 deliverables must be submitted in final form, ready to be submitted as an M&O document to DOE. Level 3 documents cannot contain any notations on the title page or on headers or footers that indicate the document is a "draft" or is otherwise not a final M&O product.
- Five copies of the final document are needed on the due date for the submission process.
- If the Level 3 document might be considered a **synthesis report** by DOE, review the requirements in the attached letter (Jones to Foust). The requirements in this letter were cited by DOE in their recent rejection of the Natural Resources report as some of the reasons for rejection. This letter contains some specific requirements (e.g., Executive Summary) and general guidance on content, level of detail, and approach.
- The "roadmap" is usually a table that lists each criterion from the PPS sheet for the deliverable and shows the text location (e.g., page number, section number, and/or figure number) in the deliverable where the criterion is addressed. The roadmap may be incorporated into the deliverable document or submitted as a separate item. If a criterion is not covered in the report for some reason (e.g., submission of a TDIF), the reasons for this should also be explained in the roadmap. Reviewers and Office Managers should carefully review the roadmap to assure that all requirements on the PPS are listed and that they are adequately addressed. YAP-5.1Q requires that the DOE reviewers use the PPS as the source of criteria for their review.
- The purpose of the review is determine whether the document is at a level of quality and completeness that acceptance by the DOE reviewers can reasonably be anticipated in the YAP-5.1Q review process. Editorial and technical quality should be at a level to allow for publication by the Project and/or release to the public.
- The review process does not automatically include a publication release review (YAP-30.12 review). If a publication clearance is needed, this must be indicated at the time of submission. Five additional copies of the document are required for publication clearance (it is a separate request and process).



**Department of Energy**  
Office of Civilian Radioactive Waste Management  
Yucca Mountain Site Characterization Office  
P.O. Box 88608  
Las Vegas, NV 89193-8608

NOV 15 1995

L. Dale Foust, M&O, Las Vegas, NV  
Robert W. Craig, USGS, Las Vegas, NV

**U.S. DEPARTMENT OF ENERGY (DOE) POLICY ON SYNTHESIS REPORTS  
(SCPB: N/A)**

The production of synthesis reports will represent a major effort for Assistant Manager for Scientific Programs during fiscal year (FY) 1996. The DOE focus is on those synthesis reports that summarize work at the Site Characterization Plan investigation level. However, these same guidelines are relevant to all technical reports produced in Work Breakdown Structure 1.2.3, regardless of milestone level. The FY 1996 planning effort has included attempts to clarify the intended content and use of synthesis reports. Acceptance criteria for each report will be included in the Planning and Control System. However, this letter addresses a need to provide a higher-level guidance on DOE expectations relative to synthesis reports. This guidance is consistent with the draft policy from the Yucca Mountain Quality Assurance Division (enclosure).

The first concern must be with the quality and completeness of the synthesis report. Recent documents produced for DOE, such as the Technical Basis Report for Surface Processes, have been criticized for being too narrow in scope and not including data and analysis from the published literature. While synthesis reports need to focus on the work that has been conducted by the Yucca Mountain Site Characterization Office (YMSCO), it is also necessary to include discussion of other relevant work, including work with which YMSCO disagrees. References to non-YMSCO work should be more than simple citations and should be broad enough in scope to identify conclusions from these studies that are relevant to the YMSCO work. In some cases, this may require reproduction of some or all of the data from the referenced report. In other cases, a simple restatement of the conclusions with a brief discussion of supporting data may be sufficient. As much data as possible should be incorporated into the synthesis report by reference. However, the reports should be stand-alone documents. This may require some repetition of data presentation with accurate citations. It is clear that the authors of synthesis reports will be asked to address many concerns, some of which are conflicting.

NOV 15 1995

Synthesis reports should be written so that a non-YMSCO scientist, knowledgeable in the topic of the report, can reconstruct the path from the basic data to the report's conclusions. This is what is meant by stand-alone document. Different amounts of detail may be required for different studies and reports. In addition to the detailed technical discussion, the synthesis report should contain an executive summary, written for the general reader, that clearly identifies the purpose of the study and the significance of the conclusion for project objectives.

Synthesis reports should include the identification of qualified and non-qualified data. A discussion must be provided that clearly differentiates qualified and non-qualified data, including non-qualified data from the published literature. The discussion must also identify qualified and non-qualified computer software used for modeling or data analysis. One way to do this is to separate the reference lists and tables into "qualified" and "unqualified" sections.

The conclusions of the report must also be separated into two categories, those that can be drawn from qualified data only and those that can be drawn if the entire data set is considered. Following the controls discussed above will enable the reports to be properly classified as "qualified." The requisite traceability should be provided through inclusion of record accession numbers and Automated Technical Data Tracking system numbers for all data cited or used in the synthesis report.

If you have any questions please call me at 794-7613 or Dennis R. Williams at 794-7968.



Susan B. Jones  
Assistant Manager  
for Scientific Programs

AMSP:RLR-478

Enclosure:  
Draft Letter

cc w/encl:

C. T. Statton, M&O, Las Vegas, NV  
L. R. Hayes, M&O, Las Vegas, NV  
R. D. Rogers, M&O, Las Vegas, NV  
W J. Boyle, YMSCO, NV  
S. J. Brocoum, YMSCO, NV

**Traceability to Criteria for Milestone SP25BMD 3** *01/18 8/21/97*

The table below provides a road map between the requirements listed in the Criteria Statement for this milestone and the specific locations in the document where these requirements are met.

This table is in the executive summary of the report.

**TECHNICAL REQUIREMENTS**

<b>CRITERIA</b>	<b>TEXT LOCATION</b>
<p>This report will include a conceptual model of the transport of radionuclides in the unsaturated zone at Yucca Mountain, including 2- and 3-D integrated transport calculations and sensitivity analyses.</p>	<p>Conceptual model: 4.3, 6.5.2                      2D integrated transport calculation: Chapter 8.                      2D sensitivity analyses: Sections 8.5, 8.6, 8.7, 8.8, 8.9                      3D integrated transport calculations: Chapter 9                      3D Sensitivity analyses: Sections 9.4-9.7</p>
<p>Both equivalent continuum and dual permeability calculations will be made, incorporating discrete structural features as available and appropriate.</p>	<p>Equivalent Continuum calculations: Sections 4.6, 11.4, 11.8                      Dual Permeability Calculations: Sections 4.4, 4.7, 5.4, 5.5, 6.7, 6.9-6.12, 8.5-8.11, 9.4-9.7, 10.6-10.9, 12.9                      Incorporation of discrete structural features: Sections 3.3, 3.4, 6.5, Included in all 2D and 3D dual permeability calculations.</p>
<p>The model will do the following:</p>	
<p>a) Incorporate and consider isotopic data which are indicative of processes and rates of fluid flow or residence times in the unsaturated zone.</p>	<p>Chapter 6.                      Processes: 6.5, 6.7-6.12                      Rates and Residence Times: 6.10-6.12</p>
<p>b) Draw upon the Report on Summary of Geochemistry/Transport Laboratory Tests to provide defensible values for important transport processes and parameters including:</p>	
<p>1) Sorption and Diffusion Coefficients</p>	<p>8.6, 8.7, 8.10, 9.4, 9.6, 9.7, 11.7</p>

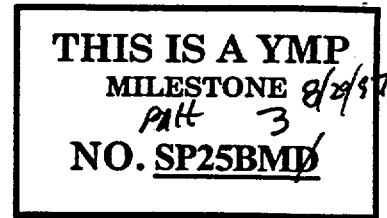
2) Radionuclide solubility and speciation	10.5, 11.4, 11.7
3) Colloids as controlled by relevant thermal effects and water chemistry.	8.10
c) Rely heavily on input from the 3-D mineralogical model of Yucca Mountain.	2.2-2.5, 3.4, 6.5, 8.6, 12.5-12.9
Update 3-D transport simulations for radionuclides including, but not limited to:	
Np	5.5, 8.5-8.7, 8.9, 9.4, 9.5, 10.7, 11.8, 12.9
Pu	8.10, 10.9
Tc	5.5, 8.5-8.7, 8.9, 9.4, 9.5, 10.6
under ambient	5.5, 8.5-8.7, 8.9, 9.4, 9.5, 10.6-10.9
and thermally perturbed	11.8
for two future climates and accompanying infiltration fluxes and effects on recharge	8.7, 8.11, 9.4, 9.5, 11.8
The report will be coupled to appropriate	
near-field source term	10.4, 10.5
and thermal models	11.7, 11.8
The deliverable will be prepared in accordance with OCRWM approved quality assurance procedures implementing requirements of the Quality Assurance Requirements Description.	Done
The product shall be developed on the basis of the best technical data, including both Q and non-Q data. The Q status of data used and cited in the report shall be appropriately noted.	QA description of software and data in acknowledgments and in each chapter.
Stratigraphic nomenclature used shall be consistent with the Reference Information Base section 1.12(a): Stratigraphy-Geologic Lithologic Stratigraphy.	Throughout milestone, Table 15.1
References to data used in the report shall include record Accession Numbers or Data Tracking Numbers when available.	QA description of data in acknowledgments and in each chapter.

<p>Technical data contained within the deliverable and not already incorporated in the Geographic Nodal Information Study and Evaluation System (GENISES) shall be submitted for incorporation into the GENISES in accordance with YQP-SIII.3Q.</p>	N/A
<p>Verification of technical data submittal compliance shall be demonstrated by including as part of the deliverable:</p> <p>a) A copy of the Technical Data Information Form generated identifying the data in the Automated Technical Data Tracking system, and</p> <p>b) a copy of the transmittal letter attached to the technical data transmittal to the GENISES Administrator.</p>	<p>a) N/A</p> <p>b) done.</p>

# Los Alamos

## NATIONAL LABORATORY

*Earth and Environmental Sciences Division*  
EES-13 — Nuclear Waste Management R&D  
Mail Stop J521, Los Alamos, New Mexico 87545  
Phone (505) 667-9768, Fax (505) 667-1934



August 29, 1997

EES-13-08-97-1666

Larry Hayes  
TRW Environmental Safety Systems, Inc.  
Mail Station 423  
1180 Town Center Drive  
Las Vegas, NV 89134

ATTENTION: T. A. Grant

*3 part 8/29/97*

Request for approval of milestone SP25BMD, "Draft Unsaturated Zone Site Transport Model," by B. A. Robinson et al.

Dear Mr. Hayes:

*part 8/29/97*

In compliance with YAP-30.12, milestone SP25BMD, "Draft Unsaturated Zone Site Transport Model," by B. A. Robinson et al. is enclosed for programmatic review.

This paper documents work done under WBS 1.2.3.4.1.5.1; does not fulfill a Level II milestone requirement; and has undergone technical and policy review.

In compliance with YAP-SIII.3Q, there are no new data in this milestone. A table, which lists the data tracking numbers associated with the data generated by other researchers and transmitted to Robinson et al., will be found in the milestone.

In compliance with AP 5.1Q, revision 3, I have attached a YAR form.

Sincerely,

  
Charles Harrington

CH/SHK/jr

- Enclosures:
1. Paper (5 copies)
  2. Review Sheets
  3. YAR

Cy w/enc. 1  
P. Dixon, M&O/LANL, Las Vegas, NV  
M. Staples, EES-13, J521  
J. McGoldrick, M&O/TRW, Las Vegas, NV  
M. T. Peters, M&O/WCFS, Las Vegas, NV  
T. Hirons, EM-DOE-FP, MS J521  
J. E. Young, LATA/EES-13, MS J521

Cy w/enc. 1, 2, and 3  
EES-13 File, MS J521  
S. H. Klein, CIC-1/EES-13, MS J521  
A. L. Thompson, EES-13/LV, MS J902  
B. A. Robinson, EES-5, MS F665  
A. Sanchez-Pope, ESS/EES-13, MS J521  
L. Souza, Mactek, MS J521

Encl. 2

# PUBLICATION TRAVELER

## SECTION I. (Author completes)

TITLE: Draft Unsaturated Zone Transport Model

AUTHOR(S): Robinson et al.

WBS NO: 1.2.3.4.1.5.1 UNIQUE IDENTIFIER: LA-EE-13-TIP-97-004 LOS ALAMOS DTN NO.: (If applicable) N.A.

### CHECK ONE

- STUDY PLAN
- TIP

### FOR TIPS:

- ABSTRACT
- MILESTONE (Number 3) *SP25 BMD*
- CONFERENCE PROCEEDINGS
- LA MANUSCRIPT REPORT *8/29/97*
- JOURNAL ARTICLE
- OTHER

NAME OF CONFERENCE, DATE, NAME OF JOURNAL ARTICLE, ETC.

LAHS report

## SECTION II. (TPO Completes)

I HAVE REVIEWED THE TIP OR STUDY PLAN FOR CONTENT, QUALITY ASSURANCE, AND POLICY.

COMMENTS ATTACHED:  YES  NO (If YES, a Review Sheet will be attached)

TPO: Charles D Harrington Charles Harrington 8-29-97  
Print name Signature Date

## SECTION III. (Author completes)

ALL REVIEW COMMENTS HAVE BEEN RESOLVED.

AUTHOR: \_\_\_\_\_  
Print name Signature Date

## SECTION IV. (TPO Completes)

THIS TIP OR STUDY PLAN IS ACCEPTABLE AND MAY BE PUBLISHED AS APPROPRIATE

TPO: \_\_\_\_\_  
Print name Signature Date

**Los Alamos**  
Yucca Mountain Site  
Characterization Project

# TIP/STUDY PLANS REVIEW RESULTS

## SECTION I. (Preparer completes)

UNIQUE IDENTIFIER: LA-EES-13-TIP-97-004 REVISION: 0 TITLE: Draft Unsaturated Zone Transport Model

PREPARER'S NAME: Robinson PHONE: \_\_\_\_\_ MS: \_\_\_\_\_ DUE BY: \_\_\_\_\_  
Print name

## SECTION II. (Reviewer completes)

### REVIEWER INSTRUCTIONS:

- Review the document for applicability, correctness, technical adequacy, and completeness. Additional criteria may be added.
- For TIPs, data presented are suitable for the intended use as presented in this report.
- For comments, enter the location of the section and the proposed actions on the review sheet continuation page. If "no comments," check the "No Comments" box.
- Any changes to original entries must be initialed and dated.
- After completing the review, return the review sheets to the preparer.
- After review comments have been addressed, sign, date, and return review sheet(s) to preparer, if applicable.

Comments Attached

I HAVE FOLLOWED THE INSTRUCTIONS FOR REVIEWING THIS DOCUMENT.

No Comments

REVIEWER: Kay Birdsell Charles Harrington for J521 8-29-97 7-1855  
Print name Signature MS or location Date Phone

## SECTION III. Signature below indicates that all comments have been resolved satisfactorily.

N/A



REVIEWER:

[Signature]  
Signature

8/29/97  
Date

## **Acknowledgments**

This work was supported by the Yucca Mountain Site Characterization Office as part of the Civilian Radioactive Waste Management Program. This project is managed by the U.S. Department of Energy, Yucca Mountain Site Characterization Project.

Harold Trease, Terry Cherry, and Kathy Bower assisted in the preparation and testing of the numerical grids used in the model calculations. Guy Roemer performed some of the numerical calculations presented in the environmental isotopes chapter; Al Valocchi and Ines Triay contributed to the study in the areas of reactive transport modeling and radionuclide property values, respectively; Stephen Henderson assisted in the development of the original particle tracking code; June Fabryka-Martin provided valuable editorial comments on the  $^{36}\text{Cl}$  modeling study; and Cliff Ho performed the one-dimensional flow calculations with the TOUGH2 code that were benchmarked against the FEHM code. George Zyvoloski consulted with us regularly at all stages of the numerical simulation studies. Kay Birdsell performed a thorough review of the technical and editorial content of this report. Susan Klein, Roger Eckhardt, Laura Wolfsberg, and Angela Sanchez-Pope provided considerable assistance in the editorial phase of the writing of this report, and helped compile the QA information. Finally, the authors are grateful to Lynn Trease for her assistance in preparing this document, and to the Los Alamos YMP Project office for their support during the course of this work.

### **QA Status of Software Used in This Report**

The FEHM code is used to perform all flow and transport calculations in this report. The code is qualified in accordance with Los Alamos quality assurance requirements and is documented in (Zyvoloski et al, 1992, 1995a, 1995b). The petroleum industry standard software packages STRATAMODEL and RC<sup>2</sup> are used in the geostatistical analyses of heterogeneous materials. These are off-the-shelf software packages and are applied only to sensitivity studies in

the present study. They are non-Q with respect to YMP and Los Alamos quality assurance requirements but they follow well documented methods for geostatistical representation of – spatially varying attributes. The GEOMESH/X3D grid generation toolkit, (Gable et al., 1995, Gable et al., 1996, Trease et al., 1996) is non-Q with respect to YMP and Los Alamos quality assurance requirements. However, version control software tracking procedures identical to those used for the Q code FEHM are followed. GEOMESH/X3D utilizes well established procedures to insure robust mesh generation results and to insure traceability of changes to the software. A suite of test problems has been developed and all new releases are verified against the test suite.

Many sources of data are used in this report. Often, results from other modeling and synthesis studies such as Bodvarsson et al. (1997) are used as input to our modeling studies. If the results of those studies can not be certified as Q, then our results can not be certified as Q either. There are also numerous references to personal communication: they are non-Q.

### Data Quality Summary

REFERENCE	DATA STATUS (Q/non-Q)	DTN	CHAPTER(S) WHERE REFERENCE CITED	COMMENT
Altman et. al., 1996, "Flow Calculations for Yucca Mountain Ground Water Travel Time (GWTT-95). Technical Report SAND96-0819, Sandia National Laboratories, 1996	non-Q	No DTN Assigned	12	No DTN Assigned
Bertetti et. al., 1996 "Neptunium (V) Sorption Behavior on clinoptilolite, Quartz, and Montmorillonite, Mat. Res. Soc. Symp., Proc., Vol. 412, 631-638, 1996			11	

<b>Bodvarsson et. al., 1997</b> "The Site-Scale Unsaturated Zone model of Yucca Mountain, Nevada, For the Viability Assessment, LBL Technical Report LBNL-40378	Q	LB970601233129.001	3, 5, 6, 8, 9, 10,12	No DTN assigned. Hydrologic property sets computed in this report are used throughout the present study.
<b>Buesch et. al., 1996,</b> "Revised Stratigraphic nomenclature and macroscopic identification of Lithostratigraphic units of the Paintbrush Group exposed at Yucca Mountain, Nevada, USGS Survey Open-File Report 94-496, 1996	Q	GS941208314211.064	6	
<b>Chipera et. al., 1997,</b> "Preliminary Three Dimensional Mineralogical Model of Yucca Mountain, Nevada, YMP Milestone SP321AM4"	non-Q	Not Assigned	2, 3, 8, 12	No DTN assigned
<b>Chipera et. al., 1997b</b> "Mineralogic Variation in Drill Holes USW NRG-6, NRG-7-7a, SD-7, SD-9, SD-12, and UZ#14: New Data from 1996-1997 Analysis Los alamos National Laboratory YMP Deliverable SP321BM4"	Q	LADV831321AQ97.001	2,8,12	
<b>Clayton, et. al., 1997,</b> "ISM2.0: A 3-D geological framework and integrated site model of Yucca Mountain: Version ISM1.0, Doc ID B00000000-01717-5700-00004 Rev 0, MOL. 19970122.0053, CRWMS M&O	Q		3	By agreement with DOE and NRC accepted as Q even though it utilizes some non-Q data



Levy et. al., 1997, "Investigations of Structural Controls and Mineralogic Associations of Chlorine-36 fast pathways in the ESF,. Yucca Mountain Project milestone report SP2301M4	Q	LASL831222AQ97.001	6	
Nitsche et. al., 1993, "Measured Solubilities and Speciations of Neptunium, Plutonium, and Americium in a Typical Groundwater (J-13) from the Yucca Mountain Region", Los Alamos National Laboratory Report Number LA-12562-MS, July 1993	non-Q non-Q	LA000000000012.001 LA000000000012.002	11	Accession Nos. MOL.19950705. 0241 NNA.19930507. 0136, and MOL.19950621. 0265, and MOL.19950711. 0329
Ogard and Kerrisk, 1984, "Groundwater Chemistry along flow paths between a proposed repository site and the accessible environment, Los Alamos National Laboratory Report LA-10188-MS, 1984	non-Q	LA000000000038.001	11	Accession No. NNA.19870406. 0021
Tait et. al., 1996, "Sorption as a function of groundwater chemistry to elucidate sorption mechanisms, Los Alamos National Laboratory Yucca Mountain Site Characterization Project Milestone 3219, 1996	Q Q	LAIT831341AQ95.001 LAIT831341DQ95.002	11	
Triay et. al., 1996a, "Summary and Synthesis Report on Radionuclide Retardation for the Yucca Mountain Site Characterization Project, Los Alamos National Laboratory YMP Milestone Report 3784	Q	LAIT831341AQ96.001	8,9, 10, 11, 12	
Triay et. al, 1996b, "Radionuclide Sorption in Yucca Mountain Tuffs with J-13 Well Water,: neptunium, Uranium, and Plutonium, Los alamos National Laboratory Yucca Mountain Site Characterization Project" Milestone 3338, Technical Report LA-12956-MS	Q	LAIT831341AQ96.001 *	8, 9,10, 11, 12	* DTN super- sedes DTN LA00000000010 4.001
Triay et. al., 1996c, "Batch Sorption Results for neptunium transport through Yucca Mountain tuffs, Los alamos National Laboratory Yucca Mountain Site Characterization Project Milestone 3349, Technical Report LA-12961-MS	Q	LAIT831341AQ96.001 *	8,9, 10, 11, 12	*DTN super- sedes DTN LA00000000009 0.001

Triay et. al., 1996d, "Comparison of Neptunium Sorption Results using batch and column techniques, Los Alamos National laboratory Yucca Mountain Site Characterization Project Milestone 3041, Technical Report LA-12958-MS	Q	LA000000000106.001	8, 9, 10, 11, 12	DTN Accession No. MOL.19950630.0300
Triay et. al., 1997, "Summary Report on Geochemistry/Transport Lab Tests, Los Alamos National Laboratory Milestone SP23QMD	Q	LAIT831341DQ97.003	10	
Yang et. al., 1992, "Flow and Transport Through Unsaturated Rock - Data From Two Test Holes, Yucca Mountain, Nevada, proc. Third International Conference on High-Level Radioactive Waste Management, Las Vegas, NV, 1992	Q		6	
Yang, et. al., 1996, Interpretations of Chemical and Isotopic Data From Boreholes in the Unsaturated Zone at Yucca Mountain, Nevada, USGS Water-Resources Investigations Report WRIR 96-4058	Q		4, 6, 11	
Yang et. al., 1997, Hydrochemical investigations and geochemical modeling in characterizing the unsaturated zone at Yucca Mountain, Nevada, ( <i>in preparation</i> ).	non-Q	Indeterminate	6,7	Not Available Yet
Zelinski and Clayton, 1996, "A 3-D geological framework and integrated site model of Yucca Mountain: Version ISM1.0, Doc ID B00000000-01717-5700-00002 Rev 1", CRWMS M&O	non-Q		2, 3	



## Table of Contents

---

# Table of Contents

Chapter 1 - Executive Summary .....	1-1
1.1 Overview .....	1-1
1.2 Incorporation of Mineralogic Model into Flow and Transport Simulations .....	1-2
1.3 Mesh Generation .....	1-3
1.4 Particle Tracking .....	1-4
1.5 Hydrologic Property Sets .....	1-5
1.6 Environmental Isotopes and the Hydrologic System .....	1-7
1.7 Water Chemistry .....	1-8
1.8 Two-Dimensional Radionuclide Transport Simulations .....	1-10
1.9 Three-Dimensional Radionuclide Transport .....	1-11
1.10 Unsaturated Zone Performance Predictions .....	1-12
1.11 Reactive Transport of <sup>237</sup> Np with Repository Heat .....	1-13
1.12 Incorporation of Geostatistics into Flow and Transport Simulations .....	1-14
1.13 Traceability to Criteria for Milestone SP25BM3 .....	1-16
Chapter 2 - Incorporation of the Mineralogic Model into the Site-Scale Flow and Transport Model .....	2-1
2.1 Abstract .....	2-1
2.2 Mesh Generation .....	2-2
2.3 Software and Data QA Status .....	2-2
2.4 Motivation for the Current Mineralogic and Hydrologic Model .....	2-3
2.5 Mineralogic Model .....	2-6
2.6 Conclusions .....	2-11
Chapter 3 - Mesh Generation .....	3-1
3.1 Abstract .....	3-1
3.2 QA Status of Software and Data .....	3-1
3.3 Unsaturated Zone Computational Mesh from Stratigraphic Model .....	3-3
3.3.1 Mesh Generation from ISM Input .....	3-4
3.3.1.1 Import ISM Data into GEOMESH/X3D .....	3-4
3.3.2 Quality Testing and Correcting of ISM TINs .....	3-4
3.3.2.1 Identify Faults .....	3-6
3.3.2.2 Define polygonal subset of TIN surface .....	3-6
3.3.2.3 Refine TIN surface grids in and adjacent to faults .....	3-7
3.3.2.4 Define upper and lower boundary truncation surfaces .....	3-7
3.3.2.5 Define minimum layer thickness .....	3-9
3.3.2.6 TIN Sheets Stacked and Converted to Prisms .....	3-9
3.3.2.7 Convert Prisms to Tetrahedra .....	3-10
3.3.2.8 Extract a Two-Dimensional Plane .....	3-10
3.3.2.9 Convert Hybrid Grid to Triangles .....	3-10
3.3.2.10 Clip Mesh to Area of Interest .....	3-11
3.3.2.11 Optimize Mesh For Computation .....	3-11
3.3.2.12 Mapping Properties From Three-Dimensional Mineral	

## Table of Contents

	Distribution .....	3-15
3.3.3	Generation of FEHM Input Files .....	3-16
3.3.3.1	Compute Finite Volume Matrix Coefficients .....	3-16
3.3.3.2	Compute Area Coefficients of Surface .....	3-16
3.3.3.3	Output Information for Boundary Conditions and Material Properties .....	3-16
3.3.4	Mesh Quality Assurance Steps .....	3-16
3.4	Computational Grids Used in the Present Study .....	3-17
3.4.1	Three-Dimensional Unsaturated Zone Grid .....	3-17
3.4.2	Two-Dimensional Unsaturated Zone Grid .....	3-17
3.5	Conclusions .....	3-19
<hr/>		
Chapter 4 -	Particle Tracking .....	4-1
4.1	Abstract .....	4-1
4.2	Software and Data QA Status .....	4-2
4.3	Introduction: Conceptual Model For Particle Transport .....	4-3
4.4	Mathematical Development .....	4-6
4.4.1	Dispersion .....	4-9
4.4.2	Matrix Diffusion .....	4-11
4.4.3	Radioactive Decay .....	4-14
4.4.4	Particle Sources and Sinks .....	4-14
4.4.5	Transient Flow Fields .....	4-15
4.4.6	Dual-Permeability Formulation .....	4-16
4.5	Code Implementation .....	4-16
4.6	Validation .....	4-19
4.6.1	One-Dimensional Transport with Dispersion and Sorption .....	4-19
4.6.2	One-Dimensional Transport with Matrix Diffusion .....	4-21
4.6.3	Transient Wetting of a 1-D Column .....	4-22
4.6.4	Benchmarking Calculation for an Interwell Tracer Simulation .....	4-24
4.7	Applications .....	4-27
4.7.1	Dual-Permeability Transport for the Unsaturated Zone .....	4-27
4.7.2	Simulations of Environmental Isotopes in the Unsaturated Zone ...	4-30
4.7.3	Sorbing tracers with matrix diffusion .....	4-34
4.8	Conclusions .....	4-38
<hr/>		
Chapter 5 -	Property Sets .....	5-1
5.1	Abstract .....	5-1
5.2	Software and Data QA Status .....	5-2
5.3	Introduction .....	5-3
5.4	Comparison of TOUGH2 and FEHM Codes .....	5-5
5.4.1	Flow Results .....	5-8
5.4.2	Transport result .....	5-10
5.5	Screening of Hydrologic Property Sets .....	5-14
5.5.1	Case 6412a .....	5-26
5.5.2	Case 6412b .....	5-36
5.5.3	Case 6511 .....	5-36
5.5.4	Case 6521 .....	5-37

## Table of Contents

---

5.5.5 Case 6522.....	5-38
5.5.6 Case 6531a.....	5-38
5.5.7 Case 6531b.....	5-39
5.5.8 Case 6541.....	5-39
5.6 Conclusions .....	5-41
<b>Chapter 6 - Environmental Isotopes and The Hydrologic System .....</b>	<b>6-1</b>
6.1 Abstract .....	6-1
6.2 Software and Data QA Status .....	6-2
6.3 Introduction .....	6-4
6.3.1 Implications .....	6-5
6.4 Background .....	6-6
6.4.1 Previous Chlorine-36 Studies at Yucca Mountain and Their Implication for Flow and Transport Modeling .....	6-6
6.4.2 Infiltration Studies .....	6-9
6.4.3 Present Study Summary.....	6-10
6.5 Hydrogeologic Setting .....	6-11
6.5.1 Stratigraphy .....	6-11
6.5.2 Conceptual model of flow and transport .....	6-12
6.6 Chlorine-36 Study .....	6-15
6.6.1 Background .....	6-15
6.6.2 Chlorine-36 input.....	6-15
6.6.3 ESF Data .....	6-18
6.7 Flow and Transport Model .....	6-18
6.7.1 Numerical Flow and Transport Model: FEHM .....	6-18
6.7.2 Transient Signals of Isotopic Sources .....	6-19
6.8 Simulated Systems .....	6-20
6.8.1 Overview .....	6-20
6.9 Carbon-14 Study .....	6-22
6.9.1 Background .....	6-22
6.9.2 Carbon-14 Data .....	6-23
6.9.3 Carbon-14 Input.....	6-25
6.10 Chlorine-36 Modeling: Two- and Three- Dimensional Studies .....	6-25
6.10.1 Model Description .....	6-25
6.10.2 Two-Dimensional Chlorine-36 Simulation Results .....	6-27
6.10.3 Three-Dimensional Chlorine-36 Simulation Results .....	6-34
6.10.4 South to North Trends in Potential Repository Block Region .....	6-44
6.11 Carbon-14 Modeling .....	6-51
6.12 One-Dimensional Process Level Modeling .....	6-54
6.12.1 Column Descriptions .....	6-54
6.12.2 One-Dimensional Modeling Approach.....	6-56
6.12.3 Steady-State Results .....	6-58
6.12.4 Comparisons: Three Property Sets for Steady-State and Transient Flow .....	6-65
6.13 Conclusions .....	6-71
<b>Chapter 7 - Water Chemistry .....</b>	<b>7-1</b>

## Table of Contents

---

7.1	Abstract .....	7-1
7.2	Software and Data QA Status .....	7-2
7.3	Introduction .....	7-5
7.4	Hydrochemical setting .....	7-5
	7.4.1 TCw: Surface Infiltration.....	7-6
	7.4.2 PTn: Transition from fracture dominated flow to matrix dominated flow.....	7-6
	7.4.3 TSw: Transition from matrix dominated flow to fracture dominated flow.....	7-6
	7.4.4 CHn: composite vertical flow and lateral diversion .....	7-7
	7.4.5 Water Table: Seepage via fractures and matrix flow from the base of the CHn into the saturated zone.....	7-9
7.5	Perched Water Chemistry .....	7-9
	7.5.1 The Origin and Significance of Perched Water.....	7-9
	7.5.2 Hydrologic evidence for perched waters .....	7-11
	7.5.3 Chemical Composition of Perched Waters .....	7-14
7.6	Conceptual Models for Perched Water .....	7-15
	7.6.1 Fast-Pathway Fracture Flow Hypothesis .....	7-15
	7.6.2 Transient Mixing Hypothesis.....	7-18
	7.6.2.1 Climatic Evidence .....	7-18
	7.6.2.2 Structural and Mineralogical Setting .....	7-19
	7.6.2.3 Hydro-geochemical Model .....	7-23
	7.6.3 Evaluation of Alternate Conceptual Models .....	7-28
	7.6.3.1 The Radioactive Isotopes of Hydrogen, Chlorine and Carbon .....	7-29
	7.6.3.2 The Conservative Environmental Tracers Chloride and Cl/Br.....	7-30
	7.6.3.3 The Stable Isotopes .....	7-32
7.7	Simulation Results .....	7-33
7.8	Summary and Discussion .....	7-40
	7.8.1 The Hydrologic Data .....	7-42
	7.8.2 The Hydrochemical Data .....	7-42
	7.8.3 The Model Results.....	7-43
7.9	Conclusions .....	7-45
Chapter 8 -	Two-Dimensional Radionuclide Transport Simulations .....	8-1
8.1	Abstract .....	8-1
8.2	Software and Data QA Status .....	8-2
8.3	Introduction .....	8-3
8.4	Methodology for Radionuclide Migration Calculations .....	8-4
8.5	The Base Case .....	8-5
8.6	The Influence of Hydrologic and Geochemical Parameter Sets .....	8-13
8.7	The Effect of Percolation Flux .....	8-16
8.8	Grid Refinement Study .....	8-21
8.9	Uncertainties in Zeolite Distributions and Property Variations .....	8-26
8.10	Plutonium Colloid Transport Analysis .....	8-30

## Table of Contents

8.10.1 Model Development .....	8-31
8.10.2 Results of Colloid Transport Simulations .....	8-36
8.10.3 Discussion of Colloid-Facilitated Transport Results .....	8-42
8.11 Transient Analyses .....	8-47
8.12 Conclusions .....	8-55
<b>Chapter 9 - Three-Dimensional Radionuclide Transport .....</b>	<b>9-1</b>
9.1 Abstract .....	9-1
9.2 Software and Data QA Status .....	9-1
9.3 Introduction .....	9-2
9.4 Radionuclide Simulations, Base Infiltration Rate .....	9-3
9.5 Radionuclide Simulations, I/3 Infiltration Map .....	9-5
9.6 Large Scale Spatial Variability in Radionuclide Transport .....	9-7
9.7 Transport parameter sensitivity studies .....	9-10
9.8 Conclusions .....	9-15
<b>Chapter 10 - Unsaturated Zone Performance Predictions .....</b>	<b>10-1</b>
10.1 Abstract .....	10-1
10.2 Software and Data QA Status .....	10-2
10.3 Introduction .....	10-3
10.4 Radionuclide Transport Properties .....	10-4
10.5 Abstracted Models for NFE Source Term .....	10-6
10.6 Transport Predictions for <sup>99</sup> Tc .....	10-9
10.7 Transport Predictions for <sup>237</sup> Np .....	10-16
10.8 Transport Predictions for Uranium Isotopes .....	10-21
10.9 Transport Predictions for Plutonium Isotopes .....	10-24
10.10 Conclusions .....	10-27
<b>Chapter 11 - Reactive Transport of <sup>237</sup>Np with Repository Heat .....</b>	<b>11-1</b>
11.1 Abstract .....	11-1
11.2 Software and Data QA Status .....	11-1
11.3 Introduction .....	11-3
11.4 Model Description .....	11-5
11.4.1 Flow and Energy Formulations .....	11-5
11.4.2 Reactive Transport Equations .....	11-6
11.4.2.1 Governing Equations for the PDVs .....	11-8
11.4.2.2 Governing Equations for the SDVs .....	11-9
11.5 Solution Procedure .....	11-10
11.5.1 Solution Method for the PDVs: .....	11-11
11.5.2 Solution Method for the SDVs .....	11-14
11.6 Yucca Mountain Unsaturated Zone Hydrology and Geochemistry .....	11-15
11.6.1 Hydrogeologic Setting .....	11-15
11.6.1.1 Unsaturated Zone Geochemistry .....	11-16
11.6.2 Fluid Percolation Rate .....	11-19
11.6.3 Computational Domain .....	11-21
11.7 Neptunium Chemistry .....	11-21
11.7.1 Solubility and <sup>237</sup> Np Inventory .....	11-23

## Table of Contents

---

11.7.2	Speciation .....	11-24
11.7.3	Sorption Data .....	11-27
11.7.4	Sorption Models .....	11-27
11.7.5	Column Studies .....	11-31
11.8	Model Results .....	11-32
11.8.1	Preliminary One-Dimensional Flow and Transport Simulations ..	11-32
11.8.2	Thermohydrologic Simulations .....	11-35
11.8.3	Neptunium Transport Simulations .....	11-41
11.9	Discussion and Conclusions .....	11-50
11.10	Conclusions .....	11-55
Chapter 12	- Incorporation of Geostatistics into Flow and Transport Simulations .....	12-1
12.1	Abstract .....	12-1
12.2	Software and Data QA Status .....	12-2
12.3	Motivation .....	12-3
12.4	Geostatistical Integration .....	12-7
12.5	Implications of Zeolite Threshold Cutoff .....	12-7
12.6	Relationships Between Physical and Chemical Heterogeneity at Yucca Mountain .....	12-12
12.6.1	Correlation between Permeability and Zeolitic Abundance .....	12-14
12.6.2	Correlation between Porosity and Permeability .....	12-14
12.6.3	Correlation Between Permeability and Reactivity .....	12-15
12.6.4	Correlation Between Permeability and Relative Permeability .....	12-17
12.6.5	Summary of Field Data .....	12-17
12.7	Generating Realistic Zeolite Distributions .....	12-18
12.8	Generating Correlated Properties from Maps of Zeolitic Abundance ...	12-23
12.9	Flow and Transport Simulations with Geostatistics .....	12-26
12.10	Conclusions .....	12-32
Chapter 13	- Conclusions .....	13-1
Chapter 14	- References .....	14-1
Chapter 15	- Appendix .....	15-1

## List of Figures

### List of Figures

- 2-1 Antler Ridge cross section (a) Continuous zeolitic layers (in red) of the Site-Scale Model used in Robinson et al. (1996), (b) Zeolitic distributions are mapped from the 3-D mineralogical model (Chipera et al, 1997a) to the FEHM finite element mesh. The profiles look different because (b) accounts for fault offsets. . . . . 2-5
- 2-2 Locations of the 21 wells in plan view of mineralogical model. . . . . 2-8
- 2-3 Comparison of the (a) Chipera et al. (1997a) model and (b) the updated mineralogical model (Chipera et al., 1997b) for the Antler Ridge cross section. . . . . 2-9
- 2-4 Comparison of Chipera et al. (1997a) and updated mineralogical model (Chipera, 1997b) at locations close to wells (a) zeolite abundance at G1 (G1 existed in both models), (b) zeolite abundance at UZ-14 (UZ-14 only exists in the updated model but is close to G1), (c) smectite abundance at NRG6 (NRG6 only exists in the updated model). . . . . 2-10
- 3-1 Layer 9 of ISM shown with colors representing elevation. The area in which a three-dimensional tetrahedral grid is build is shown by the wire frame in which each line represents a stratigraphic layer boundary. The two-dimensional grid used for computations is shown with zeolite abundance shown with red for high zeolite abundance and blue for low zeolite abundance. . . . . 3-3
- 3-2 Top view of one TIN from ISM. TIN consists of 4976 nodes and 9823 triangles. Coordinates are Nevada State Plane in meters. Each triangle vertex is assigned an elevation, resulting in a piecewise linear representation of stratigraphic surfaces. . . . . 3-5
- 3-3 Layer 38 from ISM at 3X vertical exaggeration. Stratigraphic layer boundary is colored in yellow. West facing faults are green, south facing faults are blue. . . . . 3-7
- 3-4 Top view of one TIN illustrating the subregion for the three-dimensional computational grid. TIN consists of 4557 nodes and 6165 triangles. Coordinates are Nevada State Plane in meters. Note the increased resolution near faults in comparison to the original TIN surface (see Figure 3-2). . . . . 3-8
- 3-5 Cross section at NSP coordinate 232,100 meters extracted from ISM. In the figure, the cross section is split in two near the Ghost Dance Fault (GDF). The east and west extent of the computational model at NSP 168,274 meters and 174,176 meters are marked by arrows. Colors represent hydrogeologic units incorporated into the computational mesh. . . . . 3-11
- 3-6 Two-dimensional mesh generated from YMP model ISM showing faults as part of the computational grid. The faults from west (left) to east (right) are Solitario Fault, Ghost Dance Fault and Bow Ridge Fault. The cross section is bounded on the west and east by unnamed faults in ISM. Colors represent different hydrogeologic units. Close-up views of the grid are shown at each of the faults. . . . . 3-13
- 3-7 An example of how elliptic smoothing modifies the mesh. The mesh on the left has the topology that results from extracting a two-dimensional grid from a three-dimensional tetrahe-

## List of Figures

---

- dral mesh. Material interfaces are maintained but the node distribution is very uneven. The mesh on the right has been smoothed by keeping interface nodes fixed but allowing nodes between material interfaces to move. The mesh on the right has a flat bottom by truncating the mesh at elevation 720 meters. .... 3-14
- 3-8 Zeolite distributions are mapped from a three-dimensional model onto the computational mesh. The upper figure show zeolite distributions on a grid extracted from the Stratamodel three-dimensional mineralogy model. The lower figure shows the zeolite distributions after being mapped onto the computational mesh. .... 3-15
- 3-9 Three-dimensional unsaturated zone computational grid with 71,781 nodes, 143,562 dual permeability nodes and 414,313 tetrahedral elements. .... 3-18
- 3-10 Faults are represented as distinct materials. Layer 9 from ISM is shown. There are 14,473 nodes and 45,386 tetrahedral elements used to represent the faults. Faults that dip to the west are filled in red, faults that dip to the east are filled with green. .... 3-19
- 3-11 A portion of the two-dimensional cross section is shown bounded on the west by the Solitario fault and on the east by the Ghost Dance fault. a) Stratigraphic layer boundaries, b) low resolution computational grid, c) high resolution computational grid. .... 3-20
- 3-12 A small section of the high resolution two-dimensional grid near the Solitario fault showing the triangulation and the Voronoi cells associated with the triangles. .... 3-21
- 4-1 Use of the transfer function to determine the residence time of a particle in a cell for the RTTF particle tracking technique. .... 4-8
- 4-2 Conceptual model for matrix diffusion. One dimensional flow occurs in the fracture, with molecular diffusion into the rock matrix. .... 4-12
- 4-3 Flow chart illustrating the computation sequence for the particle tracking algorithm and its relationship to the fluid flow calculations in a finite element flow code. .... 4-18
- 4-4 Cumulative RTD curves produced by the RTTF particle tracking technique for one-dimensional dispersion (filled circles), compared to analytical solution (solid curves). In the curves without sorption, was varied. For the dashed curve, linear sorption was included. .. 4-20
- 4-5 Residence time distribution (RTD) curves calculated using the RTTF particle tracking technique (symbols) for for different numbers of particles, compared to the analytical solution (solid curve). The RTD is a solute concentration normalized so that the area under the curve is unity. .... 4-21
- 4-6 Cumulative RTD curves produced by the RTTF particle tracking technique for the matrix diffusion model (filled circles), compared to the analytical solution of Tang et al. (1981) (solid curves). Curve a) small amount of matrix diffusion; Curve b) moderate amount of matrix diffusion; Curve c) Matrix diffusion and sorption on fracture and in matrix; Curve d) Dispersion, matrix diffusion, and sorption on fracture and in matrix. .... 4-22
- 4-7 Movement of particles with the saturation front for the transient wetting case. The curves are

## List of Figures

---

- the saturation profiles at regular time intervals. Simulations are depicted in which the particles start at the entrance to the flow path (the filled circles) and at a position part way down the column (the X's). For the latter case, the particles do not move until the saturation front reaches the particles. .... 4-23
- 4-8 Model geometry and finite element grid for the two-dimensional models of interwell tracer tests at the C-Wells, Yucca Mountain, Nevada. The solid circles are an injector and producer for the case of wells aligned with the grid, and the open circles are the same for the case of wells misaligned with respect to the grid. .... 4-25
- 4-9 Comparison of RTTF particle tracking simulation (solid curves) and finite element CD equation solution (dotted curve). The two particle tracking curves show the effect of varying the dispersivity (0 and 1 m). .... 4-26
- 4-10 Schematic of the one-dimensional model system of the vadose zone at Yucca Mountain used for the dual permeability particle tracking example. .... 4-28
- 4-11 Composite solute breakthrough curves (fracture plus matrix contributions) at the bottom of each hydrogeologic unit at 1 mm/y infiltration rate using the dual permeability particle tracking model (solid curves). The dashed curves are comparable results assuming an equivalent continuum model. .... 4-29
- 4-12 Reconstructed  $^{36}\text{Cl}/\text{Cl}$  input ratio used in the particle tracking simulations (from Fabryka-Martin et al., 1996c). .... 4-31
- 4-13 Simulated concentrations of  $^{36}\text{Cl}/\text{Cl}$  ratio (a) and  $^{14}\text{C}$  in the two-dimensional model domain. For  $^{36}\text{Cl}$ , the bomb-pulse signal is red, and the values at the ESF horizon are in agreement with field measurements. For  $^{14}\text{C}$ , values in the PTn (above ESF) and CHn (below ESF) are in qualitative agreement with field measurements. .... 4-33
- 4-14 Simulations with and without matrix diffusion for the two-dimensional interwell tracer experiments modeled in Figure 4-8. Also shown is a simulation of a tracer that sorbs to the matrix rock (the dotted curve). .... 4-35
- 4-15 Breakthrough curves for a homogeneous permeability field examining the effect of grid orientation on the transport behavior of the RTTF particle tracking method. Solid curves: wells aligned with the grid; curves with symbols: particle tracking solutions. .... 4-37
- 5-1 Comparison of computed matrix and fracture saturations for the FEHM and TOUGH2 simulations. .... 5-8
- 5-2 Normalized flux of water in the fracture and matrix continua: FEHM and TOUGH2 simulations. .... 5-10
- 5-3 Normalized flux of water in the fracture and matrix continua: FEHM and TOUGH2 simulations on a scale expanded to examine the CHn units. Also included is an FEHM simulation with a 4 m thick vitric CHn layer, instead of the original 10 m thick layer. .... 5-11
- 5-4 Breakthrough of  $^{99}\text{Tc}$  at the water table for the one-dimensional SD-9 model: FEHM and

## List of Figures

---

- TOUGH2 generated flow fields, FEHM particle tracking for transport. . . . . 5-12
- 5-5 Breakthrough of  $^{237}\text{Np}$  at the water table for the one-dimensional SD-9 model: FEHM and TOUGH2 generated flow fields, FEHM particle tracking for transport. . . . . 5-13
- 5-6 Case 6412a hydrologic simulation results for SD-9. a) matrix and fracture saturations, along with field data points; b) matrix and fracture fluxes; c) matrix and fracture fluxes, expanded scale including the vitric/zeolitic interface. . . . . 5-18
- 5-7 Case 6412b hydrologic simulation results for SD-9. a) matrix and fracture saturations, along with field data points; b) matrix and fracture fluxes; c) matrix and fracture fluxes, expanded scale including the vitric/zeolitic interface. . . . . 5-19
- 5-8 Case 6511 hydrologic simulation results for SD-9. a) matrix and fracture saturations, along with field data points; b) matrix and fracture fluxes; c) matrix and fracture fluxes, expanded scale including the vitric/zeolitic interface. . . . . 5-20
- 5-9 Case 6521 hydrologic simulation results for SD-9. a) matrix and fracture saturations, along with field data points; b) matrix and fracture fluxes; c) matrix and fracture fluxes, expanded scale including the vitric/zeolitic interface. . . . . 5-21
- 5-10 Case 6522 hydrologic simulation results for SD-9. a) matrix and fracture saturations, along with field data points; b) matrix and fracture fluxes; c) matrix and fracture fluxes, expanded scale including the vitric/zeolitic interface. . . . . 5-22
- 5-11 Case 6531a hydrologic simulation results for SD-9. a) matrix and fracture saturations, along with field data points; b) matrix and fracture fluxes; c) matrix and fracture fluxes, expanded scale including the vitric/zeolitic interface. . . . . 5-23
- 5-12 Case 6531b hydrologic simulation results for SD-9. a) matrix and fracture saturations, along with field data points; b) matrix and fracture fluxes; c) matrix and fracture fluxes, expanded scale including the vitric/zeolitic interface. . . . . 5-24
- 5-13 Case 6541 hydrologic simulation results for SD-9. a) matrix and fracture saturations, along with field data points; b) matrix and fracture fluxes; c) matrix and fracture fluxes, expanded scale including the vitric/zeolitic interface. . . . . 5-25
- 5-14 Case 6412a transport results for the one-dimensional SD-9 model. a)  $^{99}\text{Tc}$ ; b)  $^{237}\text{Np}$ . One mole of radionuclide is released at the repository horizon at time = 0. . . . . 5-27
- 5-15 Case 6412b transport results for the one-dimensional SD-9 model. a)  $^{99}\text{Tc}$ ; b)  $^{237}\text{Np}$ . One mole of radionuclide is released at the repository horizon at time = 0. . . . . 5-28
- 5-16 Case 6511 transport results for the one-dimensional SD-9 model. a)  $^{99}\text{Tc}$ ; b)  $^{237}\text{Np}$ . One mole of radionuclide is released at the repository horizon at time = 0. . . . . 5-29
- 5-17 Case 6521 transport results for the one-dimensional SD-9 model. a)  $^{99}\text{Tc}$ ; b)  $^{237}\text{Np}$ . One mole of radionuclide is released at the repository horizon at time = 0. . . . . 5-30
- 5-18 Case 6522 transport results for the one-dimensional SD-9 model. a)  $^{99}\text{Tc}$ ; b)  $^{237}\text{Np}$ . One

## List of Figures

---

- mole of radionuclide is released at the repository horizon at time = 0. . . . . 5-31
- 5-19 Case 6531a transport results for the one-dimensional SD-9 model. a)  $^{99}\text{Tc}$ ; b)  $^{237}\text{Np}$ . One mole of radionuclide is released at the repository horizon at time = 0. . . . . 5-32
- 5-20 Case 6531b transport results for the one-dimensional SD-9 model. a)  $^{99}\text{Tc}$ ; b)  $^{237}\text{Np}$ . One mole of radionuclide is released at the repository horizon at time = 0. . . . . 5-33
- 5-21 Case 6541 transport results for the one-dimensional SD-9 model. a)  $^{99}\text{Tc}$ ; b)  $^{237}\text{Np}$ . One mole of radionuclide is released at the repository horizon at time = 0. . . . . 5-34
- 6-1 Conceptual model of hydrologic pathways at Yucca Mountain. . . . . 6-13
- 6-2 Reconstructed  $^{36}\text{Cl}/\text{Cl}$  ratio in infiltrating water (Fabryka-Martin et al., 1996c, Plummer et al., 1996), a) last 500,000 years, b) last 50,000 years, c) last 50 years. . . . . 6-17
- 6-3 Plan view of three-dimensional model domain with locations of ESF, ESF stations, two-dimensional east-west model transect, north-south transect, and one-dimensional vertical column studies. . . . . 6-21
- 6-4 Carbon-14 decay function resulting from a 5730 year half-life. . . . . 6-25
- 6-5 Finite-element grid for the two-dimensional cross section at Antler Ridge. Northing location in NSP coordinates is 232100 m. Red arrows show easting location for potential repository horizon breakthrough study. . . . . 6-27
- 6-6 Infiltration rates extracted from Flint et al. (1996) map along Antler Ridge cross section. I map is directly extracted, I/3 map is the I map scaled by 3. Green arrows show easting location for potential repository horizon breakthrough study. . . . . 6-28
- 6-7 Plan view of three-dimensional domain outline on top of Flint et al. (1996) infiltration map. Also shown for reference are the ESF, the east-west two-dimensional cross section and the north-south transect (used to interpret the three-dimensional model results). . . . . 6-29
- 6-8 Simulated  $^{36}\text{Cl}/\text{Cl}$  ratios in Antler Ridge 2-D cross section with 6541a material property set and Flint (1996) infiltration map. . . . . 6-31
- 6-9 Simulated  $^{36}\text{Cl}/\text{Cl}$  ratios in Antler Ridge 2-D cross section with 6541b material property set (no weighting of fracture-matrix connection in PTn) and Flint (1996) infiltration map. Note the reduced amount of bomb-pulse in the top of the CHn. . . . . 6-31
- 6-10 Difference in simulated  $^{36}\text{Cl}/\text{Cl}$  ratios for property sets 6541a and 6541b. . . . . 6-31
- 6-11 Simulated saturations in Antler Ridge 2-D cross section with 6541a material property set and Flint (1996) infiltration map. . . . . 6-32
- 6-12 Simulated saturations in Antler Ridge 2-D cross section with 6541b material property set and Flint (1996) infiltration map. . . . . 6-32
- 6-13 Difference in simulated saturations for property sets 6541a and 6541b. . . . . 6-32

## List of Figures

---

- 6-14 Particle pathways from 5 different surface locations. a) pathways in the matrix for locations near faults, b) pathways in the fractures for locations near faults, c) pathways in the matrix for locations in faults, d) pathways in the fractures for locations in faults. . . . . 6-35
- 6-15 Breakthrough (or cumulative age distribution of a porewater sample) at elevation 1080 m at 10 locations along E-W Antler Ridge transect. Material properties are the 6541a set. Infiltration rate at surface is the Flint et al. (1996) map. Legend numbers indicate Easting location in NSP coordinates (Northing coordinate is 232100 m). . . . . 6-36
- 6-16 Breakthrough (or cumulative age distribution of a porewater sample) at elevation 1080 m at 10 locations along E-W Antler Ridge transect. Material properties are the 6541b set (no weighting of fracture-matrix connection in PTn). Infiltration rate at surface is the Flint et al. (1996) map. Legend numbers indicate Easting location in NSP coordinates (Northing coordinate is 232100 m) . . . . . 6-36
- 6-17 Breakthrough (or cumulative age distribution of a porewater sample) at elevation 1080 m at 10 locations along E-W Antler Ridge transect. Material properties are the 6541 set. Infiltration rate at surface is the scaled (I/3) map of Flint et al. (1996). Legend numbers indicate Easting location in NSP coordinates (Northing coordinate is 232100 m). . . . . 6-37
- 6-18 Breakthrough (or cumulative age distribution of a porewater sample) at elevation 1080 m at 10 locations along E-W Antler Ridge transect. Material properties are the 6541b set (no weighting of fracture-matrix connection in PTn). Infiltration rate at surface is the scaled (I/3) map of Flint et al. (1996). Legend numbers indicate Easting location in NSP coordinates (Northing coordinate is 232100 m). . . . . 6-37
- 6-19 Three-dimensional simulation of  $^{36}\text{Cl}/\text{Cl}$  ratios using property set 6541a and infiltration map of Flint et al. (1996). . . . . 6-38
- 6-20 Simulated  $^{36}\text{Cl}/\text{Cl}$  ratios at ESF horizon with three-dimensional transport model. Uses material property set 6541a and infiltration map from Flint et al. (1996). . . . . 6-39
- 6-21 Simulated  $^{36}\text{Cl}/\text{Cl}$  ratio in ESF with 3-D transport model and measured ratios from Levy et al. (1997). Simulations performed using 6541 parameter set and Flint et al. (1996) infiltration map . . . . . 6-40
- 6-22 Solute travel path in the matrix from the top of Yucca Crest into the UZ system. . . . 6-41
- 6-23 Solute travel path in the fractures from the top of Yucca Crest into the UZ system. . . 6-41
- 6-24 Breakthrough (or cumulative age distribution of a porewater sample) in northern ESF simulated with 3D model. Material properties are the 6541a set. Infiltration rate at surface is the map of Flint et al. (1996). Legend numbers indicate ESF Station numbers (in hundreds of meters). . . . . 6-45
- 6-25 Breakthrough (or cumulative age distribution of a porewater sample) in southern ESF simulated with 3D model. Material properties are the 6541a set. Infiltration rate at surface is the map of Flint et al. (1996). Legend numbers indicate ESF Station numbers (in hundreds of meters). . . . . 6-45

## List of Figures

---

- yr infiltration rate. Also shown is lowest 5% of total flow to highlight non-zero fracture fluxes in PTn. Layer resolution in Calico Hills not provided due to focus above ESF in these simulations. . . . . 6-62
- 6-40 Breakthrough curve at ESF for property set 6412b at Station 35. Also shown is flux distribution for 5 mm/yr case. . . . . 6-63
- 6-41 Comparison of saturations simulated in upper section of repository column with property sets 6541a and 6541b for 10 mm/yr. . . . . 6-64
- 6-42 Station 35 breakthrough comparison for 10 mm/yr average annual infiltration rate. Three property sets (identified in legend) compared for steady-state (ss) and transient (trans) infiltration. Transient model, 10-5-10, is 10 mm/yr accumulation applied over 10 days every 5 years. Log plot on right illustrates component of early arrival . . . . . 6-67
- 6-43 Station 57 breakthrough comparison for 3 property sets at steady state (ss) and in transient (trans) infiltration model, each with mean annual infiltration rate of 10 mm/yr. Property sets are 6541a, 6541b, and 6541ft. Transient mode is 10 mm/yr accumulated over 10 days every 5 years (10-5-10). . . . . 6-67
- 6-44 Repository column breakthrough comparison for 3 property sets at steady state (ss) and in transient (trans) infiltration model, each with mean annual infiltration rate of 10 mm/yr. Property sets are 6541a, 6541b, and 6541ft. Transient mode is 10 mm/yr accumulated over 10 days every 5 years (10-5-10). . . . . 6-68
- 6-45 Comparison of breakthrough curves at potential repository horizon for transient simulations with a) 20 mm/yr average and b) 50 mm/yr average. All water is applied for 10 days every 5 years. . . . . 6-69
- 6-46 Comparison of breakthrough curves for 10 day duration transient and 90 day duration transients. Average annual infiltration for all cases is 10 mm/yr. . . . . 6-69
- 6-47 Simulated flux variation responses at potential repository for 10-5-10 transient infiltration rate at the surface. 300 years of transient followed by 700 years of uniform 10 mm/yr infiltration. The shaded portion of the 6541ft curve represents the short-term transients at the repository horizon. . . . . 6-70
- 7-1 Map of Yucca Mountain site area with boreholes (i.e., G-2, UZ-14, NRG-7/7a, SD-9, SD-12, and SD-7) where perched water has been observed. Green line: site-scale model boundary. Blue: ESF. Red line: outline of potential repository. . . . . 7-8
- 7-2 Reconstructed <sup>14</sup>C and <sup>36</sup>Cl activities for the last 50 ka. From Fabryka-Martin et al. (1996c). . . . . 7-25
- 7-3 Reconstructed <sup>14</sup>C and <sup>36</sup>Cl activities in the atmosphere for the last 20 ka, from Fabryka-Martin et al. (1996c). USW UZ-14A and UZ-14C were shown to be contaminated with modern water. Perched water data from UZ-14, SD-7 and NRG-7/7a. . . . . 7-26
- 7-4 Chloride concentration predicted in the three-dimensional model. Top figure: map of chlo-

## List of Figures

---

- ride concentrations at the surface. Bottom figure: concentrations at and elevation of 900 m. Top of page is North. .... 7-35
- 7-5 EW cross-section of transport site-scale model looking North. Chloride concentrations for the base infiltration map (upper figure) and the I/3 infiltration scenario (bottom figure). .... 7-36
- 7-6 Detail of EW cross-section of transport site-scale model in area of relatively low infiltration. Close-up of chloride concentrations to the East of the Ghost Dance fault for the I/3 scenario. .... 7-37
- 7-7 EW cross-section of full site scale transport model, looking North through Yucca Crest. Chloride to bromide ratio (top figure) and sulfate to chloride ratio (bottom figure) simulated using the base case property set and infiltration map. .... 7-38
- 7-8 Detail of EW cross-sections from the site scale transport model through Yucca Crest, looking North. Fracture saturations predicted using the basal vitrophyre lateral diversion model. Top figure: base infiltration map; bottom figure: I/3 scaled map. Blue areas represent zones of perching with lateral flow along the top of the basal TSw vitrophyre. Principal source of water is from Yucca Crest in both cases. .... 7-40
- 7-9 Detail of EW cross-section (looking North) of transport site-scale model through Yucca Crest. Chloride concentration (top), sulfate concentration (middle), and sulfate to chloride ratio (bottom) for the basal vitrophyre lateral diversion hydrologic scenario. .... 7-41
- 7-10 Three-dimensional simulation of transport for particles injected at the surface above the potential repository. Image represents a cut-away fence diagram from the three-dimensional grid. Represented are the Solitario (S.C.) and Ghost Dance (G.D.) faults and the ESF. Particles undergoing matrix flow are represented with the red colors corresponding to a high particle concentration. Significant lateral diversion is predicted in the vitric Calico Hills matrix (beneath the TSw basal vitrophyre) and to the Ghost Dance fault. .... 7-44
- 8-1 Matrix (top) and fracture (bottom) saturations for the two-dimensional base-case simulation. Parameter set 6541, base infiltration map (I). Also shown are the I and I/3 infiltration map values across the model domain. .... 8-7
- 8-2 Green's function residence time distributions for transport of radionuclides in the two-dimensional site scale model. Property set 6541, base infiltration map. .... 8-8
- 8-3 Cumulative residence time distributions for transport of radionuclides in the two-dimensional site scale model. Property set 6541, base infiltration map. .... 8-10
- 8-4 Water table breakthrough of  $^{237}\text{Np}$  for the base case. Parameter set 6541, base infiltration map,  $k_d = 2 \text{ cc/g}$ , constant release rate from 1 ky to 31 ky. .... 8-11
- 8-5 Green's function residence time distributions for transport of radionuclides in the two-dimensional site scale model. Property set 6412b, base infiltration map. .... 8-14
- 8-6 Cumulative residence time distributions for transport of radionuclides in the two-dimensional

## List of Figures

---

- al site scale model. Property set 6412b, base infiltration map. .... 8-14
- 8-7 Green's function residence time distributions for transport of radionuclides in the two-dimensional site scale model. Property set 6531b, base infiltration map. .... 8-15
- 8-8 Cumulative residence time distributions for transport of radionuclides in the two-dimensional site scale model. Property set 6531b, base infiltration map. .... 8-15
- 8-9 Difference in predicted fluid saturations from an increase in the base-case percolation flux map by a factor of three at all locations. Top figure: matrix saturation difference; bottom figure: fracture saturation difference. .... 8-17
- 8-10 Green's function residence time distributions for transport of radionuclides in the two-dimensional site scale model. Property set 6541, 3 x I infiltration map. .... 8-18
- 8-11 Cumulative residence time distributions for transport of radionuclides in the two-dimensional site scale model. Property set 6541, 3 x I infiltration map. .... 8-19
- 8-12 Green's function residence time distributions for transport of radionuclides in the two-dimensional site scale model. Property set 6541, I/3 infiltration map. .... 8-19
- 8-13 Cumulative residence time distributions for transport of radionuclides in the two-dimensional site scale model. Property set 6541, I/3 infiltration map. .... 8-20
- 8-14 Green's function (left column of figures) and cumulative residence time distributions for the I/3 infiltration map for various parameter sets. a, b) 6412b; c, d) 6412c. .... 8-22
- 8-15 Green's function (left column of figures) and cumulative residence time distributions for the I/3 infiltration map for various parameter sets. a, b) 6522; c, d) 6531b. .... 8-23
- 8-16 Comparison of matrix saturations for cases 6412b and 6412c. I/3 infiltration map. Top figure: 6412b; middle figure: 6412c; bottom figure: difference in saturations (6412c - 6412b). .... 8-24
- 8-17 Comparison of Green's functions (base-case grid and refined grid) for transport of radionuclides in the two-dimensional site scale model. Property set 6541, base infiltration map. .... 8-25
- 8-18 Comparison of cumulative residence time distributions (base-case grid and refined grid) for transport of radionuclides in the two-dimensional site scale model. Property set 6541, base infiltration map. .... 8-26
- 8-19 Green's function for transport of radionuclides in the two-dimensional site scale model. Property set 6412d (high-K zeolites), I/3 infiltration map. .... 8-28
- 8-20 Cumulative residence time distributions for transport of radionuclides in the two-dimensional site scale model. Property set 6412d (high-K zeolites), I/3 infiltration map. .... 8-28
- 8-21 Green's function for transport of radionuclides in the two-dimensional site scale model. Property set 6412d (high-K zeolites), base infiltration map. .... 8-29

## List of Figures

---

- 8-22 Cumulative residence time distributions for transport of radionuclides in the two-dimensional site scale model. Property set 6412d (high-K zeolites), base infiltration map. . . . . 8-29
- 8-23 Schematic of the fracture transport model (after Tang et al., 1981) . . . . . 8-32
- 8-24 Influence of fluid residence time and dispersivity on breakthrough at the water table. No matrix diffusion or sorption. . . . . 8-37
- 8-25 Influence of fracture sorption on breakthrough at the water table. No matrix diffusion or sorption. Fluid travel time = 0.1 y. . . . . 8-38
- 8-26 Influence of matrix diffusion on breakthrough at the water table. Fluid travel time = 1 y. No matrix or fracture sorption. . . . . 8-39
- 8-27 Influence of matrix sorption on breakthrough at the water table. Fluid travel time = 1 y. = 10-12 m<sup>2</sup>/s. No fracture sorption. . . . . 8-40
- 8-28 Influence of colloid-facilitated transport on breakthrough at the water table. Fluid travel time = 1 y. = 10-12 m<sup>2</sup>/s. = 1000. No fracture sorption. . . . . 8-41
- 8-29 Influence of colloid-facilitated transport on breakthrough at the water table. Fluid travel time = 1 y. = 10-12 m<sup>2</sup>/s. = 1000. Varying fracture sorption, colloid attachment, colloid sorption. . . . . 8-42
- 8-30 Green's function for Plutonium transport through the unsaturated zone for different values of K<sub>c</sub>. Case 6541, base infiltration map, aqueous plutonium K<sub>d</sub> = 100 cc/g, all units. . . . . 8-45
- 8-31 Cumulative breakthrough curves for plutonium transport through the unsaturated zone for different values of K<sub>c</sub>. Case 6541, base infiltration map, aqueous plutonium K<sub>d</sub> = 100 cc/g, all units. Dotted curves are simulations with no matrix diffusion. . . . . 8-46
- 8-32 Water mass flow rate versus time exiting the two-dimensional model domain for the three transient cases considered. Changes in percolation rate occur at t = 0. . . . . 8-49
- 8-33 Matrix saturations in the ptn3 and ch4v units in response to the long-term transients in percolation flux. Black curves: ptn3; Blue curves: ch4v. . . . . 8-50
- 8-34 Matrix saturations in the tsw5 and bf2z units in response to the long-term transients in percolation flux. Black curves: bf2z; Red curves: tsw5. . . . . 8-51
- 8-35 Breakthrough curve of <sup>237</sup>Np at the water table for the long-term transient scenario. Also shown are the steady state curves for the two infiltration rates, and the quasi-steady state method. . . . . 8-52
- 8-36 Breakthrough curve of <sup>237</sup>Np at the water table for the long-term transient scenario, shown on an expanded scale near the time of the change in percolation flux. . . . . 8-53
- 8-37 Green's function for transport of radionuclides in the two-dimensional site scale model. Property set 6541, base infiltration map, elevated water table. . . . . 8-54
- 8-38 Cumulative residence time distributions for transport of radionuclides in the two-dimensional

## List of Figures

---

- al site scale model. Property set 6541, base infiltration map, elevated water table. . . 8-55
- 9-1 Green's function for radionuclide transport in the three-dimensional site scale model. Property set 6541, base infiltration map. . . . . 9-4
- 9-2 Cumulative breakthrough curves for radionuclide transport in the three-dimensional site scale model. Property set 6541, base infiltration map. . . . . 9-5
- 9-3 Green's function for radionuclide transport in the three-dimensional site scale model. Property set 6541, I/3 infiltration map. . . . . 9-6
- 9-4 Cumulative breakthrough curves for radionuclide transport in the three-dimensional site scale model. Property set 6541, I/3 infiltration map. . . . . 9-7
- 9-5 Green's function for radionuclide transport from five subsections of the repository in the three-dimensional site scale model. Property set 6541, base infiltration map. . . . . 9-8
- 9-6 Cumulative breakthrough curves for radionuclide transport from five subsections of the repository in the three-dimensional site scale model. Property set 6541, base infiltration map. . . . . 9-9
- 9-7 Green's function for radionuclide transport from five subsections of the repository in the three-dimensional site scale model. Property set 6541, I/3 infiltration map. . . . . 9-10
- 9-8 Cumulative breakthrough curves for radionuclide transport from five subsections of the repository in the three-dimensional site scale model. Property set 6541, I/3 infiltration map. . . . . 9-11
- 9-9 Green's function for radionuclide transport in the three-dimensional site scale model. Property set 6541, base infiltration map, no sorption, different diffusion coefficients. . . . 9-12
- 9-10 Cumulative breakthrough curves for radionuclide transport in the three-dimensional site scale model. Property set 6541, base infiltration map, no sorption, different diffusion coefficients. . . . . 9-13
- 9-11 Green's function for radionuclide transport in the three-dimensional site scale model. Property set 6541, base infiltration map, zeolite  $K_d = 2$  cc/g, different diffusion coefficients. . . . . 9-14
- 9-12 Cumulative breakthrough curves for radionuclide transport in the three-dimensional site scale model. Property set 6541, base infiltration map, zeolite  $K_d = 2$  cc/g, different diffusion coefficients. . . . . 9-15
- 9-13 Green's function for radionuclide transport in the three-dimensional site scale model. Property set 6541, base infiltration map, no sorption, different dispersivity values. . . . . 9-16
- 10-1 Schematic of abstracted rate models for radionuclide release from the NFE. a) constant-release-rate model; b) exponential-release-rate model. . . . . 10-8
- 10-2 Breakthrough of  $^{99}\text{Tc}$  at the water table for different hydrologic parameter sets. Base infil-

## List of Figures

---

- tration map,  $t_{can}=1000$  y,  $t_{rel}=3000$  y. .... 10-10
- 10-3 Breakthrough of  $^{99}\text{Tc}$  at the water table for different hydrologic parameter sets. Base infiltration map,  $t_{can}=1000$  y,  $t_{rel}=10000$  y. .... 10-11
- 10-4 Breakthrough of  $^{99}\text{Tc}$  at the water table for different durations of release. Base infiltration map,  $t_{can}=1000$  y, parameter set 6541. .... 10-12
- 10-5 Breakthrough of  $^{99}\text{Tc}$  at the water table as a function of infiltration rate.  $t_{can}=1000$  y,  $t_{rel}=3000$  y, parameter set 6541. .... 10-13
- 10-6 Breakthrough of  $^{99}\text{Tc}$  at the water table as a function of infiltration rate.  $t_{can}=1000$  y,  $t_{rel}=3000$  y, parameter set 6412d. .... 10-13
- 10-7 Breakthrough of  $^{99}\text{Tc}$  at the water table for different values of  $k_{rel}$  for the exponential release scenario. Base infiltration map,  $t_{can}=1000$  y, parameter set 6541. .... 10-14
- 10-8 Breakthrough of  $^{99}\text{Tc}$  at the water table comparing the two-dimensional and three-dimensional models. Base infiltration map and I/3 map,  $t_{can}=1000$  y, parameter set 6541 10-15
- 10-9 Breakthrough of  $^{237}\text{Np}$  at the water table for different hydrologic parameter sets. Base infiltration map,  $t_{can}=1000$  y,  $t_{rel}=10$  ky, parameter set 6541. .... 10-16
- 10-10 Breakthrough of  $^{237}\text{Np}$  at the water table for different hydrologic parameter sets. Base infiltration map,  $t_{can}=1000$  y,  $t_{rel}=30$  ky, parameter set 6541. .... 10-17
- 10-11 Breakthrough of  $^{237}\text{Np}$  at the water table for different hydrologic parameter sets. Base infiltration map,  $t_{can}=1000$  y,  $t_{rel}=100$  ky, parameter set 6541. .... 10-17
- 10-12 Breakthrough of  $^{237}\text{Np}$  at the water table as a function of duration of release.  $t_{can}=1000$  y, base infiltration map, parameter set 6541. .... 10-18
- 10-13 Breakthrough of  $^{237}\text{Np}$  at the water table as a function of infiltration rate.  $t_{can}=1000$  y,  $t_{rel}=30$  ky, parameter set 6541. .... 10-19
- 10-14 Breakthrough of  $^{237}\text{Np}$  at the water table as a function of infiltration rate.  $t_{can}=1000$  y,  $t_{rel}=30$  ky, parameter set 6412d. .... 10-19
- 10-15 Breakthrough of  $^{237}\text{Np}$  at the water table for different values of  $k_{rel}$  for the exponential release scenario. Base infiltration map,  $t_{can}=1000$  y, parameter set 6541. .... 10-20
- 10-16 Breakthrough of  $^{237}\text{Np}$  at the water table comparing the two-dimensional and three-dimensional models. Base infiltration map and I/3 map,  $t_{can}=1000$  y, parameter set 6541. 10-21
- 10-17 Uranium isotope inventory as a function of time for a 70,000 MTU repository and --- add description of inventory assumptions (initial inventory data from Wilson et al., 1994). .... 10-22
- 10-18 Water table breakthrough curves for Uranium isotopes. Property set 6541, base infiltration map, release rate similar the  $^{237}\text{Np}$  case with 30 ky release scenario (for Uranium only --% is released after one million years). .... 10-24

## List of Figures

---

- 10-19 Plutonium isotope inventory as a function of time for a 70,000 MTU repository and --- add description of inventory assumptions (initial inventory data from Wilson et al., 1994). . . . . 10-25
- 10-20 Water table breakthrough curves for total plutonium. Property set 6541, base infiltration map, different durations of release. Duration of release is directly proportional to effective solubility, which in turn is proportional to  $K_c$ . . . . . 10-27
- 10-21 Water table breakthrough curves for individual isotopes of Plutonium. Property set 6541, base infiltration map, durations of release corresponding to  $K_c = 99$ . . . . . 10-28
- 11-1 Geochemistry and stratigraphy of well UZ-14 (aqueous chemical data from Yang et al., 1996). (a) Chloride and bicarbonate concentration, (b) sodium, calcium, and magnesium concentration, (c) pH and (d) stratigraphy and zeolite abundance . . . . . 11-17
- 11-2 Stratigraphy and finite element grid used for the two-dimensional model cross section. (a) stratigraphy, including locations of zeolitic rocks, (b) finite element grid, (c) close-up of a small portion of the grid near the repository. . . . . 11-18
- 11-3  $^{237}\text{Np}$  speciation in J-13 water at 25°C with a solubility of  $5 \times 10^{-5}$  mol/l. . . . . 11-26
- 11-4 Predicted fraction of  $^{237}\text{Np}$  as cation as a function of temperature and fluid composition (J-13 fluid versus UE-25 p#1 fluid). . . . . 11-26
- 11-5  $^{237}\text{Np}$  sorption coefficient versus  $\text{Na}^+$  concentration in pure sodium bicarbonate solutions (data from Tait et al., 1996). The X's with accompanying curve is the predicted ion exchange model result. . . . . 11-30
- 11-6 Tritium and  $^{237}\text{Np}$  sorption column study using J-13 well water at a pH of 8.3. The curves represent fits to the data for equilibrium and kinetic sorption models . . . . . 11-32
- 11-7 The fraction of flow residing in the matrix and fracture for the DKM model. . . . . 11-34
- 11-8 Breakthrough of  $^{237}\text{Np}$  at the water table in the one-dimensional model. Comparison of the ECM and DKM models for different flow scenarios. . . . . 11-36
- 11-9 Influence of repository heat on thermohydrologic and chemical conditions in the unsaturated zone. (a) Fluid saturation profile (500 years), (b) temperature profile (500 years), (c) chloride concentration (2000 years). . . . . 11-38
- 11-10 Temperature versus time in the rock near an emplacement drift in the repository. "Center"-drift near the center of the repository, "Edge"-drift near the edge of the repository. The family of curves for the "Center" drift show the influence of infiltration rate on the results. . . . . 11-39
- 11-11 Temperature versus time at the top of the Calico Hills zeolitic horizon. "Center"-position located beneath the center of the repository; "Edge"-drift near the edge of the repository. The influence of the assumptions regarding the heat transfer at the water table boundary are also shown. . . . . 11-40

## List of Figures

---

- 11-12 <sup>237</sup>Np transport through the unsaturated zone. (a) <sup>237</sup>Np total aqueous concentration profile after rewetting of the repository region and mobilization of <sup>237</sup>Np at all locations (10,000 years), (c) <sup>237</sup>Np total aqueous concentration profile as <sup>237</sup>Np reaches the water table (50,000 years), and (d) <sup>237</sup>Np immobile site concentration profile (50,000 years). . . . . 11-42
- 11-13 Mobilization of <sup>237</sup>Np from the near field, and breakthrough curves at the water table for different infiltration scenarios. The declining curves starting at early times represent the <sup>237</sup>Np mass remaining as a solid in the repository region (the left y-axis). The breakthrough curves exhibiting peaks are <sup>237</sup>Np flux at the water table (the right y-axis). . . . . 11-43
- 11-14 Fracture bypass of the zeolitic Calico Hills units. . . . . 11-45
- 11-15 The effect of CO<sub>2</sub> degassing on pH at the center of the repository (heat-pipe front) and at the top of the zeolitic layers. . . . . 11-46
- 11-16 Influence of pH on the <sup>237</sup>Np breakthrough curves at the water table. The “carrier plume” result assumes an elevated pH of 10 at the repository for a period of either 500 or 5,000 years due to cement-water reactions. . . . . 11-47
- 11-17 Influence of transient infiltration and chemical conditions on the <sup>237</sup>Np breakthrough curves at the water table. The “changing climate” result assumes an increase from 1 mm/y to 4 mm/y, accompanied by a four-fold decrease in cation concentrations. The 1 mm/y and 4 mm/y steady state results without geochemical transients are shown for comparison. . . . . 11-49
- 11-18 Influence of thermal boundary condition at the water table on the <sup>237</sup>Np breakthrough curves at the water table. . . . . 11-50
- 12-1 Antler Ridge cross section (a) hydrologic zones including rock with greater than 10% zeolitic abundance, (b) hydrologic zones including rock with greater than 20% zeolitic abundance. . . . . 12-5
- 12-2 Two possible zeolitic geometries at the subgrid scale (10 m by 10 m). . . . . 12-8
- 12-3 Comparison of the characteristic curves for zeolitic and vitric tuff. . . . . 12-10
- 12-4 Velocity profile for the zeolitic lens case at three different infiltration rates. . . . . 12-11
- 12-5 Comparison of <sup>237</sup>Np breakthrough curves for the layer and lens cases. . . . . 12-13
- 12-6 Data relating % clinoptilolite to K<sub>sat</sub>, (from Flint, 1996). . . . . 12-15
- 12-7 Data from Altman et al. (1996) relating porosity to K<sub>sat</sub>. . . . . 12-16
- 12-8 Data from Altman et al. (1996) relating a to K<sub>sat</sub>. . . . . 12-18
- 12-9 Variograms depicting the spatial structure of the zeolites generated from RC2 using data from the Calico Hills and Prow Pass units. . . . . 12-20
- 12-10 Kriged zeolite abundance of full mineralogical model. . . . . 12-21

## List of Figures

---

12-11 Variance of Kriged zeolite abundance in full mineralogical model. ....	12-22
12-12 Three-dimensional block for high resolution study (4000mx2000mx300m). ....	12-23
12-13 Comparison of the kriged map and three conditional simulations. ....	12-24
12-14 Conditional simulation of percent zeolitic abundance mapped onto the refined computational mesh between the Solitario Canyon and Ghost Dance faults. ....	12-25
12-15 Permeability distribution for a conditional simulation. Percent zeolitic abundance-permeability correlation is used between the Solitario Canyon and Ghost Dance faults for all layers below the repository. The rest of the computational domain is assigned default permeability values. ....	12-27
12-16 Saturation profile of the conditional simulation. (a) matrix saturation, (b) fracture saturation. ....	12-28
12-17 Comparison of the 10% zeolite cutoff runs of Chapter 8 and a conditional simulation for a conservative tracer. ....	12-29
12-18 Conditional simulation with different Kds compared to the 10% cutoff case with a Kd of 20. ....	12-30
12-19 Conditional simulation using different Kds with 1/3 the infiltration rate in Figure 12-18. ....	12-30
12-20 Modification of the 10% zeolite case to better match the conditional simulation. The dotted lines show the results when all rocks with zeolitic abundance less than 10% are assigned a Kd of 0.1*Kd. ....	12-31

## List of Tables

---

### List of Tables

2-1	QA Status of Data used in this Chapter .....	2-3
3-1	QA Status of Data used in this Chapter .....	3-2
4-1	QA Status of Data used in this Chapter .....	4-2
5-1	QA Status of Data used in this Chapter .....	5-2
5-2	Summary of hydrologic parameter sets from Bodvarsson et al. (1997) (shaded rows indicate parameter set not simulated in the present study) .....	5-16
5-3	Parameter sets to include in multi-dimensional transport simulations. Parameter sets carried forward are unshaded in the table. .	5-40
6-1	QA Status of Data used in this Chapter .....	6-2
6-2	Apparent <sup>14</sup> C Ages from Yang et al. (1997).....	6-24
6-3	Parameter Sets for Environmental Isotope Simulations .....	6-26
6-4	Infiltration Maps Used in Environmental Isotope Simulations .....	6-27
6-5	Transient Model Description .....	6-58
7-1	QA Status of Data used in this Chapter .....	7-3
8-1	QA Status of Data used in this Chapter .....	8-2
8-2	Potential ranges of hydrologic and transport parameter values.....	8-36
9-1	QA Status of Data used in this Chapter .....	9-2
10-1	QA Status of Data used in this Chapter .....	10-2
11-1	QA Status of Data used in this Chapter .....	11-2
11-2	Groundwater Compositions (ppm) of Unsaturated Zone Fluids and Fluids Used in Sorption Studies .....	11-22
11-3	Solubility of <sup>237</sup> Np (Efurd et al. (1996)) .....	11-23
11-4	Reactions and Log Equilibrium Coefficients for Np Speciation.....	11-24
12-1	QA Status of Data used in this Chapter .....	12-2
12-2	: Hydrologic and chemical properties of vitric and zeolitic tuff .....	12-9
12-3	: Parameters used in the simulations .....	12-12
15-1	Correlation of Geologic Formations, Hydrological Units and the Model Layers of Both	

## List of Tables

---

LANL and LBL.	15-1
15-2 Property Set 6412a.....	15-4
15-3 Property Set 6412b.....	15-5
15-4 Property Set 6412c.....	15-6
15-5 Property Set 6522.....	15-7
15-6 Property Set 6531b.....	15-8
15-7 Property Set 6541.....	15-9

# Chapter 1 - Executive Summary

## 1.1 Overview

---

The unsaturated zone at Yucca Mountain is one of the primary barriers to the migration of radionuclides from the potential repository to the accessible environment, and, as such, has received great attention in site-characterization activities. This milestone report describes the revised transport model for the unsaturated zone at Yucca Mountain. The purpose of the modeling studies is to incorporate the latest hydrologic, mineralogic, and geochemical information into a set of numerical models to predict transport of radionuclides from the potential repository to the water table. Since these are predictions of repository performance after waste emplacement, the influence of repository waste heat and future climate changes must be accounted for.

Integrated transport predictions such as these require input from numerous other Project participants. The Project's databases of geology and mineral distributions are used as the structural and geochemical context in which the transport system operates. Numerical grids are built that honor these databases so that they can be populated with flow and transport parameters. The hydrologic parameters for the model were obtained from the recent report on the unsaturated zone flow system by Bodvarsson et al. (1997). These parameters include unsaturated hydrologic property values for all units defined in the geologic framework model, as well as properties of zeolitic tuffs. Two- and three-dimensional flow simulations, using the spatially varying infiltration map of Flint et al. (1996) and variations of this map, are performed to provide either steady state or transient flow fields that are used to simulate the transport of major ions or environmental isotopes, and to predict radionuclide migration. The major-ion chemistry and environmental isotope modeling studies provide important constraints on the hydrologic and transport system; therefore, we devote considerable effort toward developing models that are consistent with these data sets.

## Executive Summary

---

The dual permeability conceptual model is used extensively in this work, as it has been shown previously to provide a more robust hydrologic setting on which to predict transport of solutes through the unsaturated zone (Robinson et al., 1996). Particle tracking is used as the primary model for the transport predictions because of its ability to capture efficiently the vast difference in travel times depending on whether the radionuclide is in the fracture or matrix continuum. Although these models figure prominently in the simulations in the present study, equivalent continuum flow and reactive transport models are employed in some simulations as well. The choice depends on the application in question and the issues being addressed.

This report is divided into chapters that comprise either preliminary foundational discussions on which the numerical simulations are based, such as grid generation, or distinct topics of investigation using the models developed. The following subsections report the main conclusions of each chapter of the milestone. The final section (Section 1.13) provides a road map between the requirements listed in the Criteria Statement for this milestone and the specific locations in the document where these requirements are met.

### **1.2 Incorporation of Mineralogic Model into Flow and Transport Simulations**

---

The mineralogy of the unsaturated zone has an important bearing on the prediction of hydrologic and transport processes. The distribution of secondary minerals such as zeolites can strongly influence the flow patterns of percolating fluids through the unsaturated zone. The presence of other minerals such as smectite clays, may also be linked to, or evidence for, flow processes occurring in the unsaturated zone. The sorption of many radionuclides are also strongly controlled by the mineral distribution in the flow pathways between the repository and the water table. For these reasons, we have developed a streamlined method for incorporating mineralogic data directly into our site scale model.

## Executive Summary

---

The distribution of major and minor minerals has been organized into a numerical model using the STRATAMODEL software. An interface between this model (reported by Chipera et al., 1997a, b) and the flow and transport simulation models developed in the present study has been developed to make the investigation of mineralogic controls on flow and transport as seamless as possible. In this milestone, the distribution of zeolites in the unsaturated zone is modeled using this information either through the assignment of a cut-off percentage above which the rock is given the properties of zeolitic tuff, or by populating the model with a zeolitic abundance that then is used in assigning flow and transport properties (Chapter 12). An updated version of the mineralogic model is incorporated into the simulations of the present study.

Finally, we compare the mineral distributions measured recently with predicted values using the version of the model before these data were available. For zeolites, we show that the new data do not significantly change the mineral distribution reflected in earlier versions of the model, whereas the distribution of smectite, a less abundant mineral in the unsaturated zone, is more refined after incorporating the new data.

### 1.3 Mesh Generation

---

Computational mesh generation for this report involves translating the Integrated Site Model, ISM (Zelinski and Clayton, 1996, Clayton et al., 1997), of geologic and hydrologic structure and stratigraphy to a finite element mesh. This process maintains the geometry defined by the ISM model while meeting additional geometric constraints on element size and geometry for stable and accurate flow and transport solutions.

The GEOMESH/X3D grid generation toolkit, (Gable et al., 1995, Gable et al., 1996a and b, Trease et al., 1996), has been developed to provide an integrated software package for all grid generation steps, from initial ISM model import to quality checking of input data, mesh optimization, mesh post processing and quality checking, mesh interfacing with the FEHM flow

and transport code and property interpolation from the mineralogy and petrology model (Chipera et al., 1997a and b).

Chapter 3 describes the algorithms used for mesh generation and how the algorithms have been applied to the two- and three-dimensional meshes used for flow and transport computations.

### 1.4 Particle Tracking

---

A new particle tracking technique is presented for simulating liquid or gas phase solute transport in porous media. The method, called the Residence Time Transfer Function (RTTF) particle tracking technique, uses a cell-based approach that sends particles from node to node on a finite difference or finite element grid, after keeping each particle at the cell for a prescribed period of time. To incorporate transport mechanisms such as dispersion and matrix diffusion, the residence time of a particle at a cell is computed using a transfer function that ensures that the correct distribution of times at the cell is reproduced. Transient flow fields are approximated by assuming a non-varying flow field during a time interval of a fluid flow solution. The method is a significant departure from the traditional procedure of mapping a particle trajectory by resolving the velocity vector at a given position by interpolation between positions on the grid. The new procedure is computationally very efficient, enabling large-scale transport simulations of several million particles to be completed rapidly on modern workstations. Furthermore, since the cell-based approach uses directly mass flow rate information generated from a numerical fluid flow solution, complex, unstructured computational grids pose no additional complications. A number of numerical validation and example calculations are presented to demonstrate the strengths of the new technique. A discussion is also provided to point out those situations for which the assumptions of the method might lead to unacceptable numerical inaccuracy, and for these cases alternative numerical transport techniques are recommended. For the present study, the technique is used for unsaturated transport simulations, since the limitations of the method are minimal for the UZ, and the cell-based approach allows accurate simulation of dual-permeability systems in

## Executive Summary

---

which there is a vast disparity in the travel times depending on whether the transport is in the fractures or the matrix.

### 1.5 Hydrologic Property Sets

---

In this section we present a summary of the hydrologic property sets provided by LBNL in the site unsaturated zone flow model (Bodvarsson et al., 1997), along with modifications tested in the present study for their impact on predicted performance. Bodvarsson et al. (1997) provide a logical starting point for numerical simulations of flow and transport in the present study, since models using their parameter sets are based on calibrations to fluid matrix saturation and capillary pressure measured in cores extracted from several wells at the site. Many parameter sets are presented in Bodvarsson et al. (1997), each of which employed a different approach in either the conceptual model (e.g. different fracture/matrix interaction models) or parameter estimation methodology (e.g. different initial guesses in the inversion, different decisions on which parameters to allow to vary to obtain the fit). Since it is not feasible to carry forth with complete transport sensitivity analyses for every parameter set in the LBNL milestone, as well as test variations of these as sensitivity studies, an initial screening was performed to determine which parameter sets are apt to yield significantly different performance predictions.

The “model platform” used to test the hydrologic property sets is a one-dimensional flow and transport simulation with stratigraphy and estimated infiltration rate at SD-9. Steady state, dual permeability fluid flow fields were generated for each property set, after which particle tracking transport simulations of  $^{99}\text{Tc}$  and  $^{237}\text{Np}$  from the repository to the water table were computed. The transport metrics used to identify which property sets yield unique or distinctively different results are the first arrival time of radionuclide at the water table, the relative amount of radionuclide arriving early, and the degree of sorptive delay of  $^{237}\text{Np}$  to zeolitic tuffs. In addition, the relative flow split between the fractures and matrix in the zeolitic tuffs was used as a hydrologic metric for judging the property sets. Because transport of radionuclides escaping the repository is the subject

## Executive Summary

---

of the study, the emphasis is on predicted flow and transport below the repository horizon. Parameter sets may differ in their predictions of hydrologic conditions above the repository; these possible differences are not addressed.

Despite the potentially large spectrum of possible behaviors for different hydrologic property sets, the most striking result of the screening study is the similarity of the flow and transport results. In all cases, fracture-dominated flow in the TSw transitions to almost completely matrix flow in the vitric Calico Hills unit at SD-9. Then, at the transition from the vitric to zeolitic tuff, significant fracture flow through the zeolitic tuffs is predicted for every parameter set, even at the 3.6 mm/y infiltration rate assigned at SD-9. The permeability of the zeolitic tuffs is too low to support the 3.6 mm/y infiltration in the matrix, thus resulting in the fracture flow, which will be even more pronounced in high flux areas within the potential repository area. There are subtle differences from one parameter set to the next which we identify and use as the criteria for selecting sets for the multi-dimensional simulations.

Because of the essential similarities among the various property sets and the possibility that the parameter estimation yielded results that only sample a portion of the range of uncertainty of the actual system, we also propose variations to the calibrated property sets. These variations include higher permeability for the zeolitic rocks, full connection-area weighting for the nonwelded units, and an adjusted property set of Bodvarsson et al. (1997) that they derive as an improved match to Calico Hills fluid saturation data using the three-dimensional model. In all, ten property sets are tested in the screening process, and five are used in subsequent two- and three-dimensional flow and transport simulations.

In this section we also perform a code validation check by comparing the results of FEHM and TOUGH2 for the one-dimensional column. Steady state flow fields were generated with each code, and the flow fields were used by FEHM to compute particle tracking breakthrough curves. The saturation profiles agreed closely. Transport of  $^{99}\text{Tc}$  differed somewhat due to a slight, predicted difference in the flow split between fractures and matrix in the two cases. More

## Executive Summary

---

importantly, the transitions from matrix flow to partial fracture flow at the vitric/zeolitic interface is predicted to occur abruptly above the interface in FEHM and more gradually within the first zeolitic grid block in TOUGH2. Matrix flow within the zeolite in TOUGH2 gave rise to significantly delayed first arrival of  $^{237}\text{Np}$  at the water table. We attribute the TOUGH2 behavior to the combination of upstream weighting of the absolute permeability and the large size of the first zeolitic grid block; FEHM calculations using this same weighting scheme yielded results that approached those of the TOUGH2 run. We therefore recommend that in mountain-scale flow and transport simulations, the absolute permeability be harmonically weighted, and/or the grid be more finely discretized near interfaces of contrasting flow and transport properties.

### 1.6 Environmental Isotopes and the Hydrologic System

---

In this chapter we examine the role of studies coupling environmental isotope data and numerical modeling in identifying flow and transport processes as well as constraining the property sets used to model them. Starting with multiple, different hydrologic property sets from LBNL which are all based on fits matching matrix fluid saturation and capillary pressure (Bodvarsson et al., 1997), we perform a series of studies with one-, two-, and three-dimensional transport models and examine how well the additional isotopic data are matched. The most significant finding in this chapter is that minor changes in hydrologic parameters lead to very different flow distributions in the PTn matrix and fractures. Namely, one property set leads to matrix dominated flow in the PTn while another yields significant fracture flow. Reducing the uncertainty in property set choice may have significant implications on repository design and performance modeling. For example, if fracture flow in the PTn is ubiquitous, then repository design may need to account for periodic high fluxes resulting from transient infiltration events that are not damped in the PTn matrix.

We find that property sets that do not lead to significant fracture flow in the PTn, except in fault zones, provide a better match with the substantial set of analyses of  $^{36}\text{Cl}/\text{Cl}$  ratios measured for ESF samples (Sweetkind et al., 1997, Fabryka-Martin et al., 1996a, Levy et al., 1997). This

## Executive Summary

---

finding supports the assumption that episodic infiltration events in the PTn are damped except in fault zones.

Using a multiple model approach in this study, two- and three-dimensional models are used to assess the effects of spatially distributed infiltration and dipping strata of varying thickness and extent in a faulted system. One-dimensional models are then used to examine, in detail, the effects of episodic transients, fault zone properties, and the relationship between material properties, infiltration rate, and travel time from the surface to the potential repository horizon. This modeling approach, coupled with the data analysis, is used to identify significant processes and verify conceptual models.

### 1.7 Water Chemistry

---

This chapter explores alternative explanations for the water chemistry variations in perched and pore waters at Yucca Mountain. The chemical databases are integrated with hydrologic databases to evaluate different model conceptualizations of the hydrologic behavior of the mountain at low and high infiltration rates. The premise for this exercise is that chemical data, when combined with hydrologic data, provide the most relevant information for “validating” radionuclide transport models, as the movement of naturally occurring solutes is closely related to the potential migration of radionuclides. Our philosophy for model development and testing is one in which these data are used in the building of conceptual models, rather than as data to “calibrate” these models.

Two end-member hypotheses are evaluated for the origin of perched water at Yucca Mountain: a “fast pathway” fracture flow hypothesis, and a transient-mixing hypothesis. The overall consequence of the “fast pathway” hypothesis is that it predicts poor performance for the unsaturated zone, as the Calico Hills transport barrier is essentially bypassed by fracture flow. Since this model is based on non-calibrated fracture properties, we propose an alternative to this model in the transient-mixing hypothesis, based on the integration of all elements of the hydrologic

## Executive Summary

---

and chemical databases at Yucca Mountain. Its main strength is that it explains simultaneously the inversion in apparent ages between pore waters and perched water in the unsaturated zone, and the low chloride content of perched waters relative to the overlying TSw and underlying CHn pore waters. The apparent disequilibrium in pore water and perched water contents is consistent with a model of transient flow, and we demonstrate that the stable isotope data and apparent  $^{14}\text{C}$  and  $^{36}\text{Cl}/\text{Cl}$  ages can be interpreted as resulting from a mixture of late Pleistocene/early Holocene water with modern waters. The existence of these mixed ancient/modern perched water bodies therefore implies that an additional retardation mechanism exists above the Calico Hills formation. The ubiquitous young  $^{14}\text{C}$  ages in the Calico Hills formation pore waters beneath the perched water bodies and in other areas also imply that a lateral component of flow occurs in the vitric Calico Hills and that this formation is not bypassed. Finally, this model is consistent with the three-dimensional stochastic mineral distribution model in which zeolitic and vitric tuffs are intricately interbedded beneath the repository horizon (see Chapter 12 for a description of the stochastic model).

The implication of this model for Performance Assessment is an improved performance of the Calico Hills Transport barrier beneath the repository by 1) the additional barrier component which regulates the downward flow of water to the saturated zone, and 2) increased water residence times in the unsaturated zone due to the presence of long term perched water bodies at depth (i.e., no flow), and lateral diversion above the basal vitrophyre and/or the underlying Calico Hills vitric units. This should result in increased sorption of radionuclides at those boundaries, as actinides sorb in clays and vitric tuffs as well as in zeolites. Finally, we expect that the transient mixing model may give rise to different performance predictions than are achieved with the current hydrologic properties.

### 1.8 Two-Dimensional Radionuclide Transport Simulations

---

In most of the two- and three-dimensional simulations presented in this study, steady state flow fields are generated using FEHM, and then radionuclide transport is computed for various transport parameters. The steady state assumption allows us to compute generic breakthrough curves in response to a pulse of radionuclide injected at time 0. This simulation provides the basis for computing, external to the FEHM simulation, the actual response to a realistic near field release scenario. Numerical convolution is employed for this purpose. In this section we present the results of the generic response curves for a variety of flow and transport parameter sets and scenarios.

Multiple parameter sets from the LBNL site-scale flow model and variations on the USGS infiltration map are used in the simulation of radionuclides from the potential repository to the water table. For most of these parameter sets, radionuclides tend to bypass the zeolites of the Calico Hills via fracture transport when base-case infiltration conditions are simulated. When the infiltration rate is scaled by 1/3, significant fracture flow in the zeolites is still simulated with most parameter sets. A modification increasing CHn zeolite matrix permeabilities by a factor of 5 leads to substantially greater matrix flow and, hence, retardation of sorbing radionuclides. This process leads to dramatic improvement in the performance of the unsaturated zone. These studies demonstrate the overriding importance of proper characterization of the zeolitic units for performance assessment. Presently, there is significant uncertainty in the characteristics of these units due to data limitations. Enhanced characterization efforts, including the planned field test at Busted Butte, would reduce the uncertainty in these calculations and lead to a better understanding of the true nature of the hydrologic and transport behavior of the CHn.

Colloid-facilitated transport of otherwise immobile radionuclides like Plutonium is also addressed in this chapter. As very little data are currently available for Plutonium sorption onto colloids, we present a sensitivity analysis of the significant processes to mobility. In the absence of sorption onto the mobile colloids, Plutonium migration is limited due to large sorption coefficients. Assuming reversible sorption, when partitioning onto colloids approaches 99% or

## Executive Summary

---

more, Plutonium mobility becomes potentially important to performance. If sorption of Plutonium onto colloids is irreversible, any colloid transport would directly affect performance assessment.

Long-time transients capturing climate change related phenomena are also simulated in this chapter. The results show that the flux of radionuclide at the water table under transient conditions is closely approximated by a quasi-steady state model. Thus multiple steady-state simulations can be used to predict the effects of wetter or drier future climates on radionuclide flux at the water table. The effect of potential water table rise due to wetter, future climates is also considered. The combined effect of a shorter travel distance to the water table and high fluxes under a wetter climate scenario yield prediction of poorer unsaturated zone performance than for the present climate conditions.

### 1.9 Three-Dimensional Radionuclide Transport

---

In this chapter, the two-dimensional approach presented in the last chapter is extended to the three-dimensional site-scale model of radionuclide transport. Variations in additional transport properties such as the diffusion coefficient and the dispersion coefficient are also examined in this chapter. With the full three-dimensional transport model, implications of lateral flow, spatial variability of flux, and underlying strata thickness are examined. Compared to the two-dimensional model, greater spreading in the travel time distribution curve is simulated due to the additional flow paths sampling a greater range of property variability that occur in three dimensions. This variability leads to cumulative breakthrough curves at the water table spanning the range from 10 years to 10,000 years. The three-dimensional model predicts some sorption on to the zeolites, similar to the two-dimensional model. However, pathways bypassing the zeolites still exist and may lead to peaks in the mass flux at the water table which are not affected by retardation in the zeolites.

The three-dimensional transport model was used to examine the difference in travel time distribution as a function of the release position in the potential repository. Radionuclides released

## Executive Summary

---

from the northern end of the repository are more likely to experience rapid transport to the water table than radionuclides released in the southern portion of the potential repository. The behavior is attributed to less uniform distribution of zeolites in the southern portion of the domain. This results in slower matrix flow in the nonzeolitic units in the south compared to fracture dominated flow in the zeolitic units in the north. As with the two-dimensional simulations, this finding highlights the critical need to develop greater certainty on the material properties assigned to the zeolitic units. A slightly higher matrix permeability in the zeolites leads to substantially greater retardation of radionuclides.

The diffusion coefficient influences the breakthrough curves simulated with the three-dimensional model, especially for the portion of the inventory with the shortest travel times. Diffusion into the rock matrix and sorption onto zeolites retard the transport of  $^{237}\text{Np}$  traveling in fractures. The dispersion coefficient is shown to have very little impact on the unsaturated zone transport.

### 1.10 Unsaturated Zone Performance Predictions

---

Predicting the response at the water table to the large variety of near field environment (NFE) release scenarios is done most efficiently by decoupling the far-field and near-field models. This chapter describes the process of convolving NFE models with far-field transport simulations. With this approach, the differences in response due to varying hydrologic conditions near waste emplacement drifts, different engineered barrier designs, time varying thermodynamic effects on canister corrosion, different models of release due to dissolution of waste, and uncertainty in transport processes in backfill and invert material can all be evaluated. The present study focuses on the unsaturated zone transport barrier; simplified NFE source term functions are used.

For nonsorbing radionuclides like  $^{99}\text{Tc}$ , there is no retardation in any material between the potential repository and the water table. For all of the different property sets developed by LBNL, fracture flow through the zeolitic Calico Hills and underlying units results in bypassing of most of

## Executive Summary

---

the unsaturated zone matrix material for the USGS infiltration estimates. NFE release rates control the maximum concentration flux at the water table. Releases that occur over longer periods of time lead to lower peak mass fluxes at the water table. Reducing the infiltration rate in these predictions also leads to lower peak mass flux rates at the water table, and they occur significantly later in time.

As with nonsorbing radionuclides, those that do sorb to zeolites like  $^{237}\text{Np}$  still show early arrivals at the water table after release begins for these parameter sets due to the simulated fracture bypass of the zeolites. This early arrival appears to control the peak mass flux as well. Under these conditions, two factors control the magnitude of the peak mass flux at the water table. First, the NFE release scenario directly influences the actual peak mass flux. For example, rapid releases over short time periods yield higher peaks. Second, any parameter that influences the relative flow fraction through fractures has a direct impact on peak mass flux.

Relatively small changes from the LBNL parameters lead to vastly improved performance with respect to sorbing radionuclides. However, without modification, those parameter sets lead to predictions of very little mitigation of releases from the near field by the unsaturated zone. Reduction in uncertainty of the actual hydrologic properties of the Calico Hills (both fracture and matrix) would clarify whether these predictions of poor far-field barrier performance is indeed warranted or whether they are a by-product of a calibration procedure that was not well constrained by data indicating the degree of fracture flow in the units below the basal vitrophyre.

### 1.11 Reactive Transport of $^{237}\text{Np}$ with Repository Heat

---

Characterization and performance assessment studies for the potential high-level nuclear waste repository at Yucca Mountain have identified  $^{237}\text{Np}$  as a radionuclide of concern for the proposed repository. To predict the migration of neptunium after a repository breach, an understanding of the relevant hydrologic and geochemical processes is required. The hydrologic flow in the unsaturated zone at Yucca Mountain is dependent on the infiltration rate, stratigraphy of the vadose zone, and the heat generated by the decaying radioactive waste. The geochemical

## Executive Summary

---

processes that strongly affect  $^{237}\text{Np}$  migration include: solubility-limited release of  $^{237}\text{Np}$  from the near field environment, aqueous speciation of neptunium into non-sorbing carbonate/hydroxy-complexes and the sorbing  $\text{NpO}_2^+$  cation, sorption of neptunium onto the zeolitic tuffs via an ion exchange mechanism, and radioactive decay. We investigate the coupled effects of chemical interactions and heat on neptunium transport from the potential repository to the water table. The selective coupling method is introduced to solve these reactive transport problems. The simulations indicate that in the absence of irreversible changes in the hydrologic and transport properties, the heat pulse does not significantly affect the migration of neptunium, as the time scale of heat pulse propagation is shorter than the time scales associated with neptunium release and migration. Water chemistry, particularly pH, calcium, and sodium concentration significantly affect the retardation of neptunium by the zeolitic rocks between the repository and the water table.

### 1.12 Incorporation of Geostatistics into Flow and Transport Simulations

---

Small scale variability of chemical and hydrologic properties can play an important role on the prediction of flow and transport in the unsaturated zone. The variation in chemical and hydrologic properties is strongly dependent on the mineral distribution. Due to the correlation between mineral distribution and hydrologic and chemical properties, the distribution of minerals such as zeolites can strongly influence the flow patterns of percolating fluids and the sorption of many radionuclides. In this chapter, the zeolitic threshold method used in previous chapters is replaced with more rigorous geostatistical modeling. With this more sophisticated modeling approach, we examine whether using a threshold cutoff for zeolitic abundance is an appropriate upscaling method for characterizing small scale heterogeneity.

The methodology for integrating geostatistical techniques into the mineralogical model is first developed. These geostatistical techniques are used to develop variograms, kriging maps, and conditional simulations of zeolitic abundance. The kriging maps are used to estimate the

## Executive Summary

---

uncertainty in the mineralogical model. The conditional simulations result in equally probable maps of zeolitic abundance. Eventually, simulating flow and transport for many conditional simulations, we will be able to estimate the uncertainty in  $^{237}\text{Np}$  travel times using Monte Carlo techniques.

Using the algorithms discussed in Chapters 2 and 3, a conditional simulation of zeolitic abundance was mapped onto the geologic model. We investigate the relationship between percent alteration, permeability changes due to alteration, sorption due to alteration, and their overall effect on radionuclide transport.

A key conclusion to the study is that the retardation due to sorption predicted by a conditional simulation is much larger than the retardation predicted by the zeolite threshold method. The reason for larger retardation of  $^{237}\text{Np}$  for the conditional simulation is a small but significant  $K_d$  at locations with zeolite abundance less than 10%. At these locations, the  $K_d$  is low (less than 1 cc/g) but permeability is large enough for the flow to be matrix dominated. By contrast, the increased retardation is not due to high  $K_d$  values which occur at high zeolite abundance because very little flow travels through these low permeability regions. Modifying the 10% threshold case to include some sorption at locations with zeolite abundances less than 10% closely matches the more rigorous conditional simulation. For the purposes of abstracting these results, setting nonzero  $K_d$ 's in the vitric tuffs may be an effective way to mimic the more rigorous conditional simulations.

We therefore recommend that experimentalists determine whether rocks with low but non-zero zeolitic abundance exhibit measurable sorption of radionuclides like  $^{237}\text{Np}$  and Uranium. Rocks with high zeolitic abundance may not be as effective in retarding these radionuclides since these rocks also in general have low permeability and contaminants can only enter these regions through molecular diffusion. In addition, any fractures in these highly zeolitized rocks will provide a mechanism for fluid and radionuclides to bypass these regions. However, small but significant sorption of rocks with low zeolite content may have a very large impact on the travel times for

## Executive Summary

---

$^{237}\text{Np}$  and other radionuclides through the unsaturated zone. The planned transport test at Busted Butte should provide results for testing this hypothesis.

In order to draw more substantial conclusions, many more conditional simulations will need to be performed. In addition we plan to refine the correlations and variograms and implement linear coregionalization models. In this study, the general framework has been developed to integrate geostatistical information into the site scale flow and transport calculations. These powerful tools provide a means for determining the uncertainties associated with radionuclide transport through the unsaturated zone at small scales not normally studied in site scale models. In addition, we can use these more rigorous simulations to check the validity of the simplifying assumptions incorporated into other flow and transport simulations.

### 1.13 Traceability to Criteria for Milestone SP25BM3

---

The table below provides a road map between the requirements listed in the Criteria Statement for this milestone and the specific locations in the document where these requirements are met.

#### TECHNICAL REQUIREMENTS

CRITERIA	TEXT LOCATION
This report will include a conceptual model of the transport of radionuclides in the unsaturated zone at Yucca Mountain, including 2- and 3-D integrated transport calculations and sensitivity analyses.	Conceptual model: 4.3, 6.5.2 2D integrated transport calculation: Chapter 8. 2D sensitivity analyses: Sections 8.5, 8.6, 8.7, 8.8, 8.9 3D integrated transport calculations: Chapter 9 3D Sensitivity analyses: Sections 9.4-9.7

## Executive Summary

<p>Both equivalent continuum and dual permeability calculations will be made, incorporating discrete structural features as available and appropriate.</p>	<p>Equivalent Continuum calculations: Sections 4.6, 11.4, 11.8</p> <p>Dual Permeability Calculations: Sections 4.4, 4.7, 5.4, 5.5, 6.7, 6.9-6.12, 8.5-8.11, 9.4-9.7, 10.6-10.9, 12.9</p> <p>Incorporation of discrete structural features: Sections 3.3, 3.4, 6.5, Included in all 2D and 3D dual permeability calculations.</p>
<p>The model will do the following:</p>	
<p>a) Incorporate and consider isotopic data which are indicative of processes and rates of fluid flow or residence times in the unsaturated zone.</p>	<p>Chapter 6. Processes: 6.5, 6.7-6.12 Rates and Residence Times: 6.10-6.12</p>
<p>b) Draw upon the Report on Summary of Geochemistry/Transport Laboratory Tests to provide defensible values for important transport processes and parameters including:</p>	
<p>1) Sorption and Diffusion Coefficients</p>	<p>8.6, 8.7, 8.10, 9.4, 9.6, 9.7, 11.7</p>
<p>2) Radionuclide solubility and speciation</p>	<p>10.5, 11.4, 11.7</p>
<p>3) Colloids as controlled by relevant thermal effects and water chemistry.</p>	<p>8.10</p>
<p>c) Rely heavily on input from the 3-D mineralogical model of Yucca Mountain.</p>	<p>2.2-2.5, 3.4, 6.5, 8.6, 12.5-12.9</p>
<p>Update 3-D transport simulations for radionuclides including, but not limited to:</p>	
<p>Np</p>	<p>5.5, 8.5-8.7, 8.9, 9.4, 9.5, 10.7, 11.8, 12.9</p>
<p>Pu</p>	<p>8.10, 10.9</p>
<p>Tc</p>	<p>5.5, 8.5-8.7, 8.9, 9.4, 9.5, 10.6</p>
<p>under ambient</p>	<p>5.5, 8.5-8.7, 8.9, 9.4, 9.5, 10.6-10.9</p>
<p>and thermally perturbed</p>	<p>11.8</p>

## Executive Summary

for two future climates and accompanying infiltration fluxes and effects on recharge	8.7, 8.11, 9.4, 9.5, 11.8
The report will be coupled to appropriate near-field source term and thermal models	10.4, 10.5 11.7, 11.8
The deliverable will be prepared in accordance with OCRWM approved quality assurance procedures implementing requirements of the Quality Assurance Requirements Description.	Done
The product shall be developed on the basis of the best technical data, including both Q and non-q data. The Q status of data used and cited in the report shall be appropriately noted.	QA description of software and data in acknowledgments and in each chapter.
Stratigraphic nomenclature used shall be consistent with the Reference Information Base section 1.12(a): Stratigraphy-Geologic Lithologic Stratigraphy.	Throughout milestone, Table 15.1
References to data used in the report shall include record Accession Numbers or Data Tracking Numbers when available.	QA description of data in acknowledgments and in each chapter.
Technical data contained within the deliverable and not already incorporated in the Geographic Nodal Information Study and Evaluation System (GENISES) shall be submitted for incorporation into the GENISES in accordance with YQP-SIII.3Q.	N/A

## Executive Summary

---

<p>Verification of technical data submittal compliance shall be demonstrated by including as part of the deliverable:</p> <p>a) A copy of the Technical Data Information Form generated identifying the data in the Automated Technical Data Tracking system, and</p> <p>b) a copy of the transmittal letter attached to the technical data transmittal to the GENIS-ES Administrator.</p>	<p>a) N/A</p> <p>b) done</p>
--	------------------------------

## **Chapter 2 - Incorporation of the Mineralogic Model into the Site-Scale Flow and Transport Model**

### **2.1 Abstract**

---

The mineralogy of the unsaturated zone has an important bearing on the prediction of hydrologic and transport processes. The distribution of secondary minerals such as zeolites can strongly influence the flow patterns of percolating fluids through the unsaturated zone. The presence of other minerals such as smectite clays, may also be linked to, or evidence for, flow processes occurring in the unsaturated zone. The sorption of many radionuclides are also strongly controlled by the mineral distribution in the flow pathways between the repository and the water table. For these reasons, we have developed a streamlined method for incorporating mineralogic data directly into our site-scale model.

The distribution of minerals has been organized into a numerical model using the STRATAMODEL software. An interface between the mineralogic model (reported by Chipera et al., 1997a, b) and the flow and transport simulation models developed in the present study has been developed to make the investigation of mineralogic controls on flow and transport as seamless as possible. In this milestone, the distribution of zeolites in the unsaturated zone is modeled using this information either through the assignment of a cut-off percentage above which the rock is given the properties of zeolitic tuff, or by populating the model with a zeolitic abundance that then is used in assigning flow and transport properties (Chapter 12). The mineralogic model incorporated into the simulations of the present study is an updated version of Chipera et al. (1997a).

Finally, we compare the mineral distributions measured recently with predicted values using the version of the model before these data were available. For zeolites, we show that the new data do not significantly change the mineral distribution reflected in earlier versions of the model, whereas the distribution of smectite, a less abundant mineral in the unsaturated zone, is more refined after incorporating the new data.

### **2.2 Mesh Generation**

---

Computational mesh generation for this report involves translating the Integrated Site Model, ISM (Zelinski and Clayton, 1996, Clayton et al., 1997), of geologic and hydrologic structure and stratigraphy to a finite element mesh. The relationship between geologic and hydrologic units is presented in Table 15-1. This process maintains the geometry defined by the ISM model while meeting additional geometric constraints on element size and geometry for stable and accurate flow and transport solutions.

The GEOMESH/X3D grid generation toolkit, (Gable et al., 1995a and b, Gable et al., 1996, Trease et al., 1996), has been developed to provide an integrated software package for all grid generation steps, from initial ISM model import to quality checking of input data, mesh optimization, mesh post processing and quality checking, mesh interfacing with the FEHM flow and transport code and property interpolation from the mineralogy and petrology model (Chipera et al., 1997a and b).

Chapter 3 describes the algorithms used for mesh generation and how the algorithms have been applied to the two- and three-dimensional meshes used for flow and transport computations.

### **2.3 Software and Data QA Status**

---

The petroleum industry standard software packages STRATAMODEL and RC<sup>2</sup> are used in the geostatistical analyses of heterogeneous materials. These are off-the-shelf software packages and are applied only to sensitivity studies in the present study. They are non-Q with respect to YMP and Los Alamos quality assurance requirements but they follow well documented methods for geostatistical representation of spatially varying attributes. The status of the data utilized in this Chapter are shown in Table 2-1.

## Incorporation of the Mineralogic Model into the Flow and Transport Model

Table 2-1. QA Status of Data used in this Chapter			
REFERENCE	Q Status	DTN	COMMENT
Chipera et. al., 1997a, "Preliminary Three Dimensional Mineralogical Model of Yucca Mountain, Nevada, YMP Milestone SP321AM4"	non-Q	Not Assigned	No DTN assigned
Chipera et. al., 1997b "Mineralogic Variation in Drill Holes USW NRG-6, NRG-7-7a, SD-7, SD-9, SD-12, and UZ#14: New Data from 1996-1997 Analysis Los alamos National Laboratory YMP Deliverable SP321BM4"	Q	LADV831321AQ97.00 1	
Clayton, et. al., 1997, "ISM2.0: A 3-D geological framework and integrated site model of Yucca Mountain: Version ISM1.0, Doc ID B00000000-01717-5700-00004 Rev 0", MOL. 19970122.0053, CRWMS M&O	Q		By agreement with DOE and NRC accepted as Q even though it utilizes some non-Q data
Zelinski and Clayton, 1996, "A 3-D geological framework and integrated site model of Yucca Mountain: Version ISM1.0, Doc ID B00000000-01717-5700-00002 Rev 1", CRWMS M&O	non-Q		

### 2.4 Motivation for the Current Mineralogic and Hydrologic Model

Sorptive zeolitic minerals located between the potential repository and the water table strongly affect travel times of radionuclides such as  $^{237}\text{Np}$  through the unsaturated zone. Prior to 1997, the site-scale geologic model for the potential repository at Yucca Mountain was comprised of layers of either zeolitic or non-zeolitic material in order to model the sorptive behavior of the zeolites. This division drew upon knowledge of whether a layer was sparsely or abundantly populated with zeolitic minerals. For purposes of transport calculations, those layers containing abundant zeolites were assigned zeolitic properties while the others were given vitric properties.

## **Incorporation of the Mineralogic Model into the Flow and Transport Model**

---

This assumption may not be valid; because zeolites are formed through secondary alteration, their distribution may not follow the primary geologic stratigraphy.

The greatest weakness of such a binary framework lies in its effect on species retardation: if a layer is not as completely zeolitic as portrayed, retardation of contaminant species may not be accurately captured. Specifically, zeolitic tuff is less permeable than vitric tuff, and a radionuclide such as  $^{237}\text{Np}$  which sorbs to zeolites may therefore bypass portions of heterogeneous zeolitic layers leading to less retardation of  $^{237}\text{Np}$ . Therefore, the homogenous zeolitic layers of the site-scale model used in previous studies (Robinson et al., 1995, 1996) may have overpredicted the sorption of the zeolites (Figure 2-1a).

In March, 1997, the stratigraphic framework was revised by integrating mineralogic abundances obtained from drill core data (Chipera et al., 1997a). Incorporation of these data has provided a more accurate representation of the 3-D mineralogic distribution, and therefore zeolite abundance distribution, at Yucca Mountain. Previously simplistic homogeneous zeolitic or vitric layers have now been replaced by spatially distributed mineralogic abundances. Specifically, zeolitic properties extracted from the mineralogic model can now be mapped onto the site-scale model providing a more accurate representation of the zeolites (Figure 2-1b) (for details see section 3). After the mapping process, the percent alteration (% zeolite) is prescribed at each node of the site-scale model and the appropriate flow and transport properties are assigned. In most simulations, we chose a simple threshold of 10% to flag nodes as either zeolitic or unaltered. This threshold was used because, at that time, there were no correlations between the degree of zeolitization and the hydrologic and chemical properties. Hydrologic characterizations for purely altered (zeolitic) and unaltered (vitric) matrix materials have been developed (Flint, 1996). Therefore, the threshold provides a method for assigning either vitric or zeolitic properties to each node (i.e., nodes having less than 10% zeolite are assigned vitric properties and nodes having greater than 10% zeolite are assigned zeolitic properties). In this chapter, we will briefly describe the mineralogical model that is used to construct a distribution of zeolitic minerals, which are used

## Incorporation of the Mineralogic Model into the Flow and Transport Model

a



b

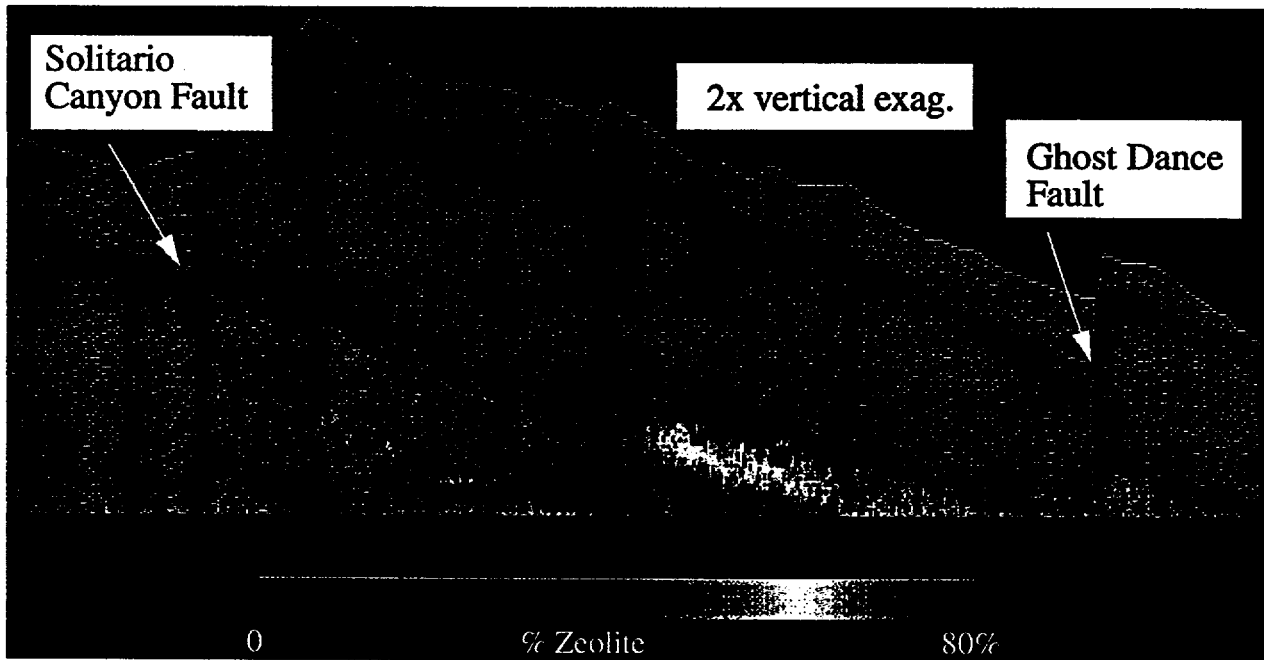


**Figure 2-1.** Antler Ridge cross section (a) Continuous zeolitic layers (in red) of the Site-Scale Model used in Robinson et al. (1996), (b) Zeolitic distributions are mapped from the 3-D mineralogical model (Chipera et al, 1997a) to the FEHM finite element mesh. The profiles look different because (b) accounts for fault offsets.

## **Incorporation of the Mineralogic Model into the Flow and Transport Model**

---

in the flow and transport simulations. In Chapter 12, we replace the zeolitic threshold method with a more rigorous geostatistical model to determine the applicability of using a threshold cutoff for zeolitic abundance.

### **2.5 Mineralogic Model**

---

Quantitative mineralogy, as obtained by XRD methods, was used as the mineralogic input into the 3-D mineralogic model. Data from a particular drill hole were included in the mineralogic model if a reasonable sample distribution existed for the drill hole or if the drill hole was located in an important location such as at the edge of the modeling area. The drill holes and the mineralogic data sources used for the 3-D model are listed in Table 2 of Chipera et al. (1997a).

Six classes of geologic materials have been incorporated in the 3-D mineralogic model. These minerals, mineral groups, or glasses used in the model are:

1. Smectite + Illite
2. Zeolites (clinoptilolite, heulandite, mordenite, chabazite, erionite, stellerite)
3. Tridymite
4. Cristobalite + Opal-CT
5. Glass
6. Analcime

Appendix I of Chipera et al. (1997a) lists the mineralogy, stratigraphy and depths of analyzed samples for each of the 17 drill holes included in this model. Data from drill holes is represented as a separate ascii file that is input directly into the model.

The commercially available computer code STRATAMODEL was used to interpolate mineral abundances onto volumes where no measurements are available. A common feature of software available for property interpolation (Stratamodel, RC<sup>2</sup>, GSLIB) is that they operate on a

## **Incorporation of the Mineralogic Model into the Flow and Transport Model**

---

logically rectangular grid. However, the ISM model (Zelinski and Clayton, 1996, Clayton et al., 1997) is not represented on a logically rectangular grid. Therefore, for property interpolation and distribution, but not during construction of the computational grids, the ISM model is interpolated onto regular grids. The geologic model is generated by importing files of surfaces that contain x (easting), y (northing) and z (elevation in meters) coordinates. STRATAMODEL then assigns a regular grid spacing to these irregular grids and generates continuous surfaces. Using knowledge of the structural relationships between the surfaces specific to this site, a stratigraphic framework model is constructed which captures any pinchouts, onlap, offlap or truncations that are known to exist.

The model volume is then populated with attributes by importing the mineralogic data (obtained from Chipera) that occur at specific x, y, and depth locations within the model. STRATAMODEL uses a  $1/r^2$  interpolation scheme to distribute the properties throughout the three dimensional volume. That is, in a model cell for which there is no mineralogic information, STRATAMODEL assigns mineralogic values by searching within a certain radius from that cell and giving weight to each data point found. The weight given is based on the distance (r) of the data point from the cell being filled. Data points farther from that cell are given less weight. STRATAMODEL is guided in this step by a user-specified search radius which is based on knowledge of the site, such as drill core spacing. The  $1/r^2$  interpolation scheme acts to smooth the mineralogic distributions. In Chapter 12, we present mineralogic distributions based on a more rigorous geostatistical package that better captures the spatial structure of the zeolitic mineral distributions.

The 3-D model had a grid spacing of 243.84 m (800 ft.), which covers a ground area of approximately  $166 \times 10^6 \text{ m}^2$ , and contains information from 17 boreholes (Chipera et al., 1997a). Figure 2-2 shows the location of the wells in the mineralogic model. The model volume is divided into 335 layers to adequately capture the vertical density of mineralogic data. The result is a model with 1,034,470 cells. Each cell of the model contains eleven values, including mineral

## Incorporation of the Mineralogic Model into the Flow and Transport Model

- Wells in Chipera et al. (1997a)
- New well data
- Wells with updated data

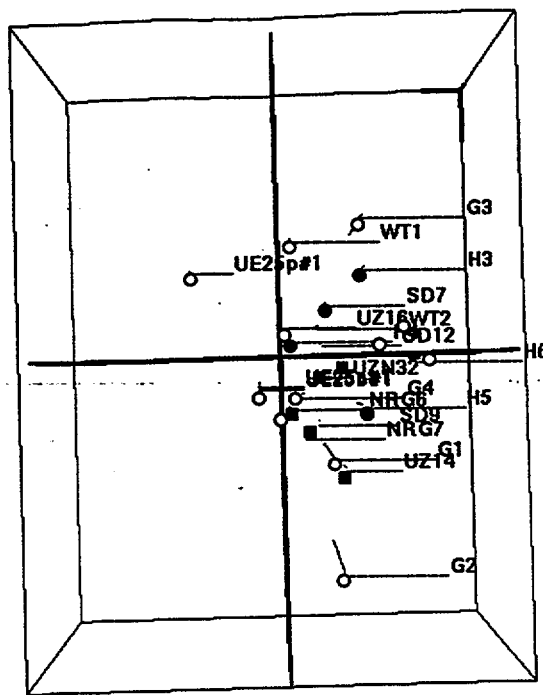


**Figure 2-2.** Locations of the 21 wells in plan view of mineralogical model.

abundance for the six mineral classes, cell location, stratigraphic layer, elevation in meters, cell volume and cell thickness. Any cell within the model volume can be queried to determine any of these values.

The more rigorous geostatistical simulations of Chapter 12 utilize an updated version of the 3-D mineralogical model (data from Chipera et al., 1997b), which incorporates data from 21 wells for a total of 3817 zeolite abundance measurements. The new wells and the location of the updated data are also shown in Figure 2-2. Figure 2-3 compares the Chipera et al. (1997a) model with the updated mineralogical model Chipera et al. (1997b) at the Antler Ridge cross section (the cross section used in the two dimensional flow and transport calculations). The figure shows that the updated model resolves more distinct zeolitic layers, but in general, the two models are similar for the Antler Ridge cross section.

Figure 2-4 compares zeolite and smectite abundance for the Chipera et al. (1997a) and updated mineralogical model (Chipera et al., 1997b) at locations close to several wells. As

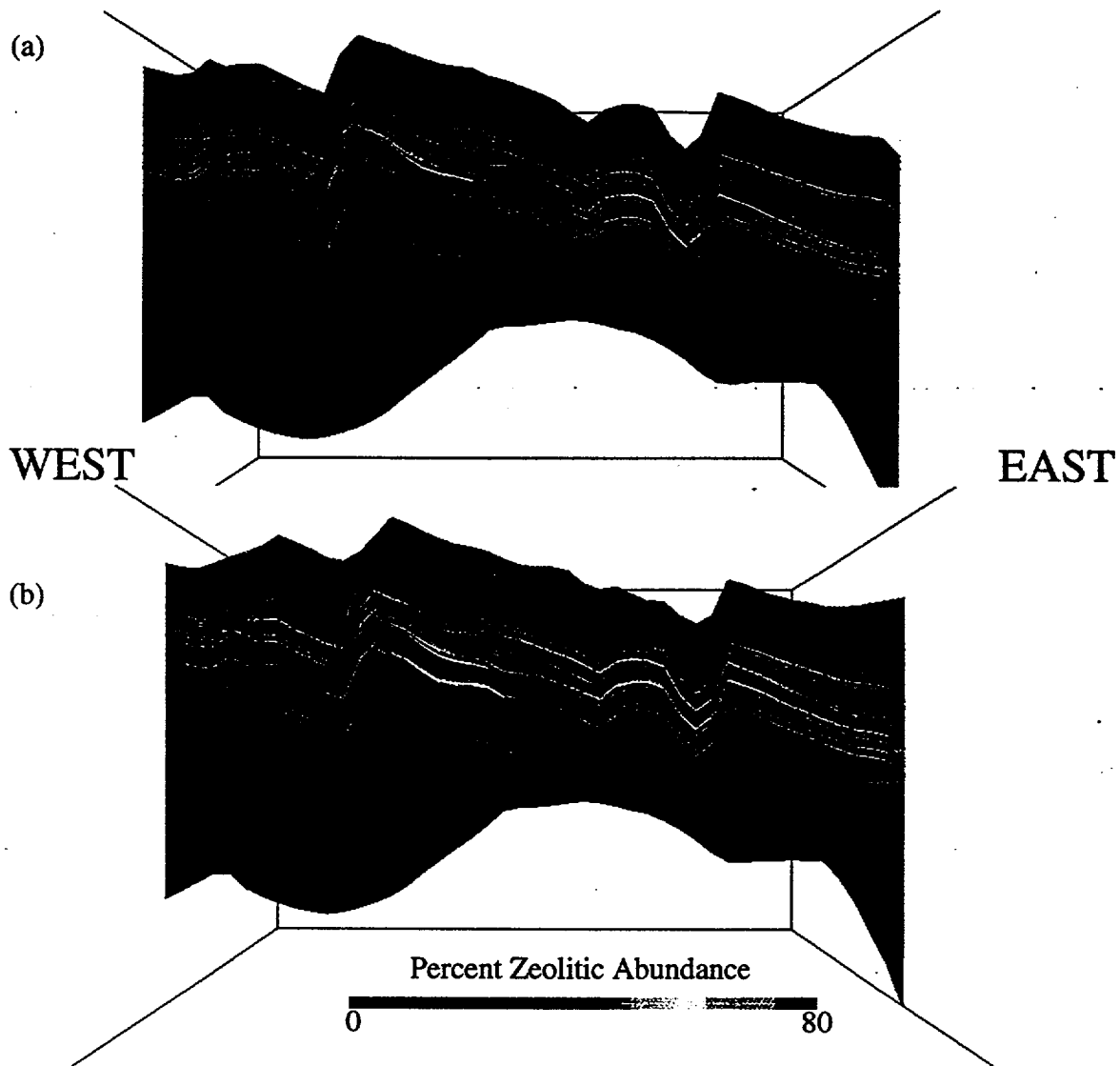


**Figure 2-3.** Comparison of the (a) Chipera et al. (1997a) model and (b) the updated mineralogical model (Chipera et al., 1997b) for the Antler Ridge cross section.

expected, the profiles for zeolitic abundance at a location near G1 are nearly identical because G1 is present in both models (Figure 2-4a). The profiles for zeolitic abundance are only slightly different at a location near UZ-14 even though UZ-14 data was not present in Chipera et al. (1997a) model (Figure 2-4b). The Chipera et al. (1997a) model captures the correct zeolitic profile near UZ-14 for two reasons: G1 is close to UZ-14, and zeolites have large correlation lengths in the horizontal direction (see chapter 12). Therefore, the data from UZ-14 and G1 are consistent and act to decrease the overall uncertainty in the model. The additional well data used in the updated well

## Incorporation of the Mineralogic Model into the Flow and Transport Model

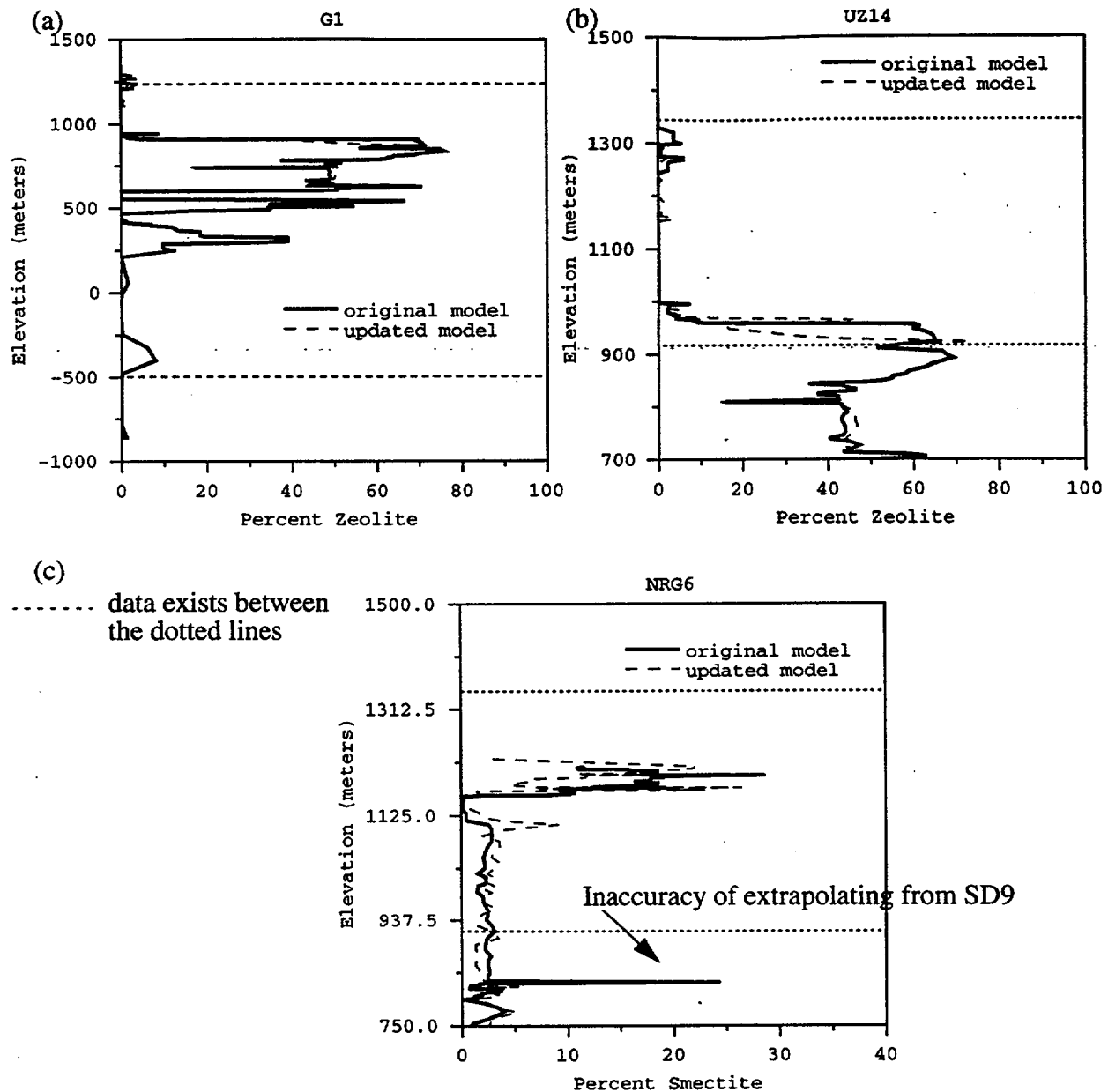


**Figure 2-4.** Comparison of Chipera et al. (1997a) and updated mineralogical model (Chipera, 1997b) at locations close to wells (a) zeolite abundance at G1 (G1 existed in both models), (b) zeolite abundance at UZ-14 (UZ-14 only exists in the updated model but is close to G1), (c) smectite abundance at NRG6 (NRG6 only exists in the updated model).

model buttresses the zeolitic abundance data from Chipera et al. (1997a). In general, the maps for zeolitic abundance are very similar between the models. However, the additional well data affects the distributions of smectite which is not as highly correlated (pers. comm. D. Vaniman). Figure

2-4c shows that the two models show significant differences in smectite abundance at a location close to NRG-6.

### **2.6 Conclusions**

---

Capturing spatial variability is necessary to assess the site performance as it relates to uncertainty in attribute (permeability, porosity,  $K_d$ ) distributions. This is particularly important for the zeolitic minerals between the basal vitrophere and the water table due to their role in either retarding migrating radionuclides or enhancing fracture flow. The geologic model of the unsaturated zone is based only on primary formation processes and, hence, does not capture the structure of the secondary alteration of vitric minerals to zeolites. Thus, capturing both the geologic structure and the mineralogic structure requires automatic integration of multiple sources of information. An approach and companion tools have been developed to couple the relevant models and generate appropriate attribute distributions to perform the analyses of the impact of zeolite spatial variability on repository performance. This same approach and tool set can then be applied to studies of the impact of uncertainty in attribute distribution. Chapter 12 takes this process through the development of heterogeneous fields of mineral distributions in an examination of the sensitivity to capturing the coupled chemical and physical heterogeneity in the subsurface at Yucca Mountain.

In this milestone, the distribution of zeolites in the unsaturated zone is modeled using the information integration processes developed here either through the assignment of a cut-off percentage above which the rock is given the properties of zeolitic tuff, or by populating the model with a zeolitic abundance which then is used in assigning flow and transport properties. An updated version of the mineralogic model of Chipera et al. (1997b), is incorporated into the simulations of the present study.

Finally, we compare the mineral distributions measured recently with predicted values using the version of the model before these data were available. For zeolites, we show that the new

## **Incorporation of the Mineralogic Model into the Flow and Transport Model**

---

data do not significantly change the mineral distribution reflected in earlier versions of the model, whereas the distribution of smectite, a less abundant mineral in the unsaturated zone, is more refined after incorporating the new data.

## Chapter 3 - Mesh Generation

### 3.1 Abstract

---

Computational mesh generation involves translating the Integrated Site Model, ISM (Zelinski and Clayton, 1996, Clayton et al., 1997), of geologic and hydrologic structure and stratigraphy to a finite element mesh. This process maintains the geometry defined by the ISM model while meeting additional geometric constraints on element size and geometry necessary for stable and accurate flow and transport solutions.

The GEOMESH/X3D grid generation toolkit, (Gable et al., 1995, Gable et al., 1996a and b, Trease et al., 1996), has been developed to provide an integrated software package for all grid generation steps including: import of initial ISM model, quality checking of input data, mesh optimization, mesh post processing and quality checking, mesh interfacing with the FEHM flow and transport code, and property interpolation from the mineralogy and petrology model (Chipera et al., 1997a and b). Chapter 3 describes the algorithms used for mesh generation and how the algorithms have been applied to the two- and three-dimensional meshes used for flow and transport computations.

### 3.2 QA Status of Software and Data

---

The GEOMESH/X3D grid generation toolkit, (Gable et al., 1995, Gable et al., 1996a and b, Trease et al., 1996) is non-Q with respect to YMP and Los Alamos quality assurance requirements. However, version control software tracking procedures identical to those used for the Q code FEHM are followed. GEOMESH/X3D utilizes well established procedures to insure robust mesh generation results and to insure traceability of changes to the software. A suite of test problems has been developed and all new releases are verified against the test suite.

## Grids

**Table 3-1. QA Status of Data used in this Chapter**

REFERENCE	Q Status	DTN	COMMENT
<b>Buesch et. al., 1996</b> , "Revised Stratigraphic nomenclature and macroscopic identification of Lithostratigraphic units of the Paintbrush Group exposed at Yucca Mountain, Nevada", USGS Survey Open-File Report 94-496, 1996	Q	GS941208314211.064	
<b>Clayton et. al., 1997</b> , "ISM2.0: A 3-D geological framework and integrated site model of Yucca Mountain: Version ISM1.0", Doc ID B00000000-01717-5700-00004 Rev 0, MOL. 19970122.0053, CRWMS M&O	Q		By agreement with DOE and NRC accepted as Q even though it utilizes some non-Q data
<b>Zelinski and Clayton, 1996</b> , "A 3-D geological framework and integrated site model of Yucca Mountain: Version ISM1.0", Doc ID B00000000-01717-5700-00002 Rev 1", CRWMS M&O	non-Q		

### 3.3 Unsaturated Zone Computational Mesh from Stratigraphic Model

---

All grids are built from the detailed geologic framework model ISM (Zelinski and Clayton, 1996, Clayton et al., 1997) which is correlated to the Project's hydrologic units and nomenclature in Table 15-1. Faults are represented as vertical features. This is consistent with the model of Bodvarsson et al. (1997), that incorporates a subset of the faults used in this work as vertical features. An example of a two-dimensional cross section, within the framework of the three-dimensional mesh it is extracted from is, shown in Figure 3-1.

The primary criterion used in mesh construction is that the mesh will retain the original

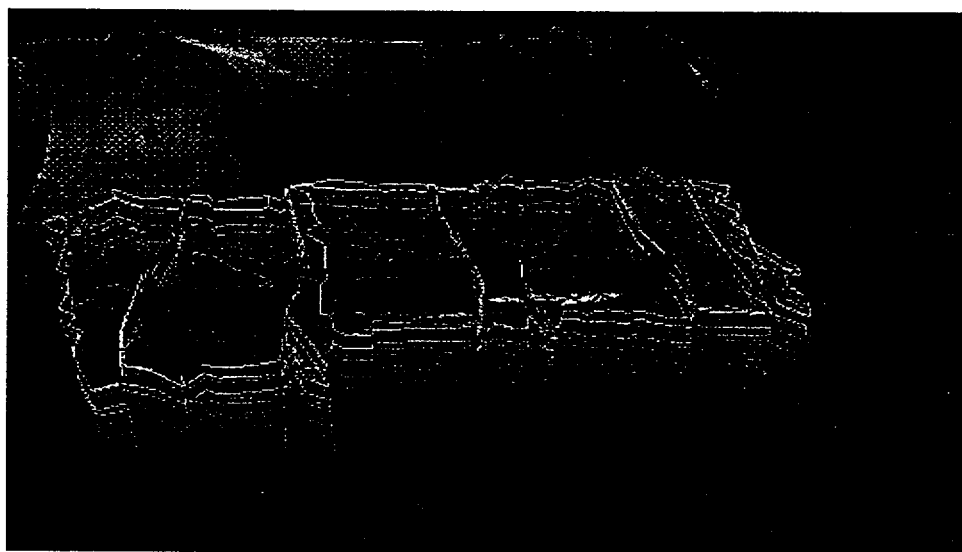


**Figure 3-1.** Layer 9 of ISM shown with colors representing elevation. The area in which a three-dimensional tetrahedral grid is build is shown by the wire frame in which each line represents a stratigraphic layer boundary. The two-dimensional grid used for computations is shown with zeolite abundance shown with red for high zeolite abundance and blue for low zeolite abundance.

geometry of the ISM model. In the grid generation process some smoothing, upscaling or reinterpretation of the ISM model is done. When approximations are necessary, they are carefully controlled and quantified to insure the final grid matches the ISM geometry.

### 3.3.1 Mesh Generation from ISM Input

The steps required to create a two or three-dimensional computable mesh from the Triangular Irregular Network (TIN) data are detailed below and include:

- Import ISM Triangular Irregular Network (TIN) data into GEOMESH/X3D
- Test and correct inconsistencies in TIN sheets
- Identify and tag the faults on the TIN surfaces
- Define polygonal subset of TIN surface
- Refine TIN surface grids in and adjacent to faults
- Define upper and lower boundary truncation surfaces
- Define minimum layer thickness
- Stack layers and build prism elements between surfaces
- Convert prism elements into tetrahedral elements
- If two-dimensional: Extract a two-dimensional hybrid grid from the three-dimensional tetrahedral mesh
- If two-dimensional: Convert the two-dimensional hybrid grid into a triangulated mesh
- If two-dimensional: Clip the mesh to area of interest
- Optimize the grid for computation using reconnection, smoothing, refinement and derefinement
- Interpolate attributes from geostatistics or Stratamodel representation of mineralogy
- Compute and output finite volume matrix coefficients
- Compute and output area coefficients of surface nodes
- Define node sets for setting initial conditions, boundary conditions and material properties
- Mesh quality checks

#### 3.3.1.1 Import ISM Data into GEOMESH/X3D

The first step required to integrate the ISM data is to import the ISM model. The ISM data is provided as 31 computer files that each contain a representation of the top surface of a geologic units. Each surface is represented by a TIN surface of 4976 x, y, z coordinates and the connectivity for 9823 triangles (Figure 3-2).

### 3.3.2 Quality Testing and Correcting of ISM TINs

To insure that the triangular sheets representing the ISM model form a valid triangulation, the tests that must be met are:

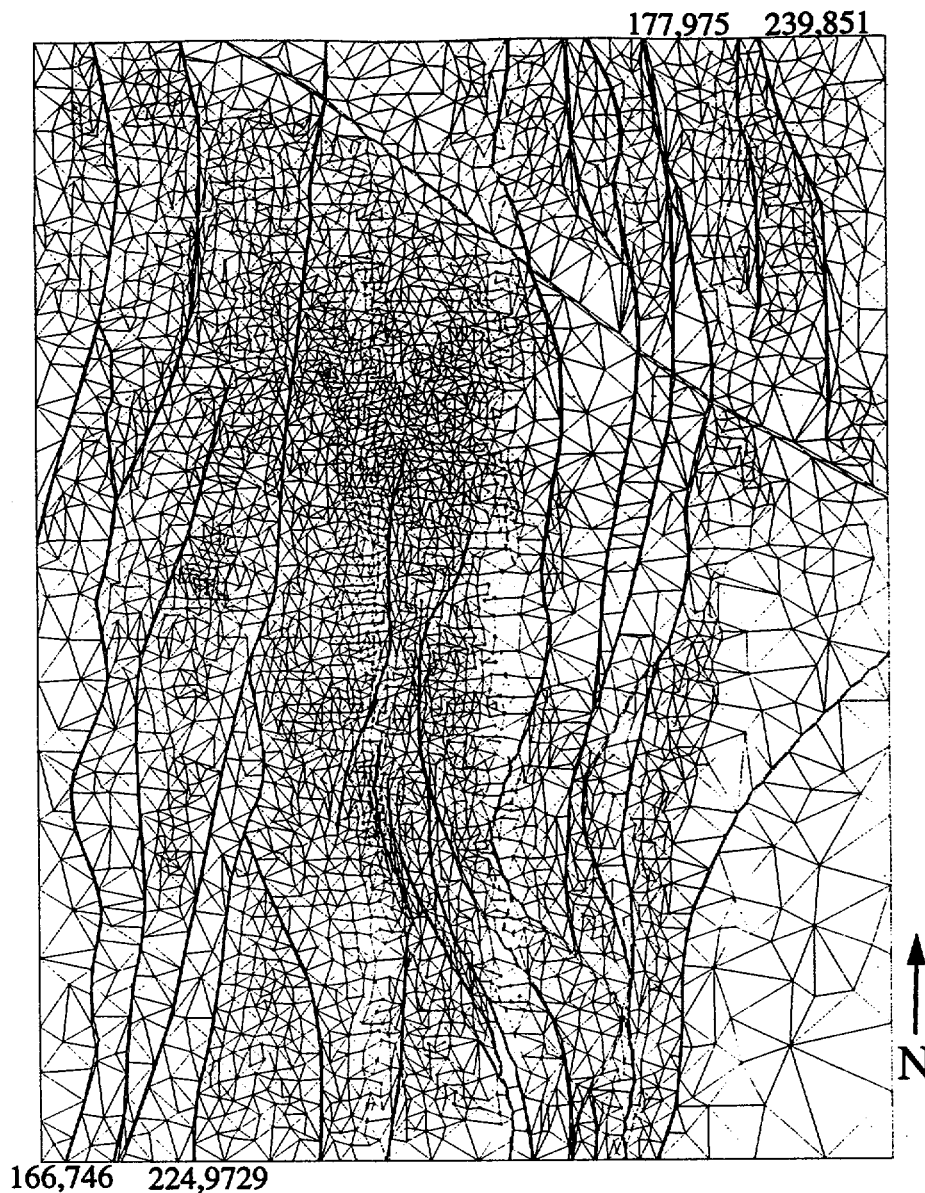


**Figure 3-2.** Top view of one TIN from ISM. TIN consists of 4976 nodes and 9823 triangles. Coordinates are Nevada State Plane in meters. Each triangle vertex is assigned an elevation, resulting in a piecewise linear representation of stratigraphic surfaces.

- TIN sheets have no holes
- No triangles overlap
- All triangles are ordered to have their normal vector on the same side of the TIN.

Examination of these data found that all the TIN sheets suffered from a small number of holes and overlaps. Although these holes and overlaps are inconsequential for creating computer visualizations of the data, these problems would make the subsequent mesh generation steps

impossible if they are not first corrected. Thus software was developed to identify, characterize and repair the inconsistent TINs. This process resulted in the addition of 3 triangles to each of the 31 TINs and some minor to the connectivity to eliminate overlaps.

### **3.3.2.1 Identify Faults**

The triangular representation of each stratigraphic boundary in ISM does not have any attribute flags indicating which parts of the TINs represent faults and which parts of the TINs represent a stratigraphic boundary. It is essential for the flow and transport studies to identify which parts of the model are fault related so that hydrologic properties of faults can be included. An algorithm was developed to identify the portions of the TIN sheets that represent faults. The algorithm is based on the observation that faults can be identified in the TIN sheets by examination of the normal vector of each facet of the TIN. The algorithm is described as follows: The normal vector to each triangle is calculated. For these sheets, all normal vectors are within ninety degrees of vertical. If the normal vector is within 45 degrees of vertical, the triangle is taken to be a stratigraphic boundary. If the normal vector is greater than 45 degrees from vertical and less than 90 degrees, it is labeled as a fault triangle. The fault triangles are further identified by their tilt to the north, east, south or west. The result is that each triangle is identified as either a stratigraphic boundary or as one of four fault types (see Figure 3-3).

### **3.3.2.2 Define polygonal subset of TIN surface**

The area of interest for the current flow and solute transport modeling effort is smaller than the area defined in the geologic framework model ISM (Zelinski and Clayton, 1996). A polygonal subset of each TIN surface is created by removing any elements that fall outside a user defined area. Typically, this area is bounded by faults (Figure 3-4). Where no faults exist and a subset boundary is desired, elements are removed outside a straight line that connects natural fault boundaries. Since the element edges do not coincide exactly with the arbitrary bounding line, some unevenness of the boundary of the subset results. This unevenness does not effect the flow and solute transport modeling results because the boundaries are chosen to be sufficiently far from the model area of interest.



**Figure 3-3.** Layer 38 from ISM at 3X vertical exaggeration. Stratigraphic layer boundary is colored in yellow. West facing faults are green, south facing faults are blue.

### **3.3.2.3 Refine TIN surface grids in and adjacent to faults**

In order to more accurately model the effect of faults on the groundwater system, the element size in, and adjacent to, identified fault triangles on each surface is decreased by adding nodes to the center of element edges (refinement). To keep the horizontal element configuration of all layers identical, refinement is done to ISM layer 24 which is the base of TSW4. This layer has the most complete identification of fault triangles. The refinement is performed after a polygonal subset of TSW4 is extracted as described in Section 3.3.2.2. Refinement consists of adding a node to the center of any element edge containing at least one node that is identified as a fault when the edge is larger than 20.0 m. This refines the element size in, and immediately adjacent to, fault triangles. The new and old nodes are then reconnected into triangular elements. The resulting mesh of Layer 24 contains 4557 nodes and 6165 elements. The z coordinates of every other layer are then mapped onto the triangular element configuration of Layer 24 to create separate surfaces with the correct depth and identical element configurations.

### **3.3.2.4 Define upper and lower boundary truncation surfaces**

The ISM model defines stratigraphic layers much deeper than were needed for unsaturated zone calculations. Therefore, the ISM surfaces are truncated and no grids are generated below an

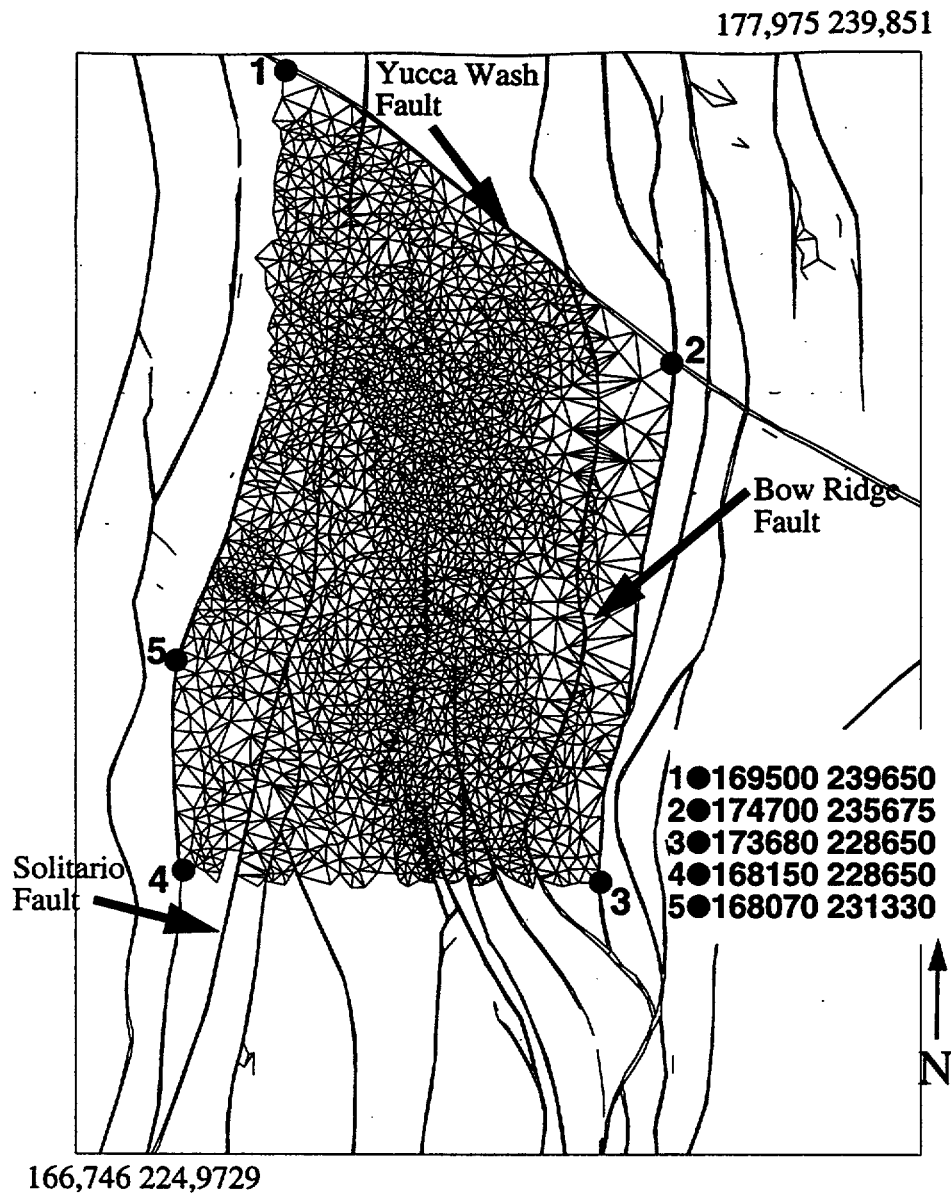


**Figure 3-4.** Top view of one TIN illustrating the subregion for the three-dimensional computational grid. TIN consists of 4557 nodes and 6165 triangles. Coordinates are Nevada State Plane in meters. Note the increased resolution near faults in comparison to the original TIN surface (see Figure 3-2).

elevation of 400 meters. This insures that 200 to 300 meters of the grid are available for calculations with different water table levels and also helps make grids smaller by not creating elements deep into the saturated zone.

The top surface of the grid must be truncated at the topographic surface. The ISM model defines stratigraphic surfaces above the topographic surface. The ISM model surfaces are filtered to check if the stratigraphic surface elevation is greater than the topographic elevation. If it is, it is reset to topographic elevation.

### **3.3.2.5 Define minimum layer thickness**

Practical and numerical considerations make it necessary to set a minimum layer thickness before producing volume grids between the stratigraphic surfaces. In areas where a particular unit pinches out to zero thickness or is truncated by faults or topography, there can be extremely thin layers. It was found that some layers in the ISM model were as small as 4 cm, an artifact of the model building process rather than an actual geological feature. In this work, if a layer thins to less than one meter, its thickness is set to zero. This insures that large aspect ratio tetrahedral and triangular elements are avoided.

### **3.3.2.6 TIN Sheets Stacked and Converted to Prisms**

The TIN sheets are stacked from lowest elevation to highest elevation, via a module from the GEOMESH/X3D system developed specifically for this application. The ISM model consists of a set of stacked triangle sheets that all share the same number of triangles and the same x and y coordinates for the triangle vertices. The only difference between sheets is the z elevation. The stacked sheet data structure is then converted to a finite element node and connectivity list. Now all elements are represented as prisms (6 nodes, 2 triangle faces, 4 quadrilateral faces) with vertical connections between adjacent layers. This module for the GEOMESH/X3D system was also developed specifically for this application.

Once stacked, we found that some sheets in the ISM model cross. Therefore, decisions were required for dealing with crossing TIN sheets. After consultation with William Zelinski, it was agreed that whenever a higher stratigraphic horizon crosses the layer below, the higher elevation sheet should be given an elevation equal to the lower layer. In this method layers pinch out to zero thickness if they cross. This approach exactly maintains the geometry of interfaces and faults

except in the cases where the ISM model represented negative volumes, overlapping or very thin layers.

### **3.3.2.7 Convert Prisms to Tetrahedra**

Tetrahedral elements are fundamental to three-dimensional computations. Therefore, prism elements must be converted into tetrahedra. Another module had to be developed for the GEOMESH/X3D system to do this. Prism elements are converted to tetrahedral elements by one of two methods. The options are to create either eighteen or three tetrahedra from each prism. Eighteen tetrahedra are created by adding a node to the center of each face and a node the center of the prism element. Connections are then made to generate eighteen tetrahedra from each prism. Creating three tetrahedra does not require node addition, it is simply a change in the connectivity of the nodes representing each prism. In this work we chose to convert each prism to three tetrahedra. The resulting representation is now in the form of a tetrahedral mesh.

### **3.3.2.8 Extract a Two-Dimensional Plane**

For two-dimensional calculations, extraction of planes from the tetrahedral mesh follows. A plane through the tetrahedral mesh is defined, which can be at any orientation, and the intersections of the tetrahedral elements with the plane are calculated. The result of intersecting a tetrahedral mesh with a plane is a two-dimensional hybrid mesh consisting of triangles and quadrilaterals.

For this work, the plane chosen was an east-west cross section extracted at Nevada State Plane (NSP) coordinate 232,100 meters. The east and west boundaries of the plane are truncated at unnamed faults in ISM at NSP coordinates 168,274 meters on the west and 174,176 meters on the east (Figure 3-5).

### **3.3.2.9 Convert Hybrid Grid to Triangles**

The hybrid mesh of quadrilaterals and triangles must be converted to a triangular mesh. This requires that quadrilateral elements are split into 4 triangles, resulting in a fully triangular mesh.

## Grids

---

These tests were employed and passed for all meshes employed in this report.

### Computational Grids Used in the Present Study

---

#### Three-Dimensional Unsaturated Zone Grid

The final grid used for three-dimensional calculations is shown in Figure 3-9. It contains 1,100,000 nodes and 414,313 tetrahedral elements. Faults represented in the ISM model are included as separate materials (Figure 3-10). Since the calculations are dual permeability, the number of grid points for FEHM calculations is 143,562.

#### 2 Two-Dimensional Unsaturated Zone Grid

Two-dimensional cross section grids have been produced at two different resolutions. The grid shown in Figure 3-6 is a low resolution triangular mesh with 21,494 nodes and 42,086 triangular elements. The FEHM dual permeability grid has 42,988 nodes.

The mesh used for interpolation of geostatistical mineral distributions has much higher resolution between the Ghost Dance and Solitario faults at and below the potential repository, with 100,984 nodes and 78,312 triangular elements and 133,968 dual permeability grid points. A small portion of the high resolution grid is shown in Figure 3-12. In the high resolution area, the spacing between nodes is approximately 4-6 meters.

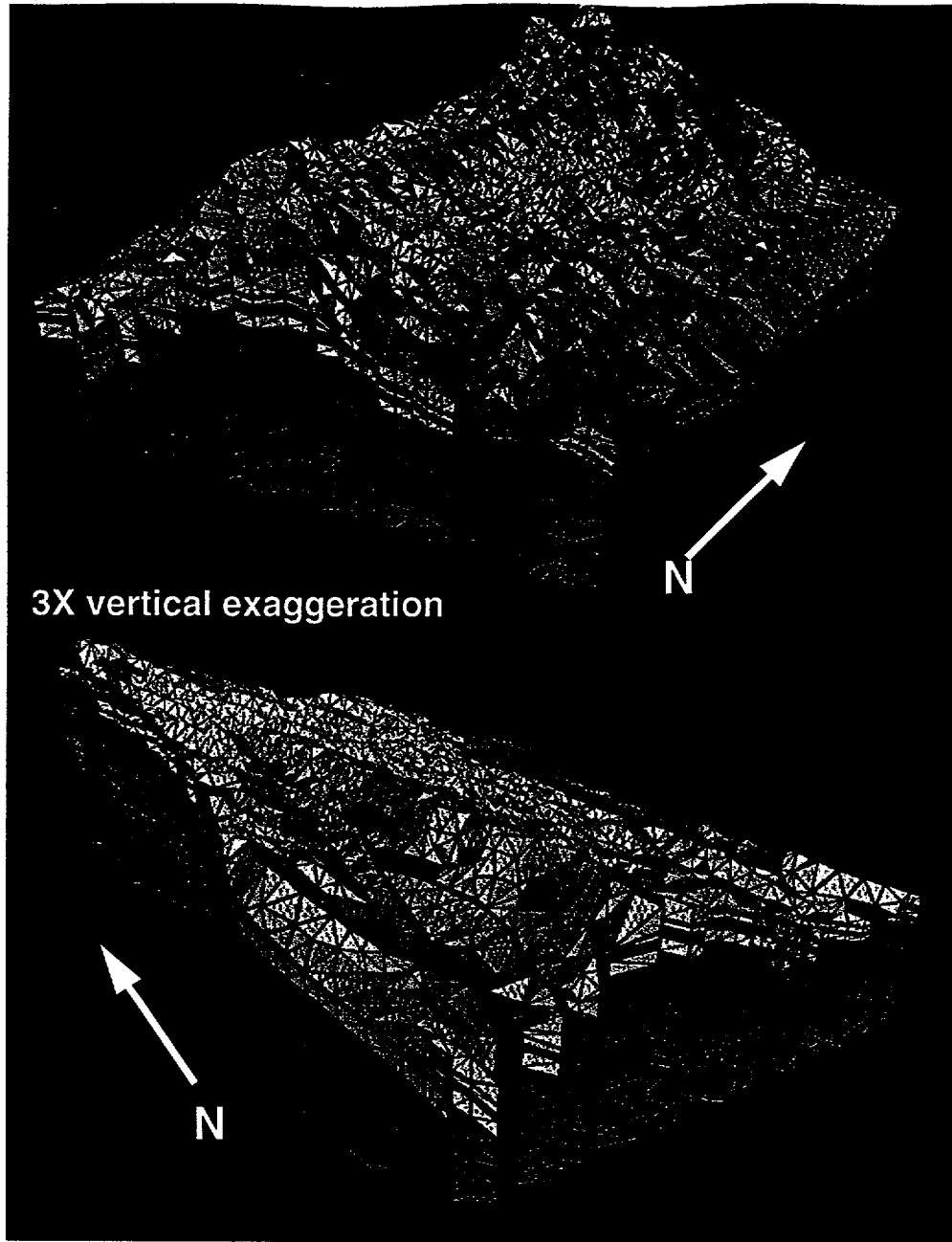


**Figure 3-9.** Three-dimensional unsaturated zone computational grid with 71,781 nodes, 143,562 dual permeability nodes and 414,313 tetrahedral elements.

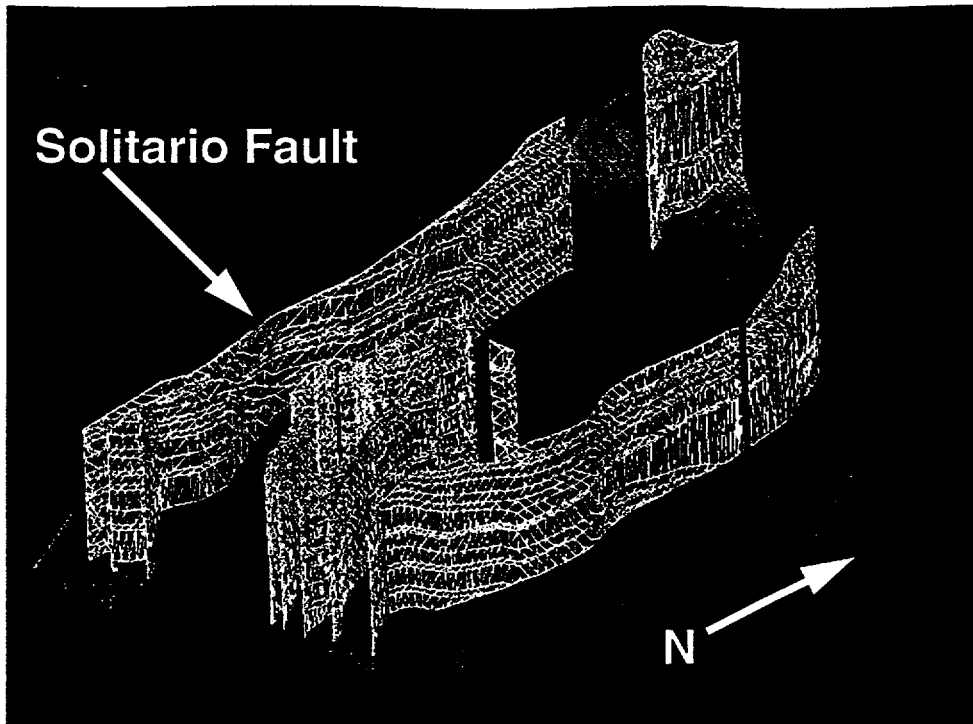


**Figure 3-10.** Faults are represented as distinct materials. Layer 9 from ISM is shown. There are 14,473 nodes and 45,386 tetrahedral elements used to represent the faults. Faults that dip to the west are filled in red, faults that dip to the east are filled with green.

### 3.5 Conclusions

---

Accurate simulation of flow and transport in the unsaturated zone at Yucca Mountain requires simulation tools capable of representing the complex stratigraphy which includes dipping, faulted geologic layers of varying thickness and extent. The GEOMESH/X3D toolkit was developed specifically to address such issues. Further, once the geometric constraints of the geologic system are resolved, the flow and transport simulations are only as accurate as the mesh upon which they are computed. GEOMESH automatically insures quality finite-element grids. Further, the GEOMESH/X3D toolkit is designed to accept electronic input directly from the geologic and mineralogic models, thus insuring nearly exact replication of the structure and attribute distributions in those models.

## Grids

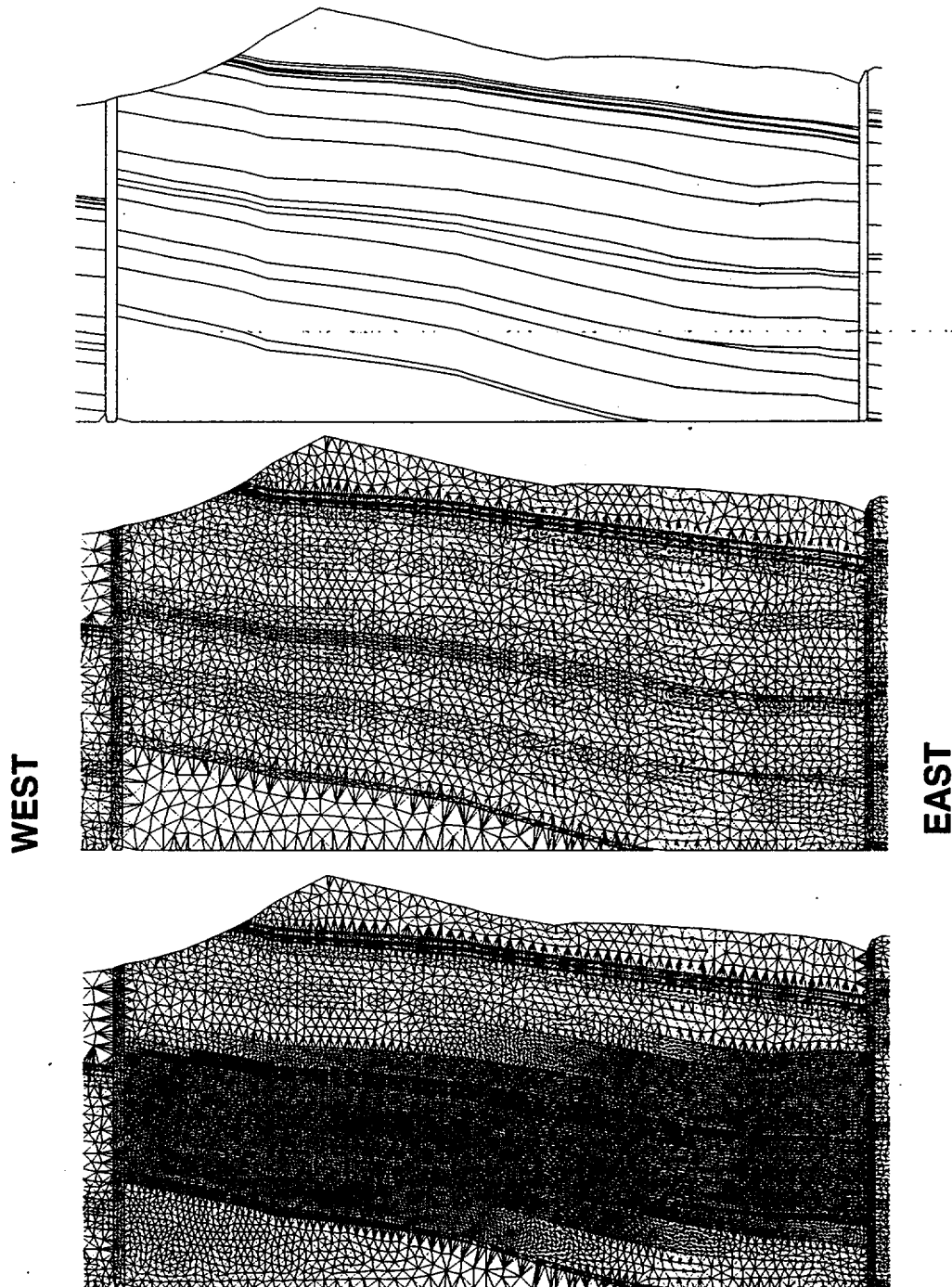


**Figure 3-11.** A portion of the two-dimensional cross section is shown bounded on the west by the Solitario fault and on the east by the Ghost Dance fault. a) Stratigraphic layer boundaries, b) low resolution computational grid, c) high resolution computational grid.

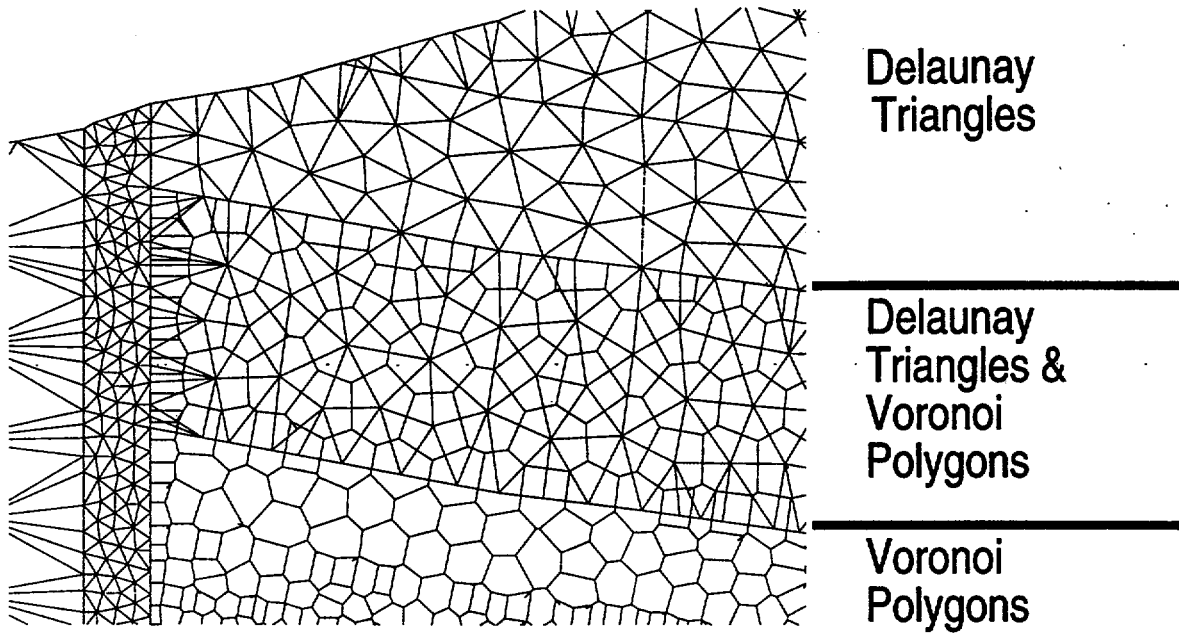


**Figure 3-12.** A small section of the high resolution two-dimensional grid near the Solitario fault showing the triangulation and the Voronoi cells associated with the triangles.

## Chapter 4 - Particle Tracking

### 4.1 Abstract

---

A new particle tracking technique is presented for simulating liquid or gas phase solute transport in porous media. The method, called the Residence Time Transfer Function (RTTF) particle tracking technique, uses a cell-based approach that sends particles from node to node on a finite difference or finite element grid, after keeping each particle at the cell for a prescribed period of time. To incorporate transport mechanisms such as dispersion and matrix diffusion, the residence time of a particle at a cell is computed using a transfer function that ensures that the correct distribution of times at the cell is reproduced. Transient flow fields are approximated by assuming a non-varying flow field during a time interval of a fluid flow solution. The method is a significant departure from the traditional procedure of mapping a particle trajectory by resolving the velocity vector at a given position by interpolation between positions on the grid. The new procedure is computationally very efficient, enabling large-scale transport simulations of several million particles to be completed rapidly on modern workstations. Furthermore, since the cell-based approach uses directly mass flow rate information generated from a numerical fluid flow solution, complex, unstructured computational grids pose no additional complications. A number of numerical validation and example calculations are presented to demonstrate the strengths of the new technique. A discussion is also provided to point out those situations for which the assumptions of the method might lead to unacceptable numerical inaccuracy, and for these cases alternative numerical transport techniques are recommended. For the present study, the technique is used for unsaturated transport simulations, since the limitations of the method are minimal for the UZ, and the cell-based approach allows accurate simulation of dual-permeability systems in which there is a vast disparity in the travel times depending on whether the transport is in the fractures or the matrix.

## 4.2 Software and Data QA Status

---

The FEHM code is used to perform all flow and transport calculations in this report. The code is qualified in accordance with Los Alamos quality assurance requirements and is documented in (Zyvoloski et al., 1992, 1995a, 1995b). The QA status of the data used in this report is shown in Table 4-1.

Table 4-1. QA Status of Data used in this Chapter				
REFERENCE	Q Status	DTN		COMMENT
<b>Fabryka-Martin et al., 1996b,</b> "Summary Report of Chlorine-36 Studies: Sampling, Analysis and Simulation for Chlorine-36 in the Exploratory Studies Facility, YMP Milestone number 3783 M"	Q	LAJF831222AQ95.005	4, 5, 6	Accession Nos. MOL.19961015. 0100 MOL.19961015. 0103 * DTN super- sedes DTN: LAJF831222AQ 95.013
	Q	LAJF831222AQ95.007		
	Q	LAJF831222AQ96.013		
		*		
	Q	LAJF831222AQ96.002		
	Q	LAJF831222AQ96.003		
	Q	LAJF831222AQ96.004		
	Q	LAJF831222AQ96.014		
	Q	LAJF831222AQ96.015		
	Q	LAJF831222AQ96.016		
	Q	GS950708315131.001		
	Q	GS960308315131.001		
	Q	GS950508314224.003		
	Q	GS960408314224.001		
	Q	GS960408314224.003		
	Q	GS960408314224.004		
Q	GS060708314224.009			
USGS DTN				
<b>Fabryka-Martin et al., 1996c,</b> "Summary Report of Chlorine-36 Studies, YMP Milestone Report 3782M"	non-Q	LAJF831222AN96.001	4, 6	
	Q	LAJF831222AQ96.002		
	Q	LAJF831222AQ96.003		
	Q	LAJF831222AQ96.004		
	Q	LAJF831222AQ96.005		
	Q	LAJF831222AQ96.006		
	Q	LAJF831222AQ96.007		
	Q	LAJF831222AQ96.008		
	Q	LAJF831222AN96.009		
	Q	LAJF831222AQ96.010		
	Q	LAJF831222AQ96.011		
	Q	LAJF831222AQ96.012		
	Q	LAJF831222AQ96.013		
	Q	LAJF831222AQ96.014		
	Q	LAJF831222AQ96.015		
	Q	LAJF831222AQ96.016		
Q	LAJF831222AQ95.003			
non-Q	LAJF831222AN95.004			Accession Nos. MOL.19961015. 0094

Yang, et al., 1996, Interpretations of Chemical and Isotopic Data From Boreholes in the Unsaturated Zone at Yucca Mountain, Nevada, USGS Water-Resources Investigations Report WRIR 96-4058	Q		4, 6, 11	
---	---	--	----------	--

### 4.3 Introduction: Conceptual Model For Particle Transport

Prediction of solute transport is a critical element of many groundwater flow studies, particularly when the transport of a contaminant is the focus of the work. Modeling efforts typically are motivated by the need to predict the movement of a pollutant in the subsurface to answer practical questions concerning the rate and direction of contaminant movement and the degree to which the quality of the groundwater may be endangered. In a typical solute transport simulation, a dissolved chemical is introduced into a steady-state or time-varying flow field, and the fate of the chemical is tracked while undergoing physical and chemical processes such as advection, dispersion, chemical and biological reaction, or diffusion into dead-end pore space. Often, a concentration front is established that must be tracked accurately. In addition, many field investigations employ tracers to study the flow and transport system, and these tests also require models to simulate the movement of dissolved species.

Traditional solutions to the advection-dispersion (CD) equation, such as those used in most finite-element or finite-difference flow and transport codes, are versatile and allow the simultaneous solution of multiple interacting species. One drawback of a finite-difference or finite-element solution to the CD equation is that significant numerical dispersion may arise in the portion of a computational domain occupied by a front of rapidly varying concentration. Reducing the numerical dispersion requires either increased grid resolution or higher-order approximation methods, both of which may lead to prohibitive computational costs. Numerical dispersion is identical in character to actual dispersion, so it is difficult to separate numerical from actual dispersion in complex transport simulations.

Approaches to cope with this problem include front-tracking algorithms with multiple grids (e.g. Yeh, 1990, Wolfsberg and Freyberg, 1994), the method of characteristics (e.g. Chiang et al., 1989), hybrid Eulerian-Lagrangian solution techniques (Neuman, 1984), and particle tracking techniques (e.g. Tompson and Gelhar, 1990). Front-tracking algorithms solve the CD equation in integrated form on a numerical grid while tailoring the mesh to increase the resolution of the calculation at fronts. In contrast, an Eulerian-Lagrangian technique casts the CD equation using the total derivative, so that the advection portion of transport can be solved accurately using particle-tracking techniques or the method of characteristics, while the dispersion component of transport is solved on a finite-difference or finite-element grid using standard techniques.

Particle-tracking transport models take a fundamentally different approach. The trajectory of individual molecules or packets of fluid containing molecules are tracked through the model domain. When the fluid path lines are the model result of interest (Pollack, 1988; Lu, 1994), a relatively small number of particles can be used to trace the streamlines. Particle tracking is also used to simulate solute transport, such as the migration of a contaminant plume (Akindunni et al., 1995) or the prediction of breakthrough curves in interwell tracer experiments (Johnson et al., 1994). For these applications, a relatively large number of such particles must be used to obtain accurate solutions to the transport problem. Particle tracking has also been used to solve the advective portion of complex reactive transport models that simulate chemical reactions among multiple species (Fabriol et al., 1993).

In a typical particle tracking algorithm, a particle is sent to a new position assuming that the magnitude and direction of the velocity vector are constant during a time step  $\Delta t$ . If small enough time steps are taken, particle pathways can be tracked accurately. Dispersion is treated as a random process that diverts the particle a random distance from its dispersion-free, deterministic path. In these so-called "random walk" models (e.g. Kinzelbach, 1988), dispersion is usually calculated stochastically subject to a Gaussian model to reproduce the specified dispersion coefficient. The technique has also been extended by employing non-Gaussian random walk

functions to represent scale-dependent dispersion (Scheibe and Cole, 1994). Linear, equilibrium sorption can be handled through the use of a retardation factor to correct the magnitude of the particle velocity.

A crucial component of all random-walk particle-tracking algorithms developed to date is the need to accurately estimate the velocity at every position in the model domain. In the context of a finite-difference or finite-element numerical code, this means that velocities at positions other than the node points of the fluid flow grid must be computed using an interpolation scheme. Many studies have proposed and studied the accuracy of different interpolation schemes, including methods developed for regular, two- or three-dimensional finite difference grids (Goode, 1990; Schafer-Perini and Wilson, 1991; Zheng, 1993), two- and three-dimensional finite-element grids (Cordes and Kinzelbach, 1992), and for codes that employ the boundary element method for computing fluid flow (Latinopoulos and Katsifarakis, 1991). Special techniques have been developed to handle complexities such as point fluid sources and sinks and abrupt changes in the conductivity of the medium (Zheng, 1994).

In the process of adding complexity to the particle-tracking algorithms, some of the intuitiveness of the original particle-tracking concept has been lost. Furthermore, many of the velocity interpolation schemes are computationally intensive, thus limiting the number of particles that can practically be used. Another drawback to traditional particle-tracking approaches is that spatial and temporal discretization often results in numerical inaccuracy in the fluid flow solution upon which velocity determinations are based. Thus, precise and time-consuming velocity interpolation schemes may not be justified in finite-difference or finite-element models. Finally, for dual porosity models that employ overlapping continua to represent fracture and matrix flow (Zyvoloski et al., 1992; Zimmerman et al., 1993), velocity interpolations on each continuum must be coupled to a transfer term that allows particles to move from one medium to the other. This additional complexity, along with the approximation associated with the dual-porosity method itself, may make precise velocity interpolation calculations of limited validity.

In this chapter, a new particle-tracking technique is developed for transient, multi-dimensional finite-difference or finite-element codes. The algorithm is designed for computing solute concentration fields quickly and easily with structured or unstructured numerical grids of arbitrary complexity. Both continuum and dual-porosity formulations can be simulated. This flexibility is accomplished by adopting a new strategy for mapping out the path of a particle, one that replaces the calculation of an "exact" pathline with a cell-to-cell migration of the particle. The mass flux from cell to cell is used directly, and no velocity interpolations are required. Since numerical solutions for fluid flow are typically mass-conservative (though not necessarily accurate) the particle-tracking method automatically conserves mass.

In this chapter, we first outline the mathematical basis for this algorithm, developing theory to incorporate the effects of sorption, dispersion, and matrix diffusion into this new particle-tracking framework. Then, after a brief description of the structure of the particle-tracking code, we validate the technique by comparing the results to analytical solutions and by benchmarking the code against a finite-element solution of the advection-dispersion equation for a complex flow system for which no analytical solution is available. Finally, we present two applications that examine solute transport issues relevant to YMP, illustrating the usefulness of the particle-tracking technique for studying complex, large-scale transport problems in both unsaturated and saturated flow systems.

### **4.4 Mathematical Development**

---

The particle-tracking method developed in the present study views the fluid flow computational domain as an interconnected network of fluid storage volumes. Particles travel only from cell to cell, requiring no greater resolution of the particle pathways. In this sense, the method is similar to the node-to-node routing method of Desbarats (1990). This simple starting point has been extended to include many different transport submodels and complex flow domains. The description that follows is applicable for steady-state, single-porosity flow fields; the corrections

## Particle Tracking

---

to the method for treating transient flow systems and dual-porosity model formulations are discussed in subsequent sections. The two steps in the particle-tracking approach are: 1) determine the time a particle spends in a given cell; and 2) determine which cell the particle travels to next. These two steps are detailed below.

The residence time for a particle in a cell is governed by a transfer function describing the probability of the particle spending a given length of time in the cell. Thus, we call this particle-tracking approach the “residence time/transfer function” (RTTF) method. The schematic plot shown in Figure 4-1 illustrates the basis of the RTTF approach. For a cumulative probability distribution function of particle residence times, we compute the residence time of a particle in a cell by generating a random number between 0 and 1 to determine the corresponding residence time from the distribution function. In this example, the advection-dispersion equation was used to generate the RTTF curve, but other transport mechanisms can be incorporated as well, as we demonstrate below. If a large number of particles pass through the cell, the cumulative residence time distribution (RTD) of particles in the cell will be reproduced. Particle-tracking models of single-fracture transport (Yamashita and Kimura, 1990) and fracture networks (Robinson, 1988) have employed this approach to simulate fracture transport of diffusion into the rock matrix.

From the solution of the flow field in a numerical model, we obtain the mass of fluid in the computational cell and the mass flow rate to or from each adjacent cell. In the simplest case, the residence time of a particle in a cell,  $\tau_{part}$ , is given by

$$\tau_{part} = \tau_f = \frac{M_f}{\sum \dot{m}_{out}} \quad (\text{Eq. 4-1})$$

where  $M_f$  is the fluid mass in the cell and the summation term in the denominator refers to the outlet mass flow rates from the cell to adjacent cells. In the absence of dispersion or other transport mechanisms, the transfer function is a Heaviside function that is unity at the fluid residence time  $\tau_f$ , because for this simple case, all particles entering the cell will possess this residence time.

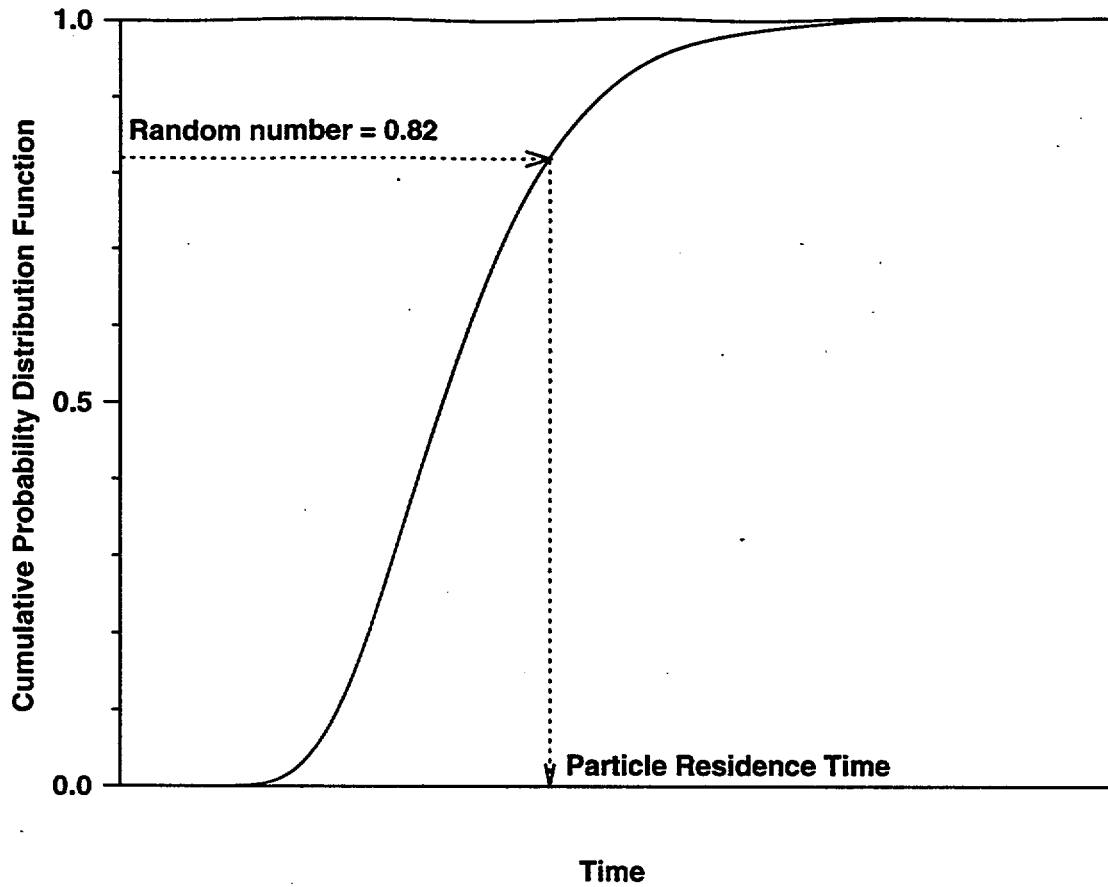


Figure 4-1. Use of the transfer function to determine the residence time of a particle in a cell for the RTTF particle tracking technique.

Equilibrium, linear sorption is included by correcting the residence time by a retardation factor  $R_f$ .

Thus,  $\tau_{part} = R_f \tau_f$ , and  $R_f$  is given by

$$R_f = 1 + \frac{\rho_b K_d}{\phi S_f \rho_f}, \quad (\text{Eq. 4-2})$$

where  $K_d$  is the equilibrium sorption coefficient,  $\rho_b$  is the bulk rock density,  $\phi$  is the porosity,  $S_f$  is the saturation of the phase in which the particle is traveling, and  $\rho_f$  is the density of the fluid.

Once again, in the absence of other transport processes, the transfer function is a Heaviside function.

Before discussing more complex transfer functions for the RTTF method, we outline the method for determining which cell a particle travels to after completing its stay at a given cell. The assumption that is consistent with the RTTF method is that the probability of traveling to a neighboring cell is proportional to the mass flow rate to that cell. Only outflows are included in this calculation; the probability of traveling to an adjacent node is 0 if fluid flows from that node to the current node. A uniform random number from zero to one is used to make the decision of which node to travel to. Thus, the particle-tracking algorithm is: 1) compute the residence time of a particle at a cell using the RTTF method; and 2) send the particle to an adjacent cell randomly, with the probability of traveling to a given cell proportional to the mass flow rate to that cell.

#### 4.4.1 Dispersion

Transport processes such as dispersion can be incorporated into the RTTF particle-tracking algorithm through the use of transfer functions. For dispersion, within a computational cell, we assume that one-dimensional, axial dispersion is valid. The transport equation and boundary conditions for the one-dimensional, advective-dispersion equation are:

$$R_f \frac{\partial C}{\partial t} = D_{eff} \frac{\partial^2 C}{\partial x^2} - u \frac{\partial C}{\partial x}, \quad (\text{Eq. 4-3})$$

$$C = 0, \quad t = 0, \quad (\text{Eq. 4-4})$$

$$C = C_0, \quad x = 0, \quad (\text{Eq. 4-5})$$

$$C = 0, \quad x \rightarrow \infty, \quad (\text{Eq. 4-6})$$

where  $C$  is the concentration,  $C_0$  is the injection concentration,  $u$  is the flow velocity, and  $D_{eff}$  is the effective dispersion coefficient, given by  $D_{eff} = \alpha u$ , where  $\alpha$  is the dispersivity of the medium. Here we assume that the flow dispersion component of  $D_{eff}$  is large compared to the molecular diffusion coefficient  $D_{AB}$ . A non-dimensional version of equation (Eq. 4-3) can be obtained by the following transformations:  $\hat{C} = C/C_0$ ,  $\hat{x} = x/L$ , and  $\theta = R_f u t / L = R_f \tau_f$ , where  $L$  is the flow path length. The solution to equation (Eq. 4-3)-equation (Eq. 4-6) is given by

Freeze and Cherry (1979):

$$\hat{C} = \frac{1}{2} \left[ \operatorname{erfc} \left( \frac{\sqrt{Pe}(1-\theta)}{2\sqrt{\theta}} \right) + e^{Pe} \operatorname{erfc} \left( \frac{\sqrt{Pe}(1+\theta)}{2\sqrt{\theta}} \right) \right] \quad (\text{Eq. 4-7})$$

where  $Pe$  is the Peclet number,  $Pe = uL/D_{eff} = L/\alpha$ .

The use of this solution in the RTTF particle-tracking method requires that the transport problem be advection dominated, such that during the time spent in a computational cell, solute would not tend to spread a significant distance away from that cell. Then, the approximate use of a distribution of times within a single cell should be adequate. Quantitatively, the criterion for applicability is based on the grid Peclet number  $Pe_g = \Delta x/\alpha$ , where  $\Delta x$  is the characteristic length scale of the computational cell. Note that in contrast to conventional numerical solutions of the CD equation, coarse spatial discretization is helpful for satisfying this criterion. Of course, the mesh spacing must be small enough to provide an accurate flow solution. Highly dispersive transport  $Pe_g < 1$  invalidates the assumptions of the RTTF particle-tracking technique. This is not viewed as a significant limitation of the method, because accurate solutions to the advective-dispersion equation are easily obtained by conventional finite-difference or finite-element techniques when dispersion coefficients are large.

For multi-dimensional flow systems, the dispersion model developed for one-dimensional systems can be extended to include dispersion coefficient values aligned with the coordinate axes. For this case, the flow direction is determined by the vector drawn from the nodal position of the previous cell to the current cell, and the dispersivity for this flow direction is computed from the equation for an ellipsoid:

$$\alpha = \frac{L}{\sqrt{\Delta x^2/\alpha_x^2 + \Delta y^2/\alpha_y^2 + \Delta z^2/\alpha_z^2}} \quad (\text{Eq. 4-8})$$

The RTTF particle-tracking technique cannot be simply formulated with a longitudinal and transverse dispersion coefficient model, with the tensor aligned with the flow direction, because the

flow rates between cells are defined rather than the actual flow velocity at a position. For a dispersion model aligned with the flow direction, a random-walk particle-tracking method such as that of Tompson and Gelhar (1990) or a conventional finite-element or finite-difference solution to the CD equation, such as the reactive transport solution module in FEHM, must be used.

The numerical implementation of this technique requires the determination of the dimensionless time  $\theta$  in equation (Eq. 4-7) for a randomly determined value of the dimensionless concentration  $\hat{C}$ . This determination is accomplished numerically in the particle-tracking code by fitting equation (Eq. 4-7) at selected values of  $Pe$  between 1 and 1000 using a piecewise continuous series of straight lines spanning the entire range of  $\hat{C}$  values. Then, the value of  $\theta$  at an arbitrary value of  $Pe$  is computed by linear interpolation between  $\theta$  values determined at the Peclet numbers that bracket the actual value. This technique, involving a simple search for the correct type curves, followed by the calculation of two values of  $\theta$  and an interpolation, is much more computationally efficient (about a factor of two in cpu time) and robust than an iterative approach to the exact solution using Newton's method. Solutions of adequate accuracy (less than 1% error) for Peclet numbers between 1 and 1000 are easily obtained using this linear-interpolation method.

### 4.4.2 Matrix Diffusion

Matrix diffusion has been recognized as an important transport mechanism in fractured porous media (e.g. Neretnicks, 1980; Robinson, 1994). For many hydrologic flow systems, fluid flow is dominated by fractures because of the orders-of-magnitude larger permeabilities in the fractures compared to the surrounding rock matrix. However, even when fluid in the matrix is completely stagnant, solute can migrate into the matrix via molecular diffusion, resulting in a physical retardation of solute compared to pure fracture transport. This effect has recently been demonstrated on the laboratory scale by Reimus (1995) and on the field scale both by Maloszewski and Zuber (1991) and, at the C-Wells by Reimus and Turin (1997).

## Particle Tracking

To derive a transfer function for matrix diffusion, we must first develop an idealized representation of the transport system. Figure 4-2 shows the geometry of the model system used for this purpose. The geometry and flow system consists of equally spaced, parallel fractures, each of which transmits equal flow. Fluid in the rock matrix is stagnant. Transport in the fractures is governed by equation (Eq. 4-6), whereas transport between the fracture and matrix is described by the one-dimensional diffusion equation:

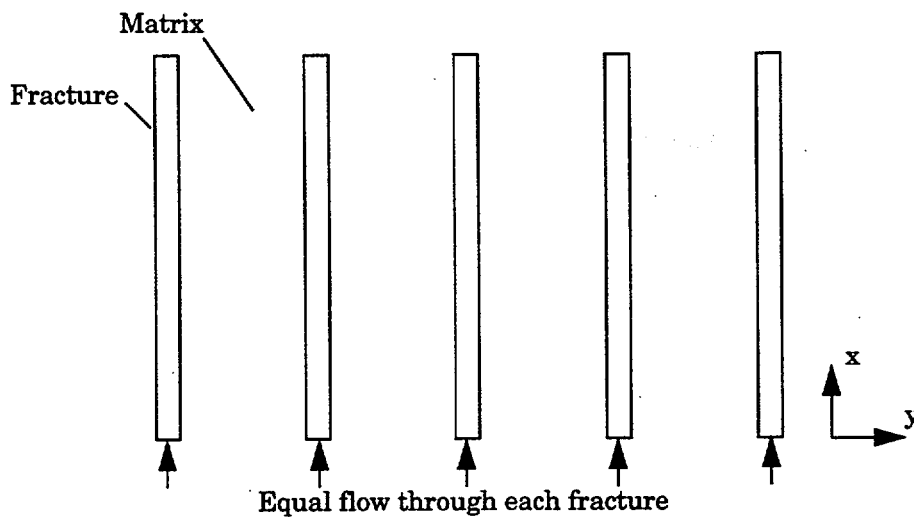


**Figure 4-2.** Conceptual model for matrix diffusion. One dimensional flow occurs in the fracture, with molecular diffusion into the rock matrix.

$$R_{f,m} \frac{\partial C}{\partial t} = D_{AB} \frac{\partial^2 C}{\partial y^2}, \quad (\text{Eq. 4-9})$$

where  $R_{f,m}$  is the retardation coefficient for the matrix. The molecular diffusion coefficient is the

product of the free diffusion coefficient of the solute in water and a tortuosity factor to account for the details of diffusion through a tortuous, fluid-filled pore network. In this model, we treat  $D_{AB}$  as the fundamental transport parameter, recognizing that it is a property of both the solute and the medium.

Solutions to this transport problem depend on the nature of the boundary condition in the y-direction. An analytical solution is given by Tang et al. (1981) for the semi-infinite boundary condition  $\frac{\partial C}{\partial y} = 0$  as  $y \rightarrow \infty$ . For the case of plug flow (no dispersion) in the fractures, Starr et al. (1985) show that the solution reduces to

$$\frac{C}{C_0} = \text{erf} \left[ \frac{\phi \tau_f \sqrt{R_{f,m} D_{AB}}}{b \sqrt{t - R_f \tau_f}} \right] \quad (\text{Eq. 4-10})$$

for  $t > R_f \tau_f$ , and  $C/C_0 = 0$  for  $t \leq R_f \tau_f$ , where  $b$  is the fracture aperture. The semi-infinite boundary condition between fractures limits the validity of either of these solutions to situations in which the characteristic diffusion distance for the transport problem is small compared to the fracture spacing  $S$ . Robinson (1994) presents a numerical solution to this problem for the boundary condition  $\frac{\partial C}{\partial y} = 0$  at  $y = S/2$ . The extent of matrix diffusion can be parameterized using the diffusion number  $Di = (\phi \sqrt{R_{f,m} D_{AB}})/b$ .

As long as the solute has insufficient time to diffuse to the centerline between fractures, the solution provided by Tang et al. (1981) can be used as the transfer function for the particle-tracking technique. A sensitivity analysis indicates that values of  $Di > 0.1$  invalidate the assumptions of the Tang et al. (1981) solution, while for  $Di < 0.1$ , the solution is adequate. At higher values of  $Di$ , diffusion into the matrix is so pervasive that the semi-infinite boundary condition is not valid. In the extreme case of very high  $Di$ , the system reverts to one-dimensional behavior, with the transport time given by the fracture transport time times the ratio of the total porosity to the fracture porosity. The RTTF particle-tracking technique developed here does not handle this limiting

behavior. Under these conditions, the transport problem should be recast using a continuum model with the matrix porosity used to compute transport times.

Although in principal the solution of Tang et al. (1981) could be used directly for the transfer function, its complex form makes it very inconvenient for rapidly computing particle residence times. Instead, a two-step process is used wherein the residence time in the fracture is first computed using the transfer function for one-dimensional dispersion (equation (Eq. 4-7)) without sorption. This fracture residence time is then used in the plug-flow equation with matrix diffusion and sorption (equation (Eq. 4-10)) to compute the particle residence time. To use equation (Eq. 4-10) as a transfer function, a numerical algorithm was developed to determine the inverse of the error function, that is, the value of  $x_d$  for a given value of  $y_d$ , such that

$y_d = \text{erf}(x_d)$ . The numerical implementation of this method entails dividing the error function into piecewise continuous segments from which the value of  $x_d$  is determined by interpolation.

The use of the two-step approach is justified because of the principle of superposition, which allows the dispersive process in the fracture to be decoupled from diffusive transport in the matrix. Proof that this numerical technique is acceptable is presented in the Validation section.

### 4.4.3 Radioactive Decay

To incorporate radioactive decay, we use the concept of particle mass (as is used by Fabriol et al. (1993) to track chemical reactions in a particle-tracking model), applying an irreversible, first-order reaction to reduce the mass of the particle from its initial value. When concentration values are computed from the composite behavior of a large number of particles, this method accurately accounts for radioactive decay.

### 4.4.4 Particle Sources and Sinks

There are two methods for introducing particles into the flow system: the particles are either injected with the source fluid entering the model domain or released at a particular cell or set of cells. The first method is used to track source fluid as it passes through the system. The number of particles entering with the source fluid at each cell is proportional to the source flow rate

at that cell, which is equivalent to injecting fluid with a constant solute concentration. For method 2, an arbitrary number of particles are released at each specified cell, regardless of the source flow rate. In the present study, method 1 is used for  $^{36}\text{Cl}$  and major-ion chemical simulations in which the solute is entering with the infiltrating fluid, and method 2 is used for radionuclide migration predictions. When fluid exits the model domain at a sink, the model treats this flow as another outlet flow from the cell. The decision of whether the particle leaves the system or travels to an adjacent cell is then made on a probabilistic basis, just as though the fluid sink were another connected cell. Thus, the complexities discussed by Zheng (1994) for handling a so-called weak sink are avoided in the RTTF particle-tracking model.

### 4.4.5 Transient Flow Fields

When the RTTF particle-tracking method is implemented for a time-varying fluid flow system, the approach is somewhat more complex but still tractable. Consider a numerical simulation in which a discrete time step is taken at time  $t$  and a new fluid flow field is computed. In this model, the new fluid flow time  $t_{new}$  is treated as an intermediate time at which the particle-tracking calculation must stop. The fate of all particles is tracked from time  $t$  to time  $t_{new}$ , assuming that the flow field is constant over this time interval. When the simulation reaches  $t_{new}$ , the position of the particle is recorded, along with its fractional time remaining at the cell and the randomly generated y-coordinate of the transfer function used for that particle in the cell. When the new fluid flow solution is established, the remaining residence time for a particle is determined from the following steps: 1) compute a new fluid residence time  $t_f$ ; 2) using the y-coordinate of the transfer function previously computed and the new transfer function, calculate a new particle residence time; then 3) multiply this time by the fractional time remaining in the cell to obtain the remaining time in the cell. This method approximates the behavior in a transient system, while reducing to the behavior that would be obtained in an unchanging flow field had the calculation not been forced to stop at the intermediate time.

Another transient effect that must be considered is that the sum of the outlet mass flow rates  $\sum \dot{m}_{out}$  in equation (Eq. 4-1) does not necessarily equal the sum of the inlet mass flow rates. When there is net fluid storage in a cell, the particle-tracking algorithm uses the sum of the inlet flow rates in equation (Eq. 4-1), whereas equation (Eq. 4-1) itself is used when there is net drainage of fluid.

### 4.4.6 Dual-Permeability Formulation

The matrix diffusion transport mechanism developed earlier accounts for the movement of solute into the matrix by molecular diffusion in the absence of advective fluid flow. However, in dual-permeability flow and transport model formulations, fluid flow occurs within each continuum, and a transfer term accounts for fluid flow between the fracture and matrix. Extension of the RTTF particle-tracking technique to handle dual-permeability systems is very straightforward, because the fracture-matrix flow term is simply an additional inlet or outlet flow rate from the node. In the algorithm, this flow term is treated like flow to any other node, and the particle can shift from one continuum to the other. In addition, to simulate molecular diffusion as an additional fracture-matrix transport interaction term, the matrix diffusion option can be invoked for particles traveling in the fracture continuum. An example illustrating the use of the dual-permeability particle-tracking formulation is described in the Applications section.

## 4.5 Code Implementation

---

The RTTF particle-tracking model developed in the present study has been implemented in the Finite Element Heat and Mass (FEHM) computer code (Zyvoloski et al., 1992), a transient heat and mass transport simulator for porous media problems in two or three dimensions. Although FEHM is a finite-element model, it uses a finite volume formulation, so that fluid mass is specified at each node of the computational grid, as well as internode mass flow rates (for details, see Zyvoloski, 1983). Thus, the requirement that the flow solution be cell-based is satisfied for FEHM. The method can also be adapted to the TOUGH2 (Pruess, 1991) or NUFT (Nitao, 1995) codes, both of which are integrated finite-difference simulators.

## Particle Tracking

---

One of the attractive features of finite-element simulators is the ability to use computational grids that precisely follow major structural features such as faults or surfaces of contact between distinct hydrostratigraphic units. The grids can be quite complex, with elements of various sizes and types and different numbers of connections for each grid point. These grids would make implementation of a robust velocity interpolation scheme problematic. By contrast, the RTTF particle-tracking algorithm requires only the internode fluid mass flow rates, information that is produced as a matter of course in the fluid flow calculation. This factor made the RTTF particle-tracking technique a good choice for incorporation into FEHM.

FEHM simulates the flow of both the liquid and vapor phases. To provide a full transport model capability, the particle-tracking algorithm was implemented for solutes that reside in either the liquid or vapor phase. Figure 4-3 is a flow chart of the particle-tracking algorithm. The heat and mass transfer simulator controls the time stepping of the simulation, and the particle-tracking is carried out with the flow field established at that time. Each time a fluid flow time step is taken, the migration of all particles is determined up to the new time. Time steps are not required within the particle tracking portion of the calculation. For this algorithm, information that is cell-dependent, such as fluid residence time and an array of normalized outflows to adjacent nodes, is computed only once (until the flow field changes) when a particle enters the cell. This information for the cell is then used for all other particles that pass through the cell. Particle-dependent information, such as the transfer function, particle residence time, and the determination of which adjacent cell to travel to, are calculated for each particle. The use of cell-based computations that are independent of the number of particles used, coupled with a transfer-function approach that does not require time stepping, results in an extremely efficient particle-tracking algorithm. For example, several million particles can easily be tracked on conventional PCs or workstations.

# Particle Tracking

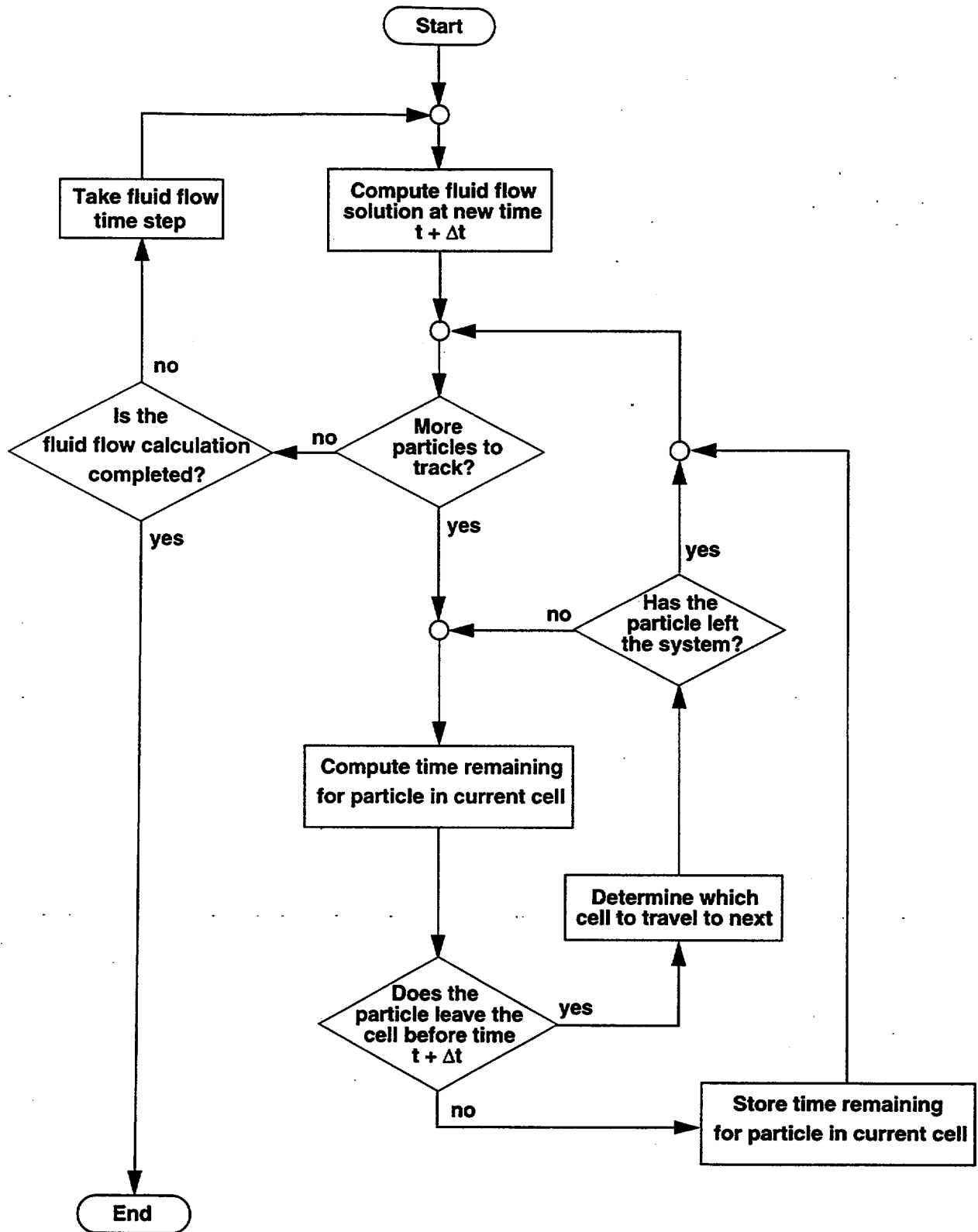


Figure 4-3. Flow chart illustrating the computation sequence for the particle tracking algorithm and its relationship to the fluid flow calculations in a finite element flow code.

## 4.6 Validation

---

### 4.6.1 One-Dimensional Transport with Dispersion and Sorption

The first set of simulations are one-dimensional flow problems for which the dispersion and sorption can be tested against analytical solutions. The flow system is a simple one-dimensional grid in the direction of flow. A steady-state flow field is established for a ten-node, one-dimensional grid, after which the RTTF particle-tracking technique is used to simulate the transport.

In the first suite of one-dimensional tests, a short pulse of particles is injected into the system to test the dispersion transfer function. The responses of these pulse injections of solutes are compared to the time-derivative of equation (Eq. 4-7), given by:

$$C = \frac{1}{2\theta} \exp\left[\frac{-Pe(1-\theta)^2}{4\theta}\right] \sqrt{\frac{Pe}{\pi\theta}} \quad (\text{Eq. 4-11})$$

The cumulative RTD is also compiled from the particle statistics at the outlet node and compared to equation (Eq. 4-7). Figure 4-4 shows that the cumulative RTD solution is reproduced almost exactly for  $Pe > 10$ , corresponding to a grid Peclet number of 1, as long as a sufficient number of particles is used in the simulation. For this transport system, the  $Pe = 20$  results become affected by statistical fluctuations when less than 10,000 particles are used, whereas for 100,000 particles, the breakthrough curve is represented quite accurately, as shown in Figure 4-5. This effect is problem dependent; a sufficient number of particles must be determined empirically for each application of the particle-tracking technique by comparing the results with a simulation using more particles.

Figure 4-4 also shows that for low enough values of  $Pe$ , such as the  $Pe = 10$  case in this example, the RTTF particle-tracking simulation begins to deviate noticeably from the analytical solution. This case corresponds to a grid Peclet number of 1, which is a practical cut-off below which one cannot obtain accurate results using this technique. The solution can be made more accurate using a coarser finite element grid, keeping in mind that the restrictions for obtaining an

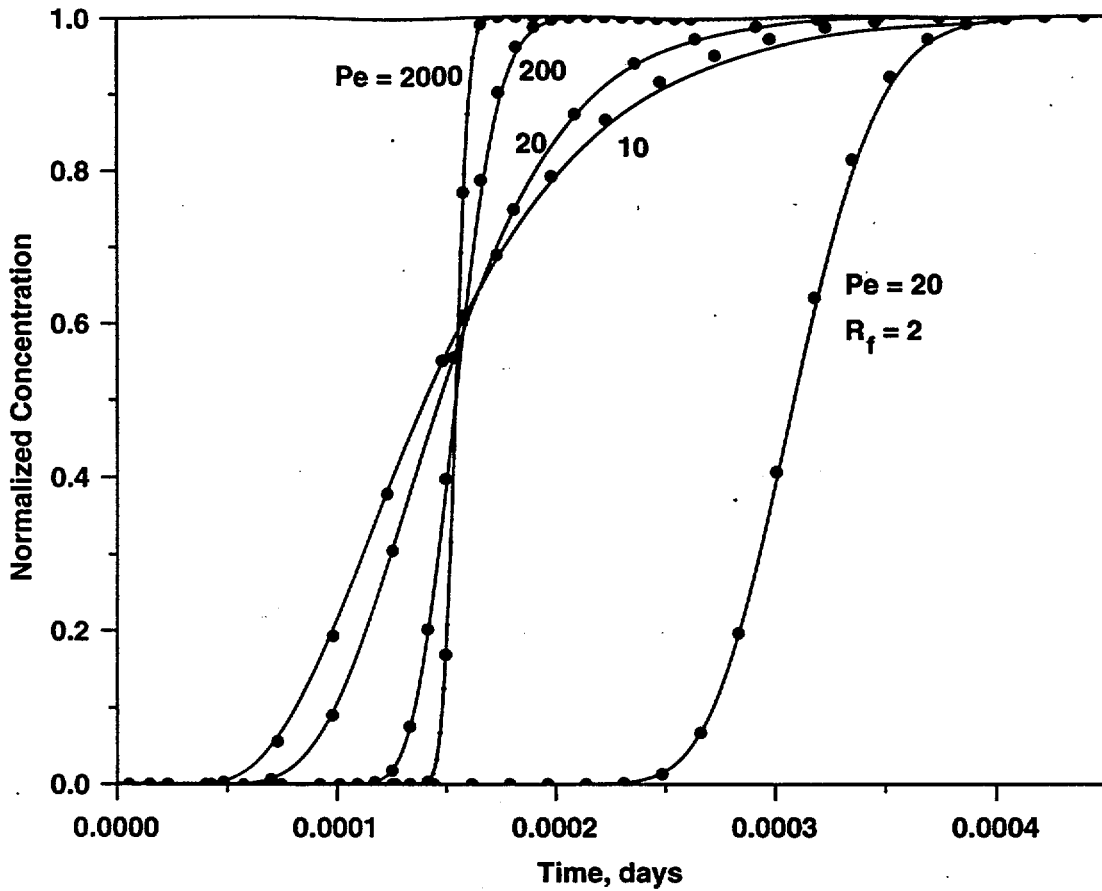


**Figure 4-4.** Cumulative RTD curves produced by the RTTF particle tracking technique for one-dimensional dispersion (filled circles), compared to analytical solution (solid curves). In the curves without sorption,  $Pe$  was varied. For the dashed curve, linear sorption was included for  $Pe = 20$ .

accurate *fluid flow* solution still exist. The practical implication of this result is that the RTTF particle-tracking technique is most useful for advection-dominated problems (large values of  $Pe$ ). This will generally be the case for large-scale two- and three-dimensional problems, which necessarily result in large spatial discretization due to computational limitations.

Finally, the agreement of the sorption curve in Figure 4-4 with the analytical solution shows that linear, equilibrium sorption is also properly accounted for by the RTTF particle-tracking model.

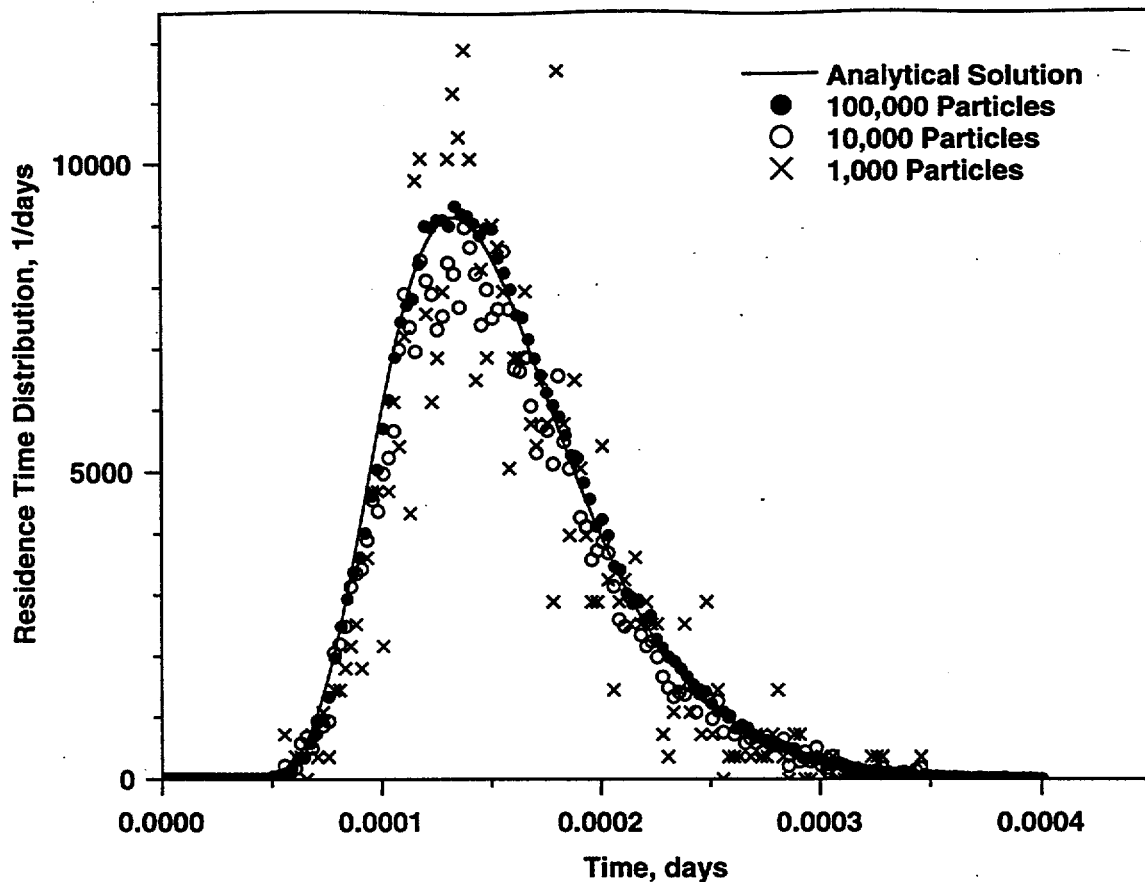


**Figure 4-5.** Residence time distribution (RTD) curves calculated using the RTTF particle tracking technique (symbols) for  $Pe = 20$  for different numbers of particles, compared to the analytical solution (solid curve). The RTD is a solute concentration normalized so that the area under the curve is unity.

#### 4.6.2 One-Dimensional Transport with Matrix Diffusion

Figure 4-6 shows a series of simulations of the RTTF particle-tracking algorithm, along with the solution of Tang et al. (1981) for matrix diffusion with and without dispersion in the fractures. The agreement with the analytical solution is very close for both small or moderate amounts of diffusion (curves a and b), for the case of diffusion and sorption on the fracture surface and in the matrix (curve c), and for dispersion, diffusion, and sorption in both media (curve d). This agreement shows that the two-step RTTF approach outlined in the Mathematical Development section provides an excellent approximation of the combined diffusive-dispersive transport system.

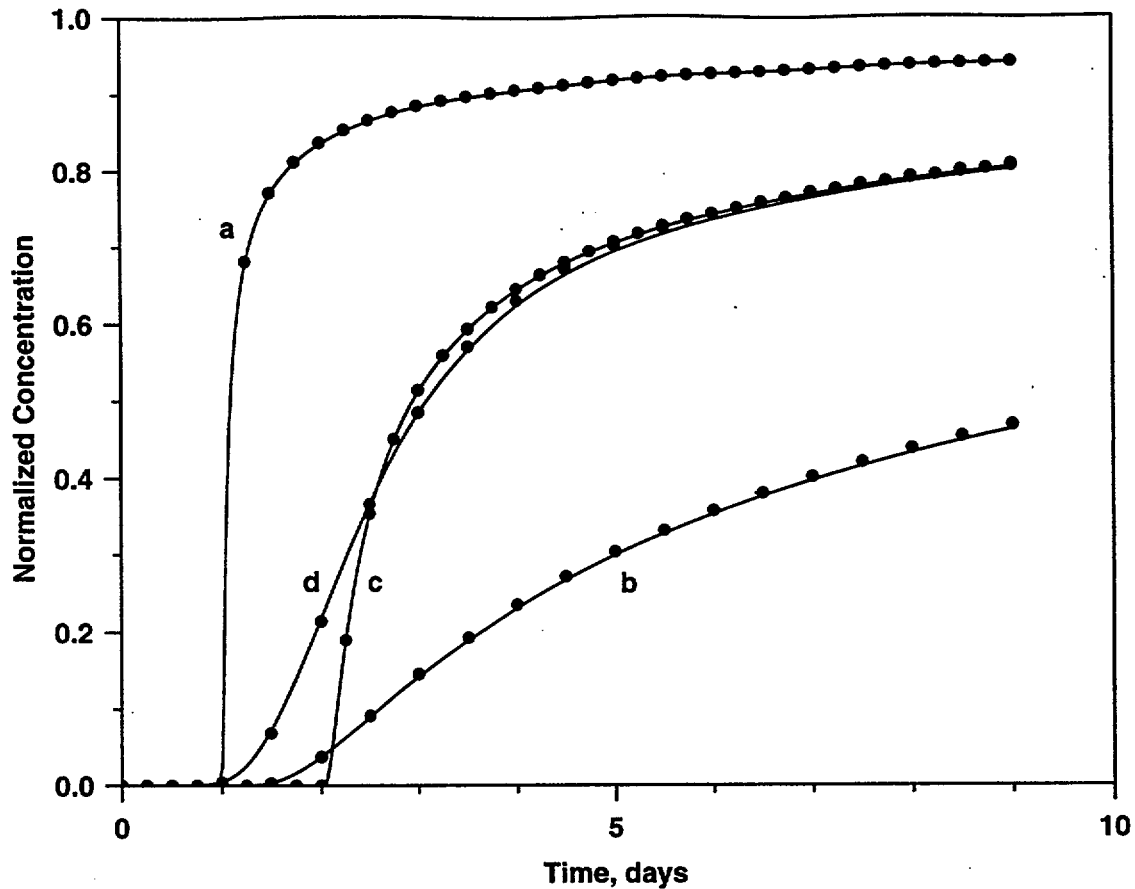


**Figure 4-6.** Cumulative RTD curves produced by the RTTF particle tracking technique for the matrix diffusion model (filled circles), compared to the analytical solution of Tang et al. (1981) (solid curves). Curve a) small amount of matrix diffusion; Curve b) moderate amount of matrix diffusion; Curve c) Matrix diffusion and sorption on fracture and in matrix; Curve d) Dispersion, matrix diffusion, and sorption on fracture and in matrix.

#### 4.6.3 Transient Wetting of a 1-D Column

In this simulation, a transient, one-dimensional, unsaturated flow system is simulated. Using a relative permeability model proposed by van Genuchten (1980), we model the movement of a water front under the influence of gravity and associated tracer particles. The entire flow path is initially set at a saturation below the residual liquid saturation of the medium, and a constant infiltration rate is applied at the inlet of the column. Two particle-tracking simulations are performed: one in which the particles are injected with the infiltrating fluid, and one in which the particles start at a location halfway down the column (cell 54 out of a total of 107). This validation problem tests the

## Particle Tracking

ability of the code to handle the situation of a transient flow field. The exercise is thus important to justify the use of the particle-tracking method for examining radionuclide migration in transient flow fields (Section 8.8).

When the particles are injected with the infiltrating fluid, the particles should move with the saturation front. Figure 4-7 shows that the expected behavior is approximated (the filled circles

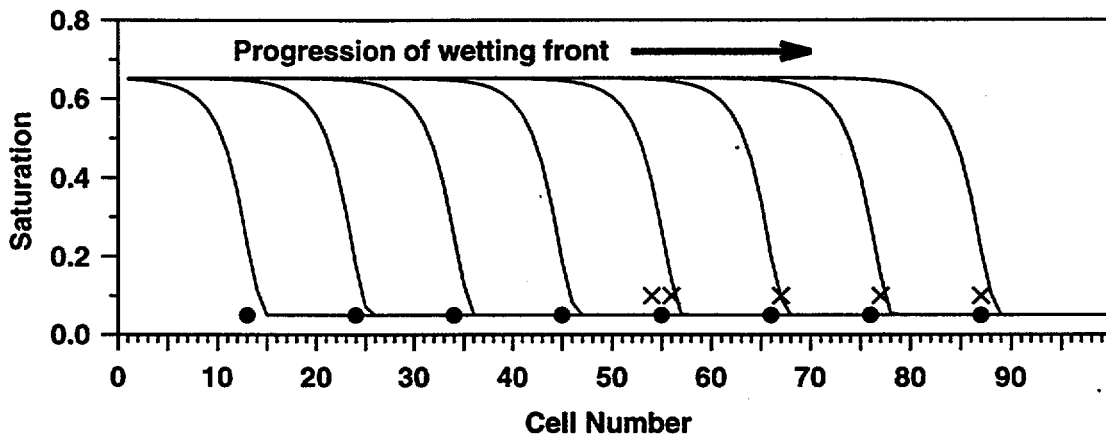


**Figure 4-7.** Movement of particles with the saturation front for the transient wetting case. The curves are the saturation profiles at regular time intervals. Simulations are depicted in which the particles start at the entrance to the flow path (the filled circles) and at a position part way down the column (the X's). For the latter case, the particles do not move until the saturation front reaches the particles.

in the plot), with the particles lagging the front edge of the wetting front by two cells. This slight lag of the particle movement is caused by a slightly dispersed wetting front that does not maintain a sharp interface. For the situation in which the particles are introduced halfway down the length of the column (the X's), the particles remain stationary until the saturation front reaches the particles, after which time the particles move with the front as before. The figure demonstrates that for this transient flow case, the RTTF particle-tracking approach provides an adequate solute transport simulation.

### 4.6.4 Benchmarking Calculation for an Interwell Tracer Simulation

In the previous section, the particle-tracking method was tested in the context of simplified flow fields and geometries, so that analytical solutions or other simple comparisons could be used. In this section, we benchmark the RTTF particle-tracking module against a numerical finite-element solution of the CD equation using FEHM for a complex, two-dimensional flow field. Although this test problem is for a saturated system, it serves as an appropriate test of the method and, thus, is presented in this report.

Figure 4-8 is a plan view of the model domain and grid. This simulation is designed after the field tracer experiments planned at the C-Wells (Robinson, 1994). These tests are designed to measure the hydrologic and transport properties of the saturated zone beneath Yucca Mountain. A permeability field that varies log-normally was generated with a Gaussian spatial correlation structure. The mean of the distribution is  $10^{-12} \text{ m}^2$ , standard deviation is 1 (units of  $\ln(\text{m}^2)$ ), and a correlation length is 20 m. The permeabilities and porosity ( $10^{-4}$  at all positions) are chosen to represent a hydrologic system dominated by fracture flow. A steady-state flow field is established between the injection and production wells (the filled circles in the figure) at a flow rate of 1.58 kg/s, after which time a slug of tracer is injected, and the inlet fluid and concentration versus time at the production well is recorded.

Figure 4-9 shows the results of the finite-element calculation and two particle-tracking simulations discussed below. The breakthrough curve is characteristic of field tracer experiments in fractured porous media. The heterogeneous permeability field and the point source and sink inlet and outlet give rise to a broad distribution of breakthrough times, long tailing of the breakthrough curve, and less than 100% recovery of tracer at the time when the experiment would typically be terminated. The RTTF particle-tracking simulations assume dispersivity values of 0 and 1 m. The finite element solution (dispersivity of 1 m) exhibits some numerical dispersion that is not present in the particle tracking solution. Nonetheless, the finite-element and particle-tracking curves exhibit virtually identical peak times and mass recovery versus time curves. The particle-tracking

## Particle Tracking

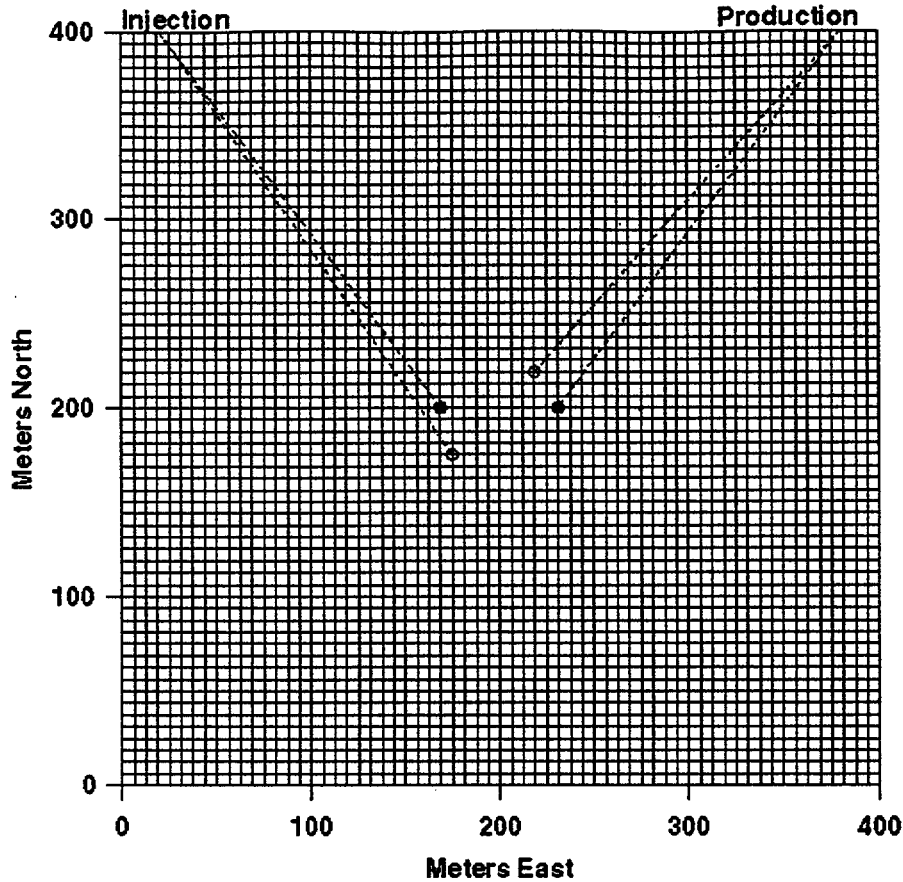


**Figure 4-8.** Model geometry and finite element grid for the two-dimensional models of interwell tracer tests at the C-Wells, Yucca Mountain, Nevada. The solid circles are an injector and producer for the case of wells aligned with the grid, and the open circles are the same for the case of wells misaligned with respect to the grid.

solution with no dispersion exhibits noise that will be present no matter how many particles are used. The noise is due to the fact that there are a finite number of pathways between the injection and production points. With the RTTF particle-tracking technique in the absence of dispersion, a particle in a particular path will always possess exactly the same transit time as others in that path. Therefore, the breakthrough curve reflects the arrival of these discrete paths as “bursts” of tracer, resulting in noise in the computed curve and a higher peak concentration. However, this is not

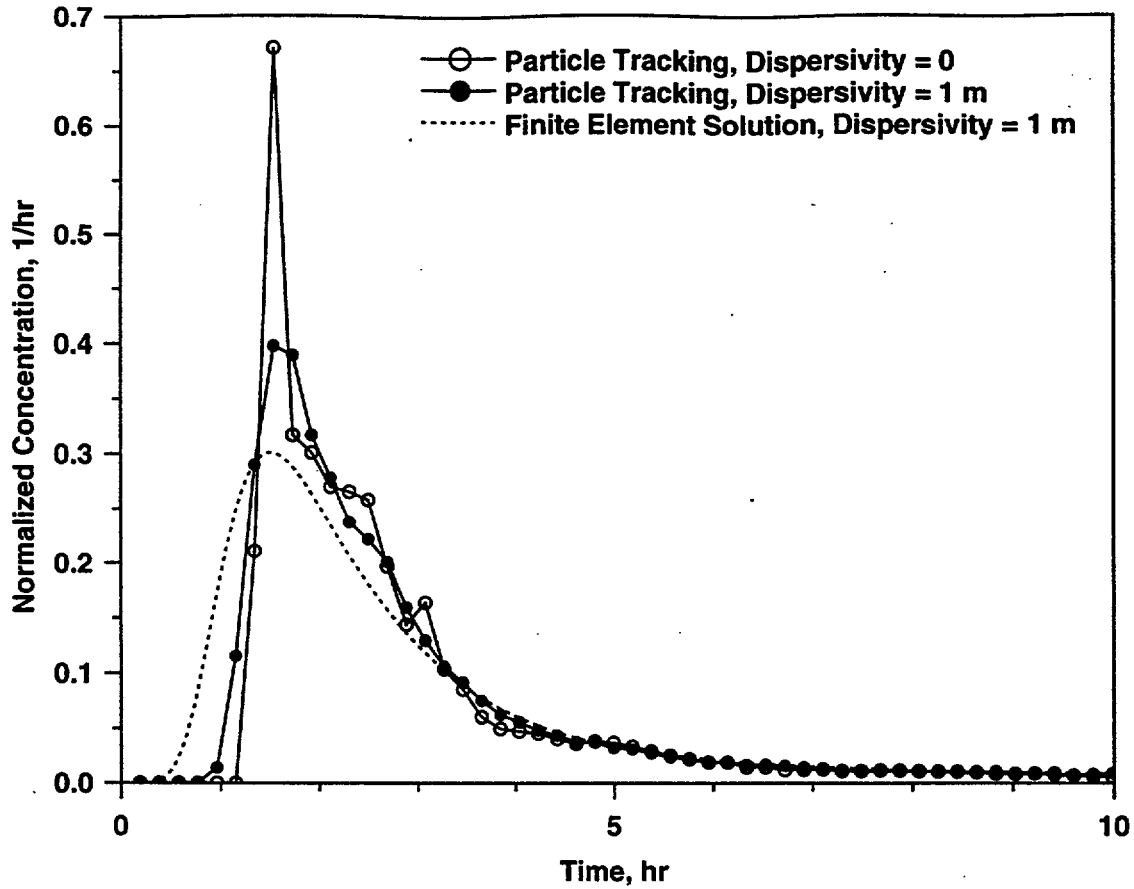


Figure 4-9. Comparison of RTTF particle tracking simulation (solid curves) and finite element CD equation solution (dotted curve). The two particle tracking curves show the effect of varying the dispersivity (0 and 1 m).

viewed as a limitation, since a dispersivity value typical of those estimated in field transport studies is large enough to eliminate the noise.

The comparison of the particle-tracking and finite-element solutions suggests that the particle-tracking algorithm can duplicate the behavior of a system exhibiting macrodispersivity in which the dispersion is due to heterogeneity in the permeability field. Furthermore, the particle-tracking solution eliminates the numerical dispersion present in the finite-element solution, which results in an underestimation in the first arrival time, a parameter often reported in interwell tracer studies. Finally, the exceptional computational efficiency of the technique makes it a logical choice

in stochastic analyses requiring multiple realizations. For this example, this 100,000-particle simulation required only 5% of the cpu time of the advection-dispersion equation solution.

### 4.7 Applications

---

The three example calculations presented in this section illustrate the use of the RTTF particle-tracking method for solute transport problems for which conventional solutions to the CD equation are not well suited. The applications are solute transport problems of interest for YMP. More comprehensive analyses on these topics will be published in separate papers or are present as analyses in this report. They are used here to discuss the particle-tracking methods as applied to simulations of interest.

#### 4.7.1 Dual-Permeability Transport for the Unsaturated Zone

In an equivalent continuum flow model, the permeability of the liquid phase is computed as a weighted average of the fracture and matrix portions of the medium. At high fluid saturations, the fractures begin to transmit the majority of the fluid. However, for solute transport, the porosity of the matrix rock is generally assumed to be available for transport, whereas in reality the much smaller available porosity of the fractures may actually transmit solute when fracture flow dominates. A dual-permeability model formulation is a more preferable way to simulate solute transport in such instances because the porosity and flow rate through each continuum is considered explicitly. In this way, the relative proportions of solute traveling rapidly through fractures and more slowly through the matrix rock can be computed.

To illustrate the use of the particle-tracking model in a dual-permeability system, a simplified one-dimensional flow and transport system representing the vadose zone infiltration problem for Yucca Mountain is considered (Figure 4-10). The fluid flow characteristics of this model problem have been examined by Ho et al. (1995). The hydrologic parameters are set by dividing the system into four hydrogeologic units. The uppermost Tiva Canyon welded (TCw) unit and third unit, the Topopah Springs welded (TSw) unit, are composed of highly fractured, welded

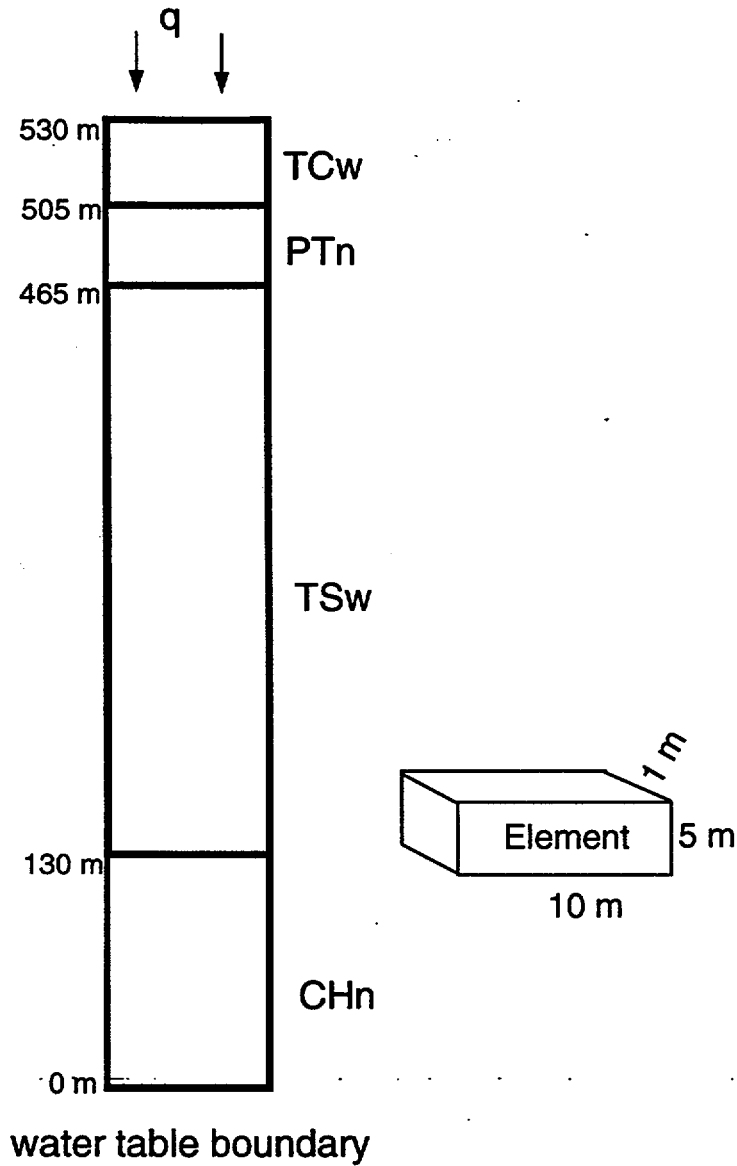


**Figure 4-10.** Schematic of the one-dimensional model system of the vadose zone at Yucca Mountain used for the dual permeability particle tracking example.

tuffs of low matrix permeability. They are separated by a nonwelded, relatively unfractured tuff of high matrix permeability called the Paintbrush Tuff nonwelded (PTn) unit. The fourth unit, the Calico Hills nonwelded (CHn) unit, is also a relatively unfractured rock of high matrix

## Particle Tracking

permeability extending to the water table in this simulation. Hydrologic property values used in the calculations below are those cited by Ho et al. (1995).

At a high-enough infiltration rate, the flow and transport system will exhibit behavior that is characteristic of a fracture-dominated system, especially in the welded TCw and TSw units.

Figure 4-11 shows the composite solute breakthrough curves at the bottom of each unit obtained

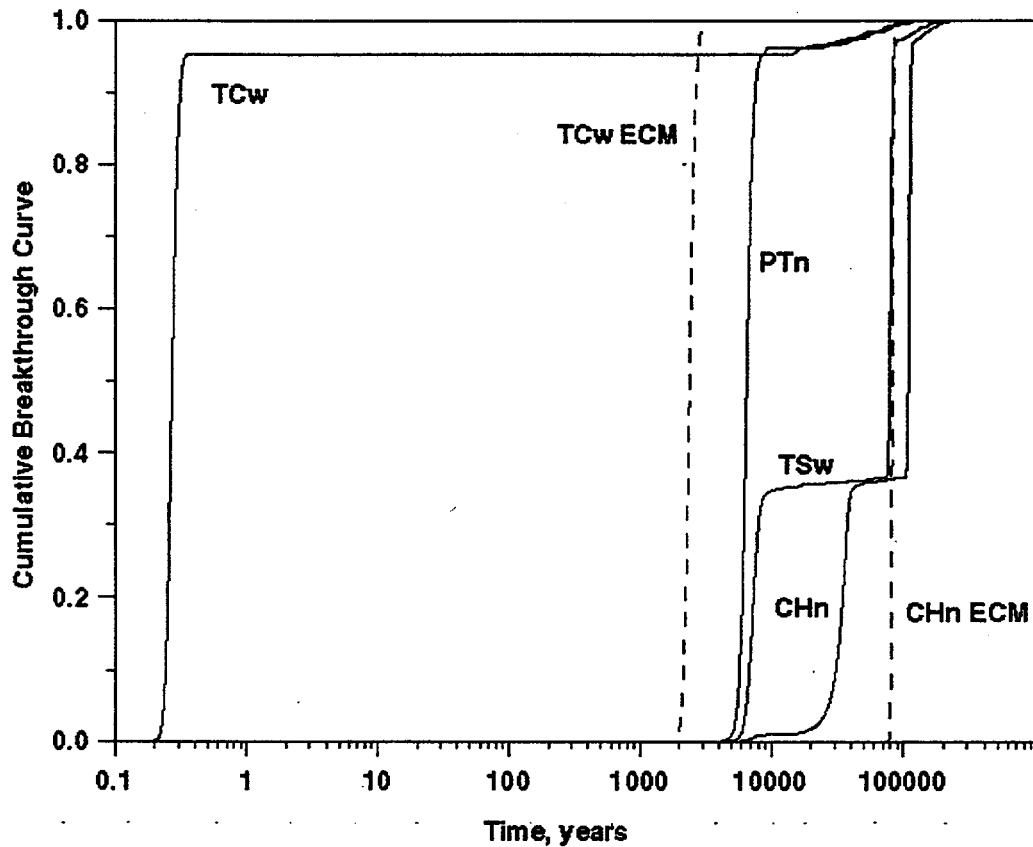


**Figure 4-11.** Composite solute breakthrough curves (fracture plus matrix contributions) at the bottom of each hydrogeologic unit at 1 mm/y infiltration rate using the dual permeability particle tracking model (solid curves). The dashed curves are comparable results assuming an equivalent continuum model.

by adding the contribution from the fractures and matrix. The response of the system to a step change in concentration at the surface is depicted in the figure. At the assumed infiltration rate of 1 mm/y, most of the solute travels rapidly through the TCw unit, bypassing the matrix altogether.

It then transfers to the matrix of the PTn unit, traveling slowly through this unfractured rock mass. Thus, the breakthrough curve at the bottom of the PTn occurs only after spending at least 5000 y in this unit. Some of the solute transfers back to the fractures in the TSw unit where it exhibits rapid travel times before moving back into the matrix of the CHn unit. This sort of behavior is not captured in the equivalent continuum model simulation shown in the figure for the breakthrough curve at the bottom of the model domain. Travel times in units that exhibit significant fracture flow are severely overestimated with an equivalent-continuum model that assumes the solute is perfectly mixed throughout the matrix rock.

The available field evidence supports some aspects of this simulation, as discussed in greater detail below in the application of the particle-tracking technique to the simulation of environmental isotopes. The equivalent-continuum model using either particle tracking or a finite-element solute transport solver cannot represent rapid transport through welded, highly fractured units, because in equivalent-continuum models, the travel times through the TCw are computed based on the matrix porosity, which results in long travel times even though significant fracture flow occurs (> 2000 y).

### 4.7.2 Simulations of Environmental Isotopes in the Unsaturated Zone

Naturally occurring radioactive isotopes such as  $^{36}\text{Cl}$  and  $^{14}\text{C}$  are often used as environmental tracers for dating the age of groundwater samples. These isotopes, produced by cosmic-ray secondaries interacting with atoms in the atmosphere, enter the subsurface in precipitation and as dry fallout. The methods used to estimate fluid travel times in the unsaturated zone at Yucca Mountain differ for these isotopes for reasons related to their half-lives and estimated time-dependent source concentrations at the surface.  $^{14}\text{C}$ , with its half-life of 5730 y, can be used to date fluids in the age range of about 1 to 30 ky by comparing its concentration with the value present in modern fluid. By contrast,  $^{36}\text{Cl}$  has a half-life of 301 ky, meaning that a similar method for age dating can only be applied for fluids at least 50 ky in age (Liu et al., 1995). However, Plummer et al. (1996) show that the source value of the  $^{36}\text{Cl}/\text{Cl}$  ratio has varied substantially in the past, perhaps due to geomagnetic variations or a decrease in stable Cl concentration during past wetter climates. Recon-

structions of the surface signal such as that in Figure 4-12 (from Fabryka-Martin et al., 1996c) can

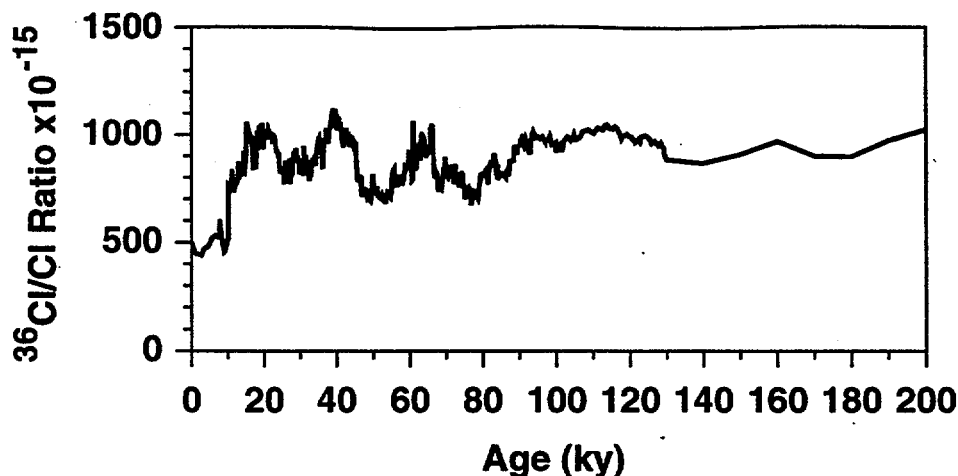


Figure 4-12. Reconstructed  $^{36}\text{Cl}/\text{Cl}$  input ratio used in the particle tracking simulations (from Fabryka-Martin et al., 1996c).

be applied in models to interpret field measurements with fluid ages of 0 to 50 ky. Instead of radioactive decay, the past variation in input signal is used for the age estimate. Furthermore, a man-made signal about 400 times larger than the present-day  $^{36}\text{Cl}/\text{Cl}$  ratio was associated with atmospheric testing of more than 70 nuclear weapons in the Pacific Proving Grounds between 1952 and 1958. This forty-year-old spike in the input function, termed “bomb-pulse”  $^{36}\text{Cl}$ , provides an indicator for fast-moving fluid in the unsaturated zone.

In principal, if enough measurements of these environmental tracers can be obtained as a function of depth and position, hydrologic flow models can be calibrated, thereby enabling more accurate predictions of radionuclide migration from the potential repository to the accessible environment. In the present study, we demonstrate the use of the RTTF particle-tracking technique for simulating the movement of  $^{36}\text{Cl}$  and  $^{14}\text{C}$  in a dual-permeability, unsaturated-zone flow and transport model. For this application, the mathematical methods outlined above were augmented to record the age of each particle passing through a given cell, so that in the case of  $^{36}\text{Cl}$ , the time-varying input signal could be reflected in the calculation of concentration at that location. In the

simulation, all particles are released at the initial time, and the average concentration at a position in the model is computed as the average concentration of all particles passing through the cell. This approach is valid for steady-state flow systems, the assumed state of the Yucca Mountain unsaturated-zone flow system in these simulations.

Figure 4-13 shows the results of simulations of the  $^{36}\text{Cl}/\text{Cl}$  ratio (Figure 4-13a) and  $^{14}\text{C}$  concentration (Figure 4-13b) in a two-dimensional, West-East cross section at Yucca Mountain for assumed infiltration rate of 5 mm/y. The bomb-pulse  $^{36}\text{Cl}$  signal (the red concentration, greater than  $1200 \times 10^{-15}$ , after Fabryka-Martin et al. (1996b)) is located in the PTn, underlying the fractured TCw unit. This result, in agreement with borehole measurements reported by Fabryka-Martin et al. (1993), is caused by fracture transport through the TCw. The prediction of ratios in excess of the present-day ratio of  $500 \times 10^{-15}$  in the TSw unit also agree with measured values in samples collected in the Exploratory Studies Facility (ESF) (Fabryka-Martin et al., 1996b).

Analyses of  $^{14}\text{C}$  in the pore water are available mainly in the PTn and CHn hydrogeologic units, as well as in the perched water samples collected at the site (Yang et al., 1996). The model result of Figure 4-13b agrees in general with the findings of Yang et al. (1996). First, young ages are predicted in the PTn, estimated to be of the order of 1000 y (or 0.9 pmc). As with the  $^{36}\text{Cl}$  analysis, rapid travel through fractures in the TCw results in young ages in the PTn. The exact age measured in fluids in the PTn matrix depends on local conditions where the sample was collected, but travel times on the order of a few thousand years through the matrix of this unit are expected. Also, perched water fluid ages on the order of 4 to 7 ky in the CHn measured by Yang et al. (1996) are also reflected in these simulations (the pmc of the matrix fluid at the top of the CHn is of the order of 0.5 in this simulation, corresponding to one half-life, or 5730 y). After spending several thousand years traveling through the PTn matrix, a significant fraction of the fluid (and particles) rapidly traverses the TSw in fractures, and relatively young ages are then recorded in the CHn matrix.

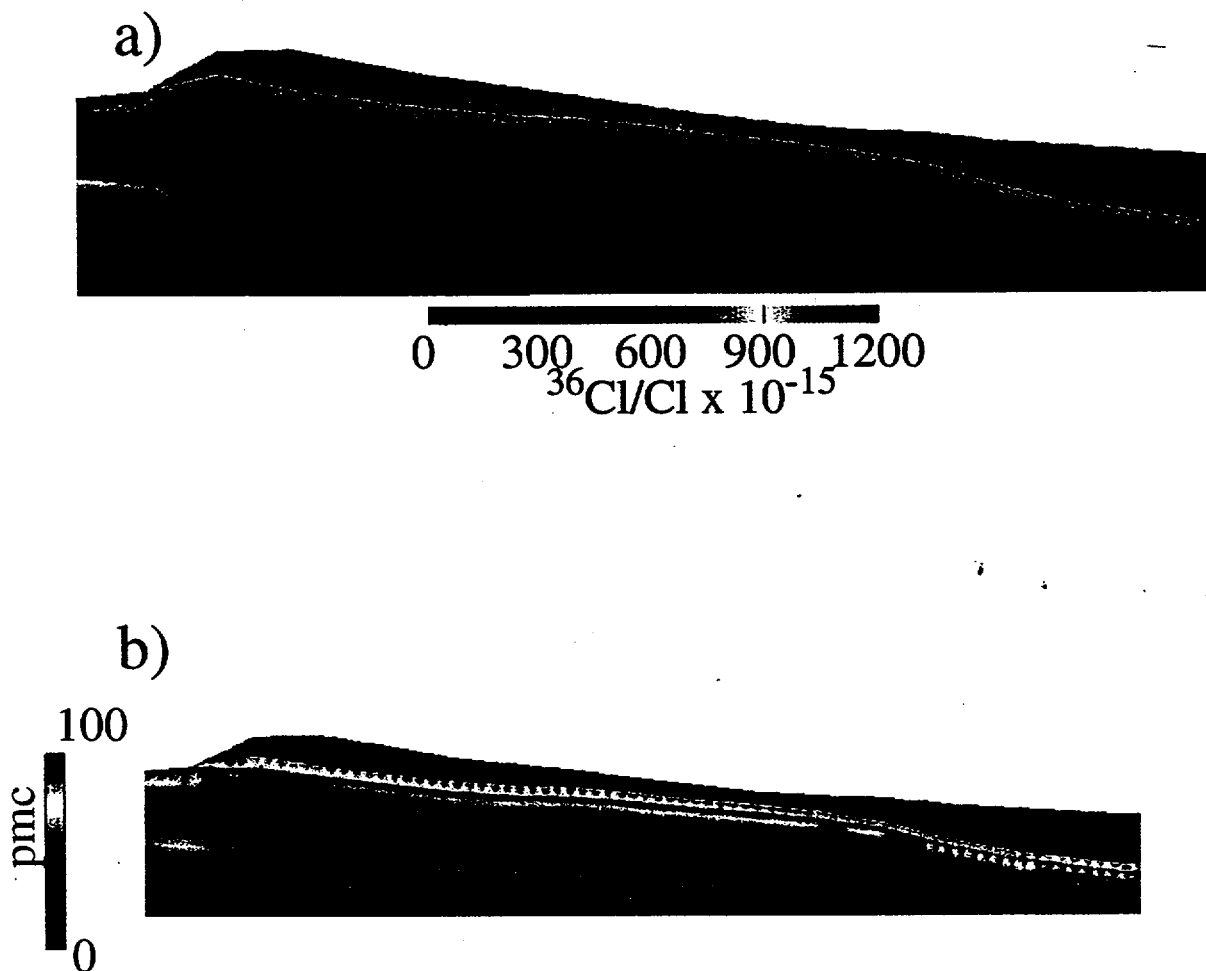


**Figure 4-13.** Simulated concentrations of  $^{36}\text{Cl}/\text{Cl}$  ratio (a) and  $^{14}\text{C}$  in the two-dimensional model domain. For  $^{36}\text{Cl}$ , the bomb-pulse signal is red, and the values at the ESF horizon are in agreement with field measurements. For  $^{14}\text{C}$ , values in the PTn (above ESF) and CHn (below ESF) are in qualitative agreement with field measurements.

There are significant limitations to carrying out a similar analysis using conventional finite-difference or finite-element solute transport simulations, especially in dual-permeability calculations. Most important is the enormous disparity in travel times in fractures and matrix, even at the same position in space. A special form of the Courant condition exists in dual-permeability simulations; for accuracy, the time step is limited to the travel time through the fractures during the

period in which significant concentration gradients exist anywhere in the fractured continuum. Either uniformly small time steps or special front-tracking and embedded time-stepping schemes would be required in certain dual-permeability applications. The cell-based particle-tracking method developed here provides accurate solutions without resorting to these sophisticated and computationally intensive methods.

### 4.7.3 Sorbing tracers with matrix diffusion

The saturated zone beneath Yucca Mountain is being studied for its potential to retard the movement and dilute the concentrations of radionuclides that might be released from a potential repository and percolate through the vadose zone to the water table. Interwell tracer tests are being planned using conservative and weakly sorbing solutes to study the transport mechanisms in the saturated zone. A key issue being addressed in these studies is the extent to which laboratory-determined sorption parameters for radionuclides can be used to predict migration rates in the field. For regulatory and practical reasons, the radionuclides themselves cannot be used in large-scale, saturated-zone field tests. Instead, the plan is to use a nontoxic, sorbing tracer of known sorption characteristics to test the methodology of using laboratory data in field-scale transport models. If accurate predictions of field transport behavior can be made based on laboratory-determined sorption parameters and a measured conservative tracer breakthrough curve, then we have increased confidence that the radionuclide sorption data are valid when used in field-scale models of radionuclide migration from a potential repository.

The simulations presented here using the RTTF particle-tracking model are on the heterogeneous, two-dimensional flow field presented in the benchmarking exercise in the Validation section. Simulations of two-well recirculating tracer tests will now be presented for this example problem. In contrast to the benchmarking calculations, these simulations will include the effects of matrix diffusion and sorption. Matrix diffusion is expected to be significant over the time scale of a field tracer test. However, this problem is exceedingly difficult to model with finite-difference or finite-element solutions to the advection-dispersion equation, as large concentration gradients would be expected adjacent to fractures. For example, for a transit time of 5 hours, the

characteristic diffusional distance into the rock matrix for a diffusion coefficient of  $10^{-10} \text{ m}^2/\text{s}$  is about 1 mm. A discrete fracture model with numerous grid points within this 1 mm distance would be required for an accurate simulation of transport by conventional means. By contrast, the transfer function approach for matrix diffusion is ideally suited for this simulation.

Figure 4-14 compares the simulated breakthrough curves with and without matrix

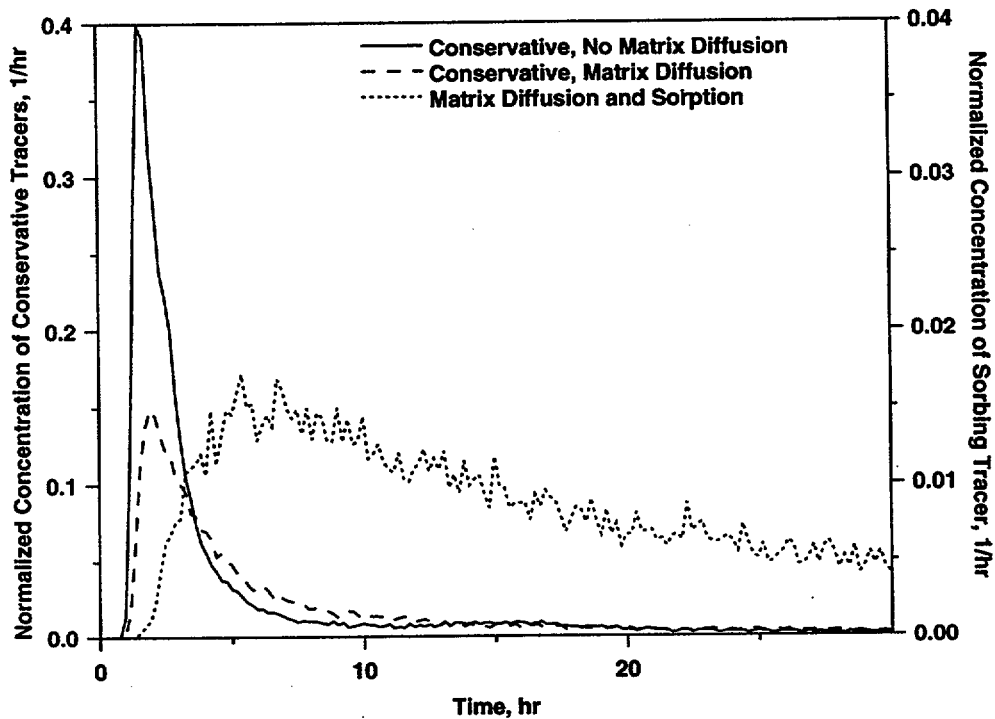


**Figure 4-14.** Simulations with and without matrix diffusion for the two-dimensional interwell tracer experiments modeled in Figure 4-8. Also shown is a simulation of a tracer that sorbs to the matrix rock (the dotted curve).

diffusion. Tracers with different diffusion coefficients could in theory be employed to measure the extent to which matrix diffusion affects transport in the saturated zone. Reimus (1995)

demonstrated this concept in laboratory-scale fracture transport tests, showing that polystyrene microspheres can be interpreted as tracers with very low diffusion coefficients.

As detailed in the Mathematical Development section, sorption is also included in the matrix diffusion transfer function. For these Yucca Mountain experiments, Robinson (1994) proposed that the lithium cation ( $\text{Li}^+$ ) be used as a sorbing tracer. The measured  $K_d$  determined for lithium is about 0.6 g/cc at a fluid concentration of 50 ppm. If we assume that this  $K_d$  value applies in the rock matrix, then the value of  $R_{f,m}$  in equation (Eq. 4-10) is calculated to be 25. For the curve marked "Matrix Diffusion and Sorption" in Figure 4-14, this retardation factor is assumed for the matrix, with sorption in the fractures assumed to be negligible. If, however, this retardation factor had been taken for both the fracture and matrix, then the model would have predicted breakthrough times that are roughly 25 times longer than those shown in the figure.

The sensitivity of the model to assumptions about sorption implies that field tests such as these in fractured media can be used to pinpoint the nature of transport in fractured rock more precisely than can conservative tracer tests. The RTTF particle-tracking approach is well equipped to handle this transport problem. The diffusional time scale, when compared to the transport time within the fractures, is such that solutes diffuse only a short distance into the rock. Finite-element and finite-difference models, even using a dual-porosity or discrete-fracture formulation, cannot realistically cope with these large concentration gradients. The transfer function for matrix diffusion allows us to simulate this transport process very precisely.

One potential concern when using the RTTF particle-tracking method that is not present in simple one-dimensional calculations is the possibility of grid orientation effects. When the flow streamlines are not oriented with the grid, this method may require that a particle take a somewhat circuitous route that follows the grid. This topic was the subject of discussion (Goode and Shapiro, 1991; Desbarats, 1991) concerning the original node-to-node routing scheme of Desbarats (1990). To examine this effect, we present two calculations on the two-dimensional grid used in this example problem. In both cases, the medium is assumed to be homogeneous, but the wells are

oriented either along a horizontal grid line (the filled circles in Figure 4-8) or diagonally with respect to the grid lines (the open circles). For comparison, finite-element transport solutions were also carried out. Figure 4-15 shows results of this comparison. First, note that although the finite-

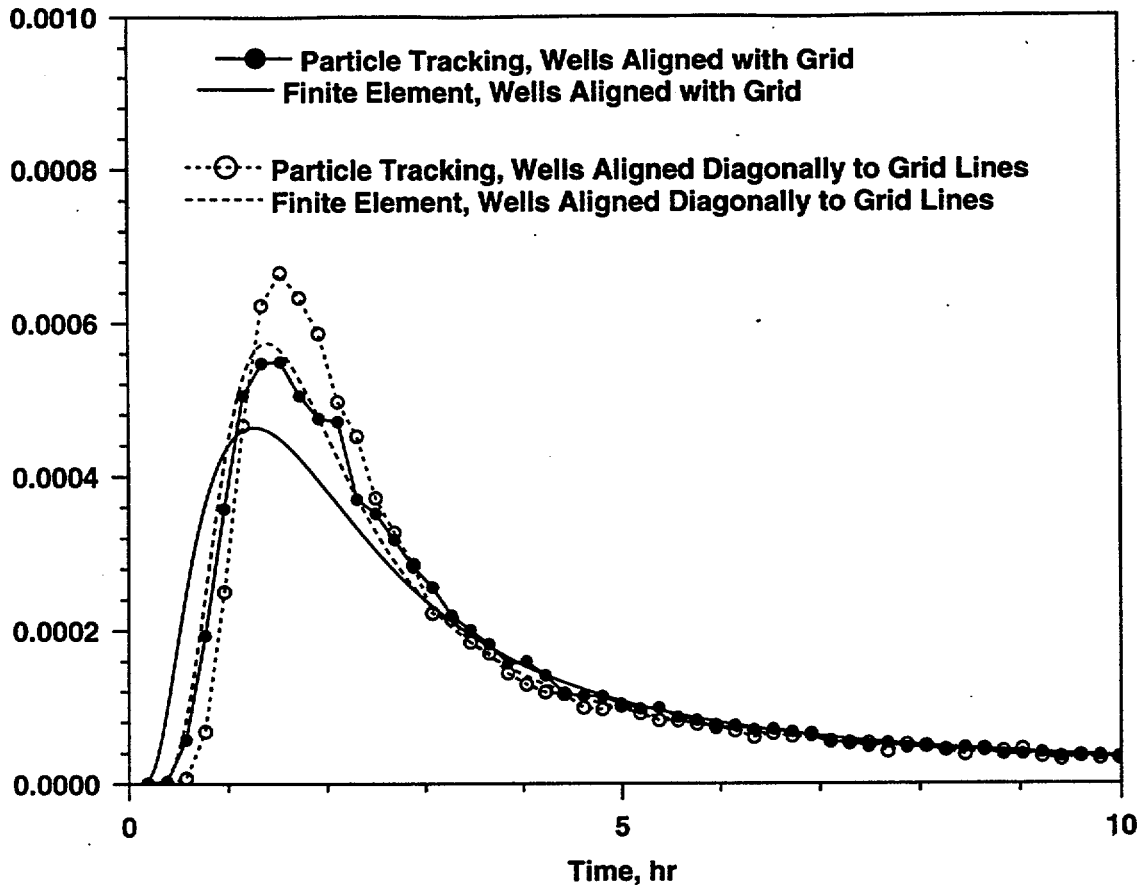


**Figure 4-15.** Breakthrough curves for a homogeneous permeability field examining the effect of grid orientation on the transport behavior of the RTTF particle tracking method. Solid curves: wells aligned with the grid; curves with symbols: particle tracking solutions.

element solution exhibits the same trend in the breakthrough curve, some numerical dispersion is also experienced. With respect to grid orientation effects, the particle-tracking breakthrough curves show grid orientation effects that are similar both qualitatively and even quantitatively to those experienced with the finite-element solution. The same basic phenomenon causing the effect (flow streamlines that are not aligned with the grid lines) exerts the same influence on the model results for the two methods. This amount of error due to grid orientation effects would almost certainly be

acceptable for analysis of field tracer breakthrough curves, because uncertainties in other model parameters, as well as experimental uncertainties, would likely exert a much stronger effect on the results. Nonetheless, the possibility of grid orientation effects that impact the results significantly should be evaluated for each specific particle-tracking model application.

With respect to unsaturated-zone solute transport, the geometry of the flow and transport system, along with actual dispersion mechanisms that compete with grid effects, are expected to minimize the importance of grid effects. The transport pathways have a distance similar to that of the thickness of the unsaturated zone or, in the case of radionuclide migration, the distance from the repository to the water table. Solute source terms are introduced into the system over the entire surface or the entire length of the repository. This geometry is quite different than the case in which a distinct, confined plume of solute must be tracked accurately over long distances at flow path trajectories that are not aligned with the grid. Also, the vast disparity in travel times between fractures and matrix, and the variations in thickness of nonwelded units such as the PTn and CHn give rise to solute spreading that should far outweigh the small amount of grid-induced dispersion. For this reason, we conclude that the RTTF particle-tracking technique is suitable for unsaturated-zone transport simulations of isotope and major-ion chemistry and for radionuclide migration predictions.

### 4.8 Conclusions

---

The particle-tracking method developed in this chapter, called the Residence Time Transfer Function (RTTF) particle-tracking technique, employs a new, efficient particle-tracking algorithm that is suitable for performing large-scale transport simulations. Like most particle-tracking methods, this algorithm provides advection-dominated solutions that are free of numerical dispersion. Thus, the technique can track a sharp front in solute concentration without the usual numerical dispersion or concentration-profile oscillations encountered in conventional finite-difference or finite-element solutions of the advection-dispersion equation.

## Particle Tracking

---

The development that distinguishes the RTTF particle-tracking method from existing groundwater transport particle-tracking techniques is the conceptualization of transport as the movement of particles from cell to cell. This approach eliminates the need to resolve the velocity vectors by interpolation at all particle positions. Instead, the mean residence time and the probabilities of travel to adjacent cells are computed once for each cell (until the flow solution changes), regardless of how many particles travel through the cell. Another advantage of the cell-to-cell approach is that the information needed to compute particle residence times and pathways is readily available in finite-difference or finite-element solutions of the flow problem. The fluid mass and intercell mass flows rates are a direct result of the fluid flow solution, and thus the method can be implemented without regard to the nature of the numerical grid (structured versus unstructured grids, element shapes, etc.). The particle-tracking technique is also simple to implement for dual-permeability flow models, since the fracture-matrix interaction term is treated as another flow rate to or from a given node.

As particles are tracked through the model domain, no particle transport time stepping is necessary; all particles are tracked from the starting time to the ending time of a segment of the simulation. The only reasons to terminate and restart a simulation are either to update a flow field in a transient flow simulation or to pause to write the particle positions to output files. Thus the method is computationally efficient: simulations of several million particles are practical on conventional workstations without employing parallel processing hardware. Like most particle-tracking techniques, the algorithm would parallelize naturally, as the fate of each particle can be computed independently of the movement of other particles. The ability to track the movement of a large number of particles allows large-scale transport simulations to be carried out.

The concept of particle residence times in each cell has been extended to relax the assumption of pure plug flow without dispersion. Transfer functions have been developed to simulate dispersion, equilibrium sorption, and matrix diffusion. For accuracy, dispersion coefficients must be small enough that the grid Peclet number remains greater than one throughout the grid. This limitation is not viewed as overly restrictive, because systems with large dispersion

## Particle Tracking

---

coefficients can be simulated accurately on relatively coarse grids with conventional finite-difference or finite-element solutions to the advection-dispersion equation. Thus, this particle-tracking method nicely complements the solute transport capabilities present in existing flow and transport codes such as FEHM. The matrix diffusion transfer function fills a void in our ability to simulate tracer experiments in fractured media using equivalent-continuum approaches. Transport time scales in tracer experiments are such that characteristic diffusional distances into the rock matrix are of the order of millimeters. The transfer function is a logical alternative to the explicit simulation of large concentration gradients in the matrix rock in the vicinity of fractures. Linear, equilibrium sorption is also incorporated into the matrix diffusion transfer function. This feature allows a variety of pollutant transport problems to be solved efficiently. When the assumptions inherent in the linear sorption isotherm are inappropriate, more complex chemical transport models should be employed.

The ability to implement the RTTF particle-tracking technique efficiently in a dual-permeability model framework is another advantage. Numerically, the communication between fractures and matrix is treated as one additional connection with a flow rate known from the fluid flow calculation. Rapid transit times through fractures can be duplicated easily using the method, whereas a typical equivalent-continuum representation will overestimate the travel time by using the matrix porosity in the computation. Finite-element solutions to the advection-dispersion equation in dual permeability, though possible, are problematic because the short travel times in fractures impose a very stringent constraint on the time step. This restriction can be minimized by increasing the diffusion coefficient between the fracture and matrix domains, which serves to reduce transport velocities by allowing solute to spend time in the matrix. However, in many transport problems, that extent of communication with the matrix is expected to be small, and compromises such as this will overestimate transport times. This limitation does not exist in the RTTF particle-tracking technique.

Like all numerical methods, the residence time/transfer function particle-tracking technique has limitations that must be considered when deciding whether its use is appropriate for

a given application. The assumptions of advection-dominated transport and linear, equilibrium sorption have just been discussed. The possibility of grid orientation effects must also be considered. The example problem presented here showed that the grid orientation effects for this technique appear to be similar in character to those encountered in conventional finite-difference or finite-element solutions to the CD equation. If grid orientation errors are too large for a given application, then more complex front-tracking algorithms should be used instead, such as conventional particle tracking or locally refined grids.

As unstructured numerical grid generation techniques become more common, the simplicity of implementing the RTTF particle-tracking technique for these grids should be a great benefit. In the Yucca Mountain Project, for example, unstructured grids are made to follow the complex stratigraphy present at the site, so that units with contrasting hydrologic properties can be represented. We suspect that for these grids, orientation errors are small because the grid is aligned with the hydrostratigraphic units and thus are more likely to be aligned with the flow field. Thus, one of the RTTF particle-tracking technique's possible limitations should be minimized.

The particle-tracking technique developed in the present study is designed to solve the CD equation to simulate the movement of tracers, pollutants, or solutes in subsurface porous media. Though not specifically designed to map fluid streamlines, the technique can also be used to view the movement of fluid from a given position, thereby providing a quick look at the flow patterns of a complex flow system. The positive attributes of the technique are its computational efficiency, its simplicity and compatibility with the information provided by numerical flow solutions, and its ability to handle unstructured grids of arbitrary complexity. Thus the RTTF particle-tracking technique should be a useful addition to the suite of numerical methods used to simulate flow and transport in porous media.

## Chapter 5 - Property Sets

### 5.1 Abstract

---

In this chapter, we present a summary of the hydrologic property sets provided by LBNL in the site unsaturated-zone flow model (Bodvarsson et al., 1997), along with modifications tested in the present study for their impact on predicted performance. Bodvarsson et al. (1997) provide a logical starting point for numerical simulations of flow and transport in the present study, since models using their parameter sets are based on calibrations to fluid matrix saturation and capillary pressure measured in cores extracted from several wells at the site. In the present study, an initial screening is performed to determine which parameter sets are apt to yield significantly different performance predictions. As part of this study, a code validation check is performed by comparing the results of FEHM and TOUGH2. The results yield important insight regarding grid discretization and use of weighting schemes.

The "model platform" used to test the hydrologic property sets is a one-dimensional flow and transport simulation with stratigraphy and estimated infiltration rate at SD-9. Steady state, dual permeability fluid flow fields were generated for each property set, after which particle tracking transport simulations of  $^{99}\text{Tc}$  and  $^{237}\text{Np}$  from the repository to the water table were computed. The transport metrics used to identify which property sets yield unique or distinctively different results are the first arrival time of radionuclide at the water table, the relative amount of radionuclide arriving early, the degree of sorptive delay of  $^{237}\text{Np}$  to zeolitic tuffs. In addition, the relative flow split between the fractures and matrix in the zeolitic tuffs is used as a hydrologic metric for judging the property sets. In all cases, fracture-dominated flow in the TSw transitions to almost completely matrix flow in the vitric Calico Hills. Then, at the transition from the vitric to zeolitic tuff, significant fracture flow through the zeolitic tuffs is predicted for every parameter set. The permeability of the zeolitic tuffs is too low to support the 3.6 mm/y infiltration in the matrix, thus resulting in the fracture flow, which will be even more pronounced in high flux areas within the

## Property Sets

---

potential repository area. There are subtle differences from one parameter set to the next which we identify and use as the criteria for selecting sets for the multi-dimensional simulations.

Because of the essential similarities among the various property sets and the possibility that the parameter estimation yielded results that only sample a portion of the range of uncertainty of the actual system, we also propose variations to the calibrated property sets. These variations include higher permeability for the zeolitic rocks, full connection-area weighting for the nonwelded units, and an adjusted property set of one Bodvarsson et al. (1997) derived to improve the Calico Hills fluid saturation using the three-dimensional model. In all, ten property sets are tested in the screening process, and five are chosen for continued testing in subsequent two- and three-dimensional flow and transport simulations.

### 5.2 Software and Data QA Status

---

The FEHM code is used to perform all flow and transport calculations in this report. The code is qualified in accordance with Los Alamos quality assurance requirements and is documented in (Zyvoloski et al, 1992, 1995a, 1995b). The QA status of the data used in this report is shown in Table 5-1.

<b>Table 5-1. QA Status of Data used in this Chapter</b>				
REFERENCE	Q Status	DTN		COMMENT
<b>Bodvarsson et. al., 1997</b> "The Site-Scale Unsaturated Zone model of Yucca Mountain, Nevada, For the Viability Assessment, LBL Technical Report LBNL-40378	Q	LB970601233129.001	3, 5, 6, 8, 9, 10	No DTN assigned. Hydrologic property sets computed in this report are used throughout the present study.
<b>Flint et. al., 1996,</b> Conceptual and numerical model of infiltration for the Yucca Mountain Area, Nevada", USGS WRIR MOL 19970409.0087	Q	GS960908312211.003/ NA	5, 6, 8, 10, 11, 12	USGS DTN 3GUI623M

### 5.3 Introduction

---

The LBNL Site-Scale flow model (Bodvarsson et al., 1997) contains numerous hydrologic parameter sets that are presented as fits to the existing hydrologic data. The correlation of the units to which hydrologic properties are assigned with the geologic framework model is shown in Table 15-1. The primary data used to perform the fits were the matrix saturation and, to a lesser extent, the capillary pressure as measured in core samples from several wells near the potential repository block. The methodology used (Bodvarsson et al., 1997) consisted first of simultaneous numerical inversions of the matrix saturation and water potential data at individual wells assuming local one-dimensional flow. This simplification allowed the system to be solved as a series of one-dimensional problems, thereby reducing the computational burden of the analysis. The infiltration rate at a given well was estimated from the proposed spatially dependent infiltration map of Flint et al. (1996). After this primary analysis was completed, these parameters are incorporated into a full three-dimensional site-scale model to check for consistency with the one-dimensional results. The inclusion in the three-dimensional model allowed for considerations of multidimensional flow effects and for incorporation of pneumatic effects. An example of the need to consider multidimensional flow effects is the presence of perched water, hypothesized to be suggestive of lateral flow. Fracture permeabilities were reduced in the vicinity of known occurrences of perched water to reproduce the location and proposed extent of the perched water bodies (Bodvarsson et al., 1997). In addition, some modification to the CHn nonwelded vitric units was performed to improve the model.

Considerations of the nature of the geochemical data (chloride ion and environmental isotope data) also entered into the choice of model formulation and corresponding hydrologic parameter values obtained. For example, numerous lines of evidence suggest that the PTn unit moderates the fracture-dominated, episodic flow through the overlying TCw unit, converting the fracture flow to predominantly matrix flow. Fabryka-Martin et al. (1996b) showed that using current estimated values of the percolation flux, the travel times to the ESF level are probably

## Property Sets

---

controlled by matrix flow in the PTn, with fracture-dominated flow in the TCw and TSw hydrogeologic units. Non-bomb-pulse  $^{36}\text{Cl}$  levels measured in ESF samples are consistent with travel times of about 10 ky to the ESF, values that would result from infiltration rates of about 1 to 10 mm/y. Due to these and other considerations, for the parameter sets in Bodvarsson et al. (1997) we chose fracture-matrix interaction models that reflect our conventional wisdom that flow should be matrix-dominated through the nonwelded PTn and CHn units. This choice is accomplished by assuming a large fracture/matrix connection area term for the nonwelded units and a small value for the welded units. For the models in which the reduction factor for connection area is a constant multiplier, the values are large in the nonwelded and small in the welded units. For models in which the weighting factor depends on the upstream relative permeability (Ho, 1997), the reduction factor is automatically large in the welded units because of the relative permeability multiplier. This model is not used in the nonwelded units in any of the LBNL model parameter sets because of the considerations discussed above.

Clearly, the form of the weighting factor model chosen will potentially influence the transport predictions, because this parameter exerts a large influence on the relative flow fractions in the fractures and matrix. Despite the various data sets employed in the numerical inversions, there is considerable uncertainty in the model parameters due to uncertainties in the conceptual model (fracture/matrix connection area and other conceptualizations), the infiltration rate, and the nonuniqueness of the resulting fits even for a given model conceptualization. The latter uncertainty is evidenced by the different parameter sets generated in Bodvarsson et al. (1997) by numerical inversion when the only difference is the starting guess in the inversion process. This result is a classic case of an undersampled system, resulting in nonunique results even for the same conceptual model. Given these uncertainties, it is necessary to examine the entire set of published parameter values to determine which uncertainties are likely to be important for unsaturated-zone radionuclide migration.

In this chapter, we present results of a series of one-dimensional simulations designed to provide a preliminary screening of the hydrologic parameter sets. Although multidimensional simulations would be more appropriate in some ways, we chose a one-dimensional model domain from the ground surface to the water table because of the simple model domain, rapid computational times, and consistency with the model calibration efforts. The model area chosen is SD-9, one of the wellbores used in the calibration. This well has been chosen for previous studies because of its proximity to the potential repository, estimated infiltration rate similar to the average value for the site, and complete data set and well-characterized hydrogeology. This well was also selected by performance assessment (PA) analysts as the one-dimensional numerical "testbed" to compare the hydrologic predictions of the FEHM and TOUGH2 (Pruess, 1991) computer codes. The LBNL hydrogeologic column was used to develop the models, with geologic picks provided by Cliff Ho of Sandia National Laboratories (Ho, pers. comm., 1997), who also ran the TOUGH2 simulations used in the model comparison presented in the next section. For the FEHM simulations, a one-dimensional numerical grid was developed with each hydrogeologic unit divided into approximately 10 grid points to provide a detailed description of the hydrology and transport.

The analyses that follow are divided into two sections:

- A detailed comparison of the flow field and transport characteristics of the one-dimensional column using the TOUGH2 and FEHM codes;
- A comparison of the behavior of the one-dimensional system with respect to flow and transport for the various hydrologic property sets published by Bodvarsson et al. (1997).

### **5.4 Comparison of TOUGH2 and FEHM Codes**

---

The validity of a flow and transport model in part depends on the correct numerical implementation of the governing differential equations. The YMP has three main computer codes for simulating flow and transport in the unsaturated zone: FEHM, TOUGH2, and NUFT (Nitao,

1995). Analyses of flow and transport under present-day and anticipated hydrologic conditions have been performed with both FEHM and TOUGH2. Both codes have been tested and approved for use by the YMP for carrying out flow and transport simulations. Nevertheless, the need for a comparison between the codes stems from the complexity of the numerical simulations for which the codes are used: there are no analytical solutions to compare the results of the codes for the complex case of flow in unsaturated, dual-permeability media. The confidence that can be placed on the results of either code will be increased if it can be shown that they provide nearly identical results for a test problem of moderate complexity.

In principle, a full three-dimensional model comparison effort could be undertaken. A comparison of three-dimensional models was performed by Robinson et al. (1995), using results provided by LBNL in their 1995 version of their unsaturated-zone flow model. In that comparison, we found, by electronically overlaying the results of the two models, that the fluid saturations throughout the model domain were quite similar to one another, with significant differences occurring only at faults. The hydrostratigraphy provided by LBNL at that time did not include faults, even though their numerical simulations included faults with distinct hydrologic properties. Away from faults, the comparisons were close.

In the present study, we decided that it is more useful to construct a simpler model domain so that the results can be compared more precisely. Though the previously described comparison was successful, the ambiguities of the hydrostratigraphy of the full three-dimensional system and the different approaches of the two modeling groups in model building and grid generating makes detailed comparisons very difficult to carry out. Given the success of the previous effort and the short time frame available we decided that a one-dimensional, dual-permeability comparison was more practical. Previous dual-permeability comparisons of the code have also been successful, as evidenced by the inclusion of such a comparison in the FEHM suite of V&V test problems run whenever code changes are made (Dash et al., 1996a, b). The goal of the effort described in this section was to build on previous model results by incorporating a conceptual model with newly developed fracture/matrix interaction terms and to include transport of radionuclides from the

## Property Sets

---

repository horizon to the water table. For transport, the FEHM particle-tracking module was used (Chapter 4). For the FEHM flow and transport simulation test, a steady-state flow field was computed and transport simulations were carried out, all with FEHM. For the test of FEHM transport simulation using a TOUGH2 flow field, the flow field and other hydrologic results generated with TOUGH2 were read into FEHM, along with connectivity information for the one-dimensional model domain, and FEHM's particle-tracking model was again used for transport. This exercise fulfilled a subsidiary goal of developing a capability requested by PA analysts to read a TOUGH2-generated steady-state flow field into FEHM for transport calculations. Because FEHM is used for transport in both cases, the comparison is not a flow and transport model comparison. It is best viewed as a check of the *hydrologic* models of the two codes, with radionuclides used as numerical tracers for comparing the flow fields. Since radionuclide transport through a dual-permeability medium depends greatly on the flow rates and volumetric water contents of the two media, transport predictions should provide a stringent test of the two codes.

The hydrologic parameter sets developed in Bodvarsson et al. (1997) are summarized in the next section. For this comparison, the model parameter set 6541 was used, with the upstream saturation weighting model for fracture/matrix interaction in the nonwelded units and the upstream relative permeability weighting for the welded units. This model required that the weighting schemes for determining the fracture-matrix coupling be implemented into FEHM. Both the upstream relative permeability weighting and the upstream saturation weighting models have now been incorporated into FEHM and the flow and transport results presented here use these weighting schemes. In FEHM, the weighting factor for the saturation model is  $S^N$ , where  $N$  is a power of 1 or greater. In this study,  $N=1$  is used in the saturation weighting model for the nonwelded units, and the relative permeability weighting is used in the welded units, as specified in the inversion to obtain the parameter sets.

5.4.1 Flow Results

Figure 5-1 shows the computed matrix saturations using FEHM, along with the TOUGH2-

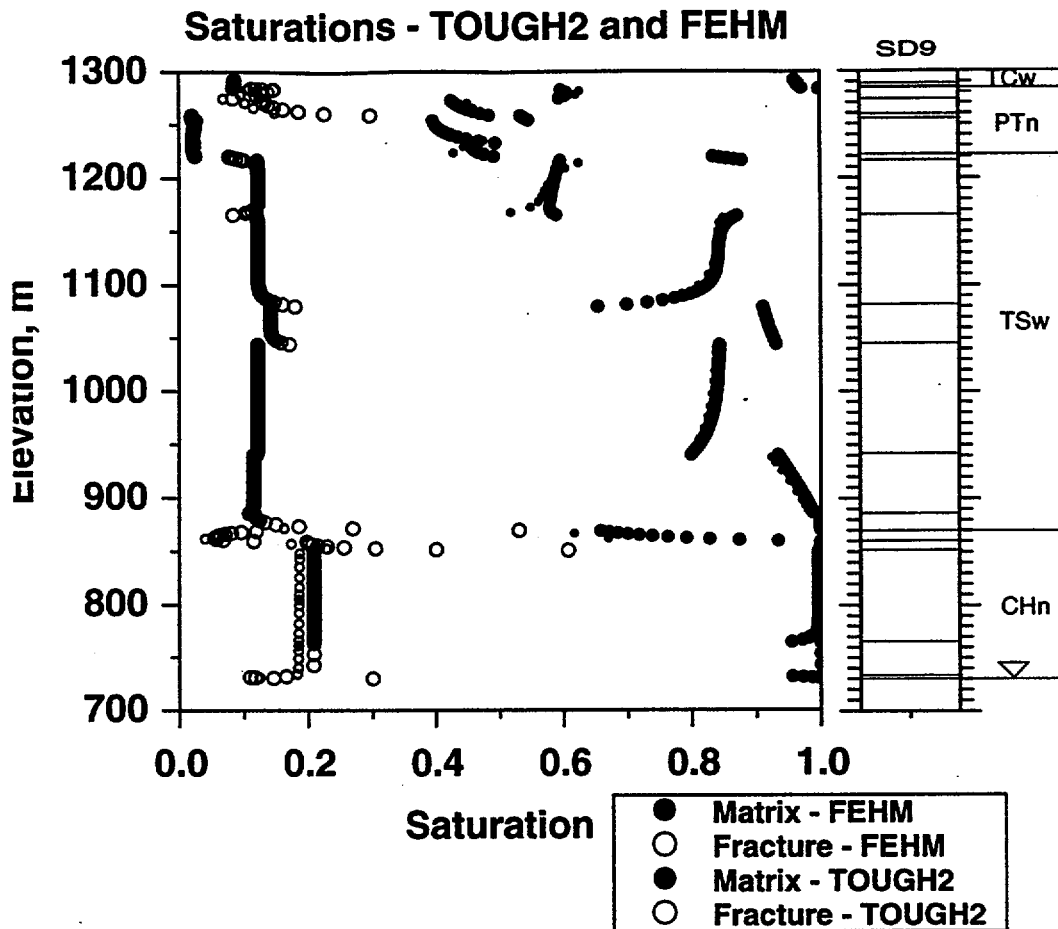


Figure 5-1. Comparison of computed matrix and fracture saturations for the FEHM and TOUGH2 simulations.

computed saturation profile. The very close agreement in the computed matrix saturation profiles using the two codes is evidence of similar implementation of the flow models in the two codes. The breaks in saturation profiles and the corresponding jumps in saturation levels are reproduced using FEHM to a high degree of similarity to the TOUGH2 solution. There are slight differences at the interfaces of some hydrologic units that are explored further below so that they may be more fully understood. However, based on this comparison of matrix saturations (the primary data set used in

## Property Sets

---

the inversions), FEHM simulations will maintain the calibration achieved using the TOUGH2 code as long as the same hydrologic parameter sets are used.

There are other model results such as fracture saturation and relative flow rate through the fractures and matrix that are useful to compare for consistency even though they are solely computed quantities for which no direct comparison to data is possible. Note that these differences are irrelevant to the question of whether the models are calibrated, because we have already demonstrated the equivalence of the models with regard to matrix saturations. Nonetheless, agreement of the codes to this level will provide more confidence in the numerical implementation of both codes, and thus is desirable. Figure 5-1 also shows the computed fracture saturations of the two codes. Over most of the model, the agreement is excellent, with two exceptions. First, at interfaces between units in which the flow is transitioning between fracture and matrix flow, the FEHM simulations predict higher fracture saturations. This result could be caused by slight differences in the implementation of the fracture-matrix weighting schemes or by subtle differences in the weighting schemes within a continuum. These possibilities are described further below.

Second, the fracture saturation throughout the Calico Hills and underlying units are different in the two models. The importance of this difference is seen more easily in Figure 5-2, a plot of normalized flux in the fractures and matrix for the two codes. The fracture saturations and, more importantly, the relative fracture fluxes are different throughout the Calico Hills unit. This difference will give rise to different performance of the unsaturated-zone (UZ) system with respect to radionuclide transport and, thus, is important to understand. The relative fluxes in this region of the model are shown on an expanded scale in Figure 5-3. In addition to differences in the eventual flow splits throughout the CHn, the transition from matrix-dominated to a more evenly divided flux distribution in the zeolitic zone occurs more sharply in the FEHM simulation than in the TOUGH2 run. There was a difference in the thickness of the first vitric Calico Hills unit due to the method used to assign properties to this unit in the TOUGH2 simulation. To check whether this difference accounts for the discrepancy in the models, a FEHM simulation was performed with a 4-m-thick

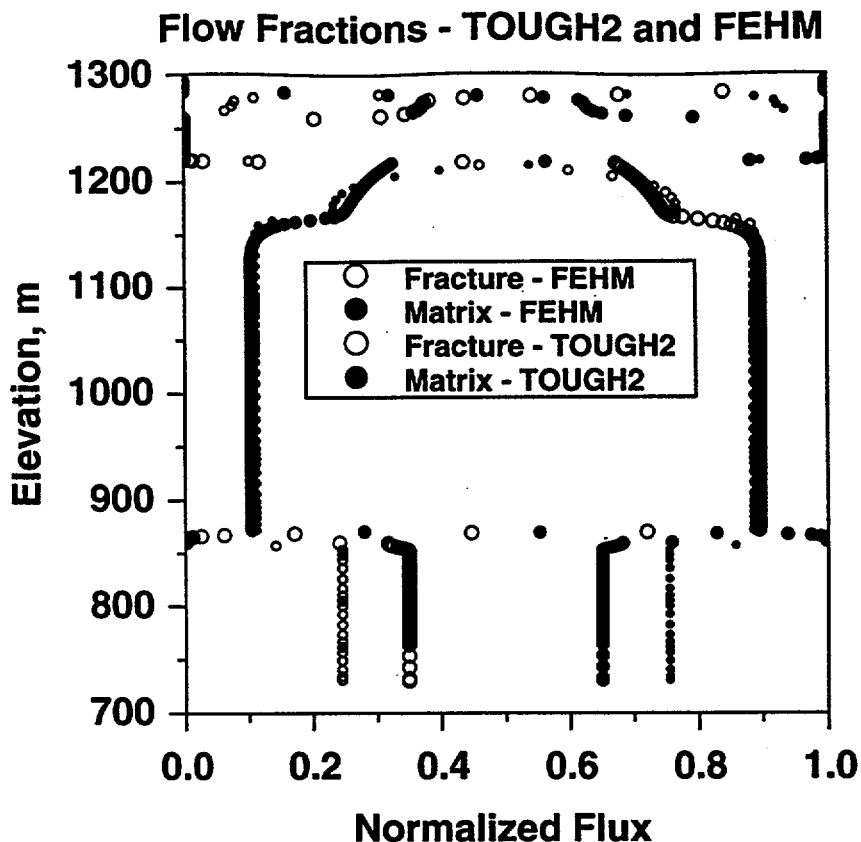
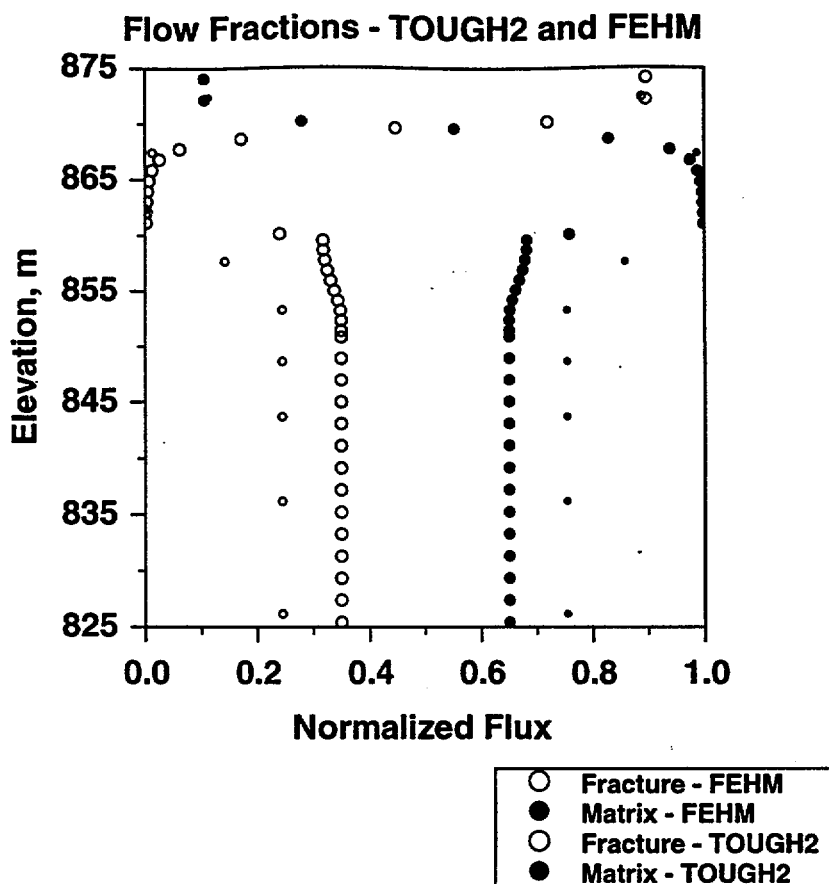


**Figure 5-2.** Normalized flux of water in the fracture and matrix continua: FEHM and TOUGH2 simulations.

vitric layer (as opposed to 10 m). The FEHM solution with the 4-m-thick vitric unit had a slightly different behavior (not shown in the figure), but the difference does not change the flow split in the underlying unit. Another possibility that was tested is that the differences are due to grid resolution effects. Rerunning the FEHM calculation on a coarse grid (not shown in the figures) ruled out this explanation as well. Further work was performed to determine the nature of this discrepancy, but transport simulations are presented first to demonstrate the extent to which such differences are likely to matter for radionuclide migration.

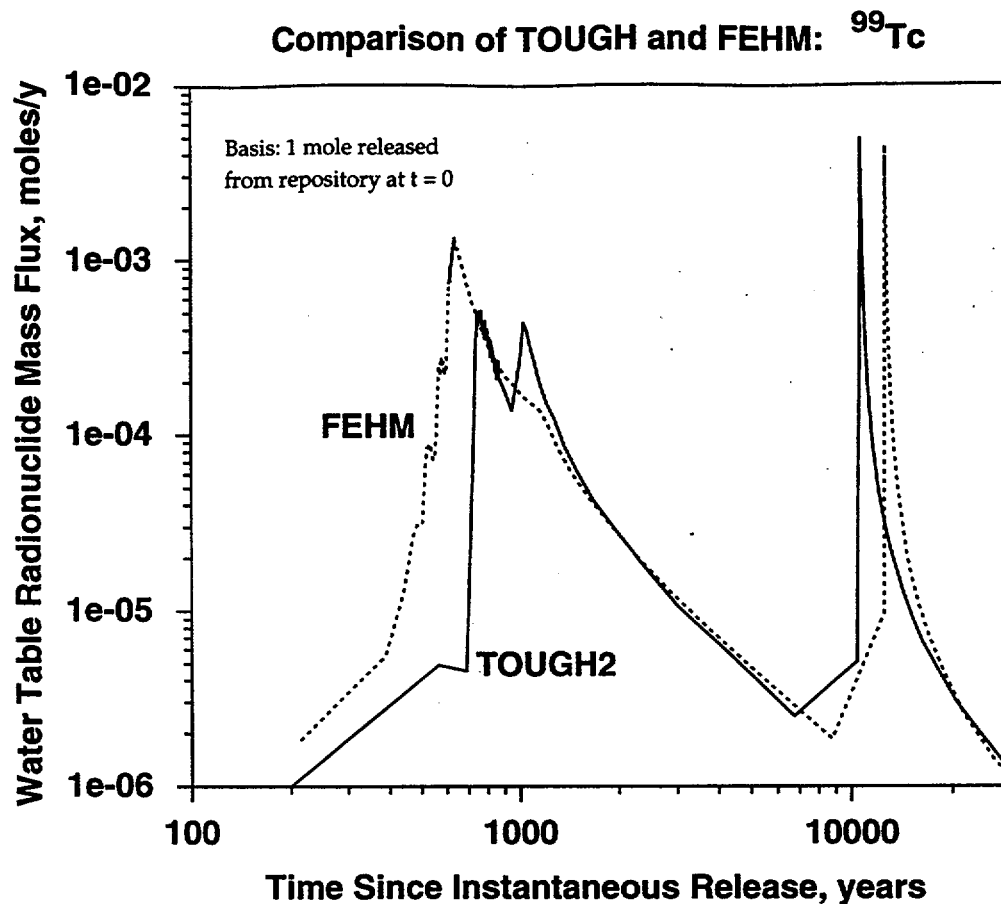
#### 5.4.2 Transport result

A comparison of the water table breakthrough curves for the two sets of simulations is shown for  $^{99}\text{Tc}$  in Figure 5-4. The two transport simulations are for all intents and purposes equivalent. Both



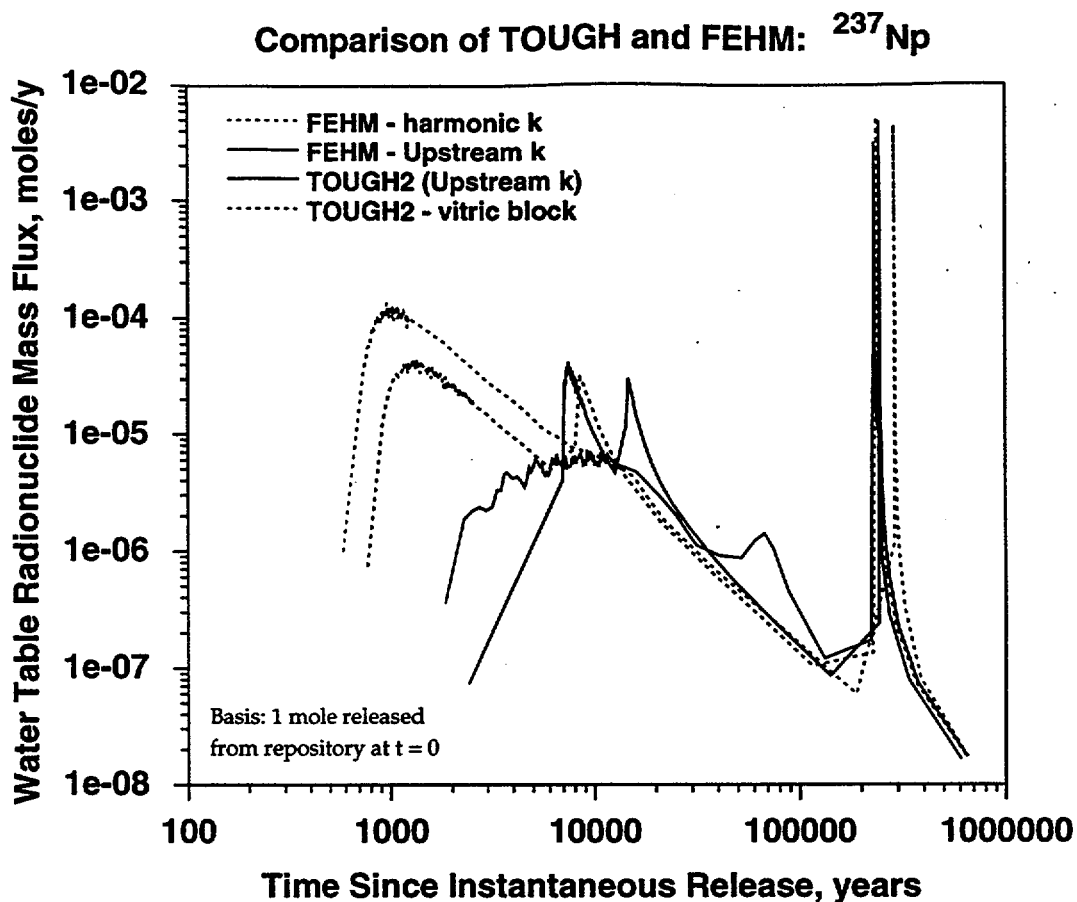
**Figure 5-3.** Normalized flux of water in the fracture and matrix continua: FEHM and TOUGH2 simulations on a scale expanded to examine the CHn units. Also included is an FEHM simulation with a 4 m thick vitric CHn layer, instead of the original 10 m thick layer.

exhibit bimodal behavior caused by the flow split in the Calico Hills units between the fractures and matrix, and the breakthrough times and peak values for the two models agree closely. There is slightly more mass reaching the water table in the first peak for the FEHM model due to the higher predicted fracture flow fraction in the Calico Hills. The arrival of the second peak is somewhat retarded relative to the TOUGH2 simulation, a consequence of the slower flow rate through the matrix for the FEHM calculation. Nonetheless, the agreement is quite close. The transport results for  $^{237}\text{Np}$  are shown in Figure 5-5. The transport parameters were identical with those for  $^{99}\text{Tc}$  except for an assumed  $K_d$  of 2.5 cc/g for  $^{237}\text{Np}$  in the zeolitic units. The greater flow fraction in the frac-



**Figure 5-4.** Breakthrough of  $^{99}\text{Tc}$  at the water table for the one-dimensional SD-9 model: FEHM and TOUGH2 generated flow fields, FEHM particle tracking for transport.

tures for FEHM is accentuated for  $^{237}\text{Np}$ , resulting in an earlier first peak and higher peak value. Once again, a check using a coarser grid showed that grid resolution was not the cause of the differences in the transport results. The cause of the differences at early times is the more gradual transition in the flux distribution at the vitric/zeolitic interface in the TOUGH2 simulation. Flow and transport occurs completely within the matrix of the first zeolitic gridblock, and retardation (with an effective retardation factor of about 20) delays the arrival of the earliest arriving  $^{237}\text{Np}$  by roughly 10,000 years. Sorption in this gridblock is the reason the agreement for the early arriving radionuclide is quite good for  $^{99}\text{Tc}$  but less so for  $^{237}\text{Np}$ . This effect is demonstrated by the second TOUGH2 transport curve in Figure 5-5, obtained by changing the sorption coefficient to 0 in this



**Figure 5-5.** Breakthrough of  $^{237}\text{Np}$  at the water table for the one-dimensional SD-9 model: FEHM and TOUGH2 generated flow fields, FEHM particle tracking for transport.

gridblock (all other properties remained the same). The agreement of this simulation with the FEHM run is quite satisfactory, suggesting that the details of the transition between layers of contrasting hydrologic and transport properties may be important.

The key to these differences lies in the way the codes compute the transition between units of contrasting hydrologic parameters. Specifically, the results are different for the transition of flow from matrix to fracture at the CHn vitric/zeolitic interface, and this fact causes the difference in Np transport. FEHM uses a standard method of harmonically weighted saturated permeabilities, with upstream weighting of the fluid properties and relative permeabilities. The TOUGH2 simulations were run using upstream weighting of all properties, including the saturated permeability (Cliff Ho, pers. comm., 1997), called “full-upstream weighting” in the discussion

below. At the interface in question, full-upstream weighting causes flow to transition more slowly from matrix-dominated to a relatively even split. Therefore, in the TOUGH2 flow field, there is matrix flow in the uppermost zeolitic grid block, which, given the size of this block in the TOUGH2 grid, caused a substantial travel time increase of the first peak. For reference,  $K_d=2.5$  slows the transport velocity by about a factor of 20, so if this occurs in just one reasonably large grid block, minimum travel times increase dramatically.

To further confirm this explanation, an additional FEHM simulation was carried out with full upstream weighting to make it comparable to the TOUGH2 simulation. In Figure 5-5,  $^{237}\text{Np}$  transport with the FEHM-generated flow field but with upstream weighted permeability (solid red curve) comes much more in line with the original TOUGH2 result. The full-upstream weighting scheme used in the TOUGH2 simulation smooths the transition, causing more matrix flow in the upper zeolitic rock, thus causing longer travel times.

The question to be addressed now is whether the remaining differences are large enough to be important to integrated performance of the site. Our claim is that such differences, though perhaps important to demonstrate a complete understanding of the model results, are not sufficiently great to warrant much more study, given the variability of property values across the site, the differences in unit thicknesses, and the uncertainty in parameter values. Therefore, from the standpoint of maintaining a "calibrated" model that agrees quantitatively with the TOUGH2 results, we conclude that the two codes predict essentially the same results and that FEHM simulations carried out in the present study should be valid with respect to their fidelity in reproducing the results of the LBNL site-scale flow model.

### 5.5 Screening of Hydrologic Property Sets

---

In this section, we use the one-dimensional SD-9 model to examine the range of behavior expected due to different calibrated hydrologic property sets. Earlier, we discussed the philosophy of performing this screening on a representative one-dimensional model such as the SD-9

## Property Sets

---

stratigraphy. Before presenting the results, we list the various caveats that must be placed on the analysis. First, the calculations assume that, for screening purposes, SD-9 is representative in terms of stratigraphy and infiltration rate. The stratigraphy contains most of the units specified in the full three-dimensional system, except that the column is almost fully zeolitic from the top of the Calico Hills to the water table. Thus, a unit that plays a key role in transitioning flow from fracture-dominated to matrix-dominated, the vitric Calico Hills, is present but of limited thickness (about 10 m). The infiltration rate obtained from an aerial average of the values near the well from the infiltration map of Flint (1996), is 3.6 mm/y, representative of the average rate near the repository but not nearly as high as values predicted below the crest of Yucca Mountain.

Finally, the calibrated parameter sets all were obtained from one-dimensional model inversions. Although the one-dimensional assumption in the calculations of the present study is consistent with the calibration method, the results may not be entirely representative of the three-dimensional system. Perched water is one example of a feature of the site not captured in one-dimensional calculations. Lateral flow also cannot be reproduced in one dimension. The ramifications of either perching or lateral flow is that the net percolation flux below such features is over-estimated in one-dimensional models, as these models force the entire surface percolation flux through the entire column. The LBNL hydrologic studies handled this limitation by adjusting the fracture properties in three-dimensional models to obtain perching conditions. For our screening studies we assume that the one-dimensional system provides an adequate representation for the purpose of evaluating multiple parameter sets and eliminating those sets that produce behavior that duplicates the results of an equivalent parameter set. Given the limitations just discussed, conservatively retain more parameter sets than would be suggested based only on the one-dimensional results, factoring in the probable outcome if multidimensional screening analyses had been performed.

The parameter sets obtained from the LBNL studies (Bodvarsson et al., 1997) are summarized in Table 5-2. The naming convention in the present study is to use the number of the table in the LBNL report to identify the parameter set. When there is more than one parameter set

## Property Sets

in a table, the letters **a** and **b** are added to the name. A brief description of the assumptions underlying each parameter set is also provided in Table 5-2. For additional details on the

**Table 5-2. Summary of hydrologic parameter sets from Bodvarsson et al. (1997) (shaded rows indicate parameter set not simulated in the present study)**

Parameter Set	Location in Bodvarsson et al. (1997)	Description
6412a	Chapter 6, Table 6.4.1-2, first column	DKM, 3.6 mm/y, const. reduction factor, init. Fm=0.667
6412b	Chapter 6, Table 6.4.1-2, second column	DKM, 3.6 mm/y, const. reduction factor, init. Fm=0.492
6412c	Chapter 19, Table 19.6.4-1	LBL re-calibration of CHv units using the 3D model and matching saturations in SD-7 and SD-12
6412d	Based on 6541c	6412c with 5x increase in zeolite permeability.
6511	Appendix A-6, Table 6.5.1-1	DKM, 3.6 mm/y, const. reduction factor, init. Fm=0.492, init. red. factor=0.05
6521	Appendix A-6, Table 6.5.2-1	DKM, 18 mm/y, const. reduction factor, init. Fm=0.492
6522	Appendix A-6, Table 6.5.2-2	DKM, 0.72 mm/y, const. reduction factor, init. Fm=0.492
6531a	Appendix A-6, Table 6.5.3-1, first column	DKM, 3.6 mm/y, upstream S reduction factor, init. Fm=0.492
6531b	Appendix A-6, Table 6.5.3-1, second column	DKM, 3.6 mm/y, upstream S reduction factor, init. Fm=0.667
6541	Appendix A-6, Table 6.5.4-1	DKM, 3.6 mm/y, upstream S reduction factor (nonwelded), upstream RLP reduction factor (welded)
6541b	Based on Appendix A-6, Table 6.5.4-1	6541 with no reduction factor in PTn only. Applied in Chapter 6
6542	Appendix A-6, Table 6.5.4-2	DKM, 3.6 mm/y, upstream S reduction factor (nonwelded), upstream RLP reduction factor (welded), pm25 fracture flow
6551	Appendix A-6, Table 6.5.5-1	ECM, 3.6 mm/y, init. Fm=0.667

## Property Sets

---

assumptions employed for each parameter set and a detailed discussion of the inversion process, see Bodvarsson et al. (1997).

Of the thirteen parameter sets listed in Table 5-2, two were not examined with an SD-9 simulation in the present study. Parameter set 6542 was determined to be very similar to set 6541, the only difference being the treatment of the fifth PTn layer. This difference is not expected to influence radionuclide transport below the potential repository horizon, because the differences are restricted mainly to the uppermost TSw layers (Bodvarsson et al., 1997). Therefore, parameter set 6542 was not studied here. Parameter set 6551, an ECM inversion result, was not included in the present study because dual permeability is used for the radionuclide transport predictions.

The results of the hydrologic simulations for the eight cases are shown in Figures 5-6 through 5-13. Figure a of each figure contains the computed matrix and fracture saturations, with the field measurements of matrix saturation shown for comparison. Even though the individual simulations themselves differ somewhat from one another, the results show that the computed matrix saturations agree well with the data, as they should for calibrated data sets. Differences from one parameter set to the next result from different fits to the data and from the fact that the LBNL inversions involved several wellbores, so that the fit to any one well may be better or worse, depending on the model assumptions. This test provides a visual confirmation that the various parameter sets have been correctly implemented.

Figure b of each figure shows the simulated fracture and matrix flow fractions (which sum to unity) throughout the one-dimensional column. The general pattern of the flow fractions is similar regardless of the parameter set chosen:

- fracture-dominated flow through the TCw units;
- a rapid transition to matrix-dominated flow in the PTn;
- rapid transition back to fracture dominated (at least 90% fracture flow) in the TSw units (two of the parameter sets (6531b and 6541) have an intermediate flow fraction value in the uppermost TSw unit but higher fracture flow values in the underlying TSw units);

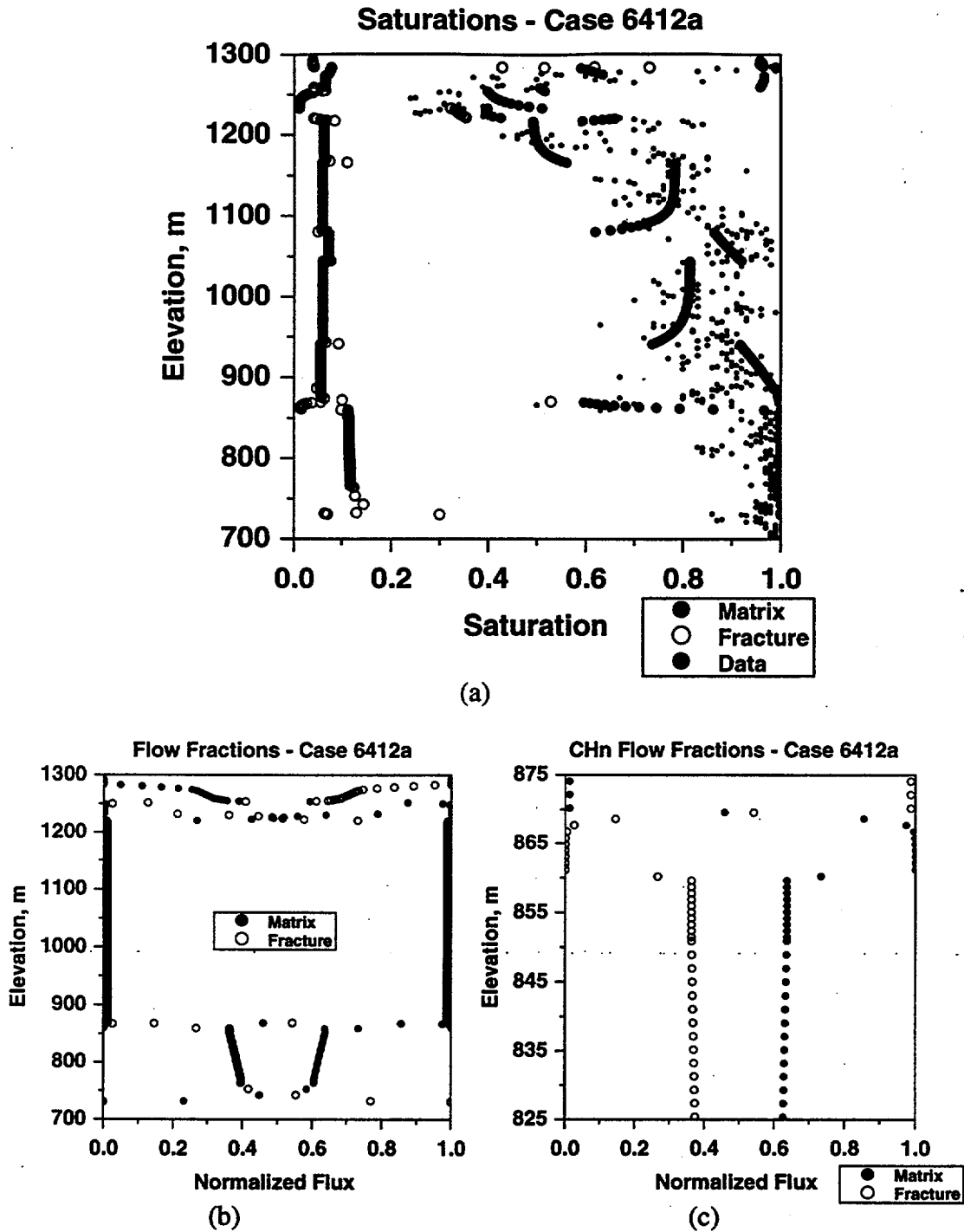
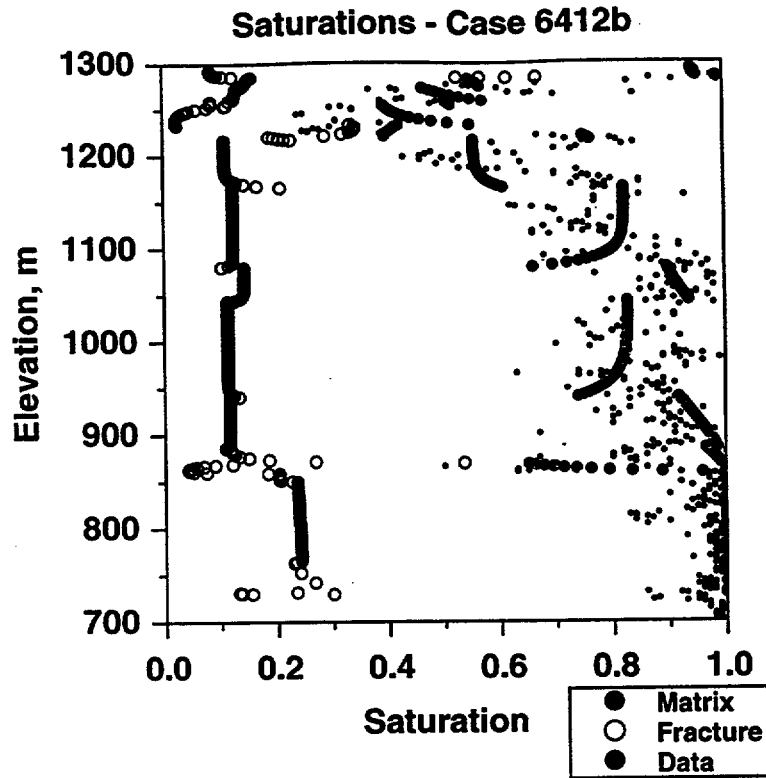
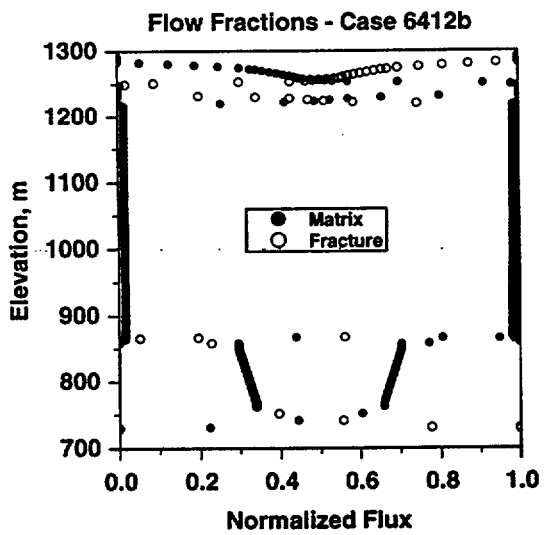


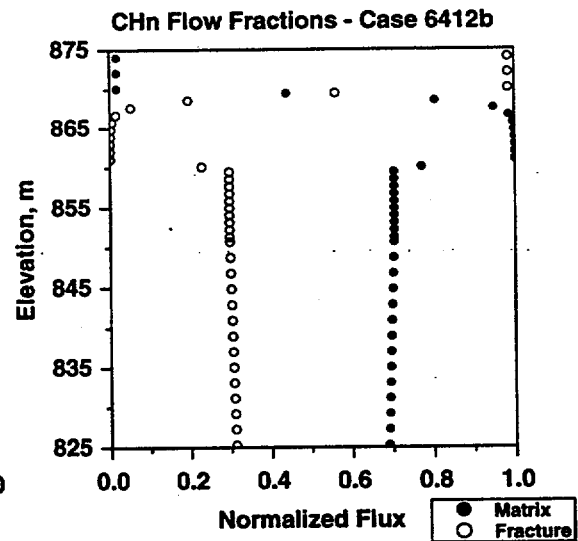
Figure 5-6. Case 6412a hydrologic simulation results for SD-9. a) matrix and fracture saturations, along with field data points; b) matrix and fracture fluxes; c) matrix and fracture fluxes, expanded scale including the vitric/zeolitic interface.



(a)



(b)



(c)

**Figure 5-7.** Case 6412b hydrologic simulation results for SD-9. a) matrix and fracture saturations, along with field data points; b) matrix and fracture fluxes; c) matrix and fracture fluxes, expanded scale including the vitric/zeolitic interface.

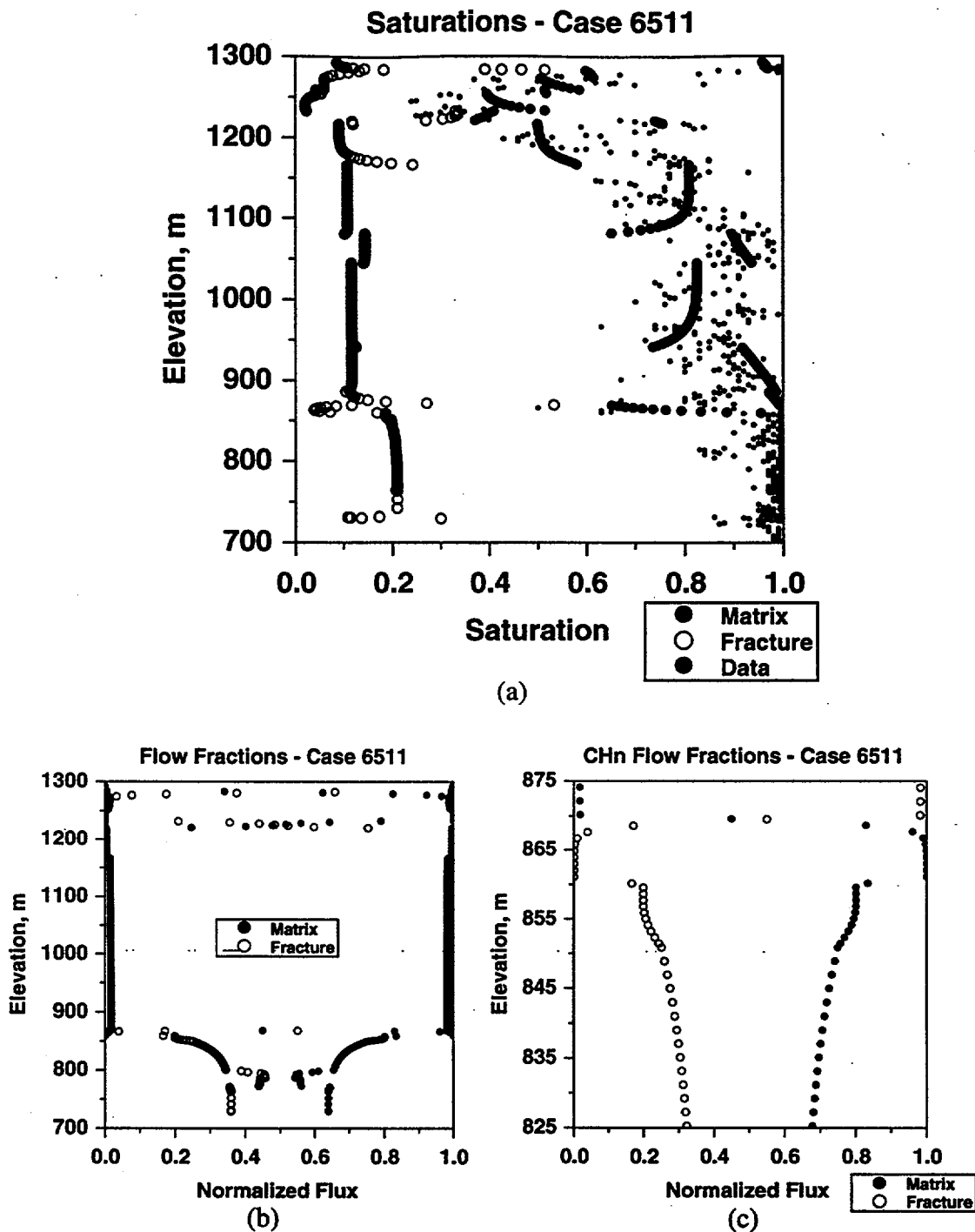
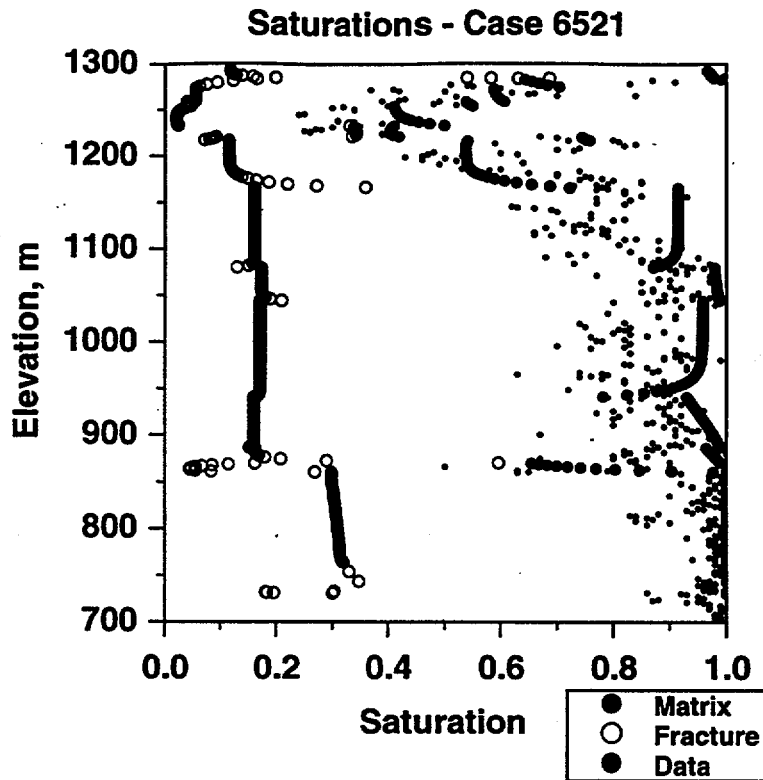
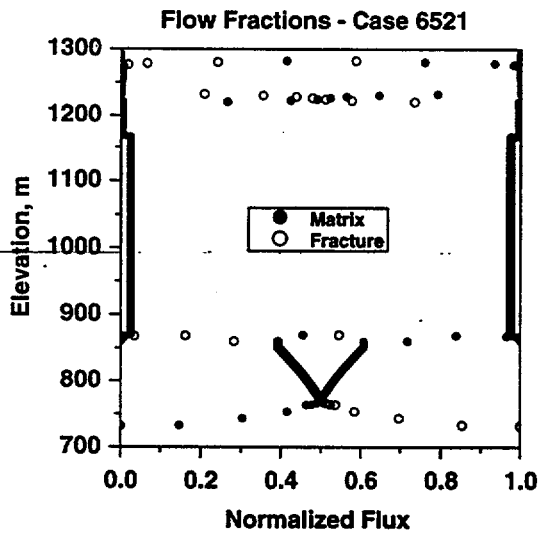


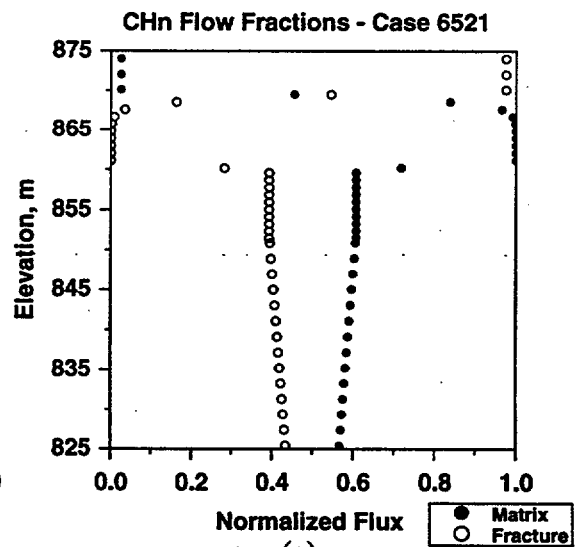
Figure 5-8. Case 6511 hydrologic simulation results for SD-9. a) matrix and fracture saturations, along with field data points; b) matrix and fracture fluxes; c) matrix and fracture fluxes, expanded scale including the vitric/zeolitic interface.



(a)



(b)



(c)

**Figure 5-9.** Case 6521 hydrologic simulation results for SD-9. a) matrix and fracture saturations, along with field data points; b) matrix and fracture fluxes; c) matrix and fracture fluxes, expanded scale including the vitric/zeolitic interface.

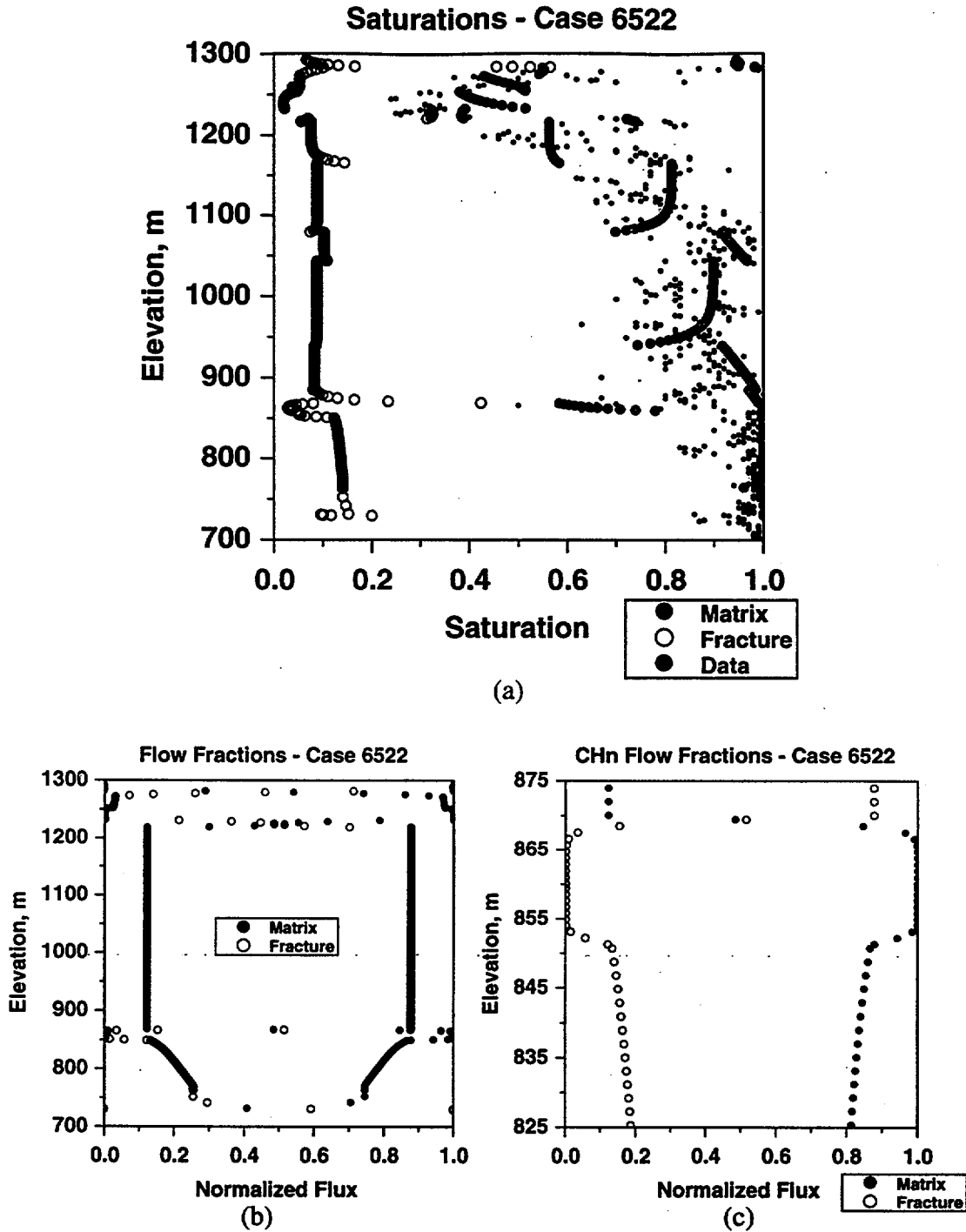


**Figure 5-10.** Case 6522 hydrologic simulation results for SD-9. a) matrix and fracture saturations, along with field data points; b) matrix and fracture fluxes; c) matrix and fracture fluxes, expanded scale including the vitric/zeolitic interface.

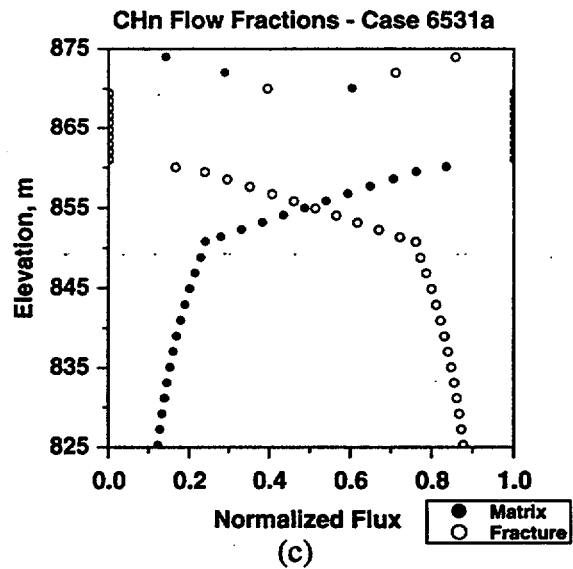
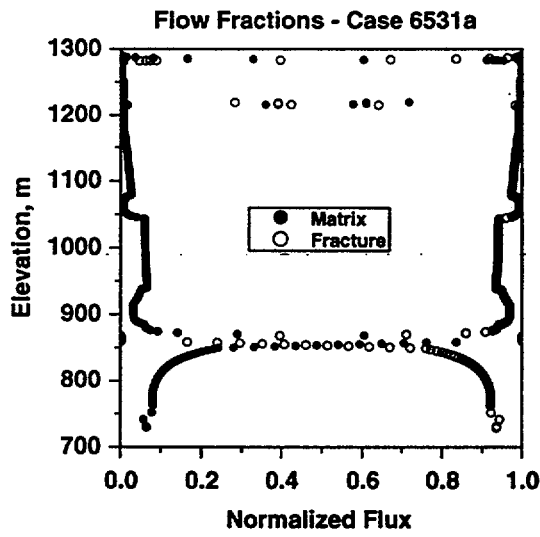
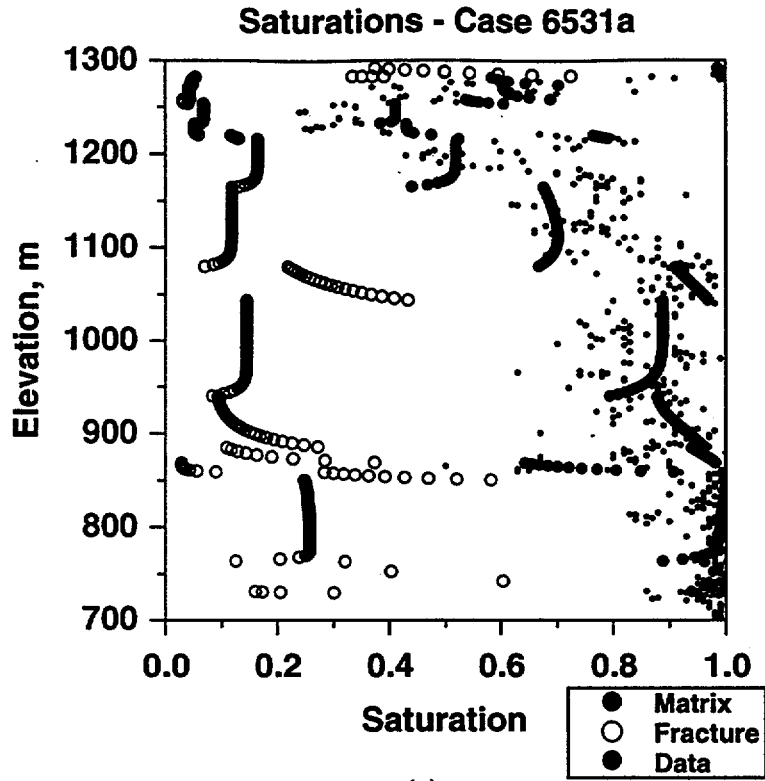
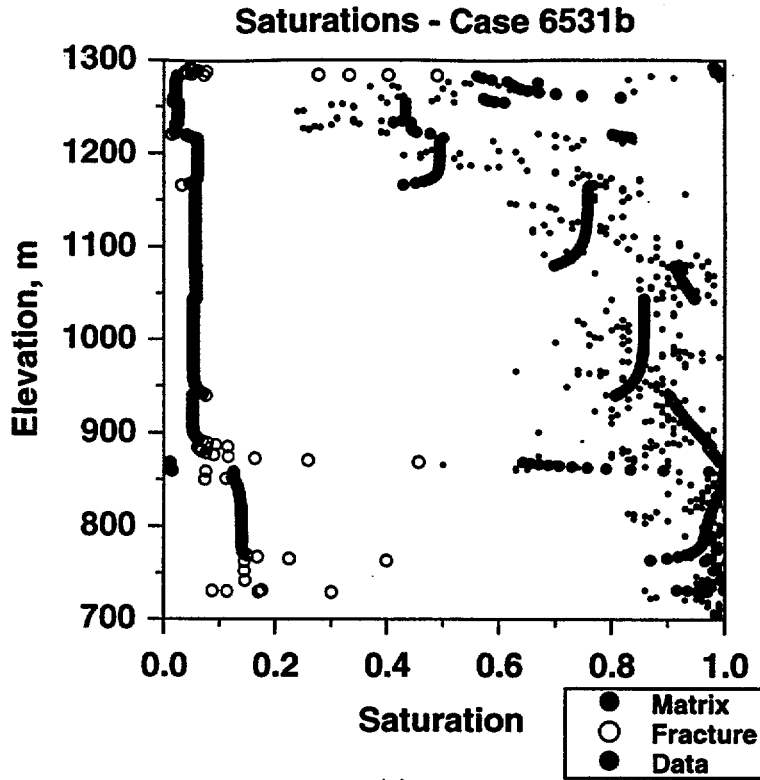
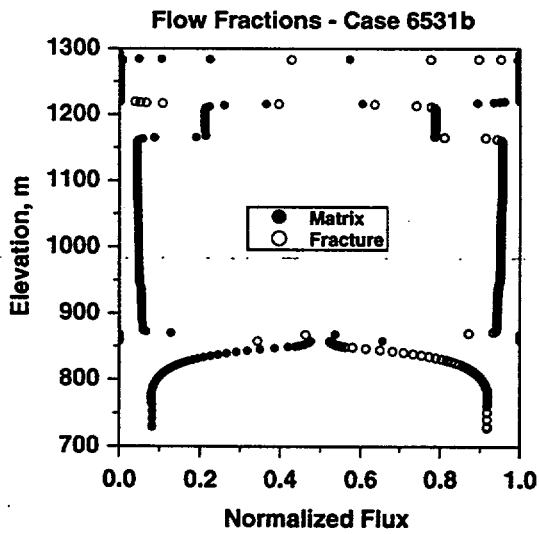


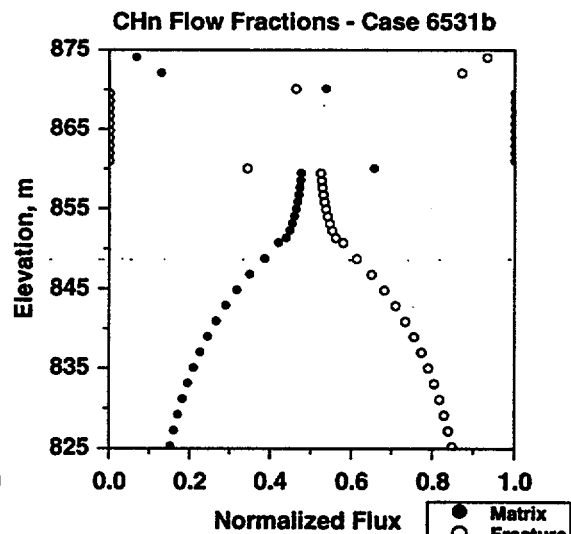
**Figure 5-11.**Case 6531a hydrologic simulation results for SD-9. a) matrix and fracture saturations, along with field data points; b) matrix and fracture fluxes; c) matrix and fracture fluxes, expanded scale including the vitric/zeolitic interface.



(a)



(b)



(c)

Figure 5-12. Case 6531b hydrologic simulation results for SD-9. a) matrix and fracture saturations, along with field data points; b) matrix and fracture fluxes; c) matrix and fracture fluxes, expanded scale including the vitric/zeolitic interface.

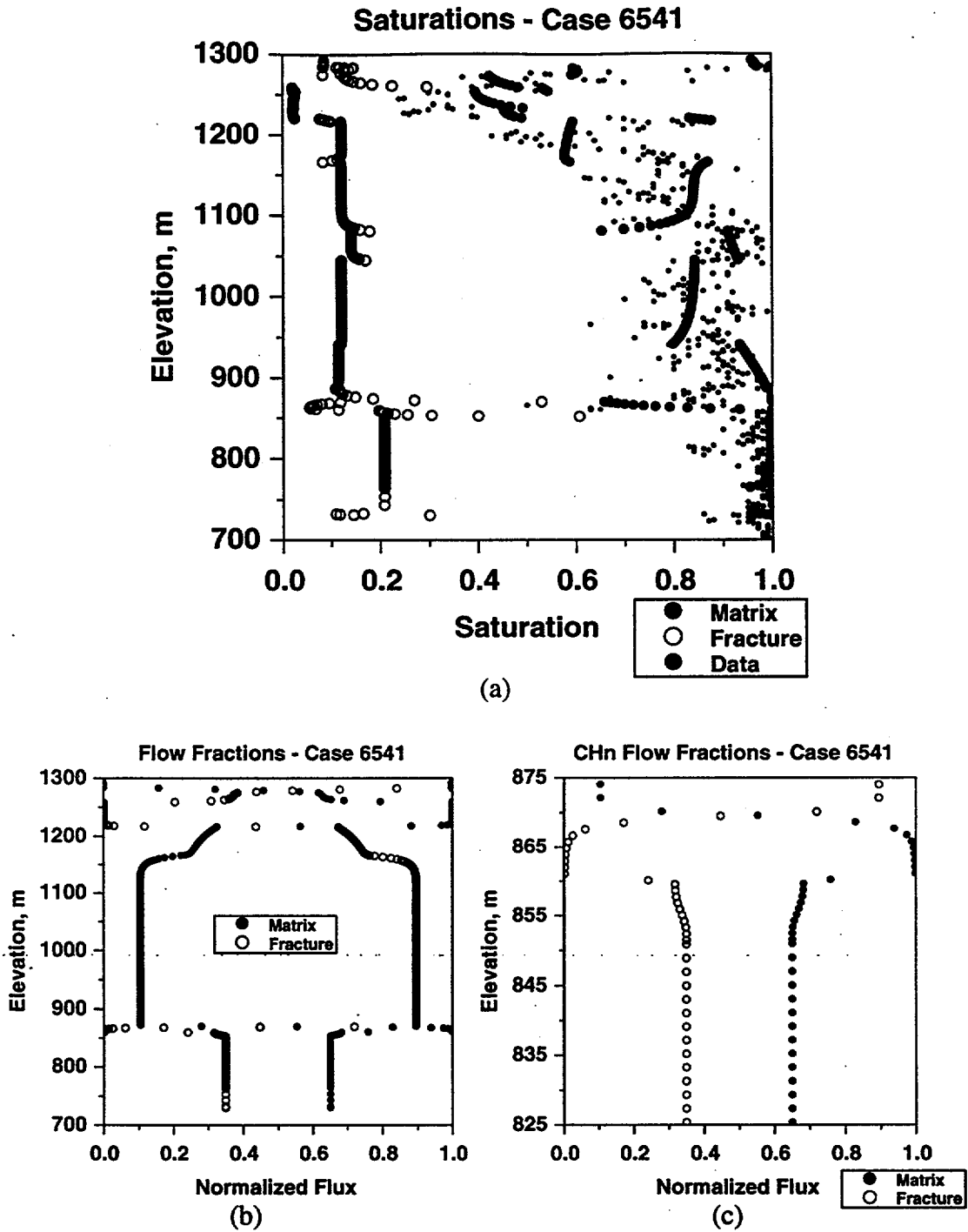


**Figure 5-13.**Case 6541 hydrologic simulation results for SD-9. a) matrix and fracture saturations, along with field data points; b) matrix and fracture fluxes; c) matrix and fracture fluxes, expanded scale including the vitric/zeolitic interface.

- matrix-dominated flow in the first vitric Calico Hills unit (shown on an expanded scale in the **c** figures); and
- differing levels of fracture flow in the zeolitic rocks comprising the remainder of the column, ranging from about 20% to 90% fracture flow, depending on the parameter set.

It is the details of flow and transport beneath the potential repository that will control radionuclide migration to the water table. Therefore, differences in flow fractions in the zeolitic rocks and the transition from matrix-dominated to an intermediate case at the vitric/zeolitic interface will exert an important influence on transport of radionuclides. We now present transport results for  $^{99}\text{Tc}$  and  $^{237}\text{Np}$  for an instantaneous release of one mole of radionuclide from the potential repository horizon at time 0. An important distinction for interpreting these breakthrough curves is that the actual release rate from the near-field environment (NFE) is expected to be much more drawn out over time. These curves are, in effect, generic breakthrough curves that define the distribution of residence times in the unsaturated zone. Given a steady-state flow assumption, the curves are a Green's function for the unsaturated-zone transport system, and can be converted to a combined NFE/UZ breakthrough curve by convolution of the Green's function with a NFE source term model. The convolution process and results are described in Chapters 8 and 10.

Figures 5-14 through 5-21 show the one-dimensional SD-9 transport results for the eight parameter sets (the **a** figures are  $^{99}\text{Tc}$ , assuming no sorption, and the **b** figures are  $^{237}\text{Np}$ , assuming sorption with a  $K_d$  value of 2.5 cc/g in the matrix of the zeolitic tuffs and 0 elsewhere). We now provide a brief discussion of each model result, using the first case to elaborate on the relevant flow and transport processes controlling the results.

### 5.5.1 Case 6412a

The  $^{99}\text{Tc}$  response curve for this case is characteristic of many of the response curves for the various parameter sets. The response curve is bimodal, with early breakthrough occurring due to fracture transport through the zeolitic rocks between the vitric CHn and the water table. The minimum residence time of about 400 years represents matrix flow and transport through this vitric unit.

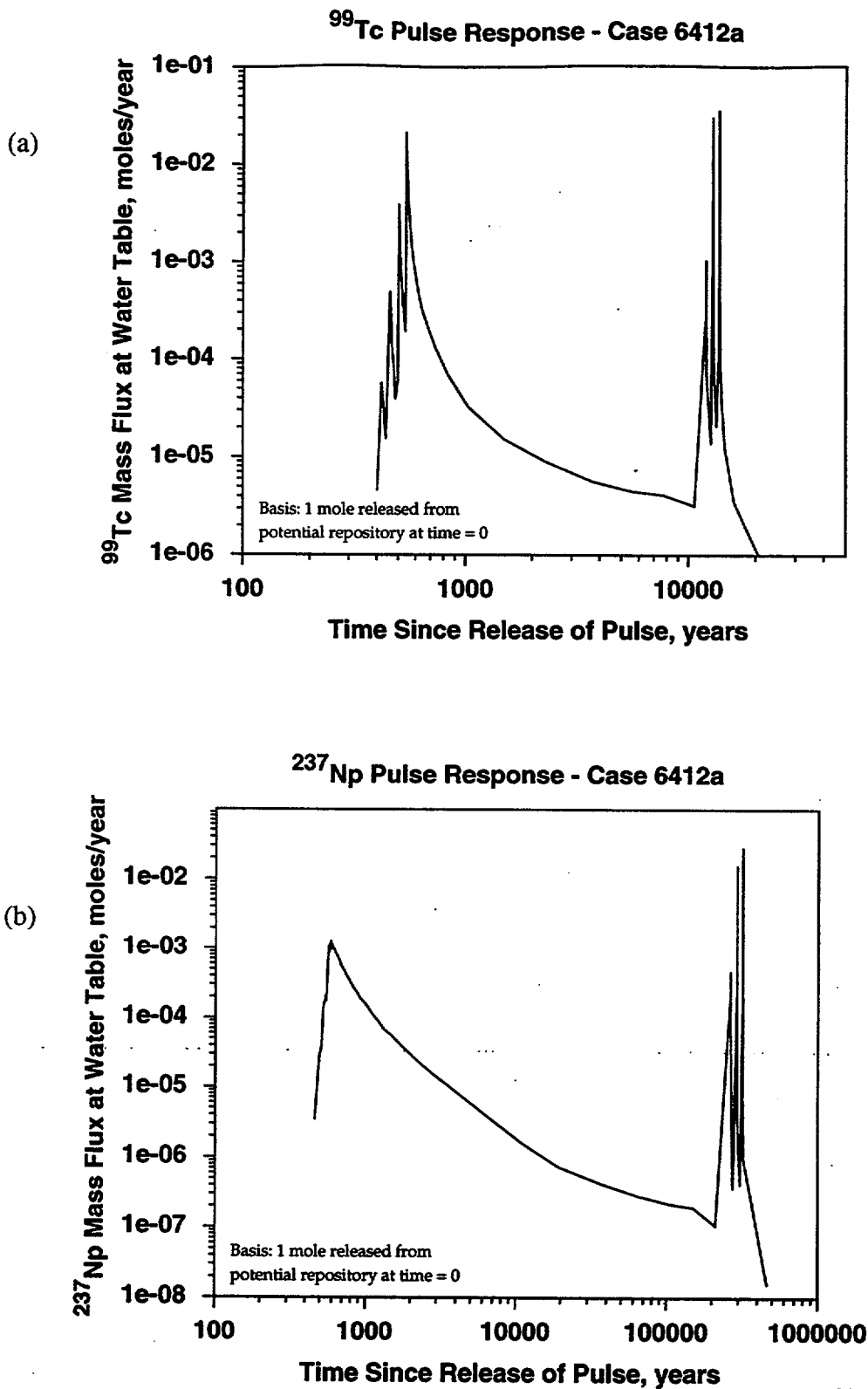


Figure 5-14. Case 6412a transport results for the one-dimensional SD-9 model. a) <sup>99</sup>Tc; b) <sup>237</sup>Np. One mole of radionuclide is released at the repository horizon at time = 0.

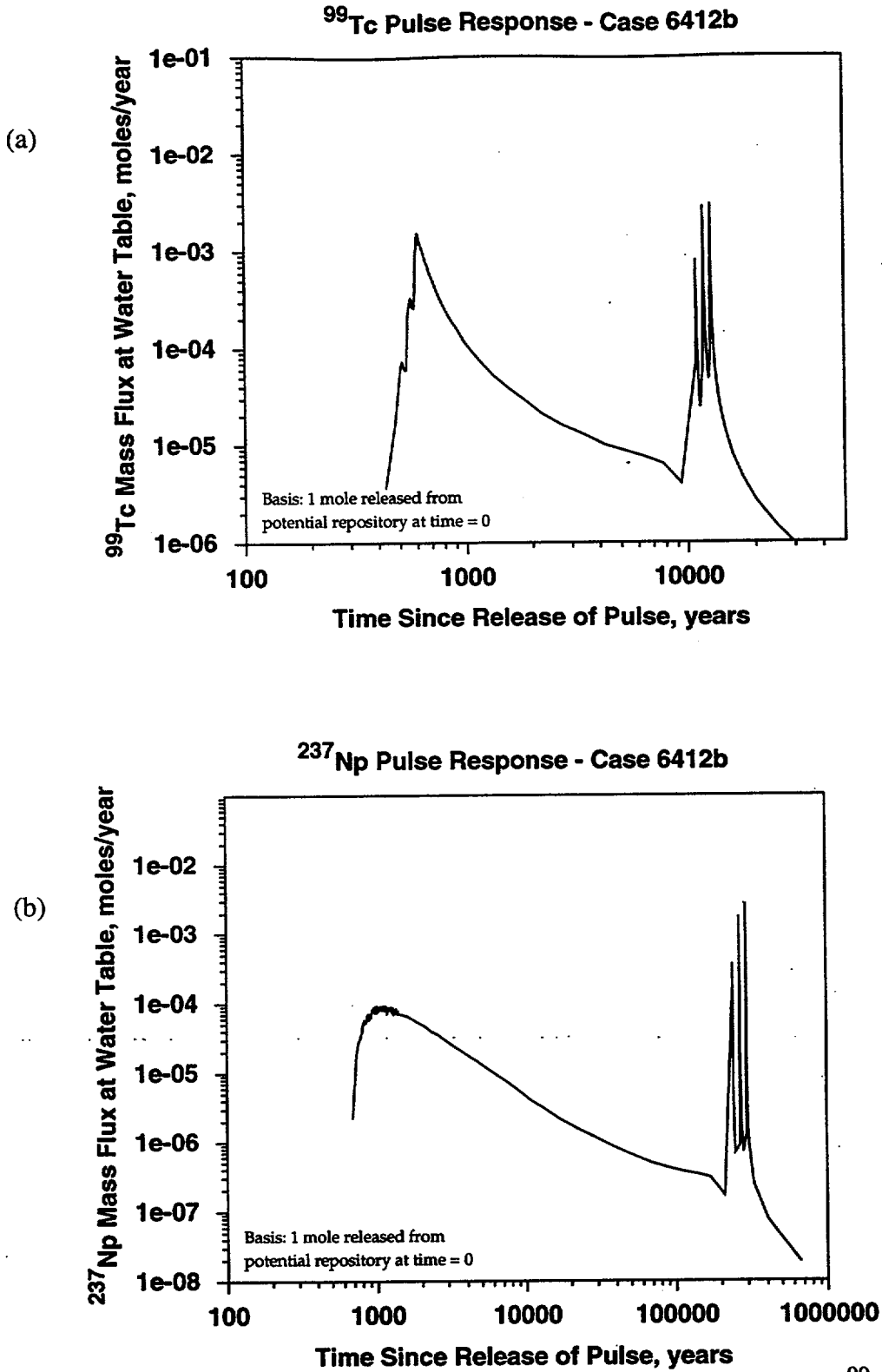


Figure 5-15. Case 6412b transport results for the one-dimensional SD-9 model. a)  $^{99}\text{Tc}$ ; b)  $^{237}\text{Np}$ . One mole of radionuclide is released at the repository horizon at time = 0.

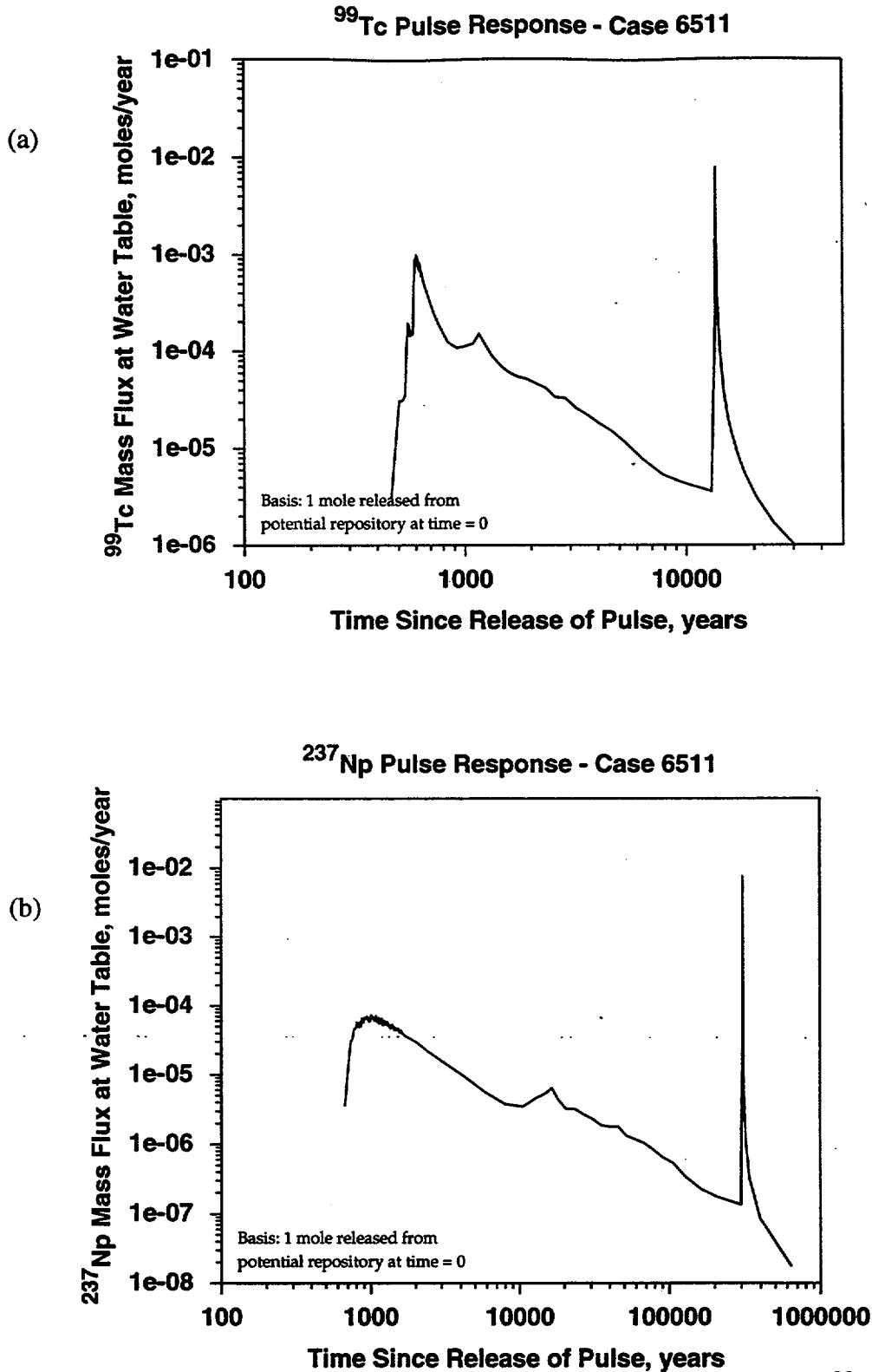
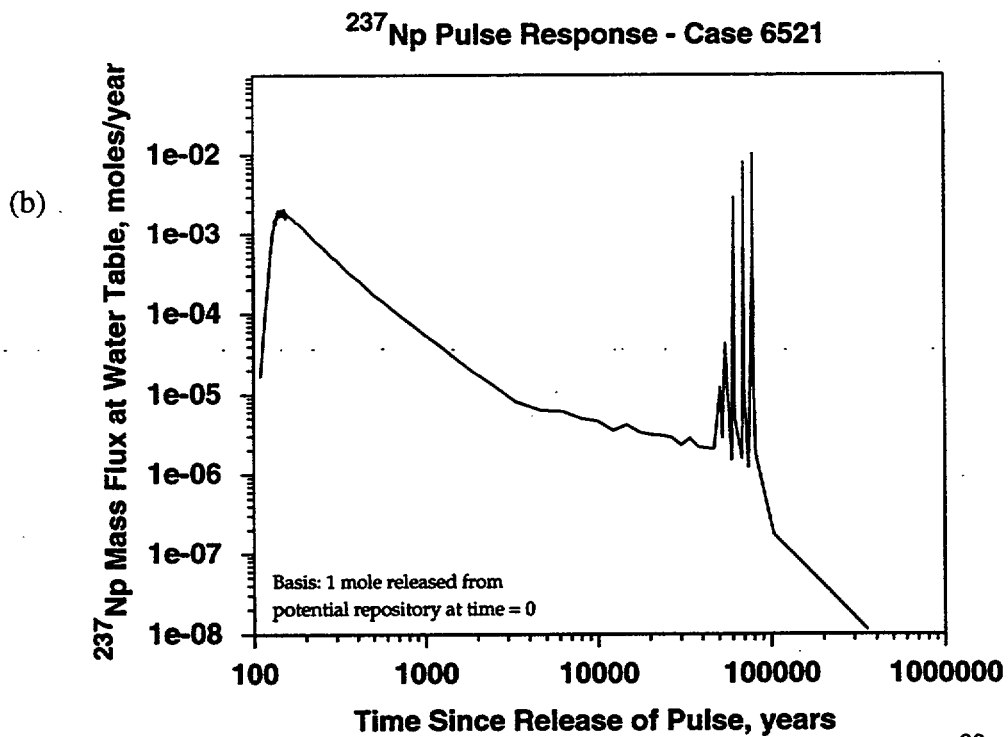
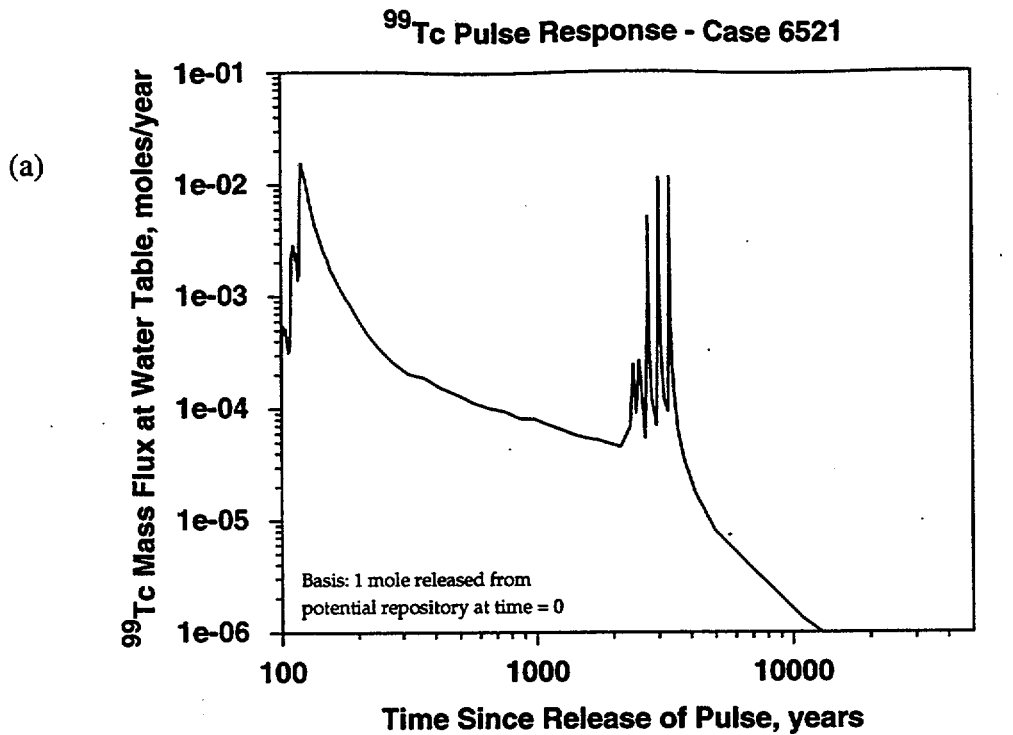


Figure 5-16. Case 6511 transport results for the one-dimensional SD-9 model. a) <sup>99</sup>Tc; b) <sup>237</sup>Np. One mole of radionuclide is released at the repository horizon at time = 0.



**Figure 5-17.** Case 6521 transport results for the one-dimensional SD-9 model. a)  $^{99}\text{Tc}$ ; b)  $^{237}\text{Np}$ . One mole of radionuclide is released at the repository horizon at time = 0.

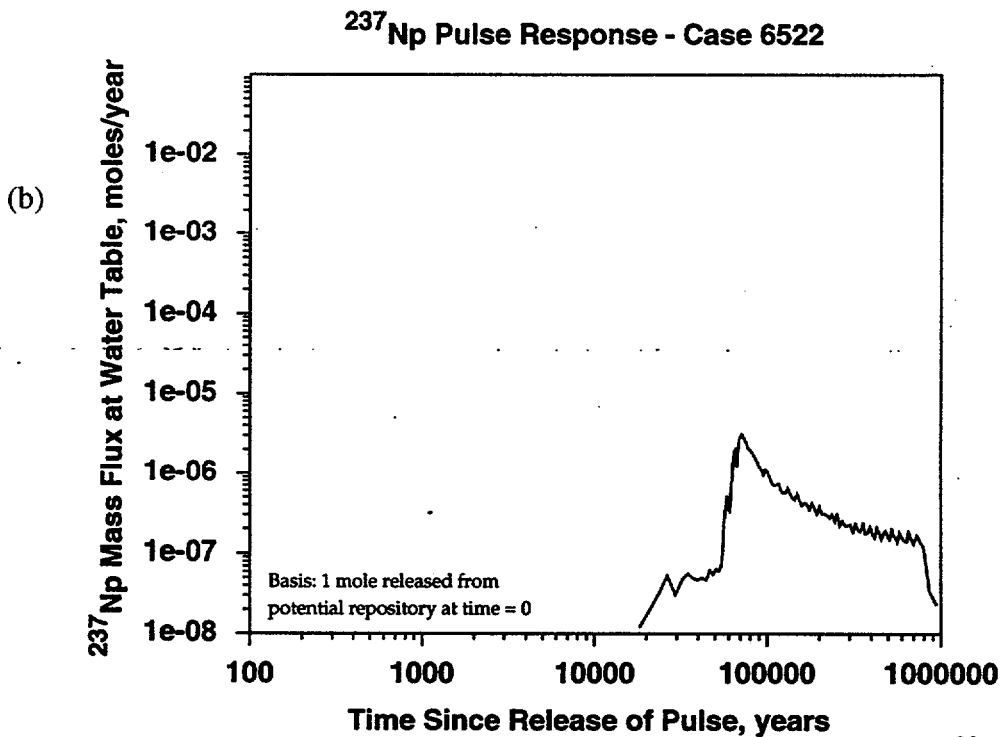
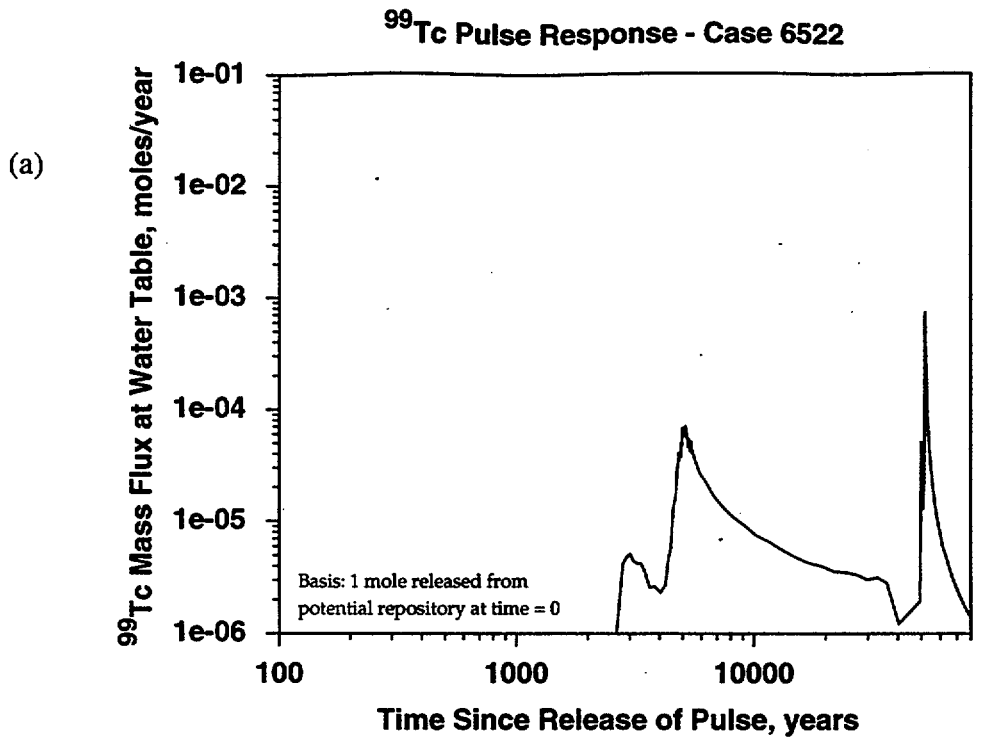
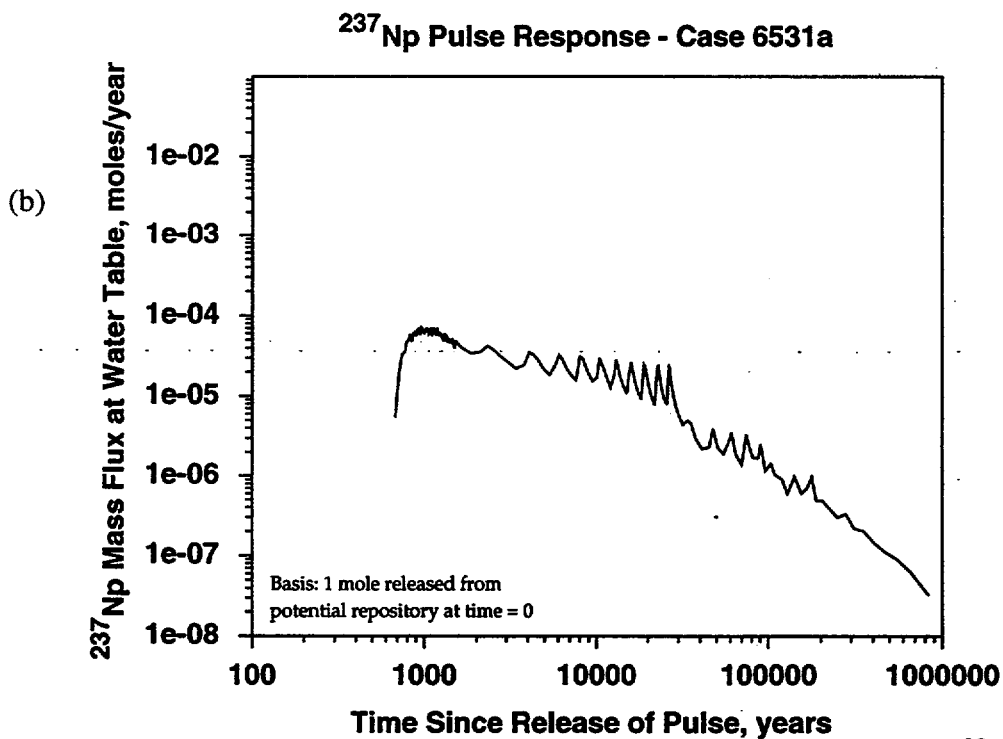
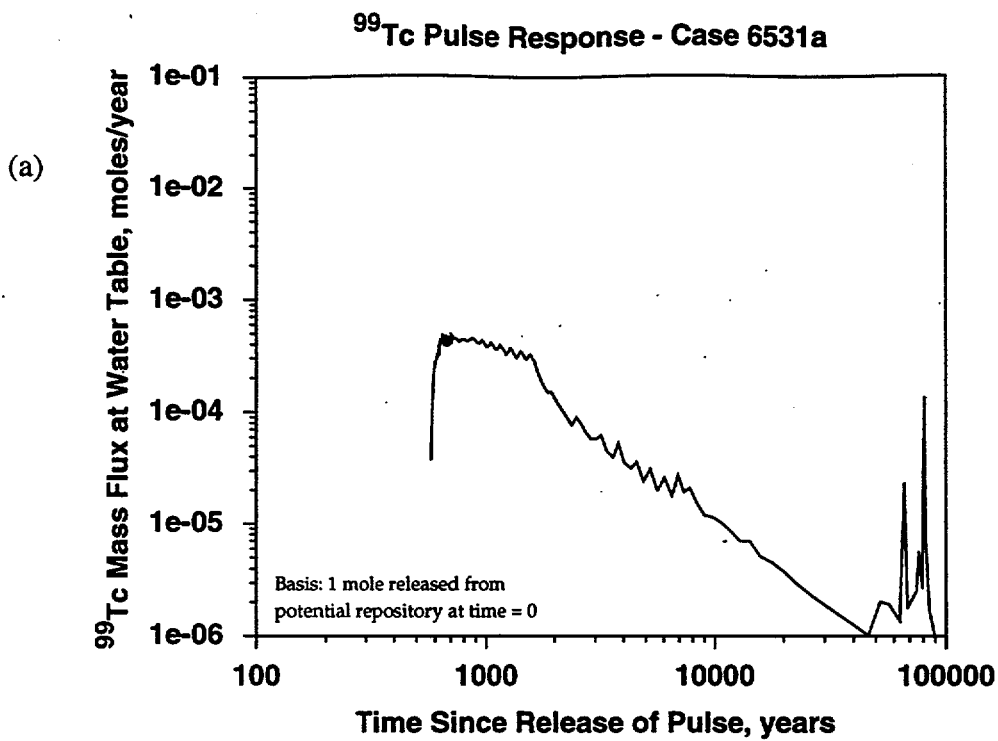


Figure 5-18. Case 6522 transport results for the one-dimensional SD-9 model. a) <sup>99</sup>Tc; b) <sup>237</sup>Np. One mole of radionuclide is released at the repository horizon at time = 0.



**Figure 5-19.** Case 6531a transport results for the one-dimensional SD-9 model. a)  $^{99}\text{Tc}$ ; b)  $^{237}\text{Np}$ . One mole of radionuclide is released at the repository horizon at time = 0.

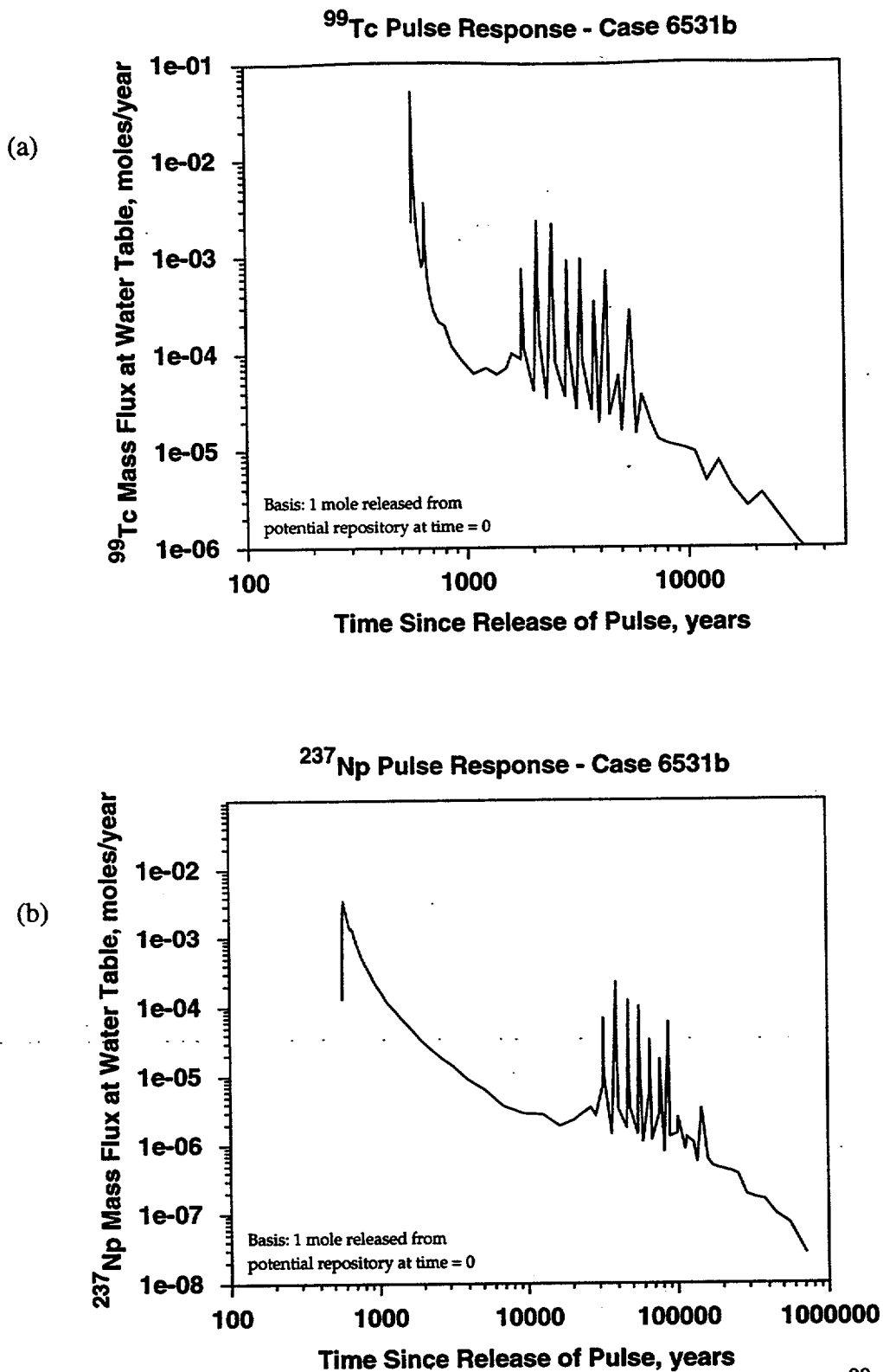


Figure 5-20. Case 6531b transport results for the one-dimensional SD-9 model. a) <sup>99</sup>Tc; b) <sup>237</sup>Np. One mole of radionuclide is released at the repository horizon at time = 0.

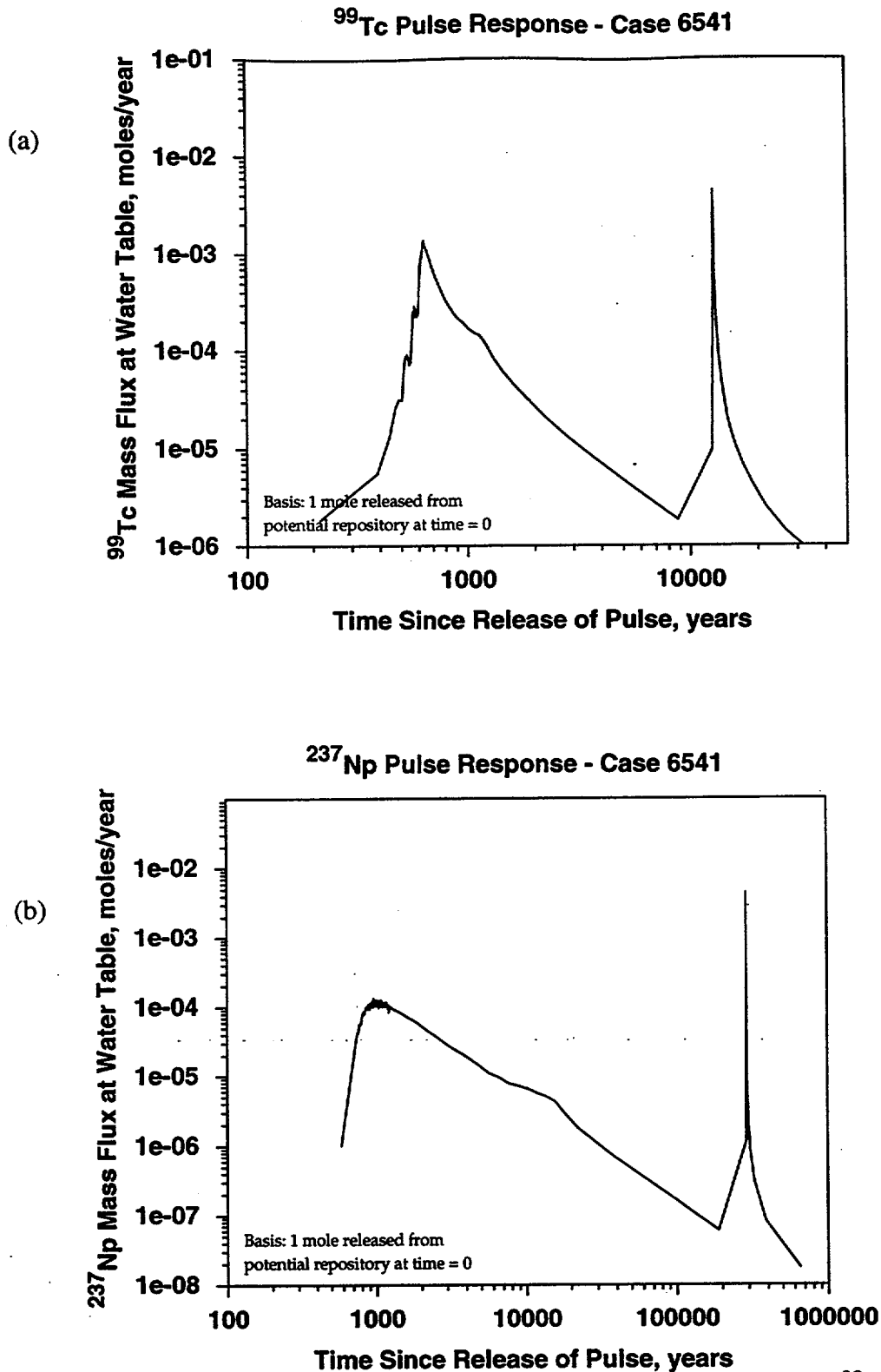


Figure 5-21. Case 6541 transport results for the one-dimensional SD-9 model. a)  $^{99}\text{Tc}$ ; b)  $^{237}\text{Np}$ . One mole of radionuclide is released at the repository horizon at time = 0.

Therefore, site-scale models must accurately include this unit to capture the early breakthrough of radionuclides properly. The spikes in the breakthrough curve are caused by several factors, which work in combination to yield the discrete pulses of arrivals at the water table. These factors include the instantaneous injection of radionuclide, the assumption of no hydrodynamic dispersion, and the one-dimensional flow field. To elaborate on the last point, all particles travel through the same locations in space, and different transit pathways arise only due to transitions from one continuum to the other at different locations. Thus the responses are spiky, but this behavior will not be present in multidimensional simulations with dispersion or reasonable NFE source-term models. The second peak in the  $^{99}\text{Tc}$  breakthrough curve is due to matrix flow in the zeolitic rocks, which results in travel times on the order of 10,000 years. The relative areas under these two peaks are proportional to the relative fluxes through the two continua in the zeolitic rocks (shown to be roughly 60% matrix flow in Figure 5-6).

The  $^{237}\text{Np}$  breakthrough curve for this case (Figure 5-14b) also exhibits bimodal behavior, but the later-arriving peak is delayed by more than a factor of 10, a consequence of  $^{237}\text{Np}$  sorption on the zeolitic rocks. The first peak is virtually undelayed in time relative to the nonsorbing  $^{99}\text{Tc}$ , despite the fact that the matrix diffusion model allows for sorption on the zeolitic rocks even for the case of fracture flow. Matrix diffusion over these time scales is relatively inefficient at delaying the arrival times of a transporting solute. Nevertheless, matrix diffusion and subsequent sorption does spread the arrival time distribution and, thus, lower the peak value for this first peak. Note that because the two radionuclides are simulated on a one-mole basis, the peak values are directly comparable. The lower peak value for  $^{237}\text{Np}$  is a consequence of matrix diffusion and sorption, even though the effect is not sufficiently large to delay the peak time. Whether this process is important to overall performance of the unsaturated-zone transport system must await multidimensional analyses incorporating a realistic NFE source term model.

### 5.5.2 Case 6412b

Transport for this case is very similar to that of case 6412a, which is not surprising given that the hydrologic parameters differ only as a consequence of a different starting condition for the LBNL parameter estimation simulation. The slight differences are due to the somewhat greater matrix flow through the zeolitic rocks for 6412b, resulting in a delay in the arrival time for the first peak and an earlier arrival for the second (greater matrix flux decreases the travel time for the matrix-flow peak).

Because the LBNL 6412 parameter set is one of the primary data sets provided to the Project, we decided to retain at least one of these cases for multidimensional transport simulations. However, this analysis shows that there is no reason to use both sets, given the minor differences in the results. In Bodvarsson et al. (1997) LBNL performed an additional analysis in which they adjusted the parameters in the CHn and underlying units to obtain a better fit to the data in the three-dimensional site-scale flow model. They used 6412b as the starting point for this analysis. Therefore, to allow us to also test that adjusted parameter set along with the base-case set, we select case 6412b to carry forth in the multidimensional transport model calculations.

### 5.5.3 Case 6511

This parameter set is based on the same fracture/matrix interaction model as in the 6412 cases, but the initial guess of the reduction factor was different in the LBNL parameter estimation simulation. Figure 5-16 shows the transport results which exhibit similar behavior to that of case 6412b, though some differences can be seen. Examining the flow fractions in the CHn units for this case (Figure 5-8 b and c), we note that the transition to the eventual matrix flow fraction of 0.65 occurs more gradually. This effect could perhaps give rise to a qualitatively different response under different conditions, such as during transient flow or a different infiltration rate scenario. However, given the similarity of the model results and conceptualization of the fracture/matrix interaction process to that of 6412b, we decided not to use case 6511 in further simulations.

### 5.5.4 Case 6521

This case assumed an infiltration rate of 18 mm/y, five times that of the base case. The consequence to transport is straightforward and well known. Figure 5-17 shows an earlier arrival time for both peaks (and for both radionuclides) due to the faster flow velocities. A corollary to faster travel times is higher peak values, compared to the previous cases considered. Ordinarily, one would also expect the fraction of mass traveling through the fractures of the zeolitic rocks to increase, giving rise to a higher first peak in the bimodal breakthrough curves. This effect is true only to a limited extent in this simulation. The reason is illustrated in the flow fraction plot in Figure 5-9b, which shows a gradual decline in matrix flux with depth down to a 50% value. This parameter set apparently required a higher value for zeolite matrix permeability to obtain a good fit to the data, thus allowing half the fluid to travel through the matrix even at 18 mm/y. This effect must have been controlled by fits at wells other than SD-9, for the following reason. The model and the data both show almost complete saturation throughout the zeolitic rocks. The rationale for an inversion code raising the matrix permeability would be to achieve a better fit, but at complete saturation of both data and model, there would be no point in the code changing the permeability. Therefore, the higher permeability must be controlled by data at other wells.

Regarding the use of this parameter set in multidimensional simulations, we have chosen a somewhat different approach to studying the influence of infiltration rate sensitivity. In Section 8.7, we show that varying the infiltration rate for the same parameter set results in rather small changes in matrix saturation. Therefore, we use the parameter sets developed at the base infiltration rate as the starting point for simulations but assume that increases in the infiltration rate by a factor of 3 has an insignificant influence on the quality of the model calibration. Therefore, we choose not to carry forth this parameter set to the multidimensional simulations, instead assuming that hydrologic parameter sets developed for the base infiltration map apply to moderately higher or lower infiltration rates.

### 5.5.5 Case 6522

This case achieved the fit at 0.7 mm/y at SD-9, five times lower than the base infiltration value. Figure 5-18 shows the transport results. Travel times are much greater for both  $^{99}\text{Tc}$  and  $^{237}\text{Np}$ , and the relative mass arriving in the first peak is reduced relative to the base infiltration case, in keeping with the predicted flow split in the zeolitic rocks of about 80% matrix flow (Figure 5-10).

In contrast to Case 6521 (the 5X higher infiltration case), we decided to incorporate this parameter set into our multidimensional calculations. One result of our environmental isotope and water chemistry modeling studies is that a somewhat lower infiltration rate than the base-case infiltration map is consistent with the chemical data sets. This result implies that a parameter set developed under a lower infiltration rate scenario should be studied more thoroughly. We therefore use this parameter set in the sensitivity study of infiltration rate in multiple dimensions, assuming it to be an appropriate alternative at lower flux values.

### 5.5.6 Case 6531a

This case, and case 6531b, use the upstream saturation weighting scheme in all layers. For the parameter set provided for this model, matrix flow decreased to about 10% of the flux within the first several meters of the zeolitic CHn (Figure 5-11). The impact on the breakthrough curves for the radionuclides is dramatic (Figure 5-19). Most of the radionuclide mass travels through the CHn and underlying units in fractures. The late-arriving mass of  $^{99}\text{Tc}$  that does travel through the zeolitic matrix has a travel time in excess of 50 ky due to the low flux through the matrix, but this constitutes only a small portion of the released mass.  $^{237}\text{Np}$  has a similar breakthrough-curve shape, with somewhat lower values caused by matrix diffusion and sorption to zeolites. Nevertheless, like  $^{99}\text{Tc}$ ,  $^{237}\text{Np}$  breaks through early (less than 1 ky) and remains at about this level for about 30 ky. This level response is caused by transition from matrix flow to mostly fracture flow in a ten-meter interval, rather than abruptly. This result means that a variety of different transition depths exist, and each of these transport pathways has a different residence time in the zeolitic matrix before transitioning to fracture flow.

Since this fracture/matrix interaction model is different than the others studied, and because the one-dimensional breakthrough curve appears to have a different character than the others, we include one of the 6531 cases in the multidimensional analyses. We chose the following case, 6531b, but in fact, there is little of importance to separate the two cases, and thus, either one could have been selected.

### **5.5.7 Case 6531b**

The breakthrough curves for this case are shown in Figure 5-20. At first glance, they differ from that of case 6531a in terms of the high initial spike of radionuclide. However, spikes of short duration play little role in the determination of breakthrough at the water table or the accessible environment for actual release scenarios (as opposed to instantaneous releases). Therefore, the two cases actually are similar, and 6531b was selected for further study. One remaining issue related to these cases is the reason for the dramatically lower flux through the matrix of the zeolites than for the other cases studied. It is not clear why this should be so, given that for the first CHn vitric and zeolite layers, the saturation weighting scheme is the same as for case 6541 (below), yet that case yielded more matrix flow through the zeolites. In cases 6531a and b, the inversion appears to have settled on property values that yield slightly lower matrix saturations in the zeolites at the expense of more fracture flow. This point is potentially important to performance, and thus, the details of the inversion to obtain property values for this case should be examined in greater detail.

### **5.5.8 Case 6541**

The breakthrough curves for this case (Figure 5-21) were discussed previously, as this parameter set was used for comparison to TOUGH2 simulations. Because this form of weighting scheme (upstream saturation in the nonwelded units and upstream relative permeability in the welded units) was deemed appropriate for PA analyses, we select it also for further study. However, we note that the behavior of the flow fractions and radionuclide breakthrough curves are similar to several other cases presented above.

## Property Sets

The results of the screening analyses are summarized in Table 5-3, which is essentially a

**Table 5-3. Parameter sets to include in multi-dimensional transport simulations. Parameter sets carried forward are unshaded in the table.**

Parameter Set	Location in Bodvarsson et al. (1997)	Description
6412a	Chapter 6, Table 6.4.1-2, first column	DKM, 3.6 mm/y, const. reduction factor, init. Fm=0.667
6412b	Chapter 6, Table 6.4.1-2, second column	DKM, 3.6 mm/y, const. reduction factor, init. Fm=0.492
6412c	Same as 6412b except as specified in Table 5-2	DKM, 3.6 mm/y, const. reduction factor, init. Fm=0.492, CHn props. revised in 3D runs
6511	Appendix A-6, Table 6.5.1-1	DKM, 3.6 mm/y, const. reduction factor, init. Fm=0.492, init. red. factor=0.05
6521	Appendix A-6, Table 6.5.2-1	DKM, 18 mm/y, const. reduction factor, init. Fm=0.492
6522	Appendix A-6, Table 6.5.2-2	DKM, 0.72 mm/y, const. reduction factor, init. Fm=0.492
6531a	Appendix A-6, Table 6.5.3-1, first column	DKM, 3.6 mm/y, upstream S reduction factor, init. Fm=0.492
6531b	Appendix A-6, Table 6.5.3-1, second column	DKM, 3.6 mm/y, upstream S reduction factor, init. Fm=0.667
6541	Appendix A-6, Table 6.5.4-1	DKM, 3.6 mm/y, upstream S reduction factor (nonwelded), upstream RLP reduction factor (welded)
6541b	Based on Appendix A-6, Table 6.5.4-1	Same as 6541 except no upstream S reduction factor is used in PTn only. This set is used in Chapter 6
6542	Appendix A-6, Table 6.5.4-2	DKM, 3.6 mm/y, upstream S reduction factor (nonwelded), upstream REP reduction factor (welded), pin25 fracture flow
6551	Appendix A-6, Table 6.5.5-1	ECM, 3.6 mm/y, init. Fm=0.667

repeat of Table 5-2, except that the shading denotes that a parameter set is not being carried forward to the multidimensional simulations. One additional parameter set, Case 6412c, is included and identified for further study even though there were no one-dimensional simulations. This case is

equivalent to case 6412b in all units except in several of the CHn and underlying units. Bodvarsson et al. (1997) performed a three-dimensional simulation using case 6412c and found that better matches in three dimensions could be obtained by changing these properties somewhat. Because the units in question are below the potential repository, this adjustment could be important for transport, and thus we include them as a separate case to examine the effects.

### 5.6 Conclusions

---

This chapter summarizes the hydrologic property sets provided by LBNL in the site unsaturated-zone flow model (Bodvarsson et al., 1997), along with modifications tested in the present study for their impact on predicted performance. Since it is not feasible to complete transport sensitivity analyses in multiple dimensions for every parameter set in the LBNL milestone, as well as test variations of these as sensitivity studies, an initial screening was performed to determine which parameter sets are yield significantly different performance predictions.

Steady state, dual permeability fluid flow fields were generated for each property set, after which particle tracking transport simulations of  $^{99}\text{Tc}$  and  $^{237}\text{Np}$  from the repository to the water table were computed. Because transport of radionuclides escaping the repository is the subject of the study, the emphasis is on predicted flow and transport below the repository horizon. Parameter sets may differ in their predictions of hydrologic conditions above the repository; these possible differences are addressed in Chapter 6.

Despite the potentially large spectrum of possible behaviors for different hydrologic property sets, the most striking result of this screening study is the similarity of the flow and transport results. In all cases, fracture-dominated flow in the TSw transitions to almost completely matrix flow in the vitric Calico Hills unit at SD-9. Then, at the transition from the vitric to zeolitic tuff, significant fracture flow through the zeolitic tuffs is predicted for every parameter set, even at the 3.6 mm/y infiltration rate assigned at SD-9. The permeability of the zeolitic tuffs is too low to

## Property Sets

---

support the 3.6 mm/y infiltration in the matrix, thus resulting in the fracture flow, which will be even more pronounced in high flux areas within the potential repository area. There are subtle differences from one parameter set to the next which are identified and used as the criteria for selecting sets for the multi-dimensional simulations.

This study also served as a code validation check by comparing the results of FEHM and TOUGH2 for the one-dimensional column. Steady state flow fields were generated with each code, and the flow fields were used by FEHM to compute particle tracking breakthrough curves. The saturation profiles agreed closely. Transport of  $^{99}\text{Tc}$  differed somewhat due to a slight, predicted difference in the flow split between fractures and matrix in the two cases. More importantly, the transitions from matrix flow to partial fracture flow at the vitric/zeolitic interface is predicted to occur abruptly above the interface in FEHM and more gradually within the first zeolitic grid block in TOUGH2. Matrix flow within the zeolite in TOUGH2 gave rise to significantly delayed first arrival of  $^{237}\text{Np}$  at the water table. We attribute the TOUGH2 behavior to the combination of upstream weighting of the absolute permeability and the large size of the first zeolitic grid block; FEHM calculations using this same weighting scheme yielded results that approached those of the TOUGH2 run. We therefore recommend that in mountain-scale flow and transport simulations, the absolute permeability be harmonically weighted, and/or the grid be more finely discretized near interfaces of contrasting flow and transport properties.

## Chapter 6 - Environmental Isotopes and The Hydrologic System

### 6.1 Abstract

---

In this chapter, we examine the role of studies coupling environmental isotope data and numerical modeling in identifying flow and transport processes as well as constraining the property sets used to model them. Starting with various hydrologic property sets from LBNL, which are all based on fits matching matrix fluid saturation and capillary pressure (Bodvarsson et al, 1997), we perform a series of transport studies with one-, two-, and three-dimensional transport models and examine how well the isotopic data are matched. The most significant finding in this study is that minor changes in hydrologic parameters lead to different flow distributions in the PTn matrix and fractures which, in turn, affect the predictions of whether fast paths exist between the surface and potential repository horizon. Since multiple property sets were developed by Bodvarsson et al. (1997), reducing the uncertainty in property set choice based on environmental isotope transport observations and modeling may have significant implications on repository design and performance modeling. For example, if fracture flow in the PTn is ubiquitous, then repository design may need to account for periodic high fluxes resulting from transient infiltration events that are not damped in the PTn matrix. Also, sustained PTn fracture flow leads to a greater incidence of predicted bomb-pulse  $^{36}\text{Cl}/\text{Cl}$  ratios in the TSw and CHn, even away from fault zones. With current material property estimates, episodic infiltration events (precipitation-related infiltration events lasting on the order of days) are more likely to be damped in regions of thicker PTn. The direct correlation of the PTn's damping potential to the magnitude of the infiltration rate is not straightforward. Fully assessing whether episodic infiltration is a significant concern for repository design and performance assessment requires a better understanding of the hydrologic properties and fracture flow potential of the PTn.

The environmental isotope data coupled with transport modeling also serve to evaluate alternative conceptual models and the infiltration estimates to which the parameters are calibrated. One alternative conceptual model suggests that all elevated  $^{36}\text{Cl}/\text{Cl}$  ratios found in the ESF represent very recent water. The current LBNL hydrologic properties tend to support this model more so than previous property sets in that simulated fracture flow in the PTn is more readily initiated and sustained. With the current infiltration map and the corresponding material properties, the simulations in this section show that more rapid transport from ground surface to the ESF should be occurring along the southern portion of the ESF than in the North. To the contrary, however, the data indicate that more early arrivals occur in the North, particularly in faulted regions. In fact there is virtually no evidence for fast travel to the ESF beyond station 50+00.

### 6.2 Software and Data QA Status

---

The FEHM code is used to perform all flow and transport calculations in this report. The code is qualified in accordance with Los Alamos quality assurance requirements and is documented in (Zyvoloski et al, 1992, 1995a, 1995b). The QA status of the data used in this report is shown in Table 6-1. The GEOMESH/X3D grid generation tool kit, (Gable et al., 1995, Gable et al., 1996, Trease et al., 1996) is non-Q with respect to YMP and Los Alamos quality assurance requirements. However, version control software tracking procedures identical to those used for the Q code FEHM are followed. GEOMESH/X3D utilizes well established procedures to insure robust mesh generation results and to insure traceability of changes to the software. A suite of test problems has been developed and all new releases are verified against the test suite.

Table 6-1. QA Status of Data used in this Chapter			
REFERENCE	Q Status	DTN	COMMENT



## Environmental Isotopes and The Hydrologic System

<b>Flint et al., 1996,</b> Conceptual and numerical model of infiltration for the Yucca Mountain Area, Nevada", USGS WRIR MOL 19970409.0087	Q	GS960908312211.003/ NA	USGS DTN 3GUI623M
<b>Levy et al., 1997,</b> "Investigations of Structural Controls and Mineralogic Associations of Chlorine-36 fast pathways in the ESF, Yucca Mountain Project milestone report SP2301M4	Q	LASL831222AQ97.001	
<b>Yang et al., 1992,</b> "Flow and Transport Through Un-saturated Rock - Data From Two Test Holes, Yucca Mountain, Nevada, proc. Third International Conference on High-Level Radioactive Waste Management, Las Vegas, NV.	Q		
<b>Yang, et al., 1996,</b> Interpretations of Chemical and Isotopic Data From Boreholes in the Unsaturated Zone at Yucca Mountain, Nevada, USGS Water-Resources Investigations Report WRIR 96-4058	Q		
<b>Yang et al., 1997,</b> Hydrochemical Investigations and Geochemical Modeling in Characterizing the Unsaturated Zone at Yucca Mountain, Nevada, (In Preparation).	non-Q	Indeterminate	Not Available Yet

### 6.3 Introduction

Direct measurement of unsaturated zone percolation flux is difficult if not impossible, especially at depths greater than a few meters. To date, no such measurement has been made at Yucca Mountain. Inferring unsaturated zone flux from physical measurements of saturation and water potential is also extremely difficult, especially in multiporosity systems such as fractured volcanic tuff. Likewise, dissolved solute migration processes have not been measured in the unsaturated zone at Yucca Mountain, although the Project is now planning an unsaturated-zone transport test. In saturated-zone studies, tracer tests are often used to help quantify physical and chemical attributes of the system as well as the groundwater flux. However, performing liquid

phase tracer tests in fractured, unsaturated porous media is not a simple task, especially at the scales of interest in the site-scale characterization program of Yucca Mountain. Fortunately, there are naturally occurring environmental isotopes that, if considered properly, provide important insights into the system characteristics. Further, they capture a time scale that cannot be addressed with conventional tracer tests. An additional utility in evaluation of environmental isotopic tracer tests is the man-made signal associated predominantly with the atmospheric testing of more than 70 nuclear weapons in the Pacific Proving Grounds between 1952 and 1958 (Glasstone, 1962). The  $^{36}\text{Cl}/\text{Cl}$  ratio in fallout in 1957 was about 400 times greater than the present ratio of  $500 \times 10^{-15}$ , thus providing the "bomb-pulse". Significantly elevated ratios of  $^{36}\text{Cl}/\text{Cl}$ ,  $^{14}\text{C}$ ,  $^{99}\text{Tc}$ , and tritium associated with the atmospheric weapons testing are generally referred to as bomb-pulse signals and their presence in subsurface samples indicate travel from ground surface to the sample location in less than 50 years.

Recent efforts to characterize the hydrologic properties of the various units at Yucca Mountain have involved laboratory measurements of porosity, permeability, and characteristic curves by Flint (1996), air permeability tests (Bodvarsson et al., 1996; Le Cain and Patterson 1996), and numerical modeling to match measured saturations and gas phase pressure response (Bodvarsson et al., 1996, 1997). Although extremely beneficial in characterizing matrix material properties, these studies do not capture the "bulk response" of the system, particularly the combined influence of fracture-matrix interactions on transport processes in the liquid phase. For that reason, the environmental tracer studies described here serve to validate and enhance our conceptual and operational model of flow and transport in Yucca Mountain.

### 6.3.1 Implications

This study demonstrates that different hydrologic properties which yield similar simulations of saturation may lead to significantly different predictions of transport rates. Simulated transport times for solutes through the PTn range from several tens of years to tens of thousand years, with differences in the percent of solute traveling along the fastest pathways

depending on which parameter set is used. Environmental isotopes and conservative ions help identify both whether fast pathways exist and the age of sampled porewaters away from fast pathways, thus providing a useful tool for narrowing the field of possible parameter sets for hydrologic characterization, particularly when the difference in parameter sets is the method of representing fracture-matrix interactions. In conjunction with transport modeling, these data also prove useful in evaluating infiltration estimates.

### 6.4 Background

---

#### 6.4.1 Previous Chlorine-36 Studies at Yucca Mountain and Their Implication for Flow and Transport Modeling

Investigations of the significance of  $^{36}\text{Cl}$  data for identifying appropriate numerical model formulations for flow and transport processes in the unsaturated zone at Yucca Mountain were initially reported by Robinson et al. (1995). That report showed that only with the dual permeability model formulation could the observed rapid transport of bomb-pulse  $^{36}\text{Cl}$  to the PTn be simulated. With the equivalent continuum model, all of the bomb-pulse stayed in the upper TCw. Also, Robinson et al. (1995) demonstrated that infiltration rates closer to those estimated by Flint et al. (1996), which average about 5 mm/year over the site-scale model domain, could be used with the dual permeability model and still simulate matrix saturations consistent with those Wittwer et al. (1995) achieved using an equivalent continuum formulation and infiltration rates on the order of 0.1 mm/yr.

The first implications of the  $^{36}\text{Cl}$  studies coupling Exploratory Studies Facility (ESF) sample analysis with flow and transport modeling were reported by Fabryka-Martin et al. (1996a). These studies were later elaborated on by Fabryka-Martin et al. (1996b) and Robinson et al. (1996). These reports demonstrate that fracture flow must play a role in the Yucca Mountain UZ flow and transport system and that infiltration rates close to those estimated by Flint et al. (1996), at least over the ESF, are required to generate the  $^{36}\text{Cl}/\text{Cl}$  signals that have been measured

in the ESF (both bomb pulse and non-bomb pulse). The most recent site-scale hydrologic model of Bodvarsson et al. (1997) primarily adopts the estimates of Flint et al. (1996) and a dual permeability model in the parameter calibration activity.

Bodvarsson et al. (1996) and Bodvarsson et al. (1997) investigate, through numerical simulation, some issues associated with bomb-pulse isotopes measured at the ESF. These simulations focus only on "fast path processes." The 1996 report examines processes in a single fault using a continuum model to specify different properties in the fault zone and host rock bounding the fault zone. The 1997 report examines transport from the surface to the ESF over the last 50 years using a two-dimensional, dual-permeability model that extends along the main drift of the ESF and which has modified PTn material properties at certain faults and hypothesized faults (undetected at the surface or at depth). Although the modification of fracture properties is not described in the 1997 report, we assume it is similar to, or based on, the approach of Robinson et al. (1996), where fracture permeabilities in fault zones are increased consistent with either more fractures or larger fracture apertures that result from tectonic activity. In transport simulations, Bodvarsson et al. (1997) use an input signal to their model which incorporates bomb-pulse  $^{36}\text{Cl}/\text{Cl}$  ratios that range up to  $1.6 \times 10^{-10}$ . The simulated  $^{36}\text{Cl}/\text{Cl}$  ratios at depth are identified as bomb-pulse in some locations, but they are less than present-day background (which is approximately  $500 \times 10^{-15}$ ). However, these simulations show, consistent with previous simulations by Robinson et al. (1996), is that in zones with properties modified to represent faulted conditions, solutes entering the mountain at the surface can arrive at the ESF in less than 50 years. Issues regarding different numerical model formulations and constraints when simulating transport in a dual permeability framework are discussed in Robinson et al. (1997).

A final concern regarding processes affecting bomb-pulse arrivals at the ESF is how significant transients on the scale of days are. Robinson et al. (1996) used a synthetic 100 year record of daily infiltration for which the infiltration rate on any given day was either 0.0 or 0.06 mm/day with an average of 30 days per year having non zero infiltration. The annual average was

2 mm/yr and the simulations showed no significant difference from the uniform infiltration rate simulations. In the simulations of transient effects by Bodvarsson et al. (1997), a pulse of 3.5 mm/day for 7 days is applied once and then the effects are examined over the next 10 years. The large pulse apparently has an effect on the maximum penetration depth, especially in faults. In this study, we further investigate the role and significance of transients by varying the length, magnitude, and frequency of recurring transients in and away from faults.

### Significant Previous Findings

Fabryka-Martin et al. (1996b) and Robinson et al. (1996) reported on a detailed study in which base-case PTn properties were modified in accordance with the increased fracturing that is expected to occur as a result of tectonic activity. In those studies, using base-case hydrologic properties from the Project's most recent analyses at the time (Bodvarsson et al., 1996; Robinson et al., 1995), we found that infiltration rates in the range of 1 to 5 mm/yr led to simulations consistent both with bomb-pulse signals found near fault zones and non-bomb pulse signals found away from fault zones in the ESF. Specifically, in regions away from faults where the PTn was not modified, simulated travel times of chloride to the ESF were on the order of 5,000 to 20,000 years and yielded  $^{36}\text{Cl}/\text{Cl}$  ratios in the  $600$  to  $900 \times 10^{-15}$  range, just as have been measured in ESF samples. With infiltration rates considerably less than 1 mm/yr, travel times often exceeded 100,000 years and decay of  $^{36}\text{Cl}$  resulted in predictions of ratios less than the measured values. With infiltration rates much greater than 5 mm/yr, all simulated travel times to the ESF are less than 10,000 years, and the resulting signal reflects a Holocene source with a nearly constant  $^{36}\text{Cl}/\text{Cl}$  ratio of  $500 \times 10^{-15}$ .

When the PTn fracture permeability is increased in simulations to reflect increased fracturing in fault zones, bomb-pulse arrivals at the ESF are predicted for infiltration rates greater than 1 mm/yr. Thus, the simulations in and away from fault zones in the ESF yield consistent results for the same range of infiltration rates.

### 6.4.2 Infiltration Studies

Estimates of infiltration rates at Yucca Mountain are performed by invoking a variety of measurements and models associated with surface and near surface processes. Flint and Flint (1994) estimated the spatial distribution of steady state infiltration rate in matrix material based on the relative permeability of the rock underlying the alluvium. Hudson and Flint (1996) developed a model correlating precipitation, alluvial depth, and measurements of water-content changes in shallow boreholes. At the shallow boreholes, Hudson and Flint used neutron logs to estimate water content. Changes in water content are assumed to give conservative estimate (low) of the volume of water that percolated deeper over the time period between neutron logging. Also Hevesi and Flint (1996) used an independent approach to estimate the spatial distribution of steady state infiltration rates. Their model is based on the assumption that basin wide recharge can be estimated for many basins in Nevada. Through geostatistical modeling of precipitation distribution and improved average annual precipitation estimates, they redistribute the infiltration rates over the extended Yucca Mountain study area, thereby providing another map of steady-state infiltration rates.

Each of these methods tends to estimate infiltration rates that are higher by at least an order of magnitude than the potential repository horizon percolation rates which have been used in the past for flow models (e.g. Wittwer et al., 1995, Bodvarsson et al., 1996). Previous studies tended to base percolation rates on the maximum hydrologic capacity of the matrix material. In such cases, however, the role of fracture flow was generally neglected. The role of fracture flow also may complicate the estimates of Flint et al. (1996) since the rock unit below the alluvium is often of low matrix permeability but highly fractured. However, between the surface and the sampling locations described below, water must move through alternating layers of fractured and less fractured volcanic tuff, thus dampening episodic events and giving rise to a constant percolation flux in the system.

### 6.4.3 Present Study Summary

The environmental isotope analyses have played a significant role in guiding both the flow and transport modeling efforts. In this chapter, we review briefly the findings from previous studies and then evaluate them through analyses using our site-scale flow and transport model which integrates with ISM geologic model (Clayton et al., 1996), parameter sets from the site-scale flow model (Bodvarsson et al., 1997), an numerous field and laboratory observations.

The recent multiple hydrologic property sets of LBNL (Bodvarsson et al., 1997) all represent calibration to measured saturation in boreholes. There are at least seven different sets of properties, each having some unique difference from the other sets. One set is based on calibrating the matrix-fracture interaction term as a scaled value of the connection area. Another uses simulated fracture saturation as a scaling term and then calibrates all other parameters. Another uses fracture saturation in the nonwelded tuff and fracture relative permeability in the welded tuff as the scaling function of the fracture-matrix interaction. Variations on each of these include the results obtained by starting the saturation calibration with different initial guesses of certain model parameters.

Bodvarsson et al. (1997) place no apparent preference on any of their calibrated parameter sets. Likewise, it is not immediately clear, a priori, whether significant differences in flow and transport simulation would occur when different sets are used. As many of the sets were evaluated in Chapter 5, here we analyze only a few of the parameter sets which with respect to their implication for simulation of environmental isotope distributions in Yucca Mountain. As with our previous studies (Robinson et al., 1996) we use one-, two- and three-dimensional models in the analysis. The one-dimensional models are used for examining in detail process-level intricacies. Here, the flow distribution between matrix and fracture can be examined as well the effect on vertical flow and transport of varying material properties. The two- and three-dimensional models provide platforms for studying the role of site-scale conditions such as dipping stratigraphy of variable thickness and extent, and spatially distributed infiltration.

In this chapter, we first describe the hydrogeologic setting in which the environmental isotope studies are conducted. Then we present the data which were collected and the interpretations which can be drawn from the data alone. Finally, we present corroborating numerical simulations and demonstrate how their results help reduce uncertainty in the interpretation of the data as well as improve our understanding of the transport environment of the unsaturated zone at Yucca Mountain.

### 6.5 Hydrogeologic Setting

---

#### 6.5.1 Stratigraphy

The stratigraphic structure of the unsaturated zone of Yucca Mountain is comprised of alternating layers of welded and nonwelded volcanic tuffs which are tilted, uplifted, fractured, and faulted. Characterization of these units and their subunits has advanced as more information from boreholes, the ESF, and other studies has become available. The classification of Scott and Bonk (1984) provided a framework around which hydrostratigraphic models were developed (e.g. Wittwer et al.; 1995; Robinson et al., 1996). Recently, Buesch et al. (1996) developed a classification scheme which enhances continuity between the various efforts in the site characterization program. Flint (1996) has provided the necessary link between the hydrologic characterization of the various units and the geologic structure of the system.

Figure 6-1 shows a schematic of the hydrostratigraphy encountered from the surface, through the potential repository horizon, and down to the water table. Below any surface alluvium, which varies in depth from 0 to 50 meters, the first major hydrologic unit encountered is the Tiva Canyon welded tuff (TCw). The saturated matrix permeability of the TCw is relatively low (on the order of  $10^{-17}$  m<sup>2</sup>) but the high degree of fracturing leads to a much higher bulk permeability. Below the TCw is the Paintbrush nonwelded tuff (PTn). The matrix permeability of the PTn is generally several orders of magnitude greater than the TCw, but the degree of fracturing is substantially less. The Topopah Spring welded tuff (TSw), below the PTn, is the horizon of the

potential repository and where most of the ESF samples have been collected for  $^{36}\text{Cl}$  analysis. The TSw is much thicker than the TCw and PTn together and is broken down into subunits depending on the density of lithophysal cavities and amount of devitrification that has occurred as a secondary process. Like the TCw, the matrix permeabilities in the TSw are low but the bulk permeability is substantially greater due to a high degree of fracturing. Finally, between the TSw and the water table are the Calico Hills, Prow Pass, and Bullfrog nonwelded tuffs. These are often grouped together and referred to as the Calico Hills nonwelded unit (CHn). A unique characteristic of the CHn is the degree of alteration to zeolitic material that has occurred. The zeolites are of particular interest for radionuclide transport sensitivity studies since they have been shown to be the primary mineral onto which Neptunium and Uranium sorb significantly. The zeolite distribution and the role zeolites play in the geologic barrier system between the potential repository and the water table are discussed in Chapters 8 and 9 of this report.

### **6.5.2 Conceptual model of flow and transport**

#### Base-Case

Our conceptual model between ground surface and the potential repository horizon, which has evolved from the conceptual hydrologic model of Montazer and Wilson (1984), can be described with the following components: Infiltration into the fractured TCw, sustained flow in the fractures of the TCw, matrix dominated flow in the PTn, and then fracture dominated flow again throughout most of the TSw. The flow in the CHn is complex due to the occurrence and distribution of vitric and zeolitic rocks. The degree of alteration to zeolites ranges from none to fully altered. Thus, the reduction in matrix permeability resulting from alteration must span a range from the high permeability vitric units to that almost as low as the welded units of the TCw and TSw. Where the matrix permeability is less than the percolation flux, flow must either occur in fractures or laterally bypass those low permeability zones. Due to the uncertainty in the permeability distribution, the degree of fracturing, and the actual percolation flux, the exact distribution and pathway of flow can not be determined. However, in Chapter 12 we demonstrate a geostatistical

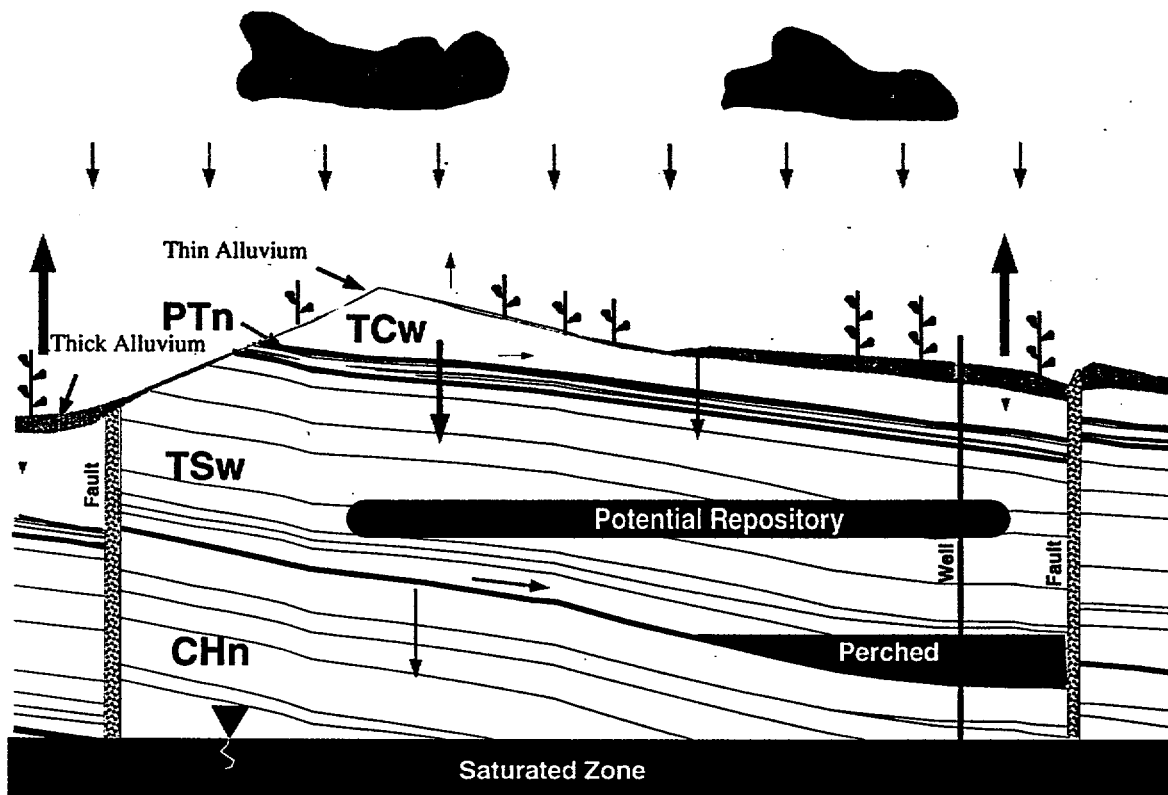


Figure 6-1. Conceptual model of hydrologic pathways at Yucca Mountain.

approach to address this uncertainty and attempt to identify the role that these distributed properties play.

Infiltration enters the system following episodic precipitation events and, that which does not go back to the atmosphere via evapotranspiration, moves quickly through the TCw. Once the moisture enters the PTn, however, the downward velocity is slowed as the water moves almost entirely in the high porosity matrix material. Due to the transition from fracture flow to matrix flow, the episodicity of the percolation is damped and, by the bottom of the PTn, the flow rate resembles an average annual percolation rate. At the PTn/ TSw boundary, there is a permeability barrier due to the highly contrasting matrix permeabilities. However, the increased fracture permeability of the TSw can support the flow coming out of the PTn matrix. One question regarding this interface is how much flow may be diverted laterally, rather than continuing vertically from the PTn matrix to the TSw fractures (the TSw matrix by itself can not support

anywhere near the flow rate of the PTn matrix). Due to the low matrix permeability, water which continues to percolate vertically flows mostly in the fractures of the TSw and is, hence, characterized with much greater velocities than the matrix flow of the PTn.

Clearly, in our conceptual model of this complex layered system, the PTn plays an important role in arresting the velocity of downward moving water as well as dampening out the episodicity of infiltration events. If this behavior can be understood and validated, then a better understanding of the actual flow rate through the system can be inferred as well. Conversely, if episodic pulses of flow are not damped by the PTn and persist at the potential repository horizon, then dripping into the drifts is more likely and the near field performance may be reduced.  $^{36}\text{Cl}/\text{Cl}$  ratios measured in the ESF provide, in conjunction with numerical modeling studies, significant insight into the relationship between flow rates, flow distribution between fractures and matrix material, and travel times through the system of welded and nonwelded tuff.

Transport of radionuclides, both naturally occurring and from a potential repository source, are considered in this system. The naturally occurring radionuclides,  $^{36}\text{Cl}$ , tends to migrate with the water as a conservative tracer. Inventory radionuclides like  $^{237}\text{Np}$  may move at a slower rate than a nonreactive tracer due to sorption in the zeolites of the CHn. Thus, the naturally occurring radionuclides serve to identify flow paths and travel times of water while the entire geochemical system must be considered to determine the actual rate  $^{237}\text{Np}$  will move at.

---

### Fault Zones

The identification of bomb-pulse  $^{36}\text{Cl}/\text{Cl}$  ratios in the ESF indicates that not all vertical flow velocities are arrested in the PTn. Otherwise, we could never get any chloride from the surface to such depth in the necessary 50 years or less to show bomb pulse. Levy et al. (1997) extend on the work of Fabryka-Martin (1996b) and provide an analysis of structural controls of fast pathways from ground surface to the ESF. They note that the locations at which these fast pathways have been identified in the ESF appear distinctive, with the primary controls on their distribution being

the presence of faults that cut the PTn, the magnitude of surface infiltration, and structural features that result in lateral diversion of flow away from fault zones. One of these key issues that we have focussed on relates to the transport of chlorine-36 through fault zones that cut the PTn.

### 6.6 Chlorine-36 Study

---

#### 6.6.1 Background

The construction of the ESF provided an opportunity to develop a spatial distribution of  $^{36}\text{Cl}/\text{Cl}$  ratios within the same horizon for assessment of the hydrologic processes in the Yucca Mountain subsurface. An additional purpose for conducting the chlorine-36 sampling project in the ESF was to identify if and where any fast paths for water movement from the surface, through the PTn, and to depth could occur. If bomb-pulse  $^{36}\text{Cl}/\text{Cl}$  ratios were detected, that would provide an indication of travel times of several hundred meters in less than 50 years. The ability to collect samples for  $^{36}\text{Cl}/\text{Cl}$  ratio analysis in the ESF marked a unique opportunity which helped to overcome previous problems with analyses from borehole samples. First, the ESF provides the opportunity to look at and characterize the rock and geologic structure at and in the vicinity of samples. This contrasts greatly with the blind samples that were obtained previously from boreholes. Only in the ESF can the samples be classified as coming from intact rock, breccias, or fracture zones, and their precise location relative to the faults be mapped. This classification has proven extremely valuable in the correlation of structural features with  $^{36}\text{Cl}/\text{Cl}$  ratios measured for these ESF samples (Levy et al, 1997). Second, borehole samples could only be collected as ground-up ream-bit cuttings. This increased the error in analysis as a result of dead chloride released during the pulverizing of the rock. The ESF samples are not pulverized and, hence, represent the ambient system more accurately.

#### 6.6.2 Chlorine-36 input

Chlorine-36 was originally picked as a tracer for very old groundwater because it has a half life of 301,000 years. Early estimates of infiltration flux into Yucca Mountain were less than 0.1

mm/yr, which could lead to pore water ages on the order of a half a million to a million years. For such ages, carbon-14, with a half life of 5700 years, was thought to be inappropriate due to its maximum age resolution of about 50,000 years. Further, whereas  $^{14}\text{C}$  can travel both in the liquid and vapor ( $\text{CO}_2$ ) phase and participate actively in mineral precipitation and dissolution,  $^{36}\text{Cl}$  remains in the liquid phase. Finally, the bomb-pulse signature of  $^{36}\text{Cl}$  is more distinct and differentiable from present and past background signals than that of  $^{14}\text{C}$  (Fabryka-Martin et al., 1996c).

Rather than indicating hundreds of thousands of years of decay as initially expected, about half of the  $^{36}\text{Cl}/\text{Cl}$  ratios measured in the ESF are actually greater than present day background. These analyses became available at the same time as the revised, higher surface infiltration rate estimates (Flint et al., 1996) were being developed. One hypothesis was that the elevated ratios reflected a widespread presence of bomb-pulse in the deep subsurface. However, an alternative interpretation was that most of the elevated signals reflected past variations in background levels. Fossil packrat midden samples dated both with  $^{14}\text{C}$  and  $^{36}\text{Cl}$  indicate that, since the end of the Pleistocene (the last 10,000 years ago), the  $^{36}\text{Cl}/\text{Cl}$  ratio has been relatively constant at the present day level. However, in the later part of the Pleistocene, a time period in which packrat midden samples can still be dated with  $^{14}\text{C}$ , the  $^{36}\text{Cl}/\text{Cl}$  ratio was as much as two and a half times greater than the present day background. Coupling the packrat midden samples with a theoretical model of tropospheric  $^{36}\text{Cl}$  production based on Earth's geomagnetic flux variation, Fabryka-Martin et al. (1996b) and Plummer et al. (1996) developed the reconstructed  $^{36}\text{Cl}/\text{Cl}$  function shown in Figure 6-2 which is used as an input to the numerical simulations in this study. Those reports give the full detail of the signal reconstruction process and the data sources.

The infiltration estimates of Flint et al. (1996) are generally on the order of 1 to 10 mm/yr above the ESF sample locations. Such infiltration rates correspond to groundwater ages on the order of 1 to 20 thousand years. These travel times are entirely consistent with the sample ratios

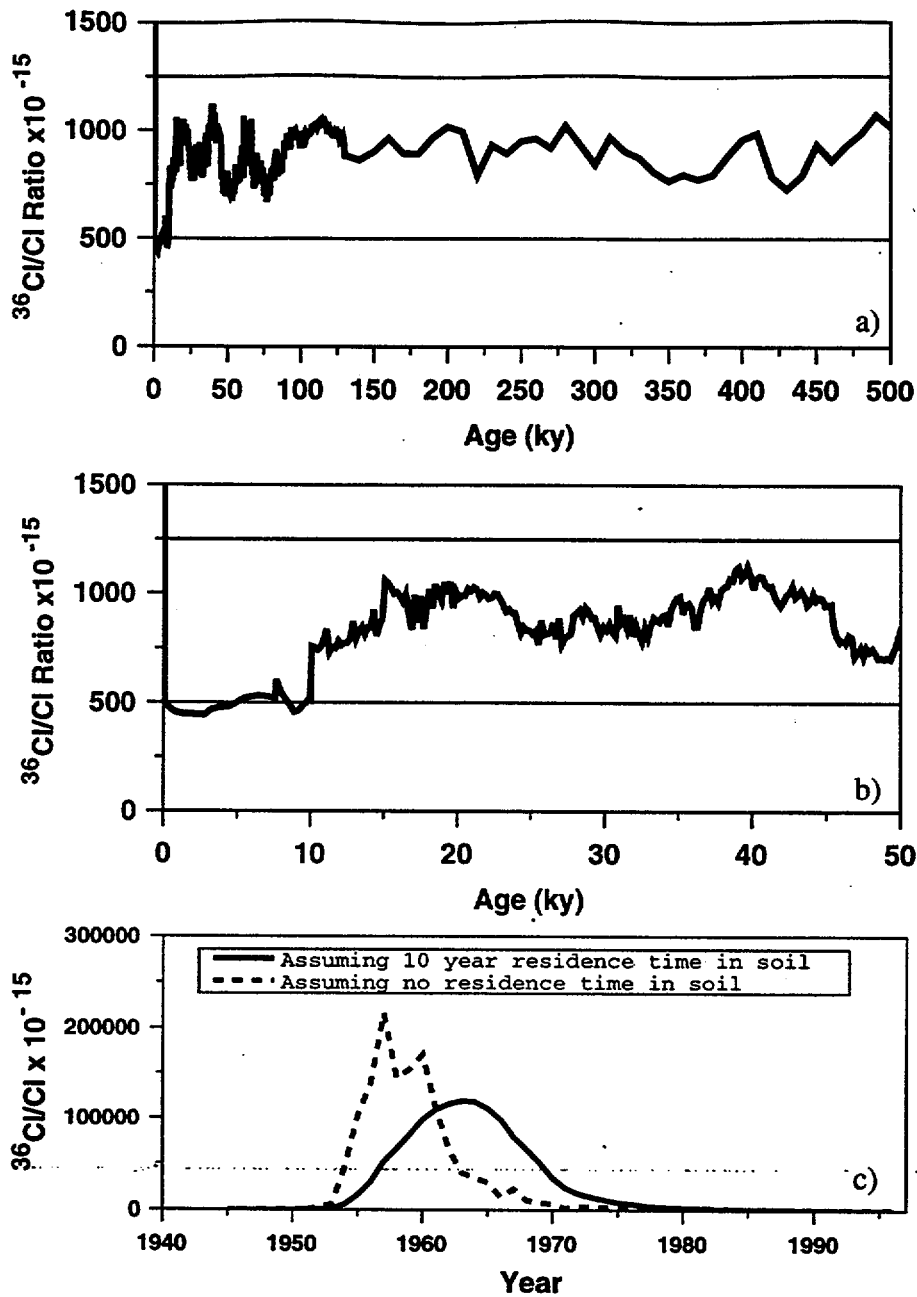


Figure 6-2. Reconstructed  $^{36}\text{Cl}/\text{Cl}$  ratio in infiltrating water (Fabryka-Martin et al., 1996c, Plummer et al., 1996), a) last 500,000 years, b) last 50,000 years, c) last 50 years.

found in the ESF. The radioactive decay dating of  $^{36}\text{Cl}$  loses its applicability for such short travel times, but the elevated ratio at the end of the Pleistocene provides a valuable tracer for groundwater age dating.

### 6.6.3 ESF Data

The ESF data collection involves sampling systematically every 200 m as well as additional feature based samples from fractures, breccias. Levy et al. (1997) report isotopic and mineralogic sample analyses up to station 68 (6.8 km into a tunnel from the entrance). Sweetkind et al. (1997) report on the additional samples that have been collected since the report of Levy et al. was published. However, the data from Levy et al. (1997) are plotted later in Figure 6-21 in conjunction with the simulated  $^{36}\text{Cl}/\text{Cl}$  ratios obtained with the 3D transport model. Additional interpretation of the data can be found in Sweetkind et al. (1997).

## 6.7 Flow and Transport Model

---

### 6.7.1 Numerical Flow and Transport Model: FEHM

The numerical simulations are conducted using FEHM (Finite Element Heat and Mass transfer) (Zyvoloski et al., 1992). The mathematical models and numerical methods are summarized in Zyvoloski et al. (1992, 1995a,b), Robinson et al. (1996) and Viswanathan (1996). Solute transport in FEHM can either be performed with the particle tracking module or the finite-element reactive transport module. Both are coupled to the flow module so transport in steady state or transient flow conditions can be simulated. The particle tracker accommodates advection, dispersion, matrix diffusion, linear sorption, and radioactive decay. With the finite-element solver, the additional process of multi-species reactions such as complexation, competitive sorption, and precipitation/dissolution can be simulated (Viswanathan et al., 1997; Chapter 11 of this study). Here, since only aqueous chloride transport is considered, the particle tracker is adequate and substantially more efficient than the finite element solver. A large part of the efficiency associated with the particle tracker results from its ability to yield accurate solutions, even when fluid velocities are large. In fractured tuff, the velocities in fractures are substantially greater than in the rock matrix and resolution of solute movement would require very small time steps or unrealistic

grid resolution with standard finite-element or finite-difference techniques. However, the particle tracker is based entirely on the already computed flux in and out of each element and its computational limitation is only dependent on the number of particles used (see Chapter 4 of this report). With modern computer workstations, transport of millions of particles can be simulated efficiently. For example, a typical run using 1 million particles to simulate  $^{36}\text{Cl}/\text{Cl}$  distributions on the 143,000 node three-dimensional grid for a time period spanning over 1 million years takes less than 10 minutes.

### 6.7.2 Transient Signals of Isotopic Sources

Among its many unique features, one utility in the FEHM particle tracker that proves invaluable in the simulation of environmental isotope transport and distribution is the capability to efficiently integrate a transient source function. All of the particles are introduced into the system instantaneously and the simulation proceeds until all particles leave the system. A record is kept at each node of when the particles went through that node. That time indicates the travel time to the node and hence the time before present that a packet of water would have had to enter the system to arrive at the node now. Hundreds or thousands of particles pass each node, giving a distribution of travel times (or ages of water) at each node. With each age, a unique  $^{36}\text{Cl}/\text{Cl}$  ratio is obtained from the function plotted in Figure 6-2. These ages are integrated at each node to give a distribution of  $^{36}\text{Cl}/\text{Cl}$  signals throughout the system. This capability enables the simulation of long-time processes (e.g.  $10^4 - 10^5$  years) as well as the bomb-pulse time scales (50 years) within the same simulation. With the standard finite-element or finite-difference method, the time of simulation would be substantially greater due to the small time steps required to accurately model transport in a dual permeability formulation. One limitation of the particle tracking method is that, to simulate the transient source function for environmental isotopes, steady-state flow is required due to the integration process. However, for simply simulating breakthrough curves at one location for a pulse of particles injected into the system at the top, transient flow can be invoked.

### 6.8 Simulated Systems

---

#### 6.8.1 Overview

One-, two-, and three-dimensional numerical models are used to interpret the  $^{36}\text{Cl}/\text{Cl}$  observations and the general hydrologic behavior of the system above the potential repository to aid in the prediction of migration rates of other radionuclides from the potential repository to the accessible environment. A schematic of the locations of the various models used in this chapter as well as in the radionuclide transport chapters is given in Figure 6-3. Based on the findings of Robinson et al. (1995, 1996), all simulations of environmental isotope transport and distribution are performed with the dual-permeability model formulation. Only with the dual-permeability formulation can rapid transport in fractures be simulated in conjunction with slow transport in matrix material as well as the coupling between the two media.

Two- and three-dimensional models are used to study the site-scale behavior including the effects of dipping stratigraphy of variable thickness and extent, spatially varying infiltration rates, and spatially distributed material attributes. The one-dimensional models are used to examine specific fracture-matrix interactions associated with flow and transport in and away from fault zones. Also, transport under transient and steady-state flow conditions is evaluated with the one-dimensional models to assess whether time scales associated with episodic infiltration events (days) need to be addressed in the model when simulations of tens of thousands of years in two and three dimensions are required for radionuclide migration studies.

The layers in the numerical models are derived from the three-dimensional, site-scale stratigraphic framework model (Zelinski and Clayton, 1996). The GEOMESH software package (Gable et al., 1996) is used to extract the region of interest from the geologic model and generate unstructured finite element grids. Material properties and parameters for the different layers are obtained from Bodvarsson et al (1997) and listed in Appendix 1.

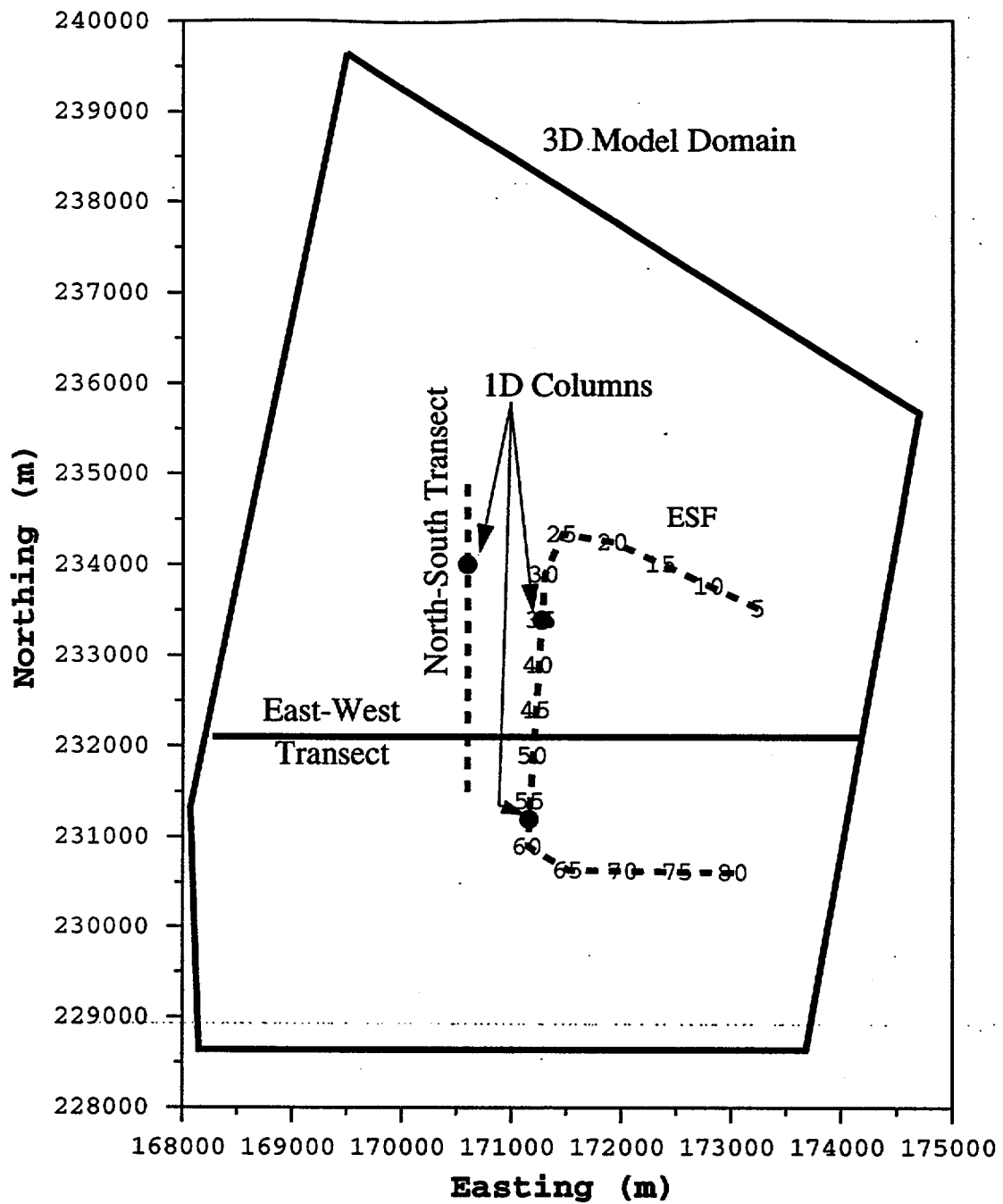


Figure 6-3. Plan view of three-dimensional model domain with locations of ESF, ESF stations, two-dimensional east-west model transect, north-south transect, and one-dimensional vertical column studies.

### 6.9 Carbon-14 Study

---

#### 6.9.1 Background

Groundwater ages in countless aquifer systems have been estimated based on the residual carbon-14 activity in the porewater. Prior to the advent of atmospheric testing of nuclear devices,  $^{14}\text{C}$  was present in the atmosphere solely due to its production by cosmic rays bombarding nitrogen nuclei. By definition, the specific activity of  $^{14}\text{C}$  in carbon that was in equilibrium with the atmosphere prior to the nuclear age is 100 percent modern carbon (pmc), corresponding to about 14 disintegrations per minute (dpm) per gram of carbon. Numerous lines of evidence indicate that this initial activity has been relatively constant for the past several tens of thousands of years, with fluctuations of about 10%. Copious quantities of  $^{14}\text{C}$  were produced in the atmosphere by nuclear testing in the 1950s and 1960s, and have also been released as a by-product of the reprocessing of spent nuclear fuel. The peak activity occurred in 1963, at 200 pmc. The decrease since then has been due to exchange of  $^{14}\text{C}$  for nonradioactive carbon in the biosphere and hydrosphere, principally the ocean. In contrast with the present-day atmospheric signals for tritium and  $^{36}\text{Cl}$ , the modern  $^{14}\text{C}$  value is still elevated about 20% above natural background due to the comparatively long residence time of carbon in the atmosphere.

In groundwater investigations,  $^{14}\text{C}$  measurements are made on inorganic carbon extracted from water and gas samples. For Yucca Mountain samples, typical volumes have been 100 mL for water, and 2 L for gas samples. In the absence of a bomb-pulse signal, an apparent age can be calculated based on the radioactive decay equation, using the  $^{14}\text{C}$  half-life of 5730 yr. However, this unadjusted age represents a maximum, and the true age can be substantially less. Because carbon-bearing species distribute among the solid, liquid and gas phases in unsaturated geologic systems, many geochemical reactions occur that dilute the initial signal. These include re-equilibration with soil-gas  $\text{CO}_2$ , which has lower  $^{14}\text{C}$  activity than that in the atmosphere; release from or isotopic exchange with carbonate and gypsum minerals along the flow path; oxidation of

dissolved organic matter; and re-equilibration with  $\text{CO}_2$  in the vapor phase in the unsaturated zone. Numerous geochemical models are available to correct the measured signal, and generally require the user to specify solution chemistry and carbonate speciation, relevant mineral-water reactions that control the carbonate chemistry of the system, stable carbon isotope signals and  $^{14}\text{C}$  activities of the various carbon sources and sinks in the system, and prevailing water temperature.

Due to the reactions that  $^{14}\text{C}$  can be involved in, it is not a conservative liquid-phase environmental tracer as  $^{36}\text{Cl}$  is. However, it does provide an additional constraining data set for porewater ages in the unsaturated zone at Yucca Mountain. Measurements of liquid and gas phase  $^{14}\text{C}$  have been reported by Yang et al. (1992, 1996, 1997). These data are primarily from nonwelded tuffs and from perched water as the sample size necessary for analysis can not be readily extracted from the welded tuff. The  $^{14}\text{C}$  analyses on the perched water samples indicate apparent ages ranging between 3,000 and 11,000 years (Yang et al., 1996) and the apparent ages in porewater of the Calico Hills range between 800 and 5500 years. Corrections to these estimates to account for caliche dissolution are discussed in Chapter 7 of this study.

### 6.9.2 Carbon-14 Data

Yang et al. (1997) present  $^{14}\text{C}$  analyses for perched water samples and porewater samples. Of particular interest are the data in the units at or below the potential repository. As porewater collection has not been achieved in the welded TSw units, the  $^{14}\text{C}$  analyses have been performed on perched water samples found at the TSw-CHn interface and in the vitric CHn units. Table 6-2 shows the apparent ages of these samples, which are discussed in greater detail in Chapter 7. The apparent ages for the porewater samples, which occur below the perched water, are younger than the apparent ages in the perched water.

**Table 6-2. Apparent <sup>14</sup>C Ages from Yang et al. (1997)**

Location	Well	Apparent Age Range (years)
CHn Porewater	UZ-14	400-3500
	NRG7	4100
	SD7	2700-4100
	SD9	400-1600
	SD12	2900-2500 800-2300
	UZ16	800-5350
Perched Water	UZ14	8000-12000
	NRG7	2000-6000

A possible explanation for the apparent discrepancy

One possible explanation for this seemingly contradictory indication is that under past, wetter climates, lateral flow occurred at the basal vitrophere because the entire flux could not be transmitted vertically through that low permeability unit. Under present drier climate conditions, most of the flow, even from the zones of highest infiltration, moves vertically through the basal vitrophere and does not divert laterally until it reaches the zeolites. This scenario would lead to younger water overlain by older water as the source of the perched water is primarily attributed to the previous climate. The sample locations such as UZ-14 tend to be in locations with relatively low infiltration. Thus the contribution of modern water to the perched body through the vertical pathway is small relative that from zones of higher percolation flux. However, it would serve to bring the apparent age up some do to mixing of water of different ages. This conceptual model is described more fully in Chapter 7.

### 6.9.3 Carbon-14 Input

Carbon-14 is input into the transport model at a uniform concentration of 100 percent

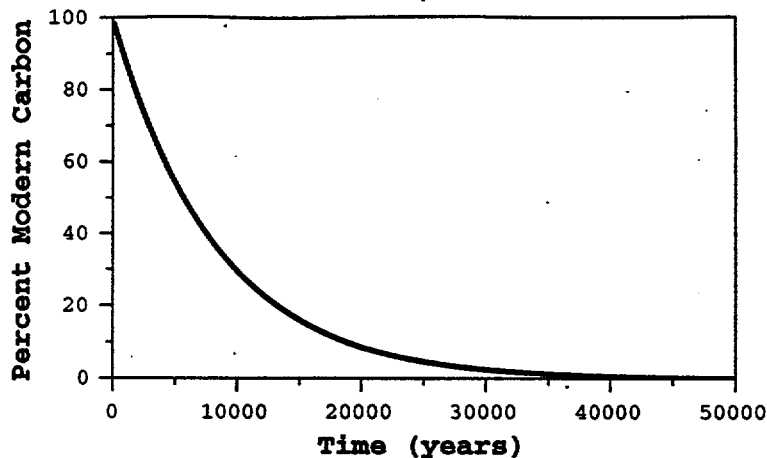


**Figure 6-4.** Carbon-14 decay function resulting from a 5730 year half-life.

modern carbon (pmc). As it migrates into the subsurface, decay is accounted for according to the curve shown in Figure 6-34. As with the  $^{36}\text{Cl}$  particle tracking model, this is performed efficiently and without the time-step constraints of conventional finite-element or finite-difference methods. However, the simulations are limited to steady state flow fields.

## 6.10 Chlorine-36 Modeling: Two- and Three- Dimensional Studies

---

### 6.10.1 Model Description

#### Domain and Boundary Conditions

Migration and distribution of environmental isotopes chlorine-36 and carbon-14 are simulated on the east-west cross section two-dimensional model and in the site-scale three-dimensional mode. The two-dimensional model domain is located at Nevada State Plane Northing coordinate 232,100 m and crosses several faults between Easting coordinates 168,275 m and 174,175 m. This domain (Figure 6-5) includes the Solitario Canyon Fault, the Ghost Dance Fault, and the Bow Ridge Fault. The infiltration map of Flint et al. (1996) (the I map) and a scaled version

## Environmental Isotopes and The Hydrologic System

---

of that map where all rates are scaled by one third (the I/3 map) are used as the top boundary condition for the two-dimensional model (see Table 6-4). These maps are shown in Figure 6-6 for the two-dimensional cross section. The aerial domain of the three-dimensional model is shown on top of the I infiltration map of Flint et al. (1996) in Figure 6-7. The extent of faults and general structure of the three-dimensional model are described in Chapter 3 of this report. A saturation boundary condition is prescribed at the water table for all models.

### Material Properties

The hydrologic properties used in this study either are taken directly from or are based on the hydrologic properties of Bodvarsson et al. (1997), which were developed through calibration to measured matrix saturation. Table 6-3 lists the property sets are used in the environmental isotope models and the source and modifications associated with each set. The input parameters to FEHM are provided in Appendix 1 of this report. The major difference in property sets is the modification of set 6541a to 6541b, in which the fracture/matrix reduction factors in the PTn were eliminated.

**Table 6-3. Parameter Sets for Environmental Isotope Simulations**

Property Set Name for This Report	LBNL set on which properties are based	Location in LBNL report of property set	Modification of LBNL properties
6541a	Table 6.5.4-1	A-28	None
6541b	Table 6.5.4-1	A-28	No reduction factor for fracture/matrix interaction in PTn
6541ft	Table 6.5.4-1	A-28	PTn fracture permeability increased by one order of magnitude
6541perched	Table 6.5.4-1	A-28	Basal vitrophere fracture permeability reduced and fault zone fracture permeability reduced.
6412b	Table 6.4.1-2b	6-12	None

**Table 6-4. Infiltration Maps Used in Environmental Isotope Simulations**

Infiltration Map Name	Source	Modification
I	Flint et al. (1996)	None
I/3	Flint et al. (1996)	Scaled everywhere by 1/3

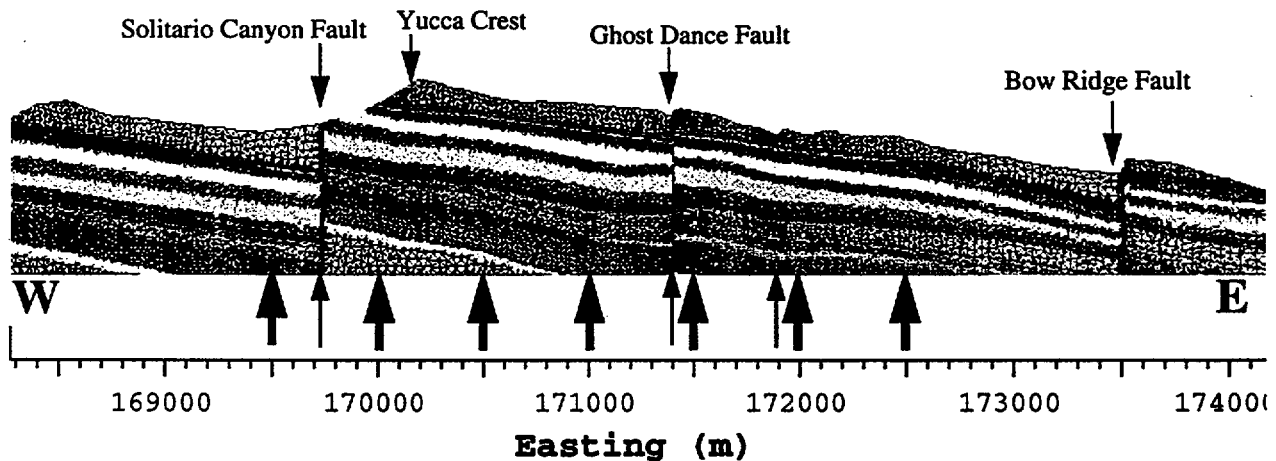


**Figure 6-5.** Finite-element grid for the two-dimensional cross section at Antler Ridge. Northing location in NSP coordinates is 232100 m. Red arrows show easting location for potential repository horizon breakthrough study.

**6.10.2 Two-Dimensional Chlorine-36 Simulation Results**

The transport of chloride and resulting  $^{36}\text{Cl}/\text{Cl}$  ratios throughout the two-dimensional cross section are simulated for a variety of different conditions. The results are evaluated both in terms of the overall resulting distributions and the temporal breakthrough curves at selected locations. Those selected locations are all at elevation 1080 m (approximately the potential repository elevation) and are generally spread out across the cross section every 500 m (see Figure 6-5 for the locations of these points).

The first simulation utilizes the 6541a material set and the resulting matrix  $^{36}\text{Cl}/\text{Cl}$  ratios are plotted in Figure 6-8. In the TSw, the simulated values resemble those that are measured in the

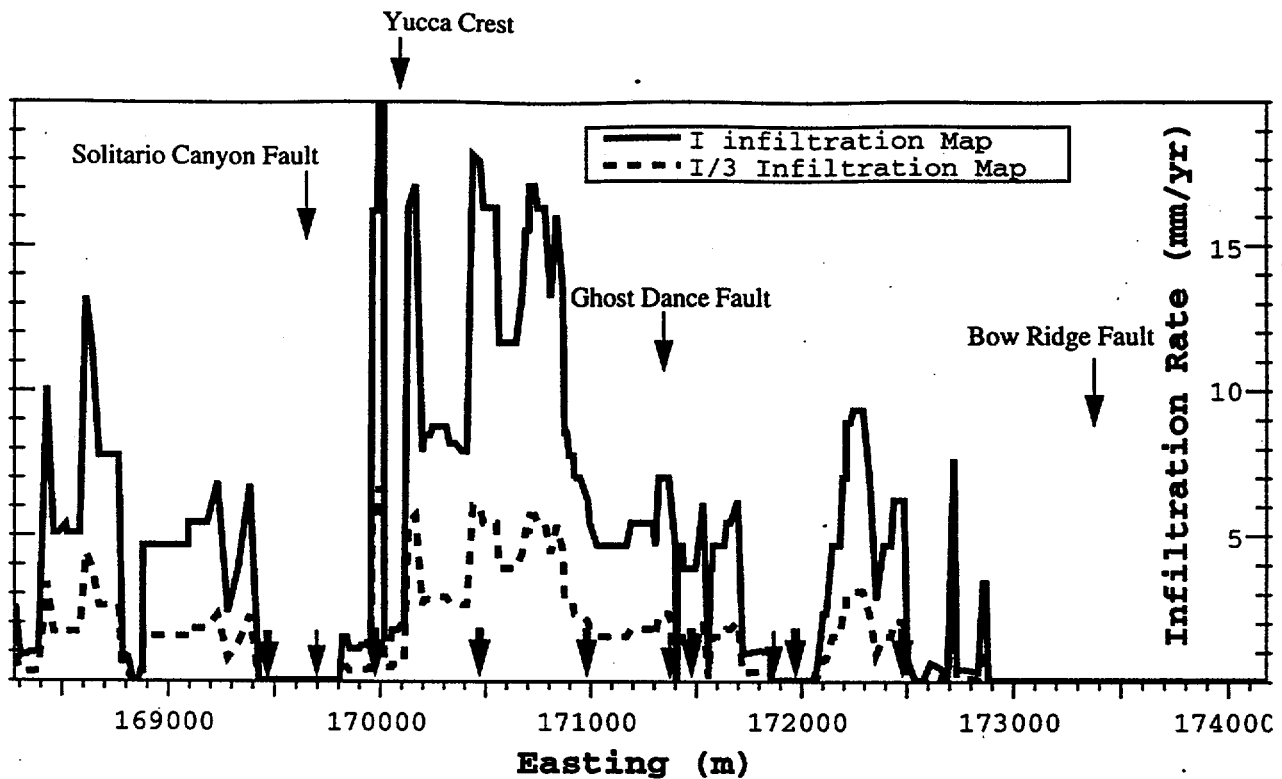
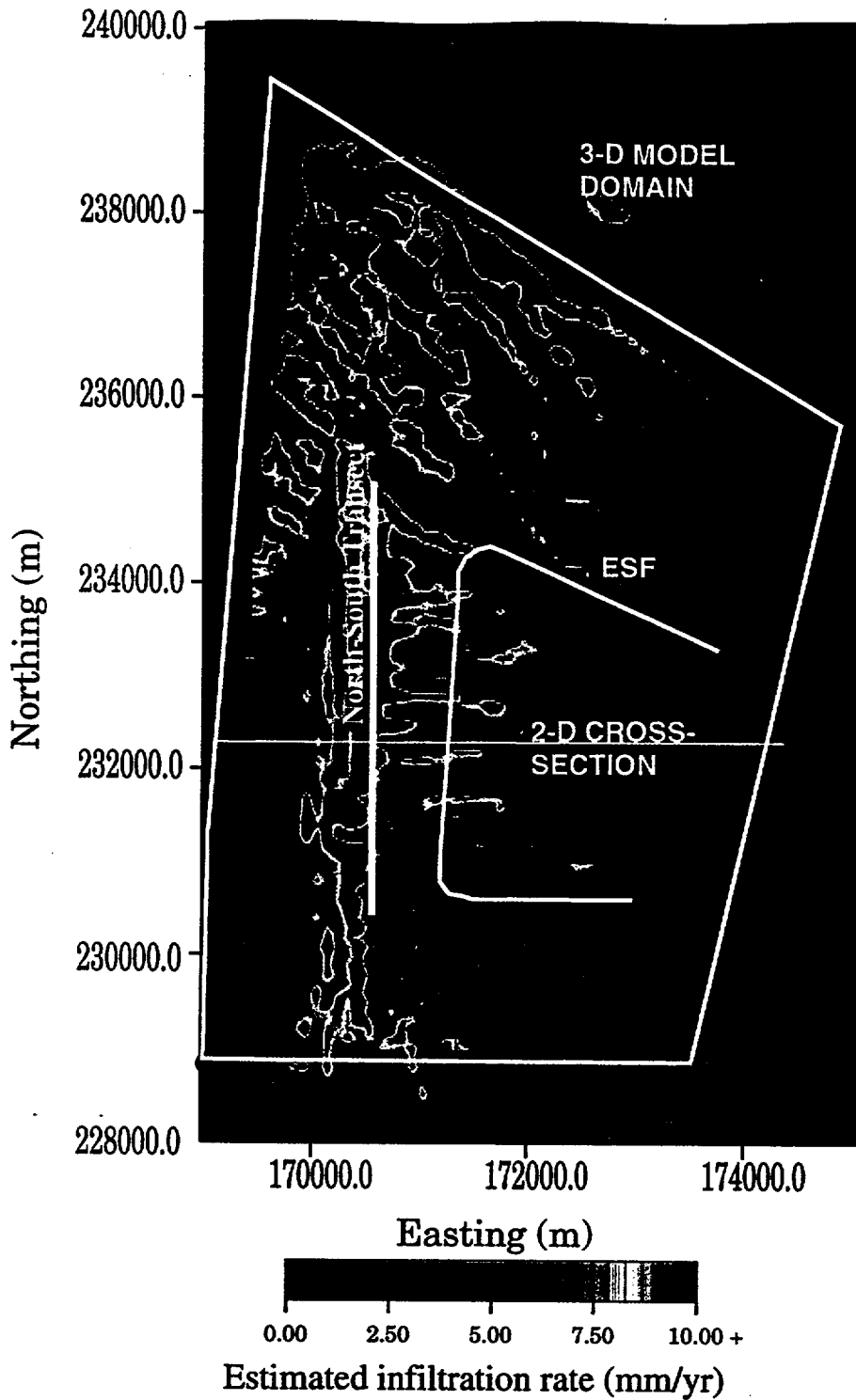


Figure 6-6. Infiltration rates extracted from Flint et al. (1996) map along Antler Ridge cross section. I map is directly extracted, I/3 map is the I map scaled by 3. Green arrows show easting location for potential repository horizon breakthrough study.

same horizon in the ESF. That range spans from 500 to 1100  $\times 10^{-15}$ . What is striking about this simulation, however, is that bomb-pulse ratios are simulated ubiquitously at the TSw/CHn interface under the entire potential repository horizon and even somewhat east of the Ghost Dance fault. This means that, for these model parameters, some flow is getting through the entire PTn in less than 50 years. Recall, however, that this parameter set reduces the fracture matrix coupling area by the fracture saturations (see Chapter 5). For this scenario, any water that gets into the fractures, in a dual permeability simulation, will be less likely to transition to matrix flow than when the coupling term is not reduced.

Since these parameter sets represent calibration to saturation (Bodvarsson et al., 1997), we tested the sensitivity of that calibration only in the PTn, the unit that controls the migration rate of  $^{36}\text{Cl}$  from the surface to the ESF and potential repository horizon. Figure 6-9 shows the resulting



**Figure 6-7.** Plan view of three-dimensional domain outline on top of Flint et al. (1996) infiltration map. Also shown for reference are the ESF, the east-west two-dimensional cross section and the north-south transect (used to interpret the three-dimensional model results).

$^{36}\text{Cl}/\text{Cl}$  ratios when parameter set 6541b is used. The only difference from set 6541a is that the PTn fracture/matrix coupling is not scaled by the simulated fracture saturation. The results clearly show that for the modified parameter set, bomb-pulse levels of  $^{36}\text{Cl}$  are constrained to being below areas where there is no PTn (e.g. in the west end of the cross section) and near faults. The difference between the two simulations is shown in Figure 6-10. This figure shows that the only significant differences between the two simulations occur in the vicinity of the simulated bomb-pulse signals in either run. For the bulk of the system, the resulting ratios are about the same for these two simulations.

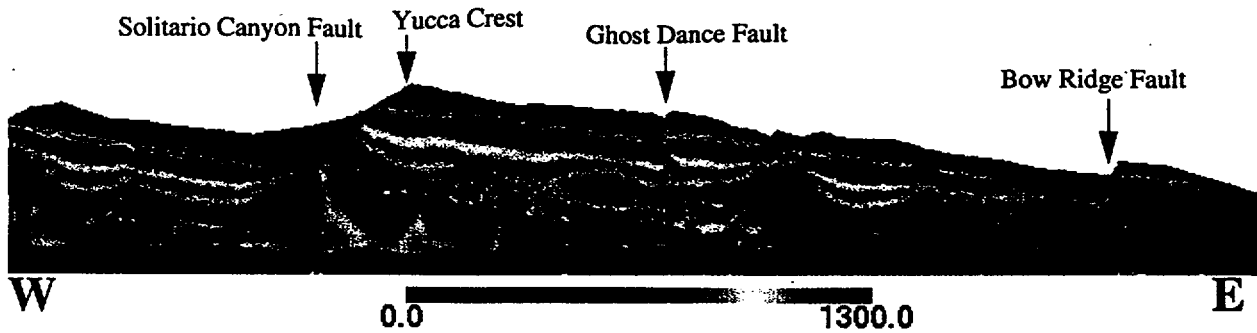


Figure 6-8. Simulated  $^{36}\text{Cl}/\text{Cl}$  ratios in Antler Ridge 2-D cross section with 6541a material property set and Flint (1996) infiltration map.

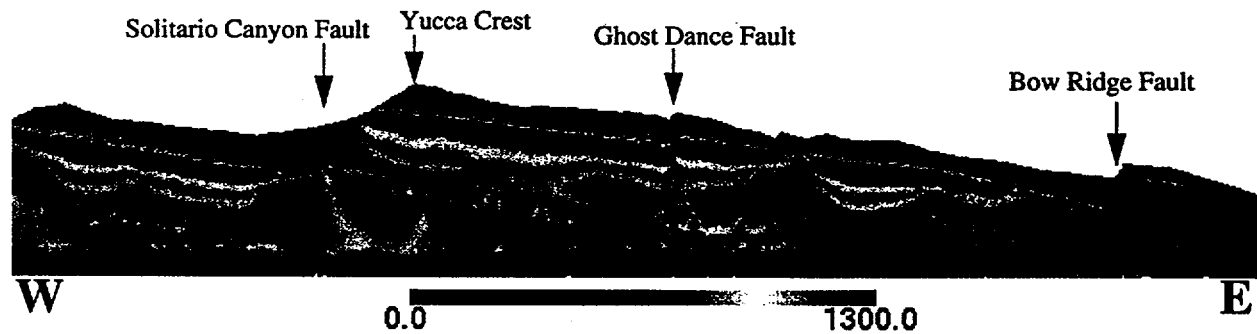


Figure 6-9. Simulated  $^{36}\text{Cl}/\text{Cl}$  ratios in Antler Ridge 2-D cross section with 6541b material property set (*no weighting of fracture-matrix connection in PTn*) and Flint (1996) infiltration map. Note the reduced amount of bomb-pulse in the top of the CHn.

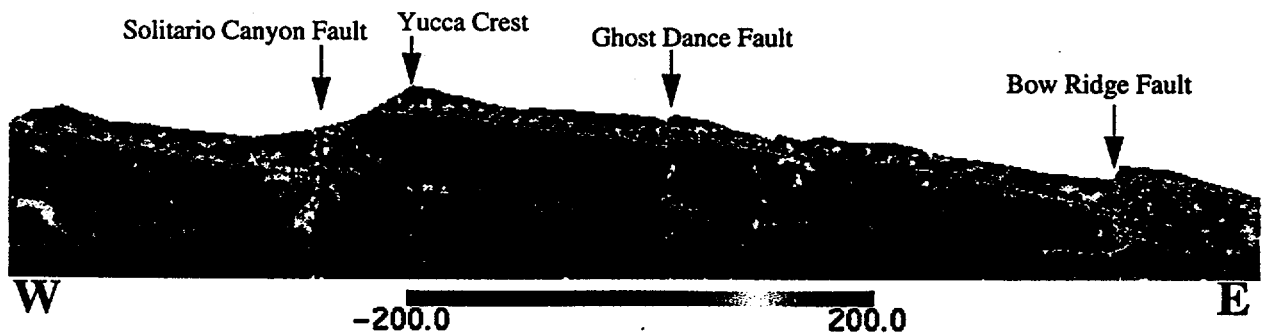


Figure 6-10. Difference in simulated  $^{36}\text{Cl}/\text{Cl}$  ratios for property sets 6541a and 6541b.

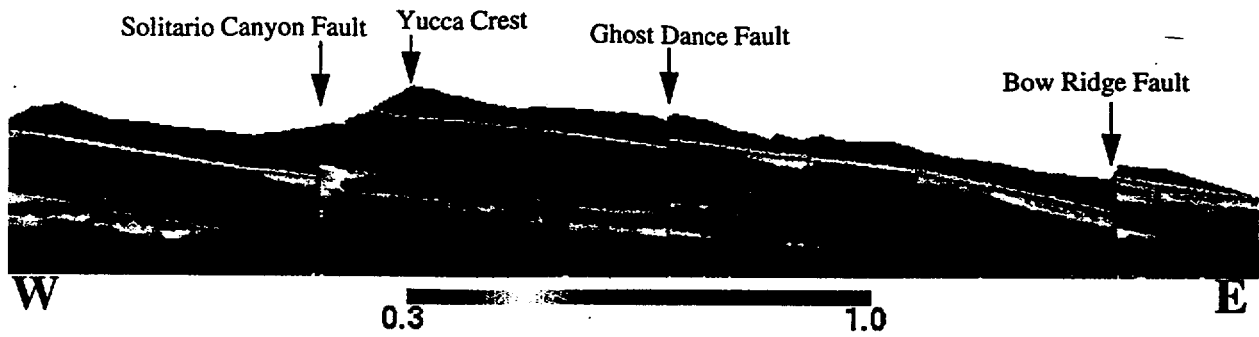


Figure 6-11. Simulated saturations in Antler Ridge 2-D cross section with 6541a material property set and Flint (1996) infiltration map.

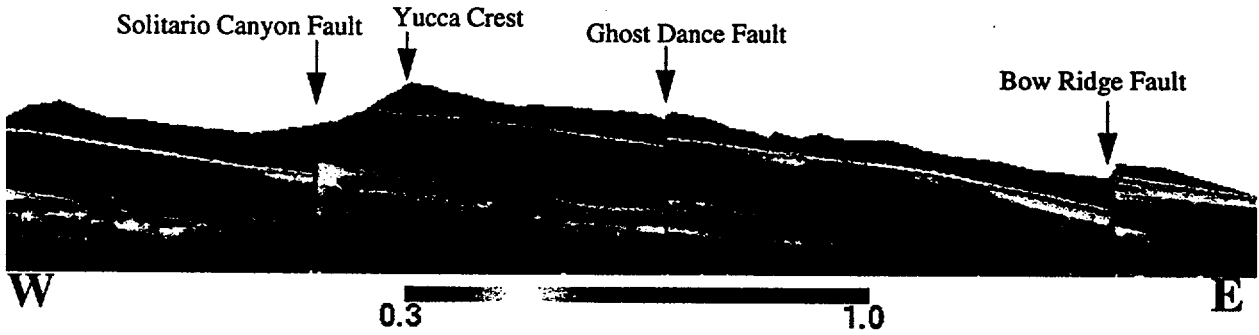


Figure 6-12. Simulated saturations in Antler Ridge 2-D cross section with 6541b material property set and Flint (1996) infiltration map.

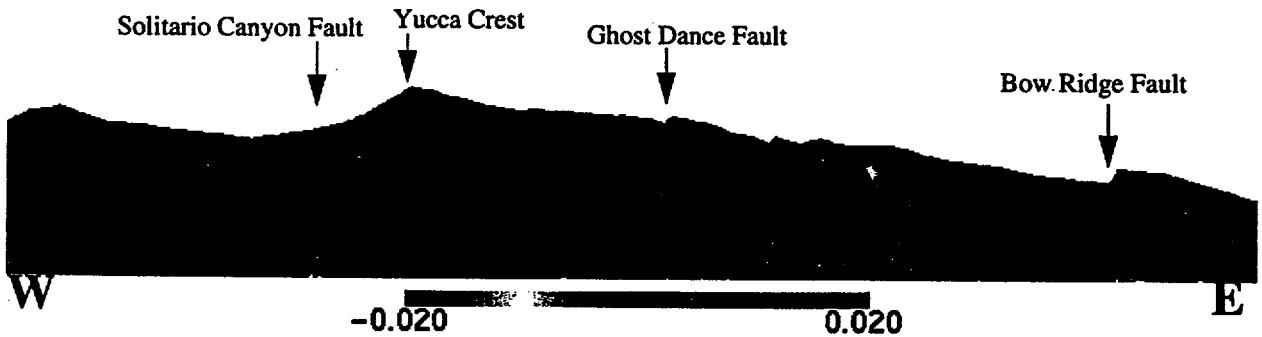


Figure 6-13. Difference in simulated saturations for property sets 6541a and 6541b.

Is one simulation better than the other? Certainly the first, 6541a, is computed with parameters calibrated to saturations. However, Figures 6-11 and 6-12 show the simulated saturations for the two parameters sets. They look virtually identical. This is confirmed in Figure 6-13 which plots the difference between the two. In the PTn, the only unit for which fracture/matrix coupling was modified, the maximum saturation difference is only 0.05.

### Implications

Two parameter sets that yield virtually identical saturation fields lead to very different predictions regarding whether or not bomb-pulse  $^{36}\text{Cl}$  penetrates the PTn above the potential repository. As a preliminary investigation into the implication regarding whether transients will be damped out in the PTn, solute breakthrough curves were computed for a set of locations in the model at the potential repository horizon. The assumption LBNL (Bodvarsson et al., 1997) and we have made in the past is that the PTn fully damps the signal and hence episodic events need not be considered in simulations spanning thousands of years. However, if travel times through the PTn are less than 50 years, then we may need to reconsider this assumption.

Breakthrough curves, which also represent the cumulative age distribution of a sample at a location in the model domain, are used to further investigate the differences that result from what appears to be a minor property change. Figure 6-15 shows the travel time breakthrough curves at the potential repository elevation throughout the cross section using the 6541a parameter set. These curves indicate that, for the 6541a set, a significant amount (7-65%) of the water going through the potential repository horizon is less than fifty years old. Moving eastward, the amount of early arrival decreases as the infiltration rate at the surface decreases. In contrast, Figure 6-15 shows that the slight modification in parameter set 6541b leads to substantially less bomb-pulse age water moving all the way through the PTn and to the potential repository elevation in the TSw constituting less than 1% of water for all samples underlying undisturbed PTn. This is far more consistent with the data reported by Levy et al. (1997). Figures 6-17 and 6-18 show the same property set comparison, but with the I/3 map. Substantial early arrivals are still predicted with the

6541a set whereas 6541b eliminates most PTn fracture flow in all locations except directly under the crest and in the Ghost Dance Fault. Note however, that the fault-zone properties in this simulation are specified with low matrix permeability and high fracture permeability.

In the next section, we demonstrate with the three-dimensional model that rapid travel through the PTn is more likely to be simulated in the southern portion of our domain (where this two-dimensional cross section falls) than in the northern portion. A final analysis with the two-dimensional model examines whether the bomb-pulse signals simulated at the top of the CHn with the 6541a parameter set actually resulted from vertical flow or whether lateral flow played a major role. Figure 6-14 shows the pathways in both the matrix and fractures for particles introduced in the system near faults and in faults. For particles injected near faults, there is a small amount of lateral diversion simulated at the top of the CHn, but most particles travel downward. For the particles injected in the fault, there is some tendency to move out of the fault into the high permeability matrix of the CHn, but most particles move downward staying in the fault.

### 6.10.3 Three-Dimensional Chlorine-36 Simulation Results

Simulations of chloride transport and  $^{36}\text{Cl}/\text{Cl}$  ratio distributions are simulated on the 143,000 node site-scale transport model. The domain and boundary conditions for the three-dimensional simulations are described in Section 6.8 and the grids are described in Chapter 3 of this report. Figure 6-19 shows north-south and east-west slices that intersect in the proposed repository block. The bomb-pulse has reached the top of the PTn, where its downward migration velocity has been retarded as the flow partitions from the TCw fractures into the PTn matrix. Figure 6-20 shows the results from the three-dimensional simulation at the ESF horizon. The simulated values in the matrix match those that were measured on ESF samples. Comparing Figure 6-20 and Figure 6-7, one can see the influence that the spatially distributed infiltration map of Flint et al. (1996) has on the simulated matrix  $^{36}\text{Cl}/\text{Cl}$  ratios. The lack of infiltration variability over most of

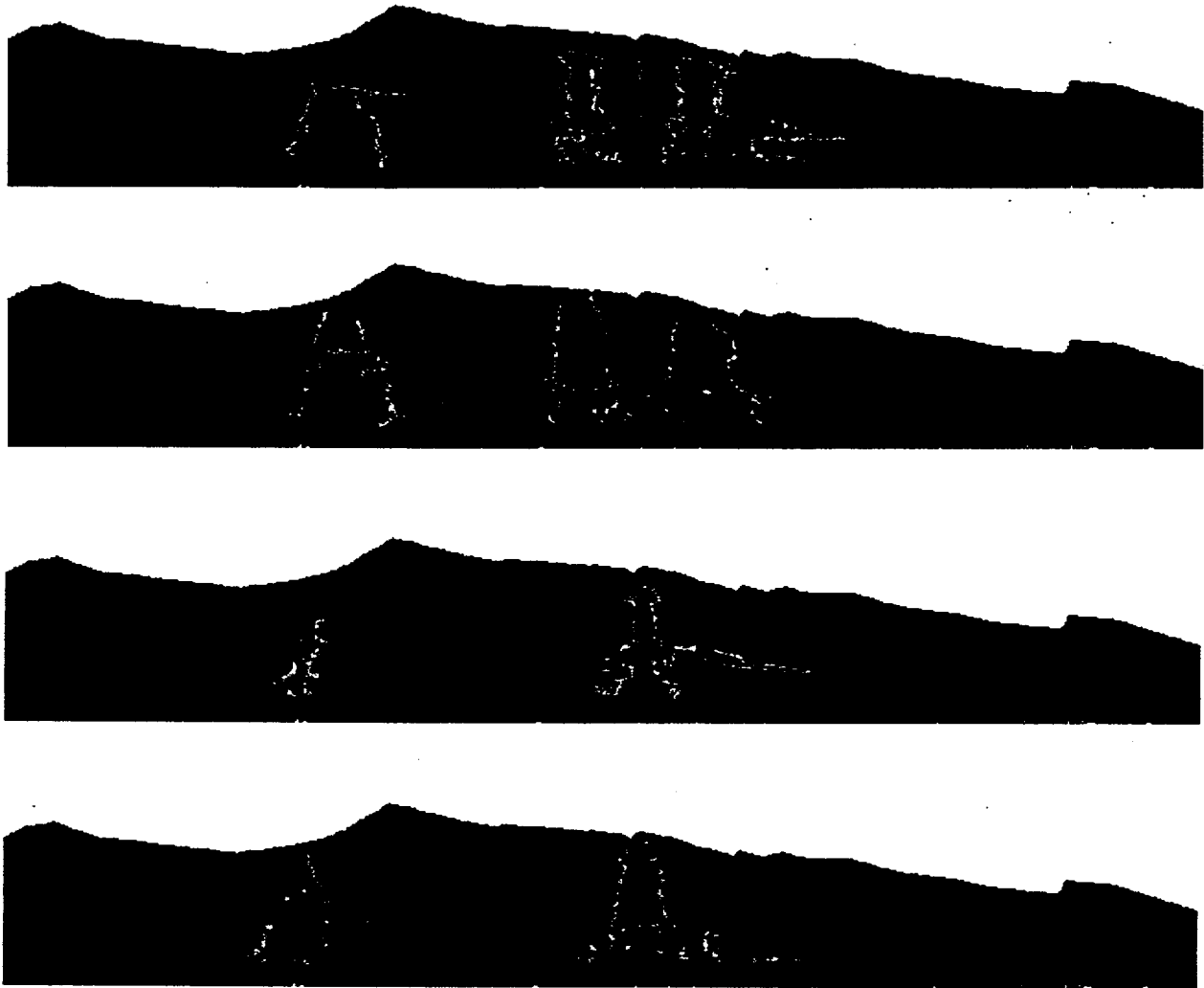


**Figure 6-14.** Particle pathways from 5 different surface locations. a) pathways in the matrix for locations near faults, b) pathways in the fractures for locations near faults, c) pathways in the matrix for locations in faults, d) pathways in the fractures for locations in faults.

the ESF relative to that over much of the rest of the domain leads to a fairly uniform simulated  $^{36}\text{Cl}/\text{Cl}$  ratio.

Figure 6-21 shows the resulting simulated matrix  $^{36}\text{Cl}/\text{Cl}$  ratio in the ESF from the three-dimensional model compared with the analyzed  $^{36}\text{Cl}/\text{Cl}$  ratios reported by Levy et al. (1997) and Sweetkind et al. (1997). After the ESF falls below the PTn, about 1100 m into the tunnel, the

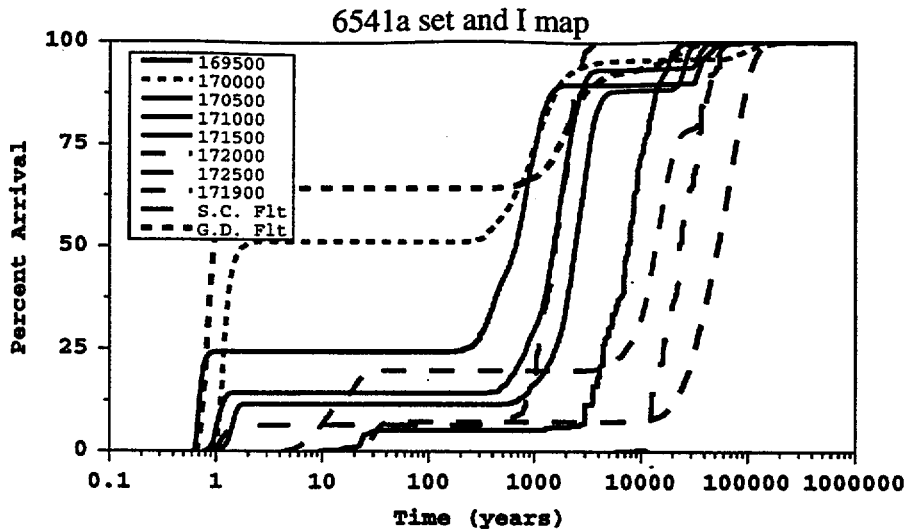


Figure 6-15. Breakthrough (or cumulative age distribution of a porewater sample) at elevation 1080 m at 10 locations along E-W Antler Ridge transect. Material properties are the 6541a set. Infiltration rate at surface is the Flint et al. (1996) map. Legend numbers indicate Easting location in NSP coordinates (Northing coordinate is 232100 m).

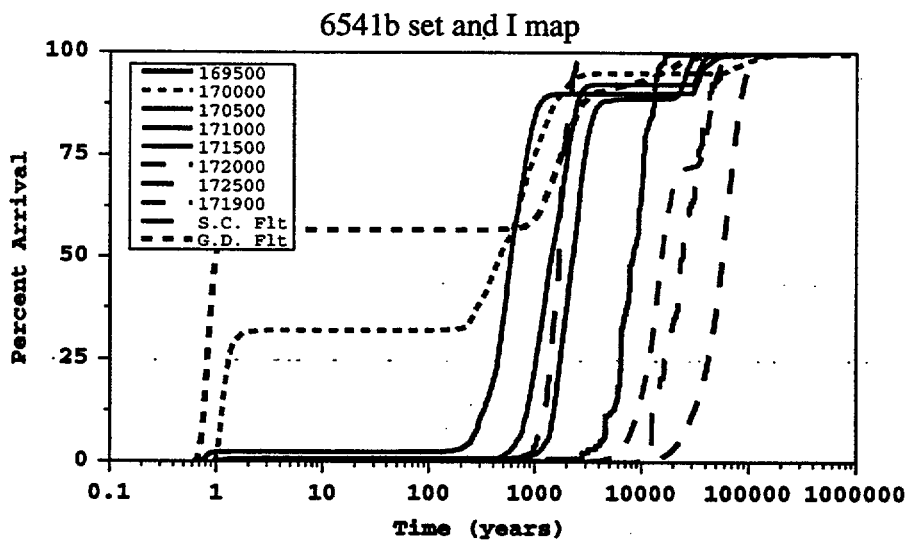


Figure 6-16. Breakthrough (or cumulative age distribution of a porewater sample) at elevation 1080 m at 10 locations along E-W Antler Ridge transect. Material properties are the 6541b set (*no weighting of fracture-matrix connection in PTn*). Infiltration rate at surface is the Flint et al. (1996) map. Legend numbers indicate Easting location in NSP coordinates (Northing coordinate is 232100 m)

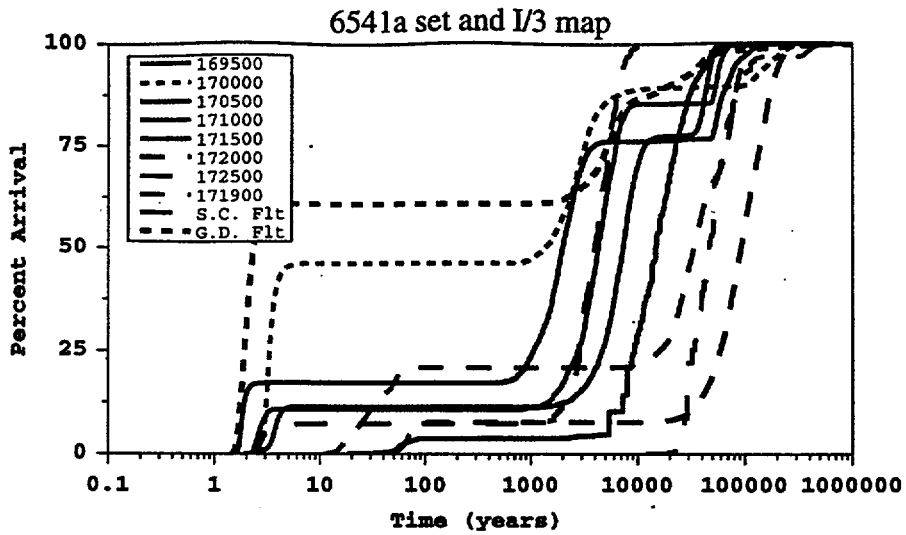


Figure 6-17. Breakthrough (or cumulative age distribution of a porewater sample) at elevation 1080 m at 10 locations along E-W Antler Ridge transect. Material properties are the 6541 set. Infiltration rate at surface is the scaled (I/3) map of Flint et al. (1996). Legend numbers indicate Easting location in NSP coordinates (Northing coordinate is 232100 m).

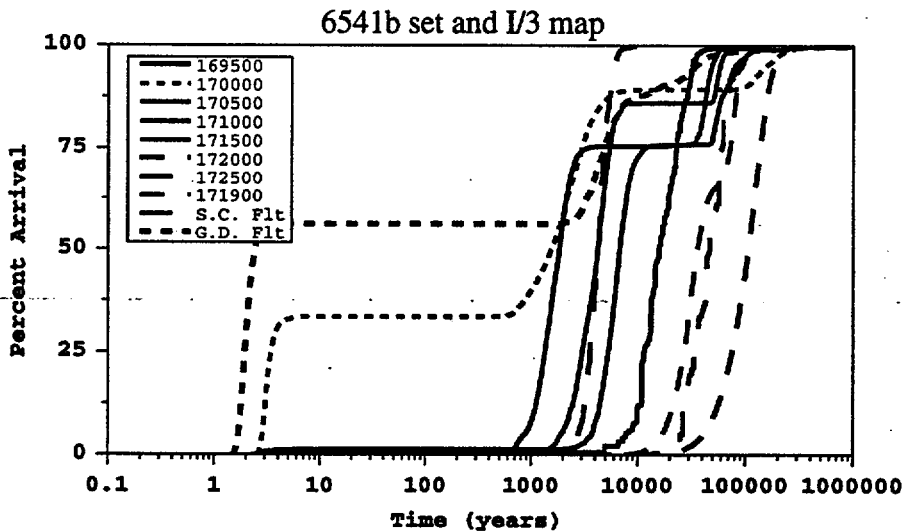
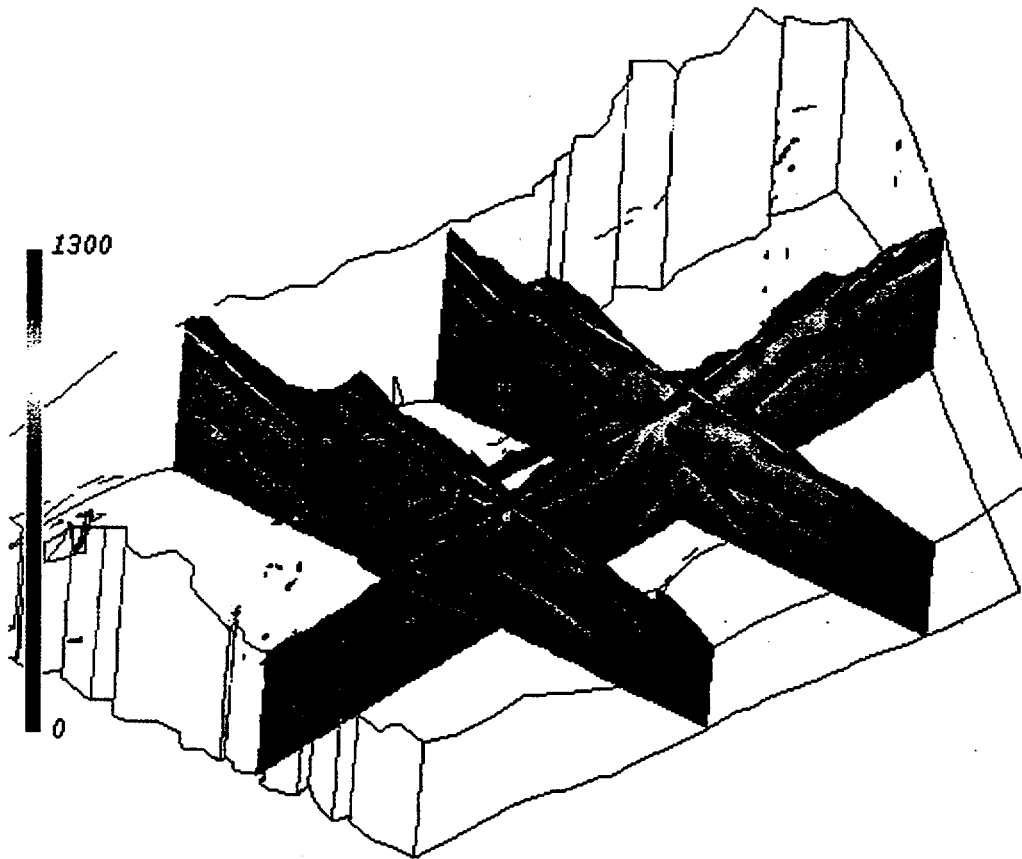
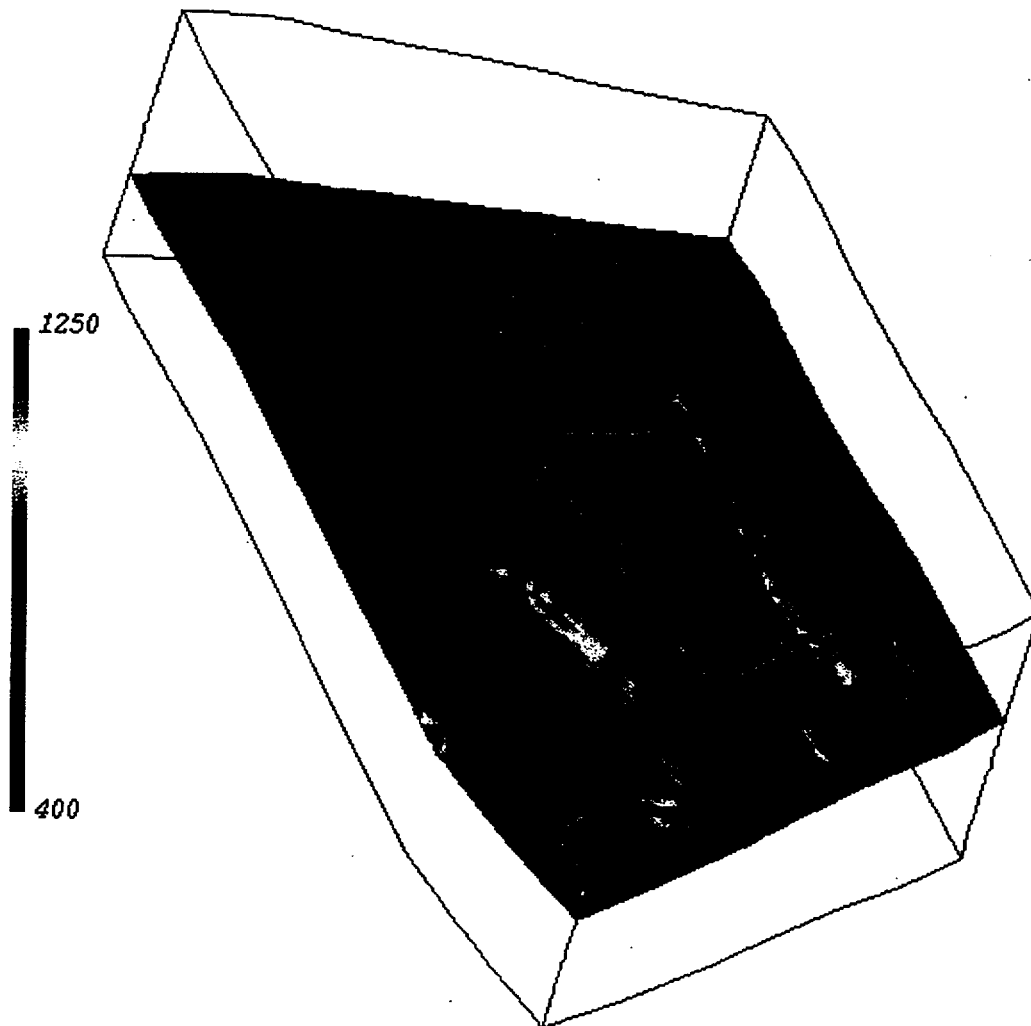


Figure 6-18. Breakthrough (or cumulative age distribution of a porewater sample) at elevation 1080 m at 10 locations along E-W Antler Ridge transect. Material properties are the 6541b set (*no weighting of fracture-matrix connection in PTn*). Infiltration rate at surface is the scaled (I/3) map of Flint et al. (1996). Legend numbers indicate Easting location in NSP coordinates (Northing coordinate is 232100 m).

simulated values tend to capture the mean behavior of the observed measurements. The bomb-pulse signals are not simulated as frequently as they occur in the data because only two of the many faults that cross the ESF (the Bow Ridge fault and the Ghost Dance fault) are included in the ISM geologic model (Clayton et al., 1996) and thus in our model. The effect of other faults such as the Sundance fault, the Drillhole Wash fault, and other unnamed faults (see Levy et al, 1997, Figure 1) must therefore be addressed with other means. These other means are discussed in the next section on process modeling in vertical columns.



**Figure 6-19.** Three-dimensional simulation of  $^{36}\text{Cl}/\text{Cl}$  ratios using property set 6541a and infiltration map of Flint et al. (1996).



**Figure 6-20.** Simulated  $^{36}\text{Cl}/\text{Cl}$  ratios at ESF horizon with three-dimensional transport model. Uses material property set 6541a and infiltration map from Flint et al. (1996).

### Flow and Transport Pathways

With the three-dimensional model, nonvertical pathways can be identified. Here, we inject a set of particles in Yucca Crest above the potential repository and model the path they take as they move into the system. The plume does not follow one distinct pathline due to the multiporosity system in which a particle has the option of several different paths at any given location. Chapter 4, the detailed description of the particle tracking algorithm, demonstrates how a particle in the matrix may either stay in the matrix or move into the fractures. Likewise a particle in the fracture

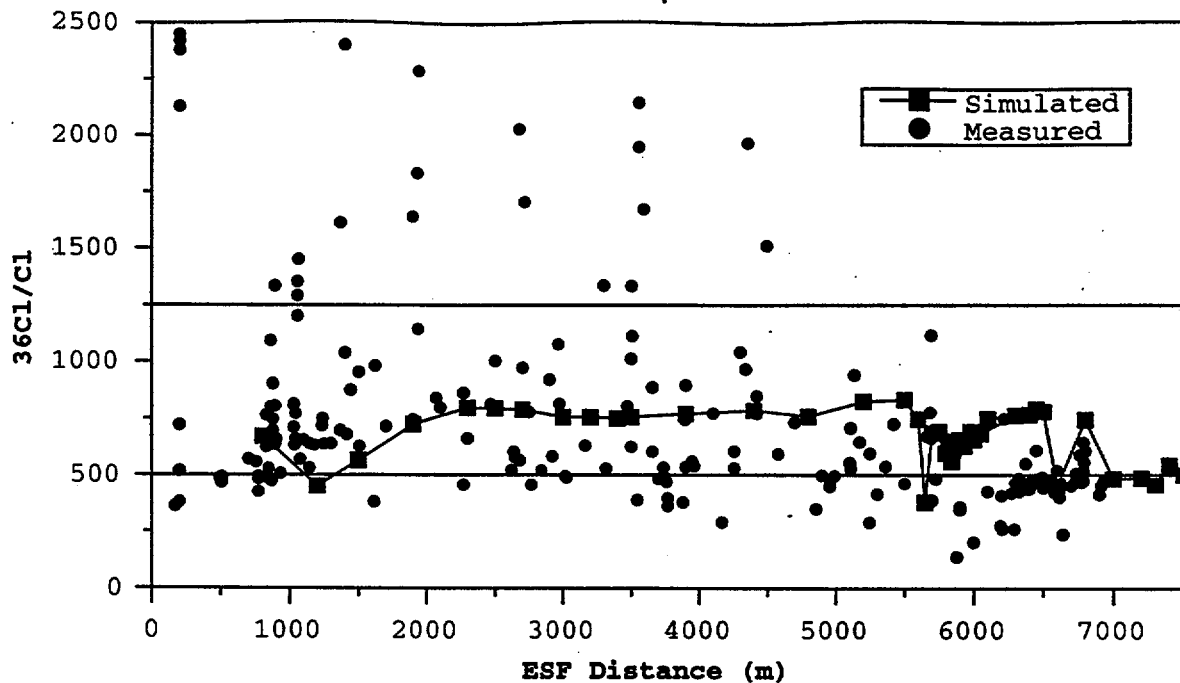


Figure 6-21. Simulated  $^{36}\text{Cl}/\text{Cl}$  ratio in ESF with 3-D transport model and measured ratios from Levy et al. (1997). Simulations performed using 6541 parameter set and Flint et al. (1996) infiltration map

may either move in the matrix or stay in the fracture. This type of behavior leads to dispersion of an instantaneously injected source in both time and space. Thus in the next section, a set of particles injected instantaneously over the surface yields breakthrough curves at the ESF spanning up to 4 orders of magnitude in time. Here the plume's injection location is (170600,234000) and Figure 6-22 shows the travel paths taken in the matrix. The less intense color in the TSw results because most simulated flow and, hence, particle transport occur in the matrix. After reaching the PTn, there is some spreading as flow partitions into the matrix. After reaching the CHn, there is increased lateral flow simulated due to the permeability contrast between the vitric and zeolitic material. Figure 6-23 shows the pathway in the Fractures for the same simulation. This figure highlights the density of flow in the TCw, TSw, and CHn zeolite fractures. Lower fracture flux densities are shown in the PTn and CHn vitric units. Even less later flow occurs in fractures than in the vitric matrix material of the CHn.

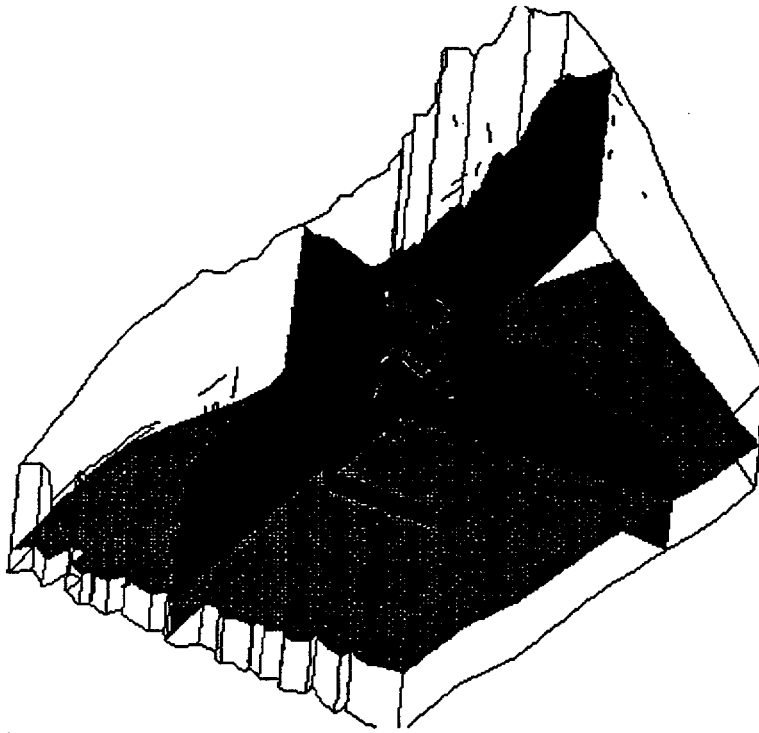


Figure 6-22. Solute travel path in the matrix from the top of Yucca Crest into the UZ system.

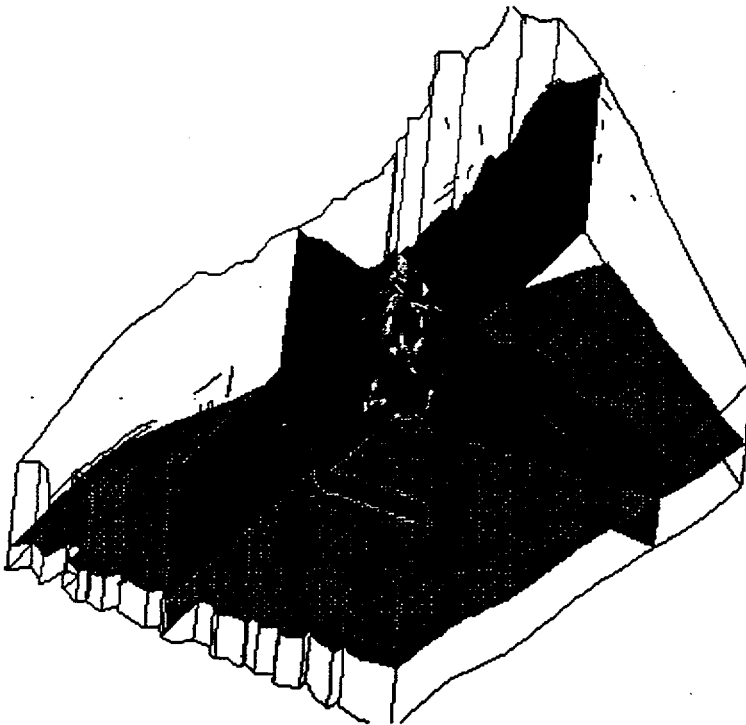


Figure 6-23. Solute travel path in the fractures from the top of Yucca Crest into the UZ system.

### Three-Dimensional Model Breakthrough Curve Analysis

As part of the parameter set comparison that was already described for the two-dimensional model, three-dimensional simulations using the 6541b property set, which was modified to eliminate the reduction factor for fracture/matrix coupling in the PTn, is compared with three-dimensional simulations using the 6541a set. The comparison involves simulating the breakthrough of solutes at the ESF from an instantaneously injected set of particles distributed over the surface of Yucca Mountain. The points for comparison are distributed along the ESF as well as at a few other representative locations such as a point in the middle of the potential repository and a point coincident with one in the two-dimensional model.

Starting with the ESF locations, Figure 6-24 shows the breakthrough curves for the first half of the ESF, up through Station 35. Figure 6-25 shows the breakthrough curves for the second half of the ESF, Stations 39 through 76. The difference between the northern half and the southern half is quite striking. Only at Station 8, a station in the TCw with no PTn above it, is there significant young water. This is entirely expected as our models predict rapid transport through the highly fractured TCw. Once the ESF dips under the PTn, however, very little early arrival is simulated all the way up through station 35. The simulated water ages at those stations range between 1000 and 10,000 years, and hence are on the correct order to yield  $^{36}\text{Cl}/\text{Cl}$  ratios similar to those measured by Fabryka-Martin et al. (1996b). The results for the southern half of the ESF differ significantly from those in the northern half. Early arrivals (up to 25% mass breakthrough) dominate this portion of the ESF, particularly once past Station 45. Simulated water ages for selected locations beyond Station 45 range between 2500 and 7000 years (Figure 6-25). However, in contrast with the breakthrough curves in the northern half of the ESF, is this faster breakthrough behavior due to the thinning of the PTn as measured in SD7 by Rautman and Engstrom (1996)? Or, do the parameters in 6541a lead to an unreasonably large proportion of fracture flow in the PTn? The occurrence of significant fracture flow in the PTn would have significant implications for repository design and performance as mentioned earlier. However, sample analyses in this

portion of the ESF show a dramatic decrease in measured  $^{36}\text{Cl}/\text{Cl}$  ratios in the southern half of the ESF, with none that can be identified as containing unambiguous bomb-pulse. In fact, as Figure 6-21 shows, some of the measured signals drop off well below background values, indicating possible decay of  $^{36}\text{Cl}$  due to long travel times from the surface to the ESF.

The poorer match of the simulated values to measured  $^{36}\text{Cl}/\text{Cl}$  ratios in the southern ESF than in the northern ESF is one cause for concern. Another is the divergence of these three-dimensional results from those obtained with the property set of Bandurraga (1996). With those properties, the simulated  $^{36}\text{Cl}/\text{Cl}$  ratios decreased substantially in the regions where measured sample ratios also decreased. There was a strong correlation between the data, those results, and the decreased infiltration rate above that region of low  $^{36}\text{Cl}/\text{Cl}$  values. Thus, we must consider the reliability of the geologic model and the property sets. The geologic model is assumed to represent the PTn fairly accurately since nearby SD7 is one of the wells on which the structural model is based. Like SD7, the geologic model is thinner in the PTn in the south, but the PTn is intact over the region where bomb-pulse time-scale arrivals are simulated.

To address the effect of small changes in PTn fracture/matrix coupling, we use the same parameter modification as we used in the two-dimensional study. Namely, the reduction in fracture-matrix coupling as a function of simulated fracture saturation is removed. Figures 6-26 shows the simulated cumulative age distributions of water at the northern ESF station when the modified parameter set, 6541b, is used. Comparing Figure 6-26 with Figure 6-24, we see that the small amount of early arrival is completely eliminated as a result of reduced fracture flow in the PTn. Station 8 still is dominated by early arrival of water as there is no PTn to delay transport to the ESF at that location.

Figure 6-27 shows the cumulative age distributions at the ESF stations beyond Station 35. Although not completely eliminated, the amount of early arrival at the ESF is significantly reduced from the 6541a case shown in Figure 6-24 for the same stations. This indicates that even without

the reduced fracture-matrix coupling, some fracture flow is simulated in the PTn with these properties.

What controls whether or not significant flow occurs in the PTn fractures? Certainly, the fracture permeability plays a major role (Robinson et al., 1996) as well as the matrix potential at the simulated saturation. Both of these are a function of the flow rate. Therefore, as with the two-dimensional model runs, we examine the effect of reducing the flow rate by a factor of three. Figures 6-28 and 6-29 show the breakthrough curves for the case of modified PTn parameters, 6541b, and reduced infiltration rate. One interesting observation is that this case leads to even less fracture flow in the PTn and hence less early arrival in the ESF at the southern stations. More interesting, however, is that at all stations, the mean sample age is closer to 10,000 years than 1,000 years. This result is a closer match to our inferred ages from all of the ESF samples. Namely, to explain the  $^{36}\text{Cl}/\text{Cl}$  ratios measured in the ESF, age distributions that include some portion which is greater than 10,000 is necessary.

An alternative conceptual model is that all ESF samples with  $^{36}\text{Cl}/\text{Cl}$  ratios greater than present day background indicate mixing with bomb-pulse signals. This conceptual model suggests that all water flowing past the ESF is very young and that none of the elevated signals represent water that entered the system with a higher than present day background signal over 10,000 years ago. We find that model inconsistent with data and any of the hydrologic parameters. With that model, greater bomb-pulse era arrivals should be simulated in the northern part of the ESF where the elevated  $^{36}\text{Cl}/\text{Cl}$  ratios are measured. To the contrary, we simulate more fast transport to the ESF in the southern ESF where most of the data are at or below present day background. This line of evidence is further explored in Chapter 7 where other chemical data sets are evaluated.

### **6.10.4 South to North Trends in Potential Repository Block Region**

In the three-dimensional simulations, we observe a greater propensity of early arrival at the southern stations of the ESF than in the northern stations. Likewise, all of the potential repository horizon locations, as well as some east of the Ghost Dance Fault, in the two-dimensional cross

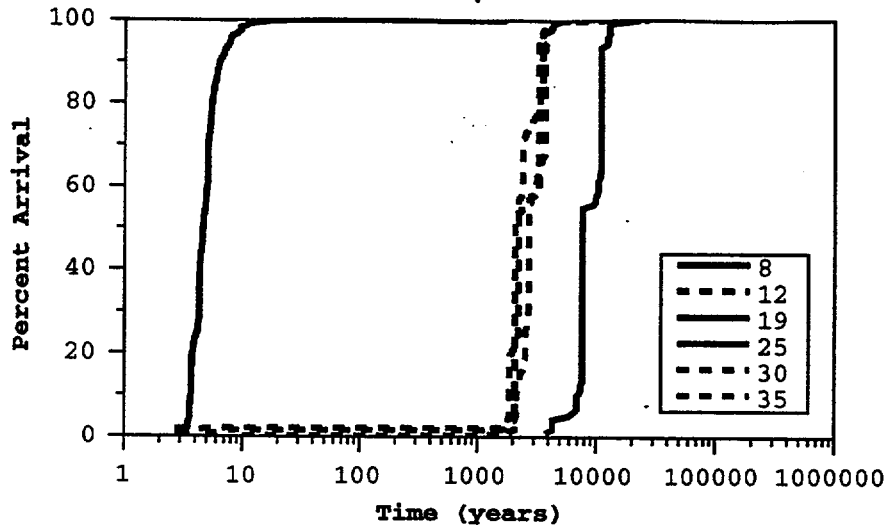


**Figure 6-24.** Breakthrough (or cumulative age distribution of a porewater sample) in northern ESF simulated with 3D model. Material properties are the 6541a set. Infiltration rate at surface is the map of Flint et al. (1996). Legend numbers indicate ESF Station numbers (in hundreds of meters).

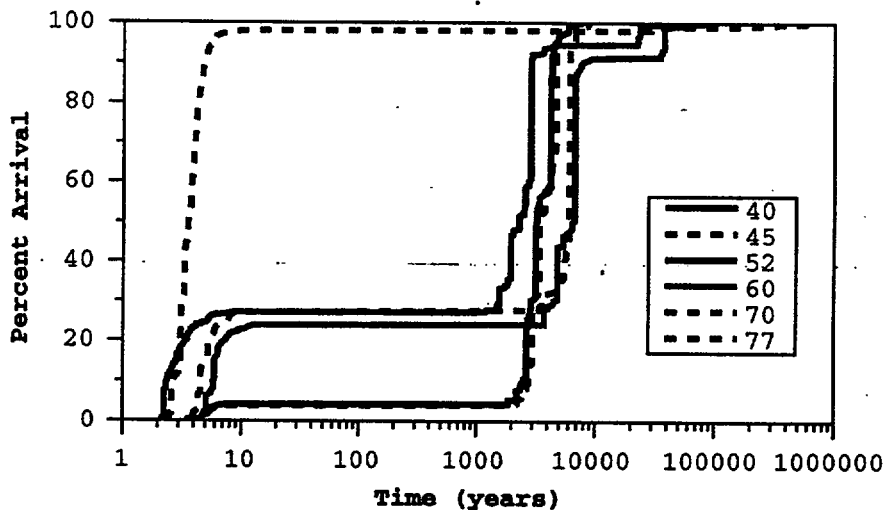


**Figure 6-25.** Breakthrough (or cumulative age distribution of a porewater sample) in southern ESF simulated with 3D model. Material properties are the 6541a set. Infiltration rate at surface is the map of Flint et al. (1996). Legend numbers indicate ESF Station numbers (in hundreds of meters).

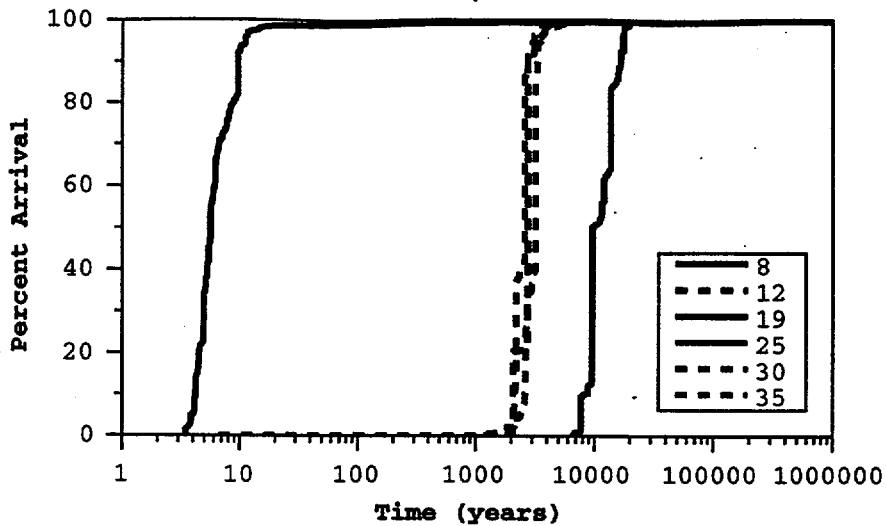


Figure 6-26. Breakthrough (or cumulative age distribution of a porewater sample) in northern ESF simulated with 3D model. Material properties are the 6541b set (*no weighting of fracture-matrix connection in PTn*). Infiltration rate at surface is the map of Flint et al. (1996). Legend numbers indicate ESF Station numbers (in hundreds of meters).

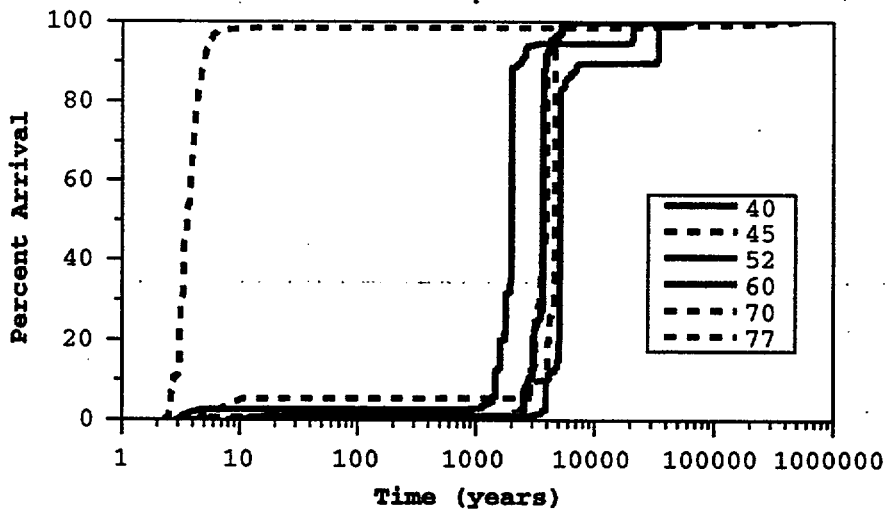
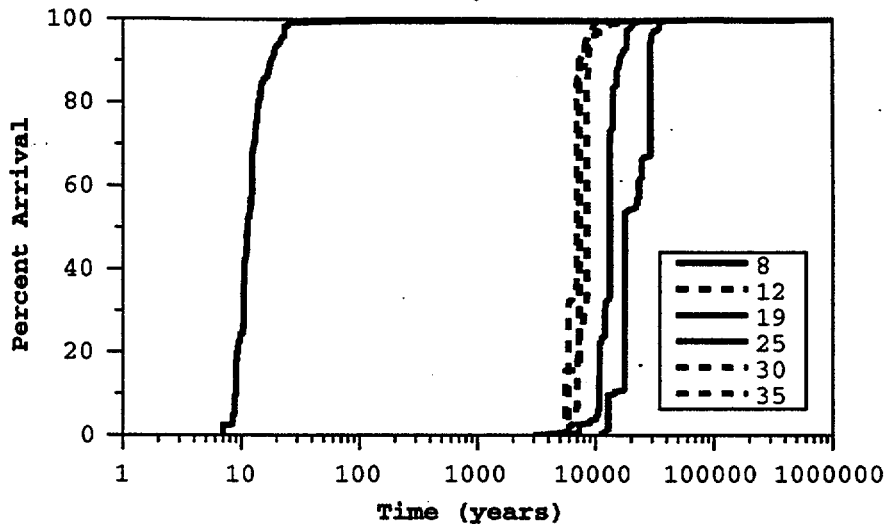
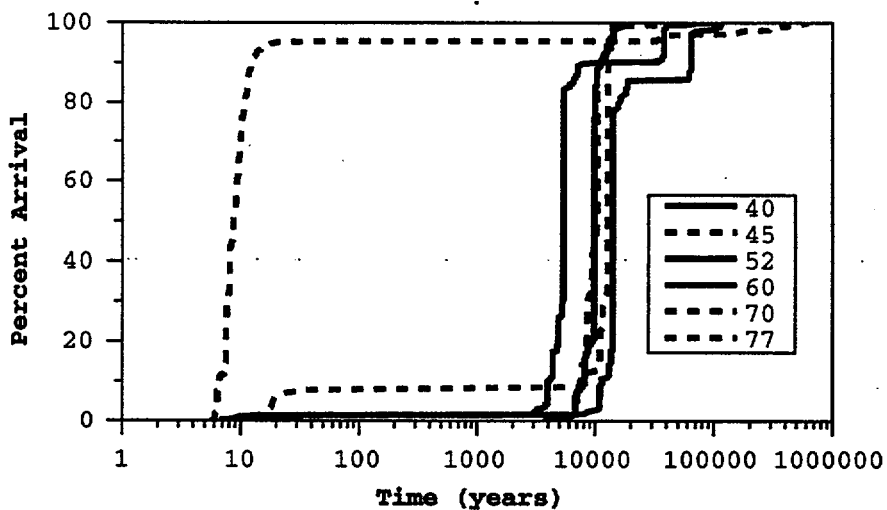


Figure 6-27. Breakthrough (or cumulative age distribution of a porewater sample) in southern ESF simulated with 3D model. Material properties are the 6541b set (*no weighting of fracture-matrix connection in PTn*). Infiltration rate at surface is the map of Flint et al. (1996). Legend numbers indicate ESF Station numbers (in hundreds of meters).



**Figure 6-28.** Breakthrough (or cumulative age distribution of a porewater sample) in northern ESF simulated with 3D model. Material properties are the 6541b set (*no weighting of fracture-matrix connection in PTn*). Infiltration rate at surface is the scaled (1/3) map of Flint et al. (1996). Legend numbers indicate ESF Station numbers (in hundreds of meters).



**Figure 6-29.** Breakthrough (or cumulative age distribution of a porewater sample) in southern ESF simulated with 3D model. Material properties are the 6541b set (*no weighting of fracture-matrix connection in PTn*). Infiltration rate at surface is the scaled (1/3) map of Flint et al. (1996). Legend numbers indicate ESF Station numbers (in hundreds of meters).

section (located at NSP Northing coordinate 232100) showed some indication that fast paths through the PTn were possible, especially with the 6141a property set. Since the PTn is thinner at that northing location, we performed a series of breakthrough simulations along a north-south transect through the potential repository block under a band of high infiltration estimates. This transect is located in Figure 6-3, and Figure 6-7 shows it relative to the estimated infiltration map of Flint et al. (1996).

The north-south transect was also designed to intersect the east-west transect that was used for the two-dimensional model simulations as well a one-dimensional column study in the middle of the potential repository block. Results from the three-dimensional transport model at eight locations approximately 500 m apart are reported for this analysis. The locations range from Northing 231500 m to 235000. Figures 6-30 and 6-31 show the breakthrough curves at all 8 locations for 4 different parameter sets. Starting with the 6541a parameter set and the I infiltration map, we see clearly that moving north leads to a decrease in the amount of early arrival that is simulated at the ESF. The potential repository location at NSP Northing 232100, which corresponds with the east-west cross sections, shows the same behavior at this Easting coordinate. Comparison of the red line in Figure 6-15 and the red line in Figure 6-30a shows virtually identical behavior with the exception that the median age in the two-dimensional simulation is slightly younger than that in the three-dimensional simulation. Both simulations show about 20 percent (25 percent in the two-dimensional case) early arrival (i.e., less than 50 years).

Moving north along the north-south transect, the effects of the thickening PTn are clearly evident. The percentage of bomb-pulse era arrivals decreases until they represent less than a few percent north of NSP 233500 m. Also, as the PTn thickens, the median travel time to the repository horizon increases.

Figure 6-30 also show the simulated breakthrough curves along the north-south transect using the 6541b set (no reduction in fracture-matrix coupling in PTn). The results for this case show similar curves to the 6541a case, except there is far less early arrival because fracture flow is

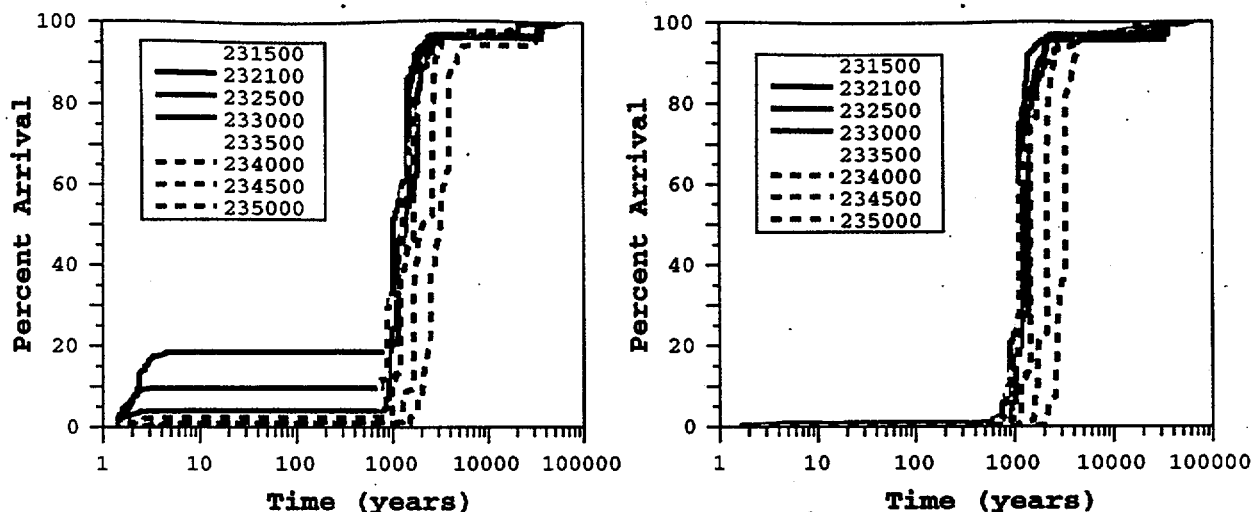


Figure 6-30. North-South transect cumulative age distributions at potential repository horizon using I infiltration map. a) Property set 6541a b) Property set 6541b. Legend indicates northing coordinate. Easting coordinate is 170600 m.

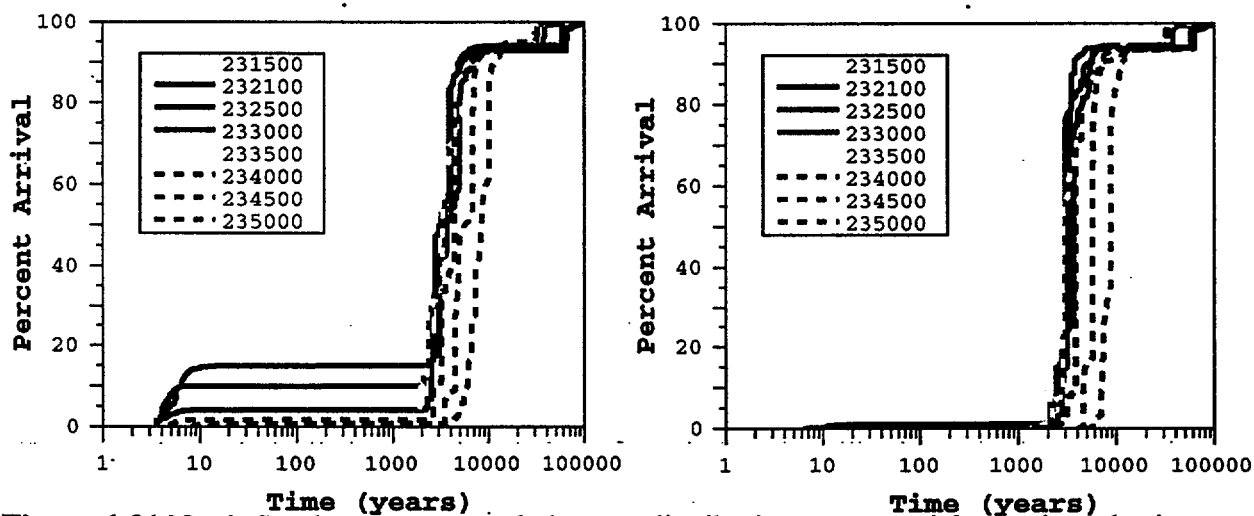


Figure 6-31. North-South transect cumulative age distributions at potential repository horizon using I/3 infiltration map. a) Property set 6541a b) Property set 6541b. Legend indicates northing coordinate. Easting coordinate is 170600 m.

not sustained in the PTn, even for these high infiltration rates. Recall that the simulated saturations in the PTn differ minimally between the 6541a and 6541b case. The implications in terms of significance of episodic pulses however may be significant. We investigate such issues in the next

section with one-dimensional column models at three representative locations capturing the variation in PTn thickness.

As part of the north-south transect study, we also investigate the response for a reduced infiltration map. Here we use the *I/3* map (Flint's map scaled by 1/3). Figure 6-31 shows the response for both parameters sets 6541a and 6541b. Even with the lower infiltration rate, early arrivals are simulated with the 6541a set whereas they are almost non-existent, even in the southern locations, with the 6541b set.

### Implications

Two important results can be derived from this study using the three-dimensional model to simulate arrival times along the north-south transect. First, a slight variation in material properties leads to significantly different results, especially in the southern section of the proposed repository block where the overlying PTn is thinnest. Reducing the uncertainty could have significant implications for repository design under that section of the PTn. Further north, the difference is less dramatic and probably less important. Second, regardless of the properties used to simulate flow and transport through the PTn, the higher percolation fluxes above the potential repository, relative to those above the ESF, lead to significantly faster transport from the surface to the potential repository. In most locations along this north-south transect, simulated ages are less than 10,000 years. Thus, we would expect to find  $^{36}\text{Cl}/\text{Cl}$  ratios more representative of the present day signal of  $500 \times 10^{-15}$ . If data collection ever occurs in that region, detection of ubiquitous bomb-pulse signals for  $^{36}\text{Cl}$  and other isotopes would help determine which PTn property set is most appropriate.

In the next section, we perform more detailed analysis at three locations. One of the locations is identical to the location used in the north-south transect study at NSP coordinates (230600, 234000) which is the red dotted line in Figures 6-30 and 6-31.

### 6.11 Carbon-14 Modeling

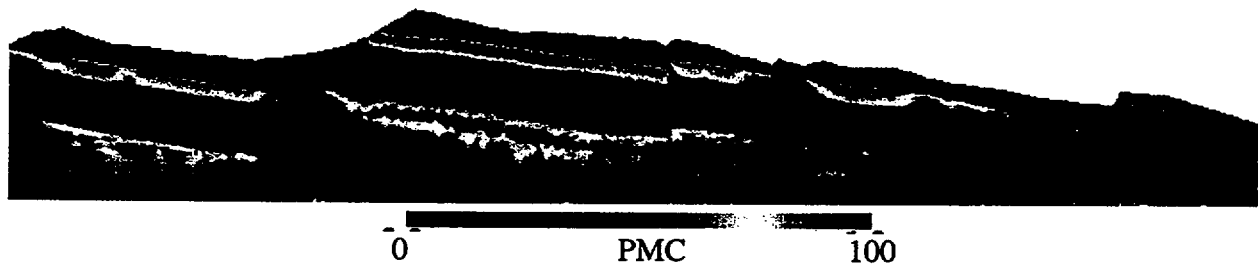
---

Although  $^{14}\text{C}$  can move both in the gas phase and the liquid phase, only liquid phase migration is considered in the present study. Previous studies by Viswanathan (1996) have examined gas phase migration of  $^{14}\text{C}$  and phase partitioning with the liquid phase at Yucca Mountain. A basic conclusion of that study is that if the gas phase and liquid phase are in contact with each other, rapid gas phase migration could cause liquid phase measurement to yield apparent ages lower than the actual age of the water at the sample location. Neglecting that possibility, accounting for liquid phase only leads to a conservative estimation on the age of the porewater or perched water samples.

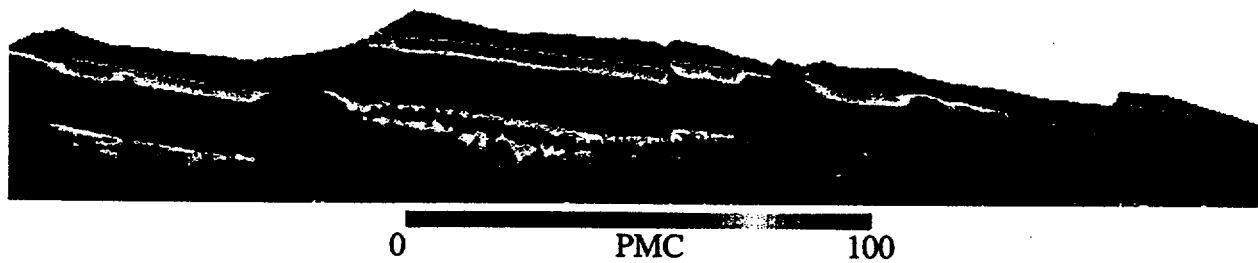
In the present study, infiltration variations as estimated by Flint et al. (1996) and a scaled version of that map are considered on the two-dimensional cross section. Two different property sets are also considered. One property set leads to more fracture flow in the PTn than the other. We also consider two different representations of the basal vitrophere properties. One case is the base-case property distribution. The other has a reduced fracture permeability that leads to lateral diversion to a semi-impervious fault which creates a perched water body.

Figure 6-32 shows the simulated percent modern carbon distribution in the matrix material. Due the fracture dominated flow in the welded units, there is no modern carbon in the matrix of those units. The PTn matrix shows very modern water as a result of the rapid transport through the TCw. After moving through the PTn, the water again moves quickly through the TSw to the CHn. Therefore, the ages in the CHn are representative of the travel time through the PTn. The ages simulated there are consistent with the breakthrough curves in Figure 6-15 with apparent ages ranging between 400 and 5000 years between Yucca Crest and the Ghost Dance fault and falling off to the west with the decrease in infiltration. Using the 6541b parameter set leads to no apparent difference as is shown in Figure 6-33. This is not surprising since the property change led only to small differences in the amount of flow in the PTn fractures. The majority of the flow, and hence the major contribution to an apparent age follows the same travel path which includes some flow

in the PTn matrix. Also, no bomb-pulse signature is attached to the  $^{14}\text{C}$  input function in these simulations, hence no elevated signal at depth. Figure 6-34 shows the resulting  $^{14}\text{C}$  for the perched water model. Percent modern carbon in the fractures is displayed as well as in the matrix. Since 6541a properties are used, young water, albeit a small amount, is shown throughout the PTn fractures under regions of adequate infiltration rate. In the saturated matrix, the apparent ages are on the order of 1000 years for the I infiltration map and 2000 years for the I/3 map. These ages certainly are not indicative of the travel times to the ESF but they occur in a region of much higher infiltration rate. Moving east, the apparent ages increase with decreasing infiltration rate. For further discussion on the perched water model, see Chapter 7.



**Figure 6-32.** Carbon-14 simulation with Flint et al. (1996) infiltration map and 6541a properties. Values plotted are percent modern carbon (PMC)



**Figure 6-33.** Carbon-14 simulation with Flint et al. (1996) infiltration map and 6541b properties. Values plotted are percent modern carbon (PMC)

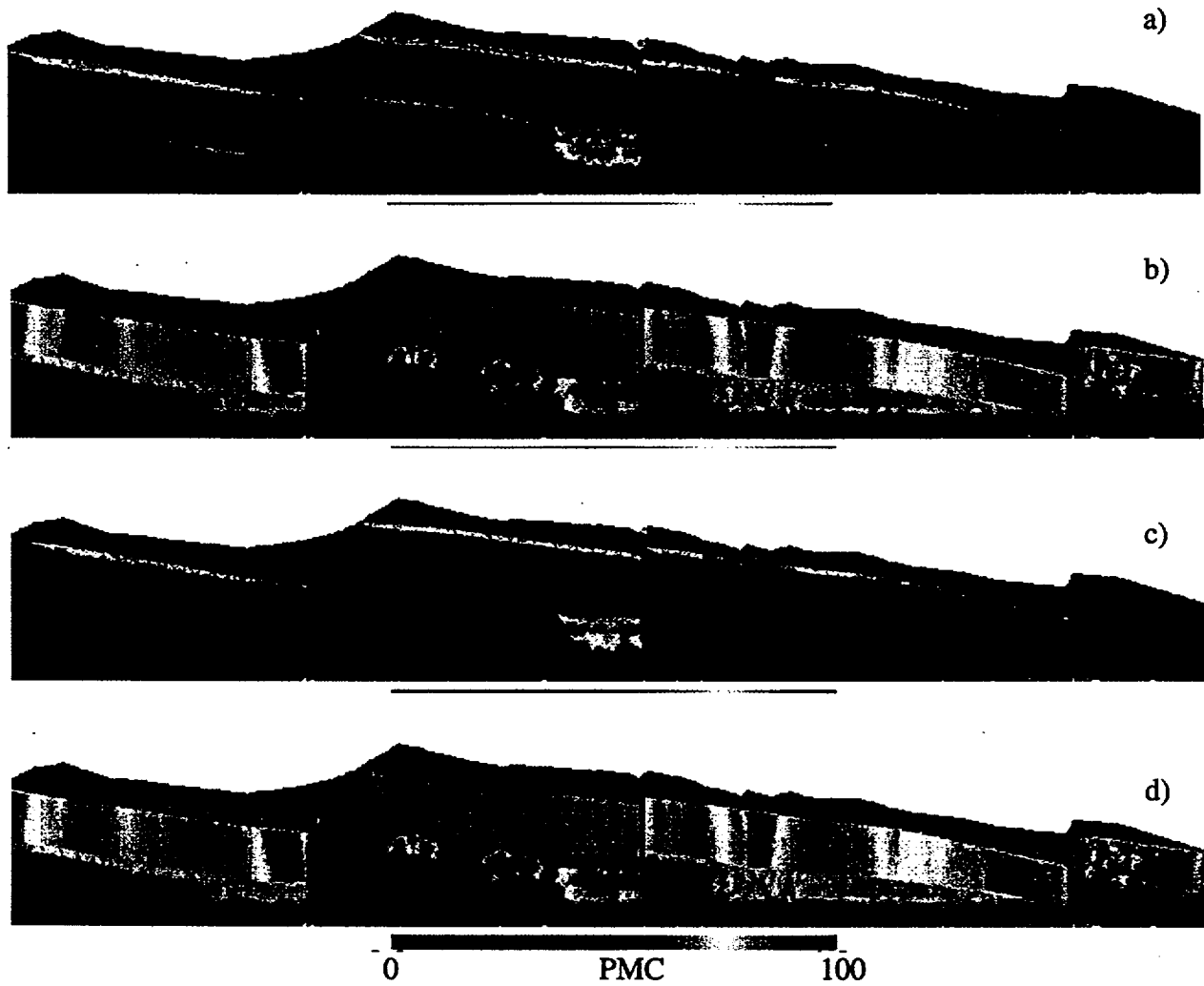


Figure 6-34. Carbon-14 simulation for perched water simulation. Values plotted are percent modern carbon (PMC). a) Matrix PMC with I map, b) Fracture PMV with I map, c) Matrix PMC with I/3 map, d) Fracture PMC with I/3 map

### 6.12 One-Dimensional Process Level Modeling

---

A series of column modeling studies were performed to provide greater sensitivity analysis of significant processes and model parameters. Three columns were selected as representative of the different regimes encountered at Yucca Mountain. Two are coincident with ESF stations 35 and 57 and one falls in the middle of the proposed repository block and occurs at the same location as one of the north-south transect study points.

#### 6.12.1 Column Descriptions

Figure 6-35 shows the unit definitions of the three columns used in this study. The primary factors controlling the solute transport rate through these systems are 1) the infiltration rate, 2) the material properties of the PTn, and 3) the thickness of the PTn. A range of infiltration rates and multiple property sets are used in the sensitivity simulations. The PTn thickness remains fixed because the columns are extracted from the 3D site-scale geologic model. In each of the column descriptions below, the PTn thickness is listed.

##### ESF Station 35

Station 35 is a location where the three-dimensional simulation did not predict significant early arrivals. It is also a location near which both bomb-pulse  $^{36}\text{Cl}/\text{Cl}$  ratios and ratios indicative of 10,000+ year old water have been found by Fabryka-Martin et al. (1996b). The bomb-pulse signal has been correlated with structural features by Levy et al. (1997). The infiltration rate above Station 35, according to Flint et al. (1996) is about 3 mm/year. This is also a location at which we demonstrated the consistency between fault-zone and base-case model results as compared with field data and infiltration estimates (Robinson et al., 1996). The location of the Station 35 column in NSP coordinates is (171277, 233393) and the PTn thickness is 42 meters.

##### Repository Column

The repository column was chosen to be located in a zone of high estimated infiltration in the middle of the proposed repository block. The estimated infiltration rate here is about 13 mm/

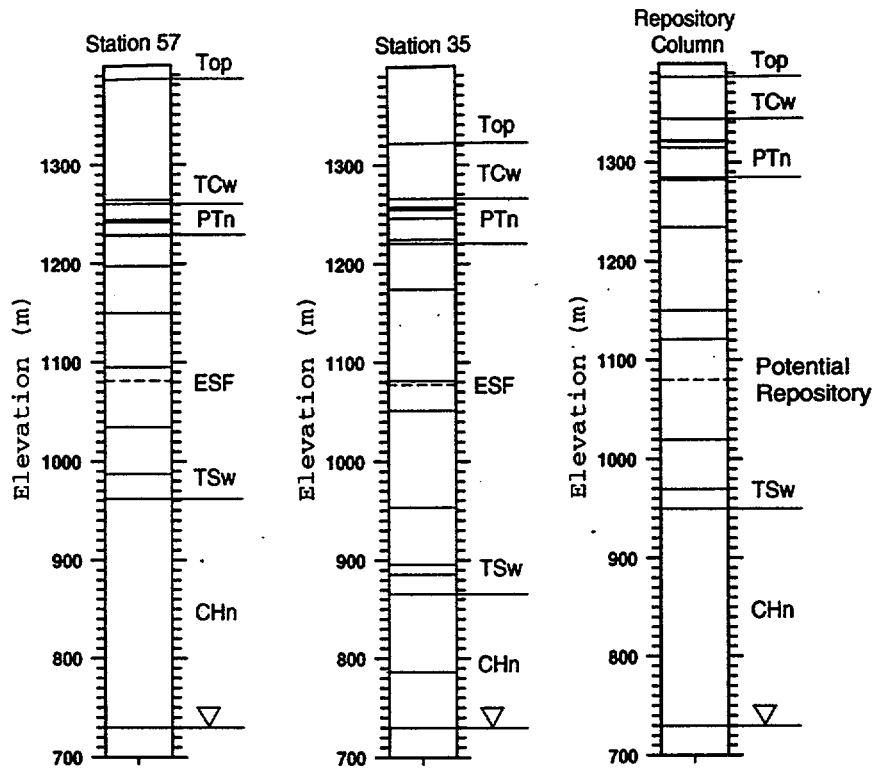


Figure 6-35. Schematics of three columns used in one-dimensional model studies.

yr. One reason this column was chosen is to test the implication that episodic transients penetrating the PTn are most important where the flow path reaches the potential repository horizon. The PTn is 58 meters thick here, significantly greater than over the ESF. The location of the repository column in NSP coordinates is (170600, 234000).

ESF Station 57

Station 57 represents a unique location both in terms of the geology and the measurements that were made on samples from that location. The geology above station 57 is characterized by thinner PTn than is found further north and west (c.f. Rautman and Engstrom, 1996). This is also near where the Ghost Dance fault crosses the ESF. However, unlike Station 35, where bomb-pulse  $^{36}\text{Cl}/\text{Cl}$  levels were found and attributed to a fault, no unambiguous bomb-pulse signal has been found at or near this ESF station. However, one isolated peak signal at Station 56 +93 may be

suggestive of bomb-pulse. Station 57 poses high potential for bomb-pulse signal in that the PTn is only 30 meters thick. But, the infiltration rates estimated by Flint et al. (1996) are significantly lower (about 1 mm/yr) than above other ESF stations where bomb-pulse  $^{36}\text{Cl}/\text{Cl}$  has been found. The Station 57 column is located at NSP coordinates (171160, 231200)

### 6.12.2 One-Dimensional Modeling Approach

The systematic modeling approach taken for each of the three columns serves to investigate process sensitivity to parameter variations and flux variations. For each parameter set investigated, simulations of flow and transport are run with mean infiltration rates ranging between 1 and 50 mm/yr. The parameter sets we look at include: the base and modified set, 6541a and 6541b respectively; the base-case set, 6412b, as reported by Bodvarsson et al. (1997); and a fault-zone set, 6541ft, that is based on the 6541a set but with increased fracture permeability in the PTn. The basis for increasing the permeability in the PTn as a result of tectonic activity is discussed in detail in Robinson et al. (1996). The principle behind this parameter set lies with the fact that nonwelded units tend to have very low bulk fracture permeability relative to the welded units. In fault zones, however, increased fracture permeability in the PTn occurs either as a result of more fractures or greater fracture apertures. The increased permeability in faults through the PTn has been inferred from the field air permeability testing (Rousseau et al., 1996). Indications are that the permeability in a fault zone in the nonwelded rock may increase by one to two orders of magnitude.

#### Steady-State Flow

Flow and transport are first simulated on each column with uniform annual infiltration rates of 1, 5, 10, 20, and 50 mm/yr. With these steady-state flow fields, particles are inserted into the fractures of the TCw and their breakthrough at the potential repository horizon is monitored. The simulated saturation and flux distribution between fractures and matrix for each flow rate and parameter set is recorded; some are plotted in this section for comparison.

### Transient Flow

Both the UZ flow model (Bodvarsson et al., 1997) and this UZ transport model operate on the assumption that episodic transients, which are precipitation events that occur on the scale of days, are damped in the PTn and that the flux leaving the PTn and entering the TSw is constant over time. This does not include large transients that occur over the scale of thousands or tens of thousands of years. The occurrence of bomb-pulse at depth in the PTn and the naturally fractured system highlights the question whether episodic events are actually damped. Therefore, in addition to the studies which use steady state flow fields, we also examine the migration of solutes from the surface to depth under transient cases.

The exact nature of transient infiltration is not known at Yucca Mountain. However, Flint (personal communication) has suggested that infiltration only occurs every several years under extensively wet conditions and over short time frames. Therefore, to effectively test the extreme case, we implemented a set of transient simulations to examine if very large pulses of water occurring only every 5, 8 or 10 years can create sustained fracture flow in the PTn when steady-state simulations with the same annual average infiltration rate do not. The implications are that, if the flow entering the potential repository is not uniform, then higher fluxes over shorter time periods will need to be considered both by engineering and by radionuclide transport modeling.

Unlike other investigations of episodic flow effects which used only a single pulse and simulated to a maximum of 50 years (Bodvarsson et al., 1996, 1997), we use a recurring episodic pulse and simulate for up to thousands of years. To compare with the transport on steady state flow fields, we take all the water that would be associated with a given period of time and apply it to the system over a specified short episode. Table 6-5 gives the transient model names and the parameters governing the amount of water, how often it is applied, and over what duration it is applied. For example, a 10-5-90 simulation indicates applying all of the water associated with 5 years at an average of 10 mm/yr infiltration (i.e. 50 mm) over a 90 day period once every 5 years.

**Table 6-5. Transient Model Description**

Model Name	Avg. Annual Infiltration rate (mm/yr)	Frequency of Application (yrs)	Duration (days)
10-1-10	10	1	10
10-1-90	10	1	90
10-5-10	10	5	10
10-5-90	10	5	90
20-5-10	20	5	10
50-5-90	50	5	10

### 6.12.3 Steady-State Results

#### Steady-State Flow with Parameter Set 6541a (the PA base-case)

Starting with the base-case parameter set, 6541a, and different flow rates, we examine the sensitivity of transport from the surface to the ESF or potential repository horizon. Figure 6-36 shows the breakthrough curves for the three columns for flow rates ranging between 0.5 and 10 mm/yr. With these simulations, the relationship between PTn thickness, flow rate, and travel time is demonstrated. For any given flow rate, the travel times are greatest in the repository column because it has the thickest PTn. However, the difference in breakthrough curves for the three columns for the 50% breakthrough (the median age), is fairly small. For example, at 5 mm/yr the difference between the high and low 50% breakthrough is less than 2000 years. The flow rate, regardless of station location, has a significant impact on simulated travel times. For flow rates spanning the range from 0.5 to 20 mm/yr, the 50% arrival ranges from 20,000 down to 800 years. With <sup>36</sup>Cl/Cl analyses in the ESF possibly indicating ages in excess of 10,000 years, these simulations indicate that a flow rate less than 5 mm/yr is necessary at that location in order to obtain travel times on that order.

Station 57, with the thinnest PTn of the three columns, yields the fastest travel times for any given flow rate. With this parameter set, Station 57 is the only one of the three columns that predicts appreciable bomb-pulse signals, although there is a trace of bomb-pulse at the other two locations for the higher flow rates. To yield a bomb-pulse signal, sustained fracture flow in the PTn is required because simulated travel times in the matrix with these properties are always greater than 50 years, even in the thin PTn at Station 57. Sustained fracture flow in the PTn is more likely where the PTn is thinner because there is less total thickness over which water starting out in PTn fractures (being fed by TCw fractures) can be imbibed into the matrix. To demonstrate this point, Figure 6-38 shows the simulated distribution of flux between matrix and fractures in the Station 35 column and Figure 6-39 shows the simulated flux distribution in the Station 57 column. At Station 35, there are over 25 meters in the PTn (between elevation 1220 and 1250) in which the fractures are dry. Conversely, at Station 57, the PTn fracture flow only approaches zero for a very short distance. In fact, the fractures in the PTn never completely dry out and account for as much as 1% of the total flow at higher infiltration rates as is shown in the expanded view in Figure 6-39. This small component of high velocity flow leads to the small component of early arrival at Station 57 as shown in Figure 6-36.

These results are consistent with both the two- and three-dimensional simulations reported earlier in this chapter. Namely, in the southern portion of the study area, the PTn is thinner and simulations with the 6541a parameter set lead to some early arrival at the potential repository horizon. Moving further north, the PTn thickens, and fracture flow in the PTn is no longer sustained for the entire thickness, except at isolated locations as discussed later under fault zones.

The  $^{36}\text{Cl}/\text{Cl}$  data analyses in the southern ESF have shown no bomb-pulse ratios. Yet, these simulations indicate that the southern ESF is the most likely place to find such signals. However, the infiltration rates estimated by Flint et al. (1996) are relatively lower here than further north. Thus, the findings of Robinson et al. (1996) and Fabryka-Martin et al. (1996b) which indicate that a sufficient condition for fast path travel to the ESF requires both the potential for sustained

fracture flow in the PTn and adequate flow rates to yield such sustained flow would indicate that adequate infiltration rates are really not occurring above the southern ESF. Even with this property set, the potential for sustained flow decreases with decreasing infiltration rates. Therefore, these results indicate that the infiltration rate in the region above Station 57 are low, probably lower than 1 mm/yr. Later in this chapter we investigate the potential for episodic infiltration events to yield fast paths to the ESF at all three of the locations considered here.

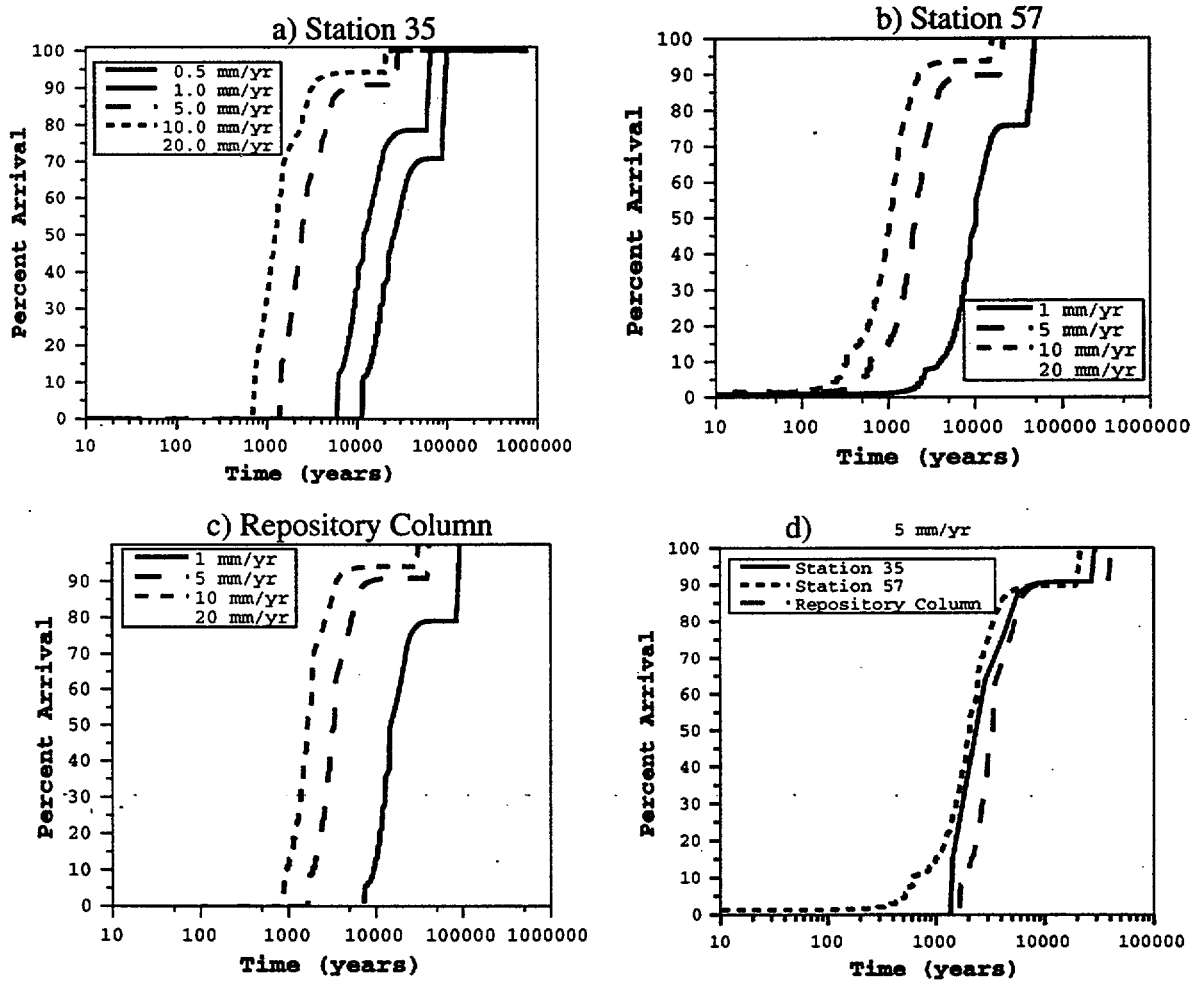


Figure 6-36. Breakthrough curves at ESF/potential repository level for a) Station 35, b) Station 57, c) the repository column, and d) a comparison of the three at 5 mm/yr. Steady state infiltration varying between 0.5 and 20 mm/yr, and parameter set 6541a

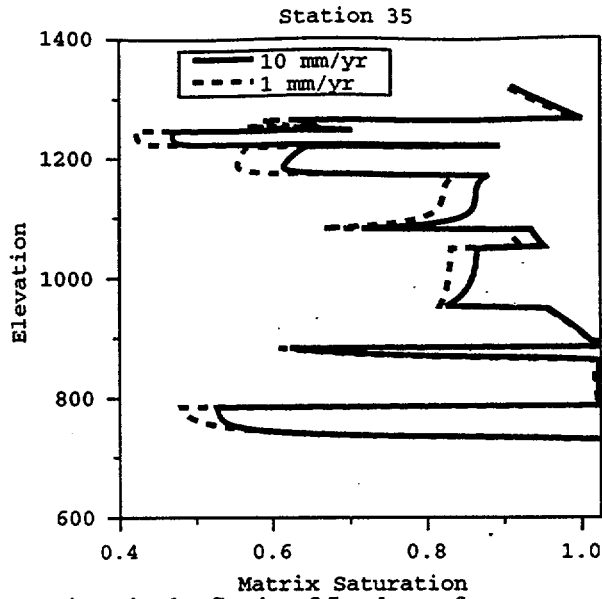


Figure 6-37. Simulated saturations in the Station 35 column for parameter set 6541a.

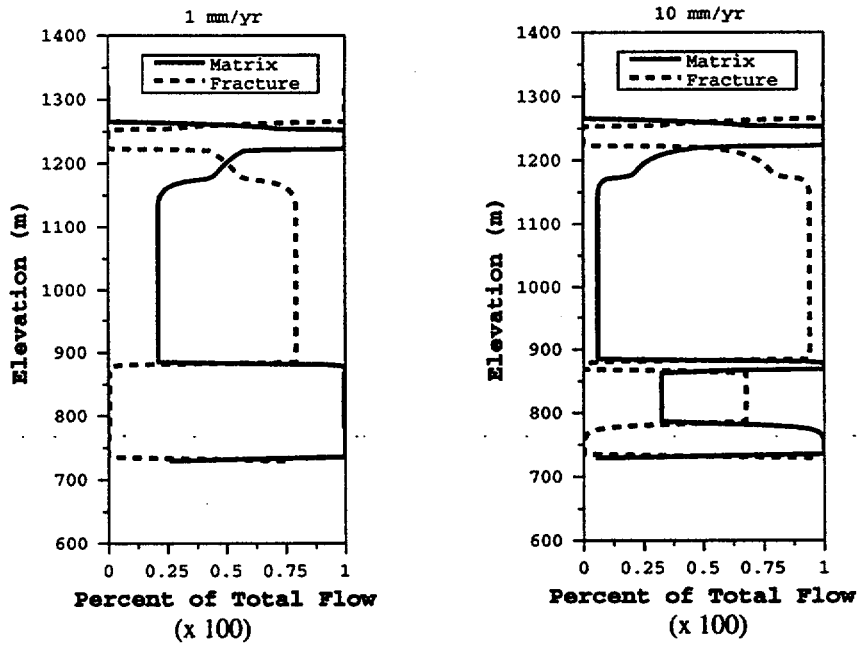
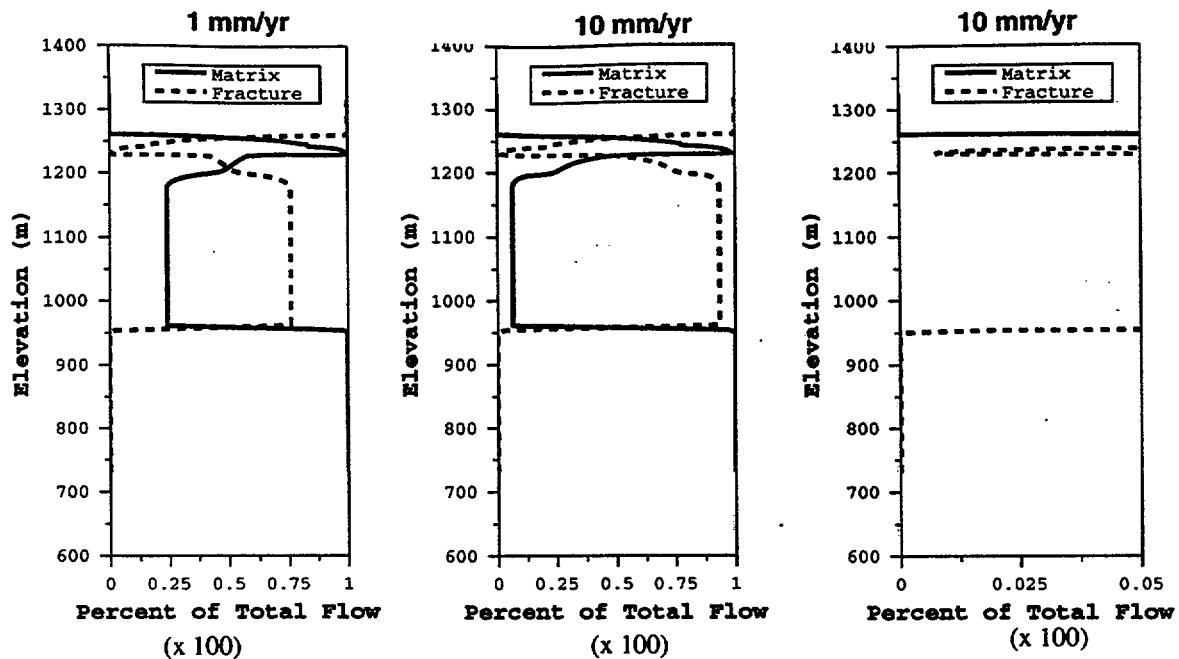


Figure 6-38. Simulated flux distribution in the Station 35 Column for parameter set 6541a at 1 and 10 mm/yr infiltration rate.



**Figure 6-39.** Simulated flux distribution in the Station 57 column for parameter set 6541a at 1 and 10 mm/yr infiltration rate. Also shown is lowest 5% of total flow to highlight non-zero fracture fluxes in PTn. Layer resolution in Calico Hills not provided due to focus above ESF in these simulations.

### Comparing Parameter Sets

As discussed in Chapter 5, the most recent LBNL Site-Scale flow model (Bodvarsson et al., 1997) contains numerous hydrologic parameter sets that are presented as fits to the existing matrix saturation data (and to some extent, matrix potential data). In this study, we primarily focus on parameter set 6541a and modifications to it due to the Performance Assessment interest in this parameter set. However, the primary parameter in the LBNL report appears to be the 6412a and 6412b sets found in Table 6-4-1.2 of that report. These sets have been compared in Chapter 5 with respect to simulated saturation profiles and simulated radionuclide transport from the potential repository to the water table. Here we briefly examine the differences in simulations of  $^{36}\text{Cl}$  from ground surface to the potential repository horizon using these two parameter sets. Figure 6-40 shows the breakthrough curve at ESF station 35 for property set 6412b. Comparing this plot with the Station 35 breakthrough in Figure 6-36 where parameter set 6541a was used, we see that there is substantially more early arrivals resulting from fracture flow in the PTn. To demonstrate this,

Figure 6-40 also displays the flux distribution for the 5 mm/year simulation. In the PTn, using the 6541a properties, the fractures account for the majority of the flow, thus the large percent of early arrival times simulated with the breakthrough analysis. Due to the large amount of flow yielding fast travel times from the surface to the ESF, one would expect indicators of young water in both the ESF as well as the perched water if the 6412b parameter set represented the actual system. The implications with respect to perched water are addressed in Chapter 7. In the ESF, we would expect a ubiquitous distribution of bomb-pulse signals. Since that does not appear to be the case, and because the perched water analyses indicate water with ages between 3,000 and 15,000 years, this parameter set can be reasonably ruled out for further consideration. The implications are that a uniform scaling of the reduction in fracture-matrix coupling is probably not the best approach for calibration of material properties to matrix saturations.

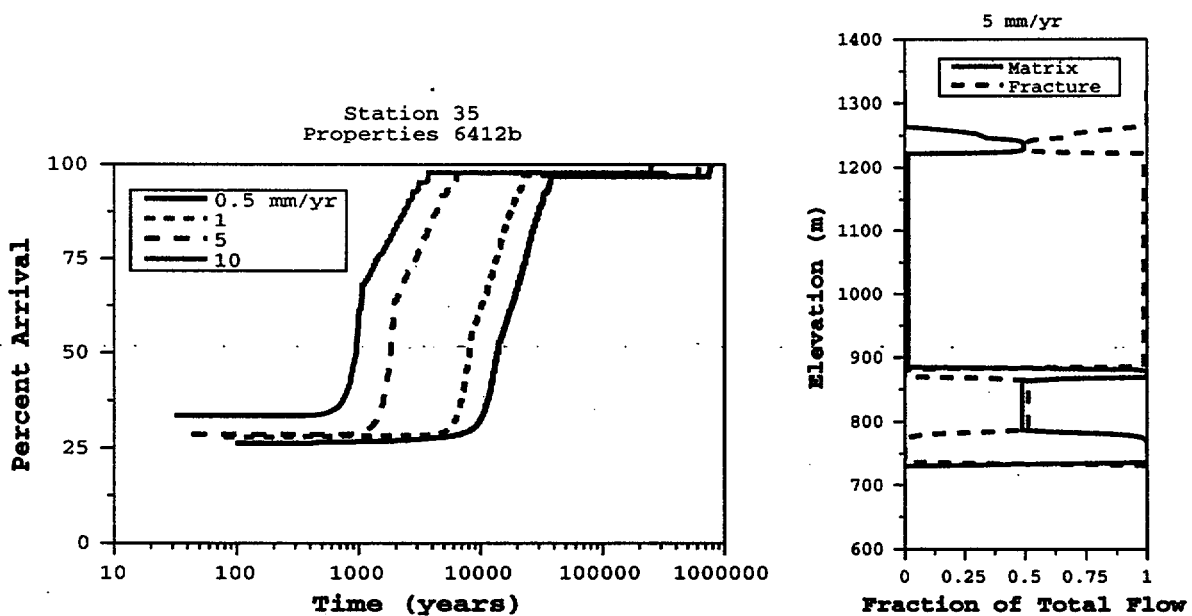


**Figure 6-40.** Breakthrough curve at ESF for property set 6412b at Station 35. Also shown is flux distribution for 5 mm/yr case.

### Parameter Set 6541b: A Slight Modification to the 6541a Parameter Set

The 6541b parameter set was described in the two- and three-dimensional simulations sections earlier in this chapter. It is our modification to LBNL's 6541a set in which we simply eliminate the fracture saturation based reduction in fracture-matrix coupling in the PTn. The result is virtually identical matrix saturation simulations. Figure 6-41 shows the minor difference in simulated saturations at the repository column for these two different parameter sets. There is a maximum difference in saturation of 0.3 in the upper PTn. However, the effect of this property modification on transport simulations is more significant than it is on saturation simulation, as is demonstrated in the next section.

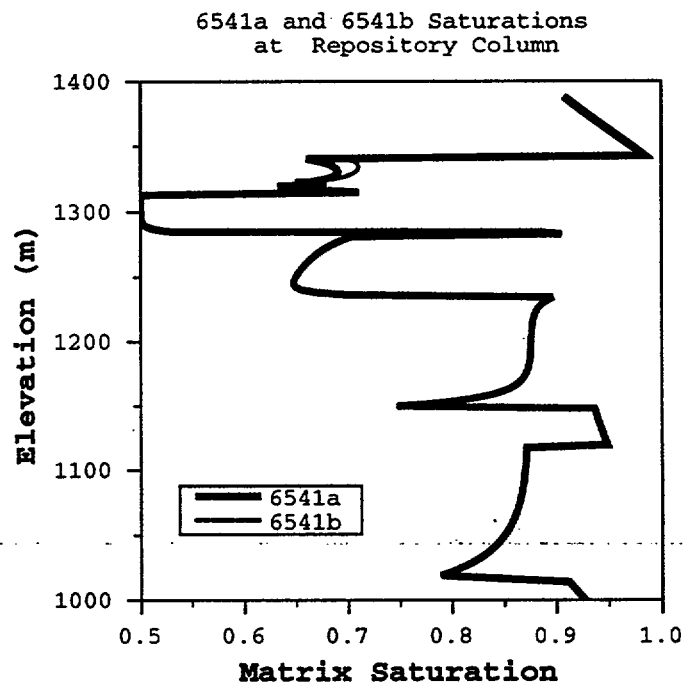


**Figure 6-41.** Comparison of saturations simulated in upper section of repository column with property sets 6541a and 6541b for 10 mm/yr.

### Fault Zone PTn Properties

In zones of tectonic activity, it is highly likely that the fracture permeability of the PTn increases. The modification of PTn fracture properties in the dual permeability model is discussed in detail in Robinson et al (1996). Here we implement a representative case from the variety of modifications investigated previously. To represent the increased fracturing in fault zones, a new property set, 6541ft, is developed. It is identical to 6541a except the fracture permeability in the PTn is increased by one order of magnitude. The result of this modification is such that fractures in the PTn that start off with flow are more likely to continue flowing to the bottom of the PTn because the residence time is lower with less opportunity imbibition into the matrix.

### Transient Flow

For the following comparisons, both steady state and transient flow are considered. The case of 10-5-10 (cumulative volume of 10 mm/yr applied once every 5 years for 10 days) is primarily considered due to its sharp contrast with steady state 10 mm/yr flow.

#### **6.12.4 Comparisons: Three Property Sets for Steady-State and Transient Flow.**

At each of the three stations considered in this section, the arrival times at the potential repository horizon are compared for three property sets (6541a, 6541b, and 6541ft) and for steady-state flow at 10 mm/yr and transient flow with 10-5-10 application. Figure 6-42 compares the breakthrough curves at Station 35. The fault-zone properties lead to greatest amount of early arrival. The 6541a and 6541b sets yield similar results with 6541a leading to slightly faster early arrivals. This pattern is exactly what should be expected as the potential for PTn fracture flow is decreased from 6541ft to 6541a to 6541b. The transient pulses lead to slightly more sustained flow in the fractures and thus a greater amount of early arrival, particularly for the 6541ft properties.

Figure 6-43 shows the responses at Station 57. Again the fault-zone properties lead to the most early arrival (bomb-pulse era signal), followed by the 6541a set and finally the 6541b set. Here, however, the difference between 6541a and 6541b is more substantial than at Station 35. Whereas the 6541b case does not lead to a bomb-pulse signal, the 6541a case does. It is also

interesting to note that the steady-state flow fields for 6541ft and 6541a lead to more early arrival than the pulsed, episodic cases. A complete testing of all possible episodic schedules has not been conducted, but, from these limited number of runs, we can infer what simulated processes are controlling the calculated results. In the episodic case, a large pulse of water enters the PTn fractures carrying the particles that were released at the surface. As the pulse moves through the PTn, more and more water imbibes into the matrix bringing particles into the slow moving matrix flow system as well. Without the fluid associated with steady state flow to keep the particles moving along in the fracture, more particles follow the flow into the matrix during the 5 year imbibition period. For this particular case, there is actually more imbibition in the transient flow scenario than in the steady-state flow scenario. At lower average annual infiltration rates, the trend is probably reduced because a greater percentage of the steady-state flow will imbibe into the drier PTn matrix.

Figure 6-44 shows the simulated breakthrough for the 10 mm/yr comparison at the repository column. This location has the thickest PTn and hence shows the least likelihood for sustained transient flow in the PTn. However, for the fault-zone properties there is some and the 6541a properties show slightly more fracture flow than 6541b, especially for episodic flow conditions.

### Additional Transient Cases

Due to the relevance of these studies at the potential repository, the remaining simulations of transient effects are performed on the repository column only. Figure 6-45 compares the effects on early breakthrough of increasing the amount of water applied for 10 days every 5 years. Other than moving the mean breakthrough time up due to the greater total flux of water, the effect on early arrival time is not particularly different than it was for the 10 mm/yr average. This indicates a favorable damping capacity of the PTn, at least where it is thicker than near Station 57 where such pulses did not appear to be damped out.

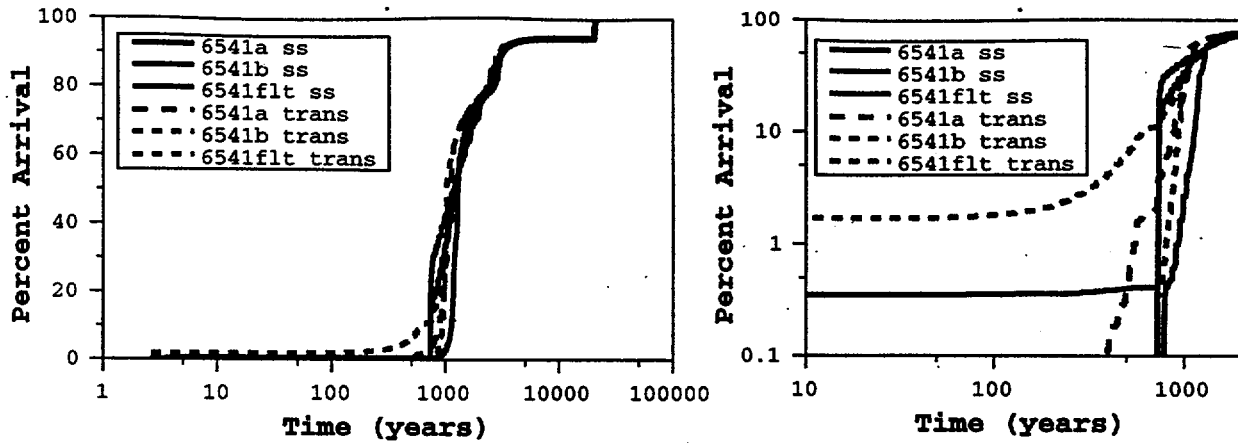


Figure 6-42. Station 35 breakthrough comparison for 10 mm/yr average annual infiltration rate. Three property sets (identified in legend) compared for steady-state (ss) and transient (trans) infiltration. Transient model, 10-5-10, is 10 mm/yr accumulation applied over 10 days every 5 years. Log plot on right illustrates component of early arrival

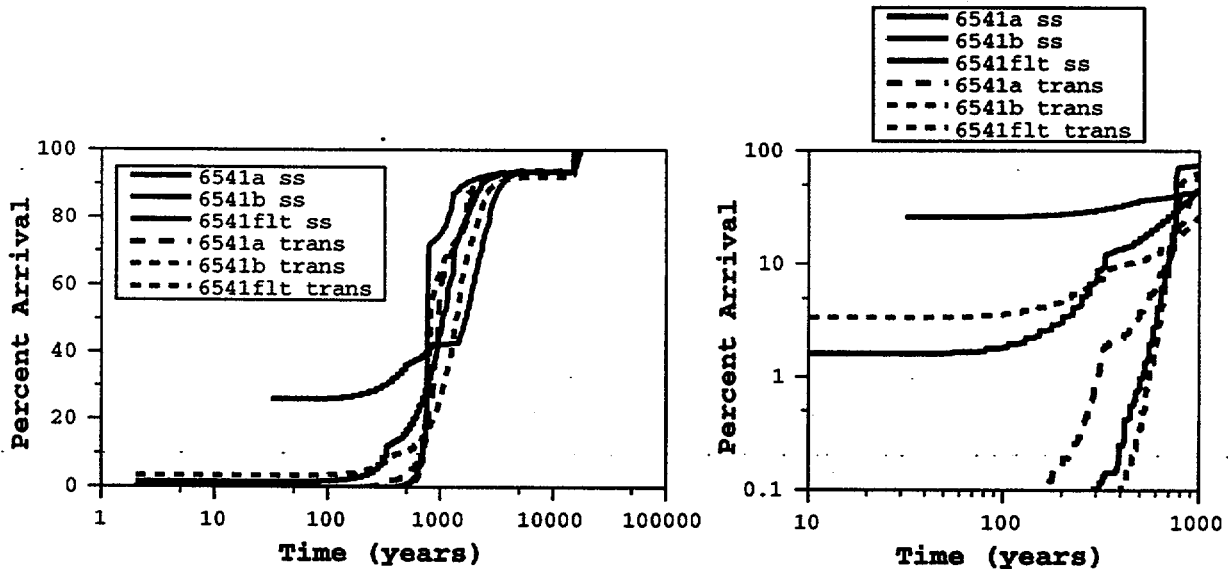
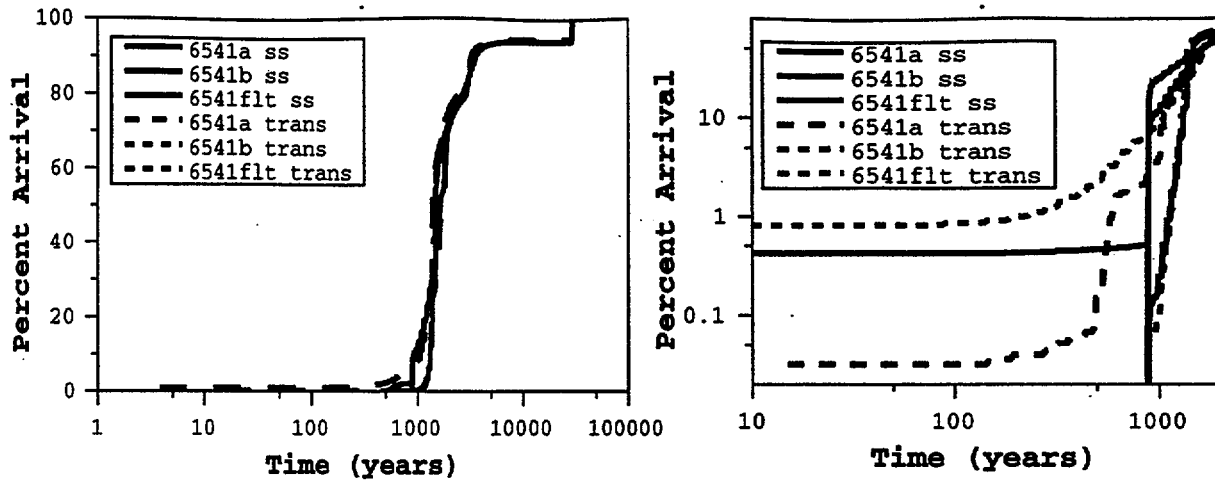


Figure 6-43. Station 57 breakthrough comparison for 3 property sets at steady state (ss) and in transient (trans) infiltration model, each with mean annual infiltration rate of 10 mm/yr. Property sets are 6541a, 6541b, and 6541flt. Transient mode is 10 mm/yr accumulated over 10 days every 5 years (10-5-10).

When considering the effect of transients on facilitating fracture flow in the PTn, the duration of the transient should be considered. In Figure 6-46, we examine the difference between 10 day infiltration events and 90 day infiltration events. In each case, the average infiltration rate



**Figure 6-44.** Repository column breakthrough comparison for 3 property sets at steady state (ss) and in transient (trans) infiltration model, each with mean annual infiltration rate of 10 mm/yr. Property sets are 6541a, 6541b, and 6541flt. Transient mode is 10 mm/yr accumulated over 10 days every 5 years (10-5-10).

is 10 mm/yr and the frequency of events is every 5 years. Although the percent of water coming through the PTn fractures (arrivals significantly earlier than the mean travel time) is small, it is interesting that the 90 day transients apparently lead to more fracture flow in the PTn, This indicates that, for the properties uses, a greater amount of a large short pulse can be imbibed into the PTn matrix than a pulse of longer duration but equal volume. Due to the transient, this simulated behavior may shed some light on the rate at which the imbibition process occurs relative to the flow rate and frequency of flow events..

Another way to examine the effect of transients at the potential repository is to simulate the flux response to infiltration transients at the surface. Figure 6-47 shows the different responses for the three different property sets considered in this section when a 10-5-10 model of transient infiltration is specified. The whereas the 6541b properties almost completely damp any fluctuations, the 6541a properties lead to an interesting long-time fluctuation at the potential repository. The 6541flt properties allow an increase of decrease in flux of about ten percent at the potential repository after each infiltration event. The flux profile also follows the long-time

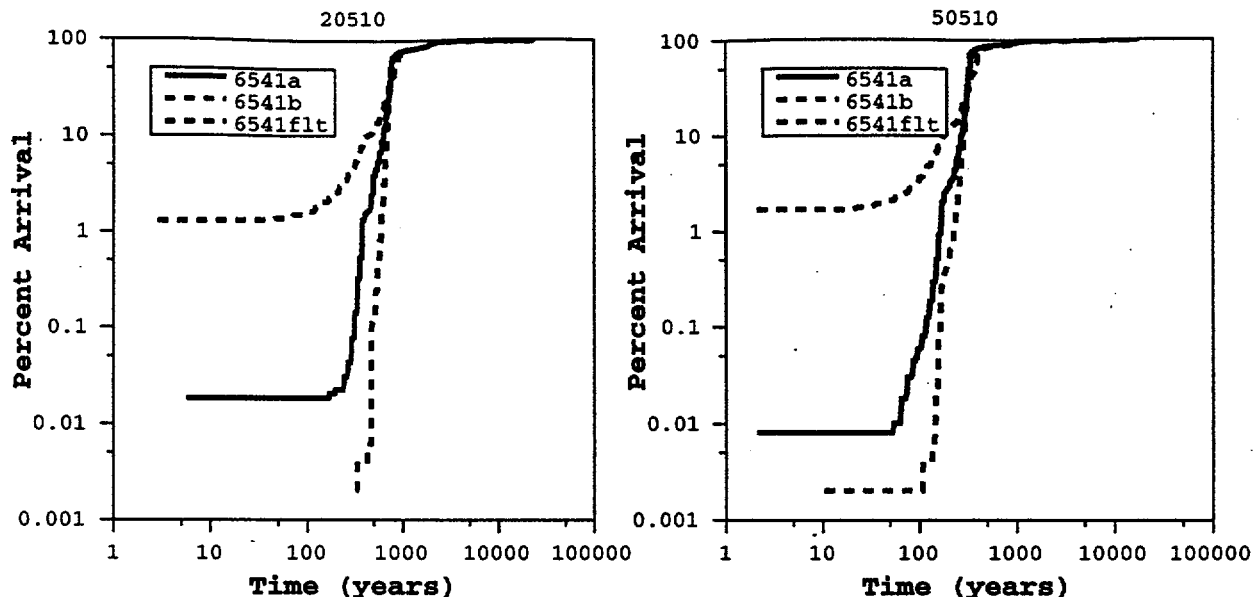


Figure 6-45. Comparison of breakthrough curves at potential repository horizon for transient simulations with a) 20 mm/yr average and b) 50 mm/yr average. All water is applied for 10 days every 5 years.

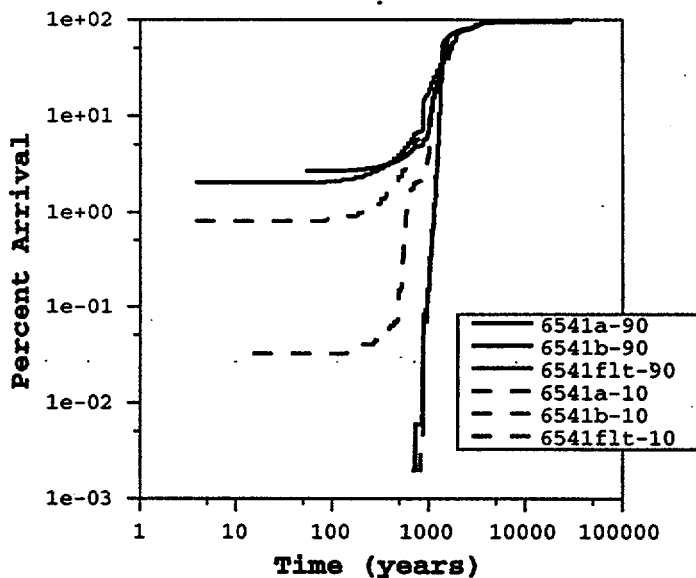
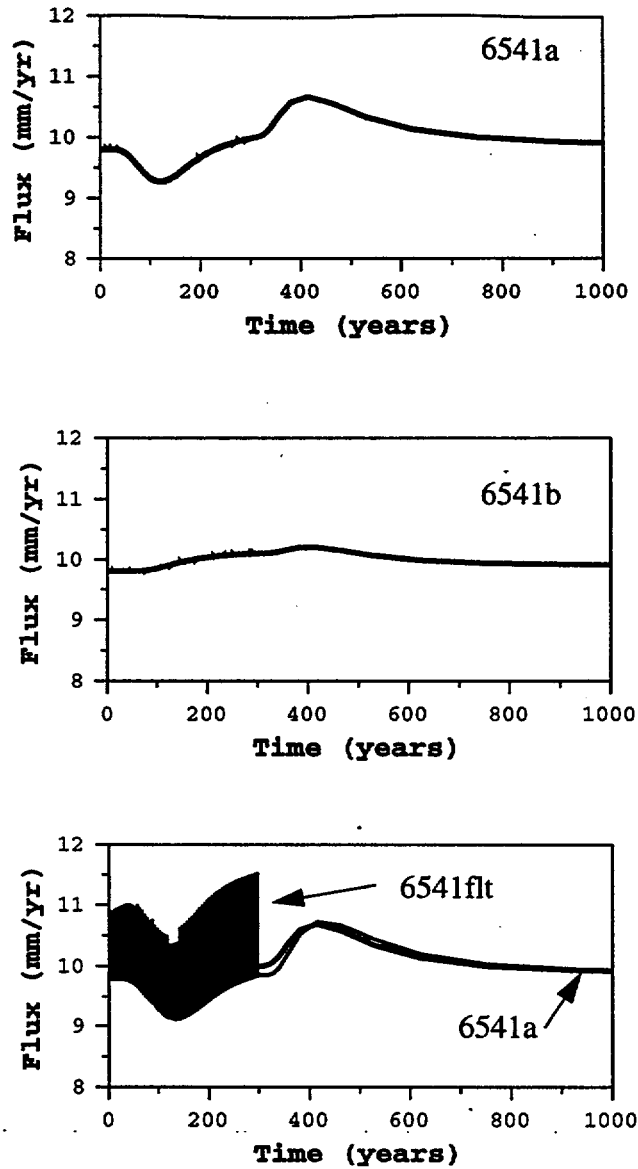


Figure 6-46. Comparison of breakthrough curves for 10 day duration transient and 90 day duration transients. Average annual infiltration for all cases is 10 mm/yr.

variation of 6541a. The reason for this behavior is not immediately known. Further investigations will determine if it is a response representative of the wetting and drying of PTn matrix material or



**Figure 6-47.** Simulated flux variation responses at potential repository for 10-5-10 transient infiltration rate at the surface. 300 years of transient followed by 700 years of uniform 10 mm/yr infiltration. The shaded portion of the 6541ft curve represents the short-term transients at the repository horizon.

just a boundary effect of the simulation. However, if it were a boundary effect, one would expect the 6541b run to behave in a similar manner.

### 6.13 Conclusions

---

In this study, we reconfirm that modified, fault-zone PTn properties lead to simulations of bomb-pulse age solutes arriving at the potential repository horizon. Away from fault zones, the prediction of bomb-pulse age solutes arriving at depth is sensitive to the hydrologic parameter set (namely the model for fracture-matrix interaction), the PTn thickness, and the flow rate. Transport models were used to investigate relationships of these three controlling factors in order to develop a methodology for predicting fast paths at unsampled locations.

The fracture-matrix interaction model for the PTn plays a significant role in predictions of whether bomb-pulse signals penetrate the PTn completely. Varying the model has little effect on simulated saturations, but large effect on the depth to which bomb-pulse solutes can travel. Of the parameter sets investigated (see Table 8-2), set 6412b led to substantial amounts of PTn fracture flow. Sets 6541a and 6541b show similar characteristics in terms of the very small amount of PTn fracture flow that is simulated. However, the small difference between the two sets is the difference between simulations of bomb-pulse signals arriving at depth or not. Therefore, this study indicates that incorporating subsurface geochemistry into the calibration process may serve to reduce the number of possible parameter sets that characterize the flow system.

The relationship between PTn thickness and infiltration rate on bomb-pulse signal predictions at the potential repository horizon was investigated with the site-scale three-dimensional transport model. As the PTn thins to the south, the prediction of bomb-pulse arrivals at the potential repository horizon increase. With the 6541a parameter set, the bomb-pulse predictions extended further north (under thicker PTn) than for the 6541b parameter set. The 6541a parameter set also leads to predictions of more bomb-pulse travel times to the ESF than the 6541b set. However, there is a strong inconsistency between either model parameter set and the data. Whereas the incidence of bomb-pulse predictions with the model is highest in the south ramp of the ESF due to thin overlying PTn, the data indicate virtually no bomb-pulse signals. The ESF stations where bomb-pulse has been found are further north, where the model predicts less bomb-

pulse travel to the ESF. However, the locations where bomb-pulse signals have been measured are mostly well correlated with faults. The site-scale model does not resolve any of the faults associated with the ESF bomb-pulse predictions. Thus, one-dimensional models are used to investigate processes and parameters. As described above, modification of PTn properties to represent increased fracturing in faults leads to predictions of bomb-pulse in the ESF, even where the PTn is relatively thick.

The transport model was also used to investigate the role of episodic infiltration on bomb-pulse transport and flux variations at the potential repository horizon. Differences between parameter sets 6541a and 6541b were minor as the PTn damps the pulsed input almost completely. The difference in predicted bomb-pulse transport between these two sets remains due to slight differences in the small amount of sustained fracture flow in the PTn. The difference is greatest where the PTn is thinnest because fracture flow with set 6541a is sustained through the entire PTn. As the PTn thickens, fracture flow through the entire unit is not sustained with either set. In fault zones, on the other hand, fracture flow is sustained and the pulses are not damped completely. Where the PTn is thinnest, simulated pulses at the potential repository are greatest, an issue of potential significance to repository design and performance assessment.

With the new geologic model (Zelinski and Clayton, 1996), the new hydrologic parameters (Bodvarsson et al., 1997), and the spatially distributed infiltration map (Flint et al., 1996), simulated transport times through the PTn matrix are quicker than with previous models (Fabryka-Martin et al., 1996b). Whereas most of the solutes arriving at the ESF or the potential repository horizon in transport simulations had travel times on the order of 10,000 years in earlier studies, the median simulated travel times are now between 1,000 and 7,000 years. There still is a component of simulated solute arrival times (or water ages) that are greater than 10,000 years, but it represents only 5 to 20% of a sample. Thus, there may be a discrepancy in the interpretation of elevated  $^{36}\text{Cl}/\text{Cl}$  signals away from fault zones. Previously, our interpretation was that these signals indicated water that entered the system in the Pleistocene with a higher  $^{36}\text{Cl}/\text{Cl}$  ratio than

is found in modern water. We also interpreted these signals as being representative of the water flowing past the sample location. If, however, most of the water flowing past a sample location is really Holocene in origin (e.g. less than 10,000 years old) as the current simulations indicate, then the ESF samples are not representative of most of the water flowing through the TSw. In other words, an ESF sample may, in fact, indicate water older than 10,000 years, but it may indicate very little about the age of water flowing in the TSw fractures. The other conceptual model is that all of the elevated ESF samples contain a small bomb-pulse component. Whereas the recent PTn model of fracture-matrix interaction supports this conceptual model, the TSw fracture-matrix interaction model would need revision to prevent all bomb-pulse signals from completely bypassing the TSw matrix. Such a conceptual model also leaves questions about the apparent present day signal under thin PTn and higher signals in fault zones and away from fault zones under thicker PTn. We expect further closure on these apparent discrepancies will be reached with additional geochemical analysis.